

Mass transfers during fluid–rock interactions at divergent and convergent plate boundaries

Dissertation

zur Erlangung des
Doktorgrades der Naturwissenschaften
(Dr. rer. nat.)

am Fachbereich Geowissenschaften
der Universität Bremen

vorgelegt von

Elmar Albers

Bremen, Dezember 2018

Gutachter

Prof. Dr. Wolfgang Bach
Fachbereich Geowissenschaften
Universität Bremen
Klagenfurter Str. 2-4
28359 Bremen
wbach@uni-bremen.de

Prof. Dr. Timm John
Institut für Geologische Wissenschaften
Freie Universität Berlin
Malteserstr. 74-100
12249 Berlin
tim.john@fu-berlin.de

*Science, my lad, is made up of mistakes,
but they are mistakes which it is useful to make,
because they lead little by little to the truth.*

Jules Verne,
Journey to the Center of the Earth
(1864, in French)

Contents

Preface	vii
Abstract	1
Kurzfassung	4
1 Introduction	9
1.1 Fluid–rock interactions in the marine realm and their significance	9
1.2 Life cycle of oceanic lithosphere	11
1.2.1 Divergent plate boundaries	11
Detachment faulting	13
Hydrothermal fluid–rock interactions	16
15°20' N Fracture Zone area, Mid-Atlantic Ridge	19
1.2.2 Convergent plate boundaries	21
Fluids, fluid–rock interactions, and element cycling	22
Mariana serpentinite mud volcanism	27
1.3 Motivation for this thesis and scientific questions	31
1.4 Outline and scientific contributions	34
References	36
2 High-temperature hybrid rock hydration	45
Abstract	45
2.1 Introduction	46
2.2 Analytical procedures	48
2.2.1 Rock alteration and deformation textures	48
2.2.2 Whole-rock analyses	49
2.2.3 Electron microprobe analyses	50
2.2.4 Laser ablation ICP-MS analyses	50
2.3 Results	51
2.3.1 Petrography and mineral chemistry	51

2.3.2	Whole-rock geochemistry	57
2.3.3	Temperature estimates	60
2.4	Thermodynamic calculations	64
2.4.1	Reaction path modeling with EQ3/6	64
2.4.2	T – X sections with Theriak/Domino	67
2.5	Discussion	70
2.5.1	Fluid-induced metasomatism versus magmatic impregnation	70
2.5.2	Alteration of hybrid lithologies at elevated temperatures	72
2.5.3	High-temperature deformation of altered hybrid lithologies	73
2.5.4	Prevailing static alteration at low temperatures	75
2.5.5	Implications for oceanic detachment faults	75
2.6	Summary and conclusions	77
	Acknowledgements	77
	References	78
3	Clues on carbon cycling	85
	Abstract	85
3.1	Introduction	86
3.2	Study area and materials	88
3.3	Methodology	88
3.3.1	<i>In situ</i> analyses	88
3.3.2	Isotope analyses	90
3.4	Results	91
3.4.1	Host rocks	91
3.4.2	Carbonate \pm silicate \pm sulfate veins	92
3.5	Discussion	99
3.5.1	Recycling of Pacific crust through serpentinite mud volcanism	99
3.5.2	Carbonate formation in the subduction channel	100
3.5.3	Processes in the mud volcano conduits	104
3.5.4	Fluid release, element transfers, and fluid–mineral interactions	107
3.5.5	Element sources	108
3.5.6	Implications for carbon cycling	109
3.6	Conclusions	110
	Acknowledgements	111
	References	111

4	Shallow subduction zone serpentinization	119
	Abstract	119
4.1	Introduction	120
4.2	Methodology	123
	4.2.1 Electron microprobe analyses	124
	4.2.2 Laser ablation ICP-MS analyses	124
4.3	Petrography	124
	4.3.1 Primary lithologies	124
	4.3.2 Serpentinization	125
4.4	Mineral chemistry	129
	4.4.1 Major element mineral chemistry	129
	4.4.2 Trace element mineral chemistry	131
4.5	Discussion	136
	4.5.1 Polyphase serpentinization at the basal plane of the mantle wedge	136
	4.5.2 Evolution of serpentinizing fluids and FME sources	138
4.6	Summary and conclusions	145
	Acknowledgements	146
	References	146
5	Conclusions and outlook	153
	Acknowledgements	157
	Appendix	159
	A.1 Supplementary Information to Chapter 2	159
	A.2 Supplementary Information to Chapter 3	166
	A.3 Supplementary Information to Chapter 4	169
	B Additional publications	174

Preface

This thesis is submitted to obtain the degree of *Doctor rerum naturalium* (Dr. rer. nat.) at the University of Bremen. Research in the context of this project has been conducted under the supervision of Prof. Dr. Wolfgang Bach within the research group ‘Petrology of the Ocean Crust’ at the Department of Geosciences and in close collaboration with the MARUM – Center for Marine Environmental Sciences. It was carried out from November 2015 until December 2018.

Rock samples studied in this project originate from the International Ocean Discovery Program (IODP) Expedition 366 as well as from Ocean Drilling Program Leg 209. I was invited to sail Expedition 366, a research drilling campaign onboard D/V *JOIDES Resolution* to the Mariana forearc in the Western Pacific from December 2016 to February 2017. Leg 209 was a drilling expedition to the Mid-Atlantic Ridge, 15°20' N, that took place in 2003; I re-sampled Leg 209 recovery at the IODP Bremen Core Repository at MARUM.

This cumulative dissertation is subdivided into

- an introductory chapter providing an overview on interactions between fluids and rocks,
- the manuscripts presenting new insights into this complex topic as gained from the research conducted during my PhD project, and
- a summarizing chapter with conclusions and implications of my work.

The first chapter familiarizes the reader with the topic of fluid–rock interactions in the World Ocean and is thought to provide the necessary background to judge the significance of this work. Particular topics addressed here cover fluid–rock interactions in the marine realm; magmatic, tectonic, and hydrothermal processes at divergent plate boundaries and information on the 15°20' N Fracture Zone area at the Mid-Atlantic Ridge, study site of my first research project; and fluid-related processes at convergent plate boundaries and information on the forearc of the Mariana subduction system, my second working area. Arising from these backgrounds, open questions and objectives of my research are addressed.

An overview on the manuscripts that resulted from my scientific work is given towards the end of the first chapter. The three manuscripts have been written for individual publication in international peer-reviewed scientific journals. Along with the studies, contributions of the individual authors are listed. I hold the first authorship for these manuscripts. The manuscripts themselves are presented in the following chapters.

The thesis closes with overarching implications derived from the findings presented in the manuscripts as well as with an outlook on future work.

The appendix comprises supporting materials on the individual manuscripts. It further lists information on publications to which I contributed as co-author and which were published during my PhD, and on conference contributions I made over the last three years.

This work has been financed through the German Research Foundation (Deutsche Forschungsgemeinschaft) grant BA 1605/13 and grant BA 1605/18-01 in the Special Priority Program 527 ‘International Ocean Discovery Program.’ Additional financial support was provided by the Bremen International Graduate School for Marine Sciences (GLOMAR) and by the BremenIDEA – International Doctoral Education Action program, a initiative by the German Academic Exchange Service (DAAD), the Federal Ministry of Education and Research (BMBF), and the University of Bremen.

Elmar Albers
Bremen, 2018

Abstract

Fluids and reactions between fluids and rock evoke significant mass and energy transfers in the marine realm. These interactions connect the lithosphere with the ocean and bear the potential to alter the physical and chemical states of both considerably. Fluid-induced metamorphic or metasomatic processes have direct implications for global geochemical cycles, geodynamics, or the biogeochemical Earth system. Under favorable temperature and pressure conditions, the processes take place all the way from spreading ridges to deep-sea trenches—but the major sites of fluid–rock interactions are the mid-ocean ridges and subduction zones themselves. The rates and underlying mechanisms of many processes are, despite recent advances, still poorly understood.

Within this thesis, I investigated mass transfers associated with fluid–rock interactions at the Mid-Atlantic Ridge and the Mariana subduction system. The data obtained bring hitherto novel insights how reactions between fluids and rock affect the oceanic lithosphere during its life cycle.

The first manuscript addresses the common occurrence of mechanically weak minerals in shear zone rocks of oceanic detachment faults and their role in strain localization. The secondary mineral assemblages seem to be alteration products of lithologies with compositions intermediate between those of mantle peridotite and magmatic rocks. Such compositions either reflect metasomatic mass transfers or they relate to the impregnation of lithospheric mantle with basaltic or more evolved melts. My co-authors and I studied chlorite–amphibole-rich shear zone rocks from a detachment fault zone in the 15°20′ N Fracture Zone area, Mid-Atlantic Ridge. Geochemical compositions of these rocks imply that they formed by mixing between peridotite and gabbro. Textural observations indicate a strong contrast between the deformation intensity of these hybrid peridotite–gabbro rocks and the host serpentized peridotite. Geothermometry data give formation temperatures of >500 °C for synkinematic amphibole, zircon, rutile, and titanite. Chlorite appears intergrown with these phases and likely grew at similar temperatures. These results are compliant to thermodynamic computations that predict comparable mechanically weak mineralogies when hydrating hybrid rocks at 500 to 600 °C, whereas secondary assemblages after pure peridotite or gabbro are considerably stronger.

Consequently, metamorphic weakening takes place to a much greater extent in rocks with a hybrid ultramafic–mafic composition than in purely ultramafic or gabbroic lithologies. Deformation may enhance fluid flow, which will in turn increase the extent of hydration and mechanical weakening. A positive feedback loop between hydration and strain localization may hence develop and facilitate the concentration of extensional tectonics into long-lived, high-displacement faults. We suggest that hybrid lithologies may play a key role in detachment faulting at slow spreading ridges worldwide.

The fate of subducted C in shallow portions of a subduction zone was examined in the second study. Few data exist that provide insight into processes affecting the long-term carbon cycle at shallow forearc depths. To better understand the mobilization of C in sediments and crust of the subducting slab, we investigated carbonate materials originating from the subduction channel below the Mariana forearc (<20 km). The Ca carbonates exist in the form of vein precipitates within metavolcanic and metasedimentary clasts. The clasts represent portions of the subducting lithosphere that were altered at lower blueschist facies conditions and were subsequently transported to the forearc seafloor by serpentinite mud volcanism. Euhedral aragonite and calcite crystal faces and the lack of deformation within the veins suggest carbonate formation in a strain-free environment, that is, after peak metamorphism affected their hosts. Intergrowth with barite and marked negative Ce anomalies in carbonate attest the precipitation within a generally oxic environment that was not controlled by serpentinitization. Carbonate isotopic compositions ($^{87}\text{Sr}/^{86}\text{Sr} = 0.7052$ to 0.7054 , $\delta^{18}\text{O}_{\text{VSMOW}} = 20$ to 24‰) imply precipitation from slab-derived fluids at temperatures within the range of ~ 130 to 300 °C . These temperature estimates are consistent with the presence of blueschist facies phases, such as lawsonite, co-occurring with the carbonates in some veins. Incorporated C is inorganic ($\delta^{13}\text{C}_{\text{VPDB}} = -1$ to $+4\text{‰}$) and likely derived from the decarbonation of carbonaceous sediment and/or oceanic crust.

The mineralizations provide evidence for the mobilization of C in the downgoing slab at depths of ~ 14 to 18 km. Our study for the first time shows in detail that a portion of this C is bound in carbonate precipitates in the subduction channel of an active convergent margin. This process may be an important asset in understanding the deep carbon cycle since it highlights that C is lost from the subducting lithosphere before reaching greater depth.

To better understand the mobilization and subsequent mass transfers of fluid-mobile elements at shallow subduction depths, my co-authors and I investigated recovery from the serpentinite mud volcanoes at the Mariana forearc within the third manuscript. The ultramafic rocks originate from the basal plane of the mantle wedge (<20 km depth to the slab) where they recorded the interaction with different slab-derived fluids during multiple serpentinitization stages. These stages are preserved in microfabrics, mineralogy, and major and trace elemental compositions in distinct generations of serpentine. *In situ* analyses of the serpentine revealed that initial hydration occurred under reducing conditions by Si-rich fluids. Serpentine is characterized by high concentrations of Li, B, Sr, Rb, Cs, and Ba. Subsequent interactions with Si- and FME-poor fluids occurred in the serpentinite mud volcano conduits and commonly lead to the formation of Fe-rich brucite. Oxidic conditions prevailed during alteration of the clasts within the mud volcanoes.

Variations of FMEs in serpentine, being a function of slab depth, allowed us to reconstruct fluid and FME sources. Serpentine from the shallow-sourced Yinazao mud volcano exhibits high Rb/Cs ratios of ≤ 37 , highest concentrations of Li and B, but lowest Rb, Sr, Ba, and Cs contents. The serpentinitizing fluids were influenced by pore waters and the breakdown of opal in the subducted sediments. Serpentine at intermediate-sourced Fantangisña has Rb/Cs ratios of < 10 , but higher Rb and Cs contents as Yinazao,

representing the H₂O- and FME-release from clays in the subducting sediments. Fluids at deep-sourced Asit Tesoru as well originate from clay breakdown but highest concentrations of Rb, Sr, Cs, and Ba are further indicative of the beginning dehydration of altered oceanic crust. Including data from South Chamorro serpentinite mud volcano (Kahl et al., 2015, doi:[10.1016/j.lithos.2015.03.015](https://doi.org/10.1016/j.lithos.2015.03.015)), we provide a continuous record of slab dehydration reactions at forearc depths (~13 to 18 km slab depth) and the related mobilization of FMEs as well as their transport into the mantle wedge. Whereas some of the FMEs contained in serpentinite are transported back to the seafloor through serpentinite mud volcanism in the Mariana subduction zone, they will remain at depth in most other continental margins.

Kurzfassung

Im marinen Milieu sind Massen- und Energietransporte zu einem großen Teil auf Wechselwirkungen zwischen Fluiden und Gestein zurückzuführen. Die Wechselwirkungen verbinden den Meeresboden mit dem Ozean und bewirken Veränderungen dieser in Hinsicht auf ihre physikalischen und chemischen Eigenschaften. Durch Fluide hervorgerufene metamorphe und metasomatische Reaktionen können dabei direkten Einfluß auf globale Stoffkreisläufe und geodynamische Prozesse, sowie auf biogeochemische Abläufe, nehmen. Unter geeigneten Temperatur- und Druckbedingungen finden diese Prozesse von der Bildung der Ozeankruste an divergenten bis hin zu ihrem Absinken an konvergenten Plattengrenzen statt – hauptsächlich jedoch an den mittelozeanischen Spreizungszentren und den Subduktionszonen selbst. Obwohl in der Forschung jüngst große Fortschritte erzielt wurden bleiben nicht nur die Abläufe vieler Prozesse sondern auch deren zugrundeliegende Mechanismen unverstanden.

In dieser Dissertation habe ich mich mit Massentransporten am Mittelatlantischen Rücken und der Marianen-Subduktionszone beschäftigt, die mit Fluid-Gesteins-Wechselwirkungen in Verbindung stehen. Die neugewonnenen Daten liefern Erkenntnisse wie die Lithosphäre während ihres Lebenszyklus durch Reaktionen zwischen Fluiden und Gestein beeinflusst wird.

In der ersten Studie wird das häufige Vorkommen von mechanisch weichen Mineralen in Scherzonen ozeanischer Abscherstörungen sowie deren Rolle in der Initiierung und Entwicklung der Scherzonen behandelt. Die sekundären Mineralvergesellschaftungen scheinen Alterationsprodukte von Lithologien zu sein, deren Zusammensetzungen intermediär zwischen Mantelperidotit und magmatischem Gestein liegen. Solche Zusammensetzungen können entweder durch metasomatische Massentransfers oder durch das Eindringen von basaltischen oder differenzierteren Schmelzen in ultramafische Gesteine zustande kommen. Zusammen mit meinen Co-Autoren habe ich Chlorit-Amphibol-reiche Scherzonengesteine von einer Abscherstörung nahe der 15°20' N Transformstörung am Mittelatlantischen Rücken untersucht. Die geochemischen Zusammensetzungen der Gesteine deuten auf eine Vermischung von Peridotit und Gabbro hin. Mikrot Texturen implizieren starke Unterschiede in der Deformationsintensität zwischen diesen hybriden Peridotit-Gabbro-Gesteinen und dem umliegenden serpentinierten Peridotit. Geothermometrisch bestimmte Bildungstemperaturen für Amphibol, Zirkon, Rutil und Titanit in den Hybriden ergeben >500 °C. Chlorit kommt zusammen mit diesen Phasen vor, was seine Bildung bei ähnlichen Temperaturen nahelegt. Diese Ergebnisse werden in thermodynamischen Berechnungen widerspiegelt, die für die Hydratation von hybriden Gesteinen bei 500 bis 600 °C ähnliche mechanisch weiche Mineralogien vorhersagen. Sekundäre Mineralvergesellschaftungen nach reinem Peridotit oder Gabbro sind mechanisch deutlich stärker.

Die metamorphe Schwächung des Gesteins findet daher, im Gegensatz zu rein ultramafischen oder gabbroischen Lithologien, in weitaus größerem Maße in Gesteinen mit hybriden ultramafischen–mafischen Zusammensetzungen statt. Deformation in diesen Zonen ermöglicht erhöhte Fluidflüsse, was seinerseits zu weiterer Hydratisierung und mechanischer Schwächung führen kann. Auf diese Weise kann sich eine positive Rückkopplungsschleife zwischen Hydratisierung und der Lokalisierung von Scherkräften entwickeln, was wiederum die Fokussierung von Extensionstektonik in den langlebigen Abscherstörungen begünstigt. Wir nehmen daher an, dass hybride Lithologien in Abscherstörungen an langsam spreizenden Rücken weltweit eine Schlüsselstellung einnehmen.

Das Schicksal von subduziertem Kohlenstoff in flachen Abschnitten einer Subduktionszone wurde im zweiten Manuskript untersucht. Bisher existieren kaum Daten die Einblicke in den Kohlenstoffkreislauf unterhalb der Vorbögen bieten. Um die Mobilisierung von Kohlenstoff in Sedimenten und Ozeankruste der subduzierten Platte besser zu verstehen haben wir Karbonate, die aus Tiefen von <20 km aus dem Subduktionskanal des Marianen-Vorbogens stammen, untersucht. Die Kalziumkarbonate liegen als Aderpräzipitate in metavulkanischen und -sedimentären Klasten vor. Die Klasten selbst verkörpern die abtauchende Lithosphäre, die unter niedrigen blauschieferfaziellen Bedingungen alteriert und danach durch Serpentin-Schlammvulkane auf den Meeresboden des Vorbogens transportiert wurden. Die Aderpräzipitate wurden nach der metamorphen Überprägung der Wirtsgesteine in einem spannungsfreien Milieu gebildet; dies spiegelt sich in idiomorphen Aragonit- und Kalzitkristallformen und in mit den Karbonaten verwachsenen undeformierten Silikatphasen wider. Die Verwachsung mit Baryt und ausgeprägte negative Ce-Anomalien im Karbonat zeigen deren Ausfällung unter oxischen Bedingungen auf – die Umgebung war also noch nicht von Serpentinisierungsreaktionen dominiert. Die Isotopenzusammensetzungen der Karbonate ($^{87}\text{Sr}/^{86}\text{Sr} = 0.7052$ bis 0.7054 , $\delta^{18}\text{O}_{\text{VSMOW}} = 20$ bis 24‰) implizieren zum einen den Einfluss von Fluiden die der subduzierten Platte entsprungen sind und zum anderen die Karbonatbildung bei Temperaturen von ~ 130 bis 300 °C . Blauschieferfazielle Minerale wie Lawsonit, die zusammen mit den Karbonaten in einigen Adern vorkommen, bestätigen diese Temperaturabschätzungen. Der eingebundene Kohlenstoff ist anorganisch ($\delta^{13}\text{C}_{\text{VPDB}} = -1$ bis $+4\text{‰}$) und wurde vermutlich während der Dekarbonisierung von subduzierten kalkreichen Sedimenten und/oder karbonisierter Kruste gelöst.

Die Mineralisierungen veranschaulichen, dass Kohlenstoff in der abtauchenden Lithosphäre bereits in Tiefen von ~ 14 bis 18 km gelöst wird. Unsere Studie zeigt erstmalig ausführlich, dass ein Teil des Kohlenstoffs in Karbonatpräzipitaten im Subduktionskanal einer aktiven konvergenten Plattengrenze gebunden wird. Dieser Prozess stellt eine wichtige Erkenntnis im Verständnis des tiefen Kohlenstoffkreislaufes dar: er zeigt auf, dass Kohlenstoff bereits aus der subduzierten Lithosphäre gelöst werden kann bevor er in größere Tiefen gelangt.

Ziel der dritten Studie war es das Wissen über die Mobilisierung und den anschließenden Transport von fluid-mobilen Elementen (FME) in geringen Subduktionstiefen zu erweitern. Untersuchungsgegenstand waren ultramafische Gesteinsproben von den Serpentin-Schlammvulkanen im Marianen-Vorbogen, die der Unterseite des Mantelkeils

in Tiefen von bis zu 20 km entstammen. Während anhaltender Wechselwirkungen mit Fluiden, die der abtauchenden Platte entspringen, haben die Klasten verschiedene Serpentinisierungsstadien aufgezeichnet; daraus resultierten mehrere Serpentinisationen mit unterschiedlichen Mikrogefügen, Mineralogien und Haupt- und Spurenelementzusammensetzungen. Serpentin-Mikroanalytik ergab, dass die initiale Serpentinisierung unter reduzierenden Bedingung mit Si-reichen Fluiden stattgefunden hat. Diese Serpentine sind durch hohe Gehalte von Li, B, Sr, Rb, Cs und Ba charakterisiert. Spätere Wechselwirkungen mit Si- und FME-verarmten Fluiden fanden in den Aufstiegskanälen der Schlammvulkane statt und resultierten in der vermehrten Bildung von Fe-reichem Brucit. Während der Alteration der Klasten in den Schlammvulkanen waren die Bedingungen oxidisch.

Die Spurenelementgehalte im Serpentin sind abhängig von der Tiefe zu der subduzierten Platte und charakteristisch für die FME- und Fluidquellen. Serpentin im flachen Yinazao hat Rb/Cs-Verhältnisse von ≤ 37 und die höchsten Konzentrationen von Li und B, aber die niedrigsten Gehalte von Rb, Sr, Ba und Cs. Die Serpentinisierungsfluide wurden maßgeblich von Porenwässern und der Entwässerung von Opal beeinflusst. Die Rb/Cs-Verhältnisse in Serpentin im mitteltiefen Fantangisña sind < 10 und gleichzeitig sind Gehalte von B niedriger und von Rb und Cs höher als im Yinazao; dies spiegelt die Entwässerung von tonigem Sediment wieder. Die Fluide unter dem tiefen Asù Tesoru entstammen ebenfalls aus dem Zerfall von Ton – sie weisen aber deutlich höhere Konzentrationen von Rb, Sr, Cs und Ba auf, was auf die zeitgleich stattfindende Entwässerung der alterierten abtauchenden Ozeankruste hindeutet. Unter Einbeziehung der Daten vom South Chamorro Schlammvulkan (Kahl et al., 2015, doi:[10.1016/j.lithos.2015.03.015](https://doi.org/10.1016/j.lithos.2015.03.015)) legen wir einen Datensatz vor, der die Entwässerung der subduzierenden Platte unterhalb des Marianen-Vorbogens aufzeigt. Die Daten belegen die damit einhergehende Mobilisierung von FME und deren Transport in den Mantelkeil. Es liegt nahe, dass die im Serpentin eingebundenen FME an den meisten konvergenten Plattengrenzen in größere Subduktionstiefen befördert werden.

1 Introduction

1.1 Fluid–rock interactions in the marine realm and their significance

“Aqueous fluids make things happen inside the Earth” was recently stated by Thompson (2010). And indeed, many processes on the Earth upon which we live seem to be directly influenced or even controlled by the presence of fluids and associated interactions with rocks.

Fluids play a particularly crucial role to the marine realm. About 96.5% of the total volume of water on Earth is stored in the oceans (e. g., Shiklomanov, 1993). Fluids also circulate through the oceanic lithosphere whereby they connect the lithosphere with the oceans that itself again interact with the atmosphere. One complete ocean water volume is thereby cycled through the oceanic crust every 10 Ma (Kadko, 1993). On their journey, the fluids pick up and transfer vast amounts of heat and mass—hydrothermal circulation hence plays a major role in the physico-chemical state of the oceanic crust as well as of the World Ocean (e. g., Elderfield and Schultz, 1996; Stein and Stein, 1994).

A great deal of the hydrothermalism takes place at or close to mid-ocean ridges. After entering the seafloor, large gradients in chemical potential between fluids and rocks drive reactions between the two. Fluids dissolve, move, or precipitate cations, which directly imply an alteration of the chemistry and mineralogy of the oceanic crust and result, for example, in the formation of economic deposits (e. g., Tivey, 2007). Ions dissolved in the fluids are carried back into the ocean, the chemistry of which is consequently also modified (e. g., German and Seyfried, 2014). However, the impacts of fluid–rock interactions can as well be more long-termed and complex. For instance, along slow-spreading ridges (Fig. 1.2) tectonically hosted hydrothermal systems are particularly abundant and allow fluids to penetrate deep into the lithosphere (e. g., deMartin et al., 2007; German et al., 2010). In the subseafloor, fluids cause metamorphic reactions that can lead to the formation of mechanically weak minerals that in turn facilitate faulting and seafloor spreading (e. g., Picazo et al., 2012). Seafloor spreading has a direct effect on the seafloor topography, which again may influence ocean circulation patterns (e. g., Gille et al., 2004). The circulation patterns on their part may have a bearing on local and global climate (e. g., Rahmstorf, 2002).

In addition, interactions between fluids and rock can have essential consequences for the biological Earth system. Trace fossils of a deep biosphere, which uses chemical species released during fluid–rock interactions as sources of energy, are found throughout the upper 500 m of the oceanic crust (e. g., Furnes and Staudigel, 1999). Microbial communities thriving on the chemical fluxes also frequently occur where hydrothermal fluids vent at the



Figure 1.1 World map depicting locations of major slow- and ultraslow-spreading mid-ocean ridges and intra-oceanic subduction zones (in *italic*). Map after Fowler (2004); for plate boundaries see, e. g., Bird (2003).

seafloor (e. g., Jannasch and Mottl, 1985). Above all other lithologies within the oceanic crust, ultramafic rocks bear the potential to supply large amounts of metabolic energy when undergoing serpentinization (e. g., McCollom and Bach, 2009). This process releases molecular hydrogen, which can be utilized by a number of chemosynthetic organisms—it has hence been suggested that energy made available during serpentinization may have aided in the origin of life itself (e. g., Martin et al., 2008, and references therein).

Owing to the increasing thickness of sealing sediment layer, fluid circulation through older seafloor is thought to play a less important role (e. g., Anderson and Hobart, 1976). During the eventual burial of old oceanic lithosphere at convergent plate boundaries (Fig. 1.2), however, fluid–rock interactions once again take on a fundamental role. As H_2O -rich sediments and altered, hydrated basement subduct, they undergo prograde chemical and physical transformations that result in the release of large amounts of fluids and mass (e. g., Peacock, 1996). The fluids migrate into the overriding plate where they react with the mantle lithologies; since volatile and incompatible elements are to a little degree incorporated into the newly formed minerals, they are carried along by the fluids and are in this way transferred to the mantle wedge (e. g., Schmidt and Poli, 2014; Tenthorey and Hermann, 2004).

Subduction processes consequently are among the main controllers of global chemical cycling (e. g., Stern, 2002, and references therein). This cycling has had and still has severe implications for the geochemical evolution and differentiation of the Earth; it lead, for instance, to the formation of the continents (e. g., Taylor and McLennan, 1995). In greater detail, fluids liberated from the slab at depths of ~ 70 to 120 km migrate over

tens of km into the overriding plate where they provoke hydrous partial melting of the mantle that in turn results in felsic volcanism and, over large periods of time, continental crust formation (e. g., Peacock, 1990; Ringwood, 1969). During crustal formation, which depicts an immense chemical fractionation by itself, highly incompatible trace elements were efficiently extracted from the mantle into the crust—about 30 to 50% of the Earth’s budget of these species are incorporated within the continental crust even though it only accounts for 0.6% of the Earth’s mantle (Hofmann, 1988).

Fluids and reactions between fluids and rocks hence provide a common ground in the complex interconnections between hydrothermal, tectonic, magmatic, hydrologic, and biological processes within the marine realm. The many facets of fluid–rock interactions take place on nanometer to regional scales and to a large degree shaped the surface and subsurface of the modern Earth. Despite recent insights, the rates of many of the processes as well as underlying mechanisms are still poorly understood. Further multidisciplinary research is required to gain deeper knowledge into the understanding of these fundamental processes.

1.2 Life cycle of oceanic lithosphere

The crust and upper mantle form the hard, rigid outer layer of the Earth known as lithosphere. As pointed out above, the lithosphere’s uppermost part chemically reacts to the atmosphere, hydrosphere, and biosphere.

The lithosphere is subdivided into continental and oceanic types, the former of which is usually associated with granitic crust whereas that of the latter is basaltic. Oceanic lithosphere constantly forms along mid-ocean ridge spreading centers where two lithospheric plates separate (Fig. 1.2). Continued spreading moves this newly formed crust away from the spreading axis. As the distance, and with it the crust’s age, increase it progressively subsides as a consequence of conductive cooling and an associated increase in density. Ongoing spreading ultimately leads to the collision of tectonic plates at convergent margins. Here, one lithospheric plate is overridden by the leading edge of the other plate and is cycled back into the asthenospheric mantle (Fig. 1.2).

Key principle for this cycling of oceanic crust, and for plate tectonics in general, is the large-scale convection of the underlying asthenospheric mantle. The causes of this convection are, however, still subject of debate. The most widely held theories include pushing mechanisms induced by the separation of plates at spreading ridges, pulling of descending plates at convergent boundaries due to their relatively lower temperatures and densities, or combinations of both (e. g., Harper, 1975; Conrad and Lithgow-Bertelloni, 2002).

1.2.1 Divergent plate boundaries

Each year, approximately 3 km² of new seafloor is created along the global network of divergent plate boundaries (Fig. 1.1; Chase, 1972). Plate separation is accompanied by passive upwelling and decompressional partial melting, i. e., to the crossing of the

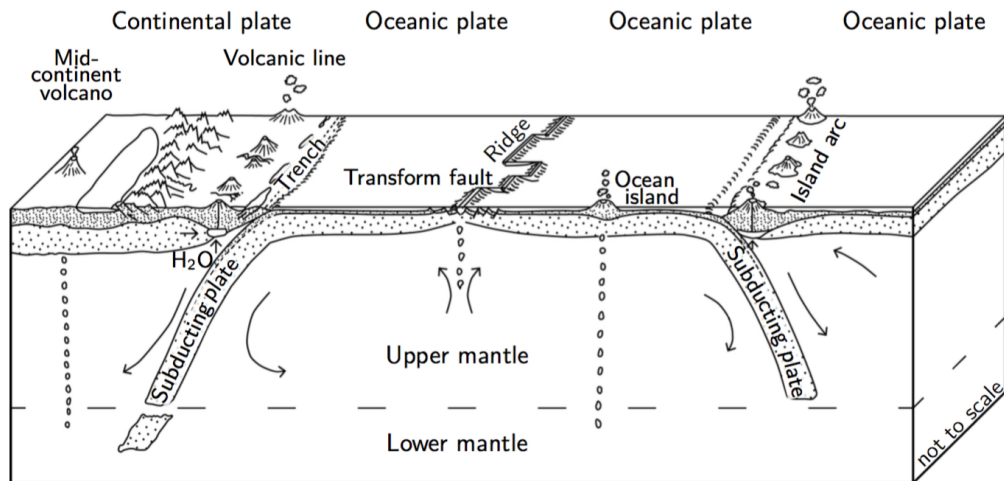


Figure 1.2 Schematic diagram illustrating the formation of new oceanic lithosphere along divergent mid-ocean ridges and its eventual subduction back into the mantle at convergent plate boundaries. Dotted, lithospheric mantle; densely dotted, crust. Figure after Fowler (2004).

solidus, of the underlying ultramafic asthenosphere (Fig. 1.2; e.g., Langmuir et al., 1992, and references therein). Resulting melts, usually mafic in composition, rise towards the seafloor and either crystallize at upper crustal sections or erupt at the seafloor where they form the basaltic crust that covers much of the global ocean floor.

The oceanic crust has an averaged thickness of about (6 to 7 km). Its thickness, however, varies with the amount of melt that is being produced, which in turn is strongly dependent on the temperature of the mantle as it rises (see, e.g., review by Dick et al., 2006). A major factor influencing this temperature seems to be the spreading rate at which the respective tectonic plates rift apart—at slow rates, upwelling mantle material generally cools down more efficiently and subsequently crosses the solidus and melts at lower depth, resulting in reduced magmatism as compared to faster-spreading ridges. With the crustal thickness, the architecture and composition of the crust as well change with the spreading rate and thus with melt production (Dick et al., 2006, and references therein). It is oftentimes homogeneously layered along fast-spreading ridges. In idealized models the crust consists of a thin layer of effusive basaltic rocks, usually in the form of pillow lavas, on top of sheeted diabase–basalt dikes that themselves overlie a layer of isotropic gabbroic rocks and, at the base, ultramafic cumulates. Oceanic lithosphere with such ‘Penrose’ type crust is, for instance, produced at the East Pacific Rise that diverges with full spreading rates of up to 180 mm a^{-1} (e.g., Müller et al., 2008). Contrary to this, magmatism does not compensate for the plate extension at slow- or ultraslow-spreading ridges. Strong temporal and spatial variations in magmatic activity result in the formation of more heterogeneous crustal structure with large variations in thickness along segmented ridges (Fig. 1.3; e.g., Karson et al., 1987). Layered crust forms where magma budgets are high, typically at the magmatically more robust segment centers of individual ridge segments, i. e., sections between two transform faults (e.g., Bach and

Früh-Green, 2010, and references therein). These areas are characterized by many small normal faults that cause the rough axial topography of slow-spreading MORs. Towards the ends of the ridge segments, that is, at ridge–transform intersections, magma budgets generally appear to be lower. Here, tectonic displacement and faulting prevail and few major faults account for crustal accretion. These large faults, termed detachments, are usually deep-rooted and characterized by km-wide displacement and the exposure of mantle-dominated lithospheric material at the seafloor (see below). Slow-spreading ridges comprise nearly 50% of the global mid-ocean ridge segments (e. g., Müller et al., 2008), highlighting their significance for global geologic processes. One of the slow-spreading ridges is the Mid-Atlantic Ridge (Fig. 1.1) that spreads with less than 40 mm a^{-1} .

Detachment faulting

Detachment faults appear to occur where magmatism cannot counterbalance plate extension (Fig. 1.3; e. g., Tucholke et al., 1998; Buck et al., 2005). Large-offset tectonic displacement in these cases leads to the creation of ocean basement composed of lower lithospheric rocks. Detachment faults have been reported from the Mid-Atlantic Ridge, the Southwest Indian Ridge, the Central Indian Ridge (*cf.* Fig. 1.1), and other slow- or ultraslow-spreading ridges. Their formation is thought to be restricted to spreading rates of less than $\sim 80 \text{ mm a}^{-1}$ (Tucholke et al., 2008). They typically develop in the inside corners of ridge–transform intersections, usually on one side of the ridge axis only, making the ridge structurally asymmetric (Karson, 1999).

The contribution of detachment faulting to the lithospheric accretion and the generation of new seafloor is significant; Smith et al. (2008), for instance, argue that lower lithospheric rocks exposed by detachment faulting comprise up to 60% of the seafloor along segments of the Mid-Atlantic Ridge.

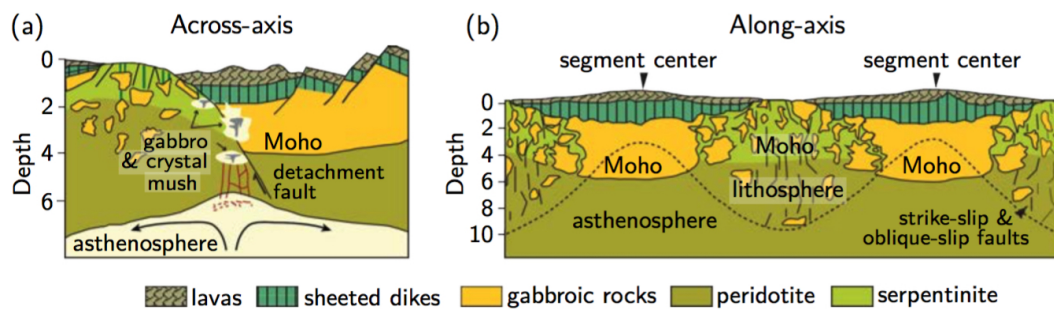


Figure 1.3 Conceptual model of tectonomagmatic processes at slow-spreading ridges. (a) In areas of high magma supply, layered crust of gabbroic rocks overlain by sheeted dikes and basaltic lava forms. Where magma budgets are lower, tectonic processes prevail and extension takes place via faulting. Long-lived detachment faults commonly expose gabbroic and peridotitic rocks at the seafloor. Pronounced seawater alteration of these lower lithospheric lithologies causes serpentinitization. (b) Along-axis variations in magma supply are reflected by segment centers with relatively continuous magmatic crust that becomes thinner and discontinuous towards magma-poor segment ends. Enhanced seawater circulation at segment ends effectively cools these areas, contributing to a thick lithosphere. After Bach and Früh-Green (2010).

Cann et al. (1997), Tucholke et al. (1998), and others recognized oceanic core complexes—that are flat or dome-shaped lower lithospheric rock exposures at the seafloor—at mid-ocean ridges during the 1990s. They described them as features with corrugated and striated surfaces that dip gently towards the ridge axis and that extend over tens of kilometers parallel to the axis.

Underlying principle of detachment faulting and the associated formation of oceanic core complexes is the continued extension along a normal fault (Fig. 1.4; e.g., Buck, 1988; Smith et al., 2008). In detail, rather steep normal faulting, which is a common constituent of slow-spreading ridges, initiates close to the ridge axis (Fig. 1.4a). Continued, km-wide offset along such normal faults leads to the described placement of mantle-derived ultramafics and associated mafic plutonic rocks at shallow crustal levels (Fig. 1.4b) and, if extension on the respective detachment continues long enough, to the exhumation of these rocks at the seafloor (Fig. 1.4c). As a result of regional isostatic compensation, initially steep faults flatten during exhumation and form the characteristically dome-shaped core complexes; oceanic detachments are hence oftentimes described as ‘rolling-hinge-type normal faults’ (e.g., John and Cheadle, 2010). The corrugated and striated fault plane surfaces result from displacement along the fault zones and are hence oriented parallel to the plate spreading direction. Detachment faults commonly accommodate extension of up to several tens of km, which represents several millions of years of plate spreading (e.g., Tucholke et al., 1998; Schroeder et al., 2007).

Oceanic core complexes are regarded as ‘tectonic windows’ into the oceanic lithosphere (e.g., Karson, 1998). Owing to this significance, numerous detachment faults and core complexes have been studied along slow- and ultraslow-spreading ridges worldwide.

The core complexes generally comprise subvolcanic lithosphere, i.e., lower crustal gabbro and/or peridotitic mantle (e.g., Schroeder and John, 2004; Kelemen et al., 2004). Gabbros in many cases occur as variably sized melt intrusions in peridotite host rocks (e.g., Kelemen et al., 2004) or may form plutons with local thicknesses of >1 km (e.g., Blackman et al., 2006). Indeed, observational evidence (e.g., Ildefonse et al., 2007; MacLeod et al., 2009) and modeling studies (e.g., Tucholke et al., 2008; Olive et al., 2010) led these investigators to suggest that detachments, despite their general occurrence at the magma-poor portions of ridge segments, develop if some of the total plate extension is accounted for by magmatism, and that detachments root in zones where melts intrude into the lower lithosphere. Tucholke et al. (2008) proposed that detachments form when ~30 to 50% of the total extension is accommodated by magmatic accretion, and that there is significant magmatic accretion in the fault footwalls. In line with this concept are observations from the ultraslow-spreading Southwest Indian and Gakkel Ridges—spreading centers with extremely little magmatism—where extension rarely happens via detachment faulting (e.g., Cannat et al., 2006; Michael et al., 2003).

Detailed microtextural investigations provide evidence for initial deformation and faulting in the detachment fault zone at magmatic temperatures and high pressures, i.e., at deep lithospheric levels (Fig. 1.4; e.g., Schroeder and John, 2004; Picazo et al., 2012). These in many cases mylonitic fabrics are overprinted by lower-temperature deformation and alteration during continued denudation of the fault. Deformation at shallower depth becomes increasingly more brittle and cataclastic fabrics develop.

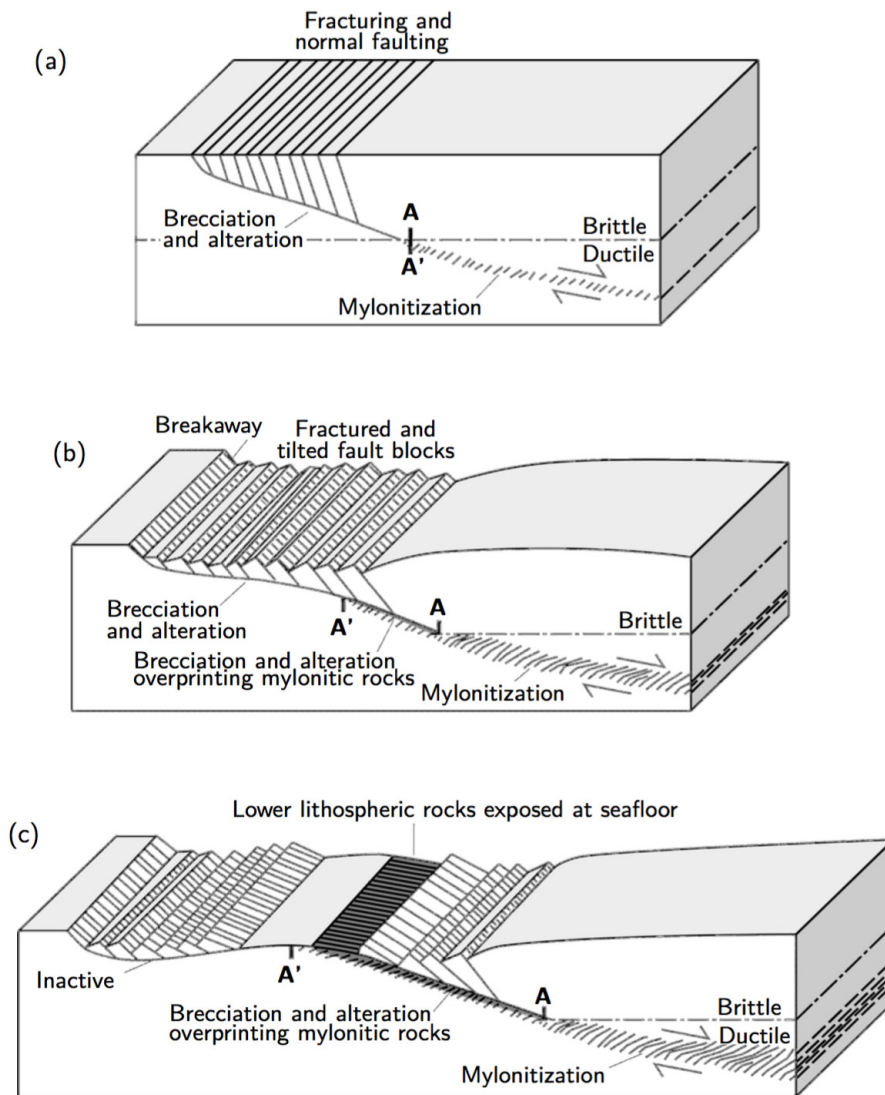


Figure 1.4 Schematic illustration depicting the evolution of a detachment fault and the concomitant formation of an oceanic core complex. (a) Steep normal faulting occurs near the spreading axis (to the right). Displacement produces mylonitic fabrics at depth and brittle deformation along shallower segments of the fault. (b) Continued extension on the detachment fault is accompanied by a rotation of the footwall, leading to flattening of the fault plane. Mylonitic rocks are overprinted by successively more brittle structures. (c) Ongoing extension eventually exposes lower lithospheric rocks and a corrugated footwall at the seafloor. This oceanic core complex (light gray plane) results from isostatic adjustments that form its characteristic domal geometry. Figure after Reynolds et al. (1988).

Rock alteration, in particular by fluid–rock interaction, is strongly associated with and is hence ubiquitous at detachment faults. Escartín et al. (2017) pointed out the association of detachment faults and hydrothermal activity along the Mid-Atlantic Ridge. All oceanic core complexes studied along the spreading center host active hydrothermal vents, show extinct hydrothermal deposits, or both (Escartín et al., 2017, and references therein). The hydrothermal activity causes the reaction of lithospheric lithologies with circulating fluids at depth. Rock samples from detachment faults, in particular from the fault surfaces themselves, are in many cases strongly altered and hydrated and metamorphosed into secondary mineral assemblages (e. g., MacLeod et al., 2002; Schroeder and John, 2004; Boschi et al., 2006; Picazo et al., 2012). Serpentinite, i. e., hydrated and metamorphosed peridotite, is one of the dominant lithologies found at detachment faults along the Mid-Atlantic Ridge (e. g., Bach et al., 2004; McCaig et al., 2007) and also at other oceanic detachment faults worldwide (e. g., Dick et al., 2003; Bach et al., 2002; Kumagai et al., 2008).

Hydrothermal fluid–rock interactions

Advective percolation of seawater into the cooling, pervasively fractured lithosphere at slow-spreading rifts induces hydrothermal interactions leading to widespread and locally intense alteration, metamorphism, and metasomatism. These interactions influence ocean chemistry, cause significant heat exchange between seafloor and ocean, form metal-rich deposits, and provide energy sources for deep-sea and subseafloor biological communities. The most decisive factors defining the nature of these reactions include the rock types and the chemistry of the aqueous solutions involved in the respective interaction, as well as conditions like fluid-to-rock ratio, temperature or pressure under which the reactions occur.

As summarized by Tivey (2007), active hydrothermal circulation of fluids at ridge crests is favored by the presence of a permeable medium, a heat source, and a fluid that saturates the crust. At slow-spreading ridges, normal faults provide excellent pathways for seawater to penetrate deep into the crust where it is heated by magma or newly solidified hot rock. Chemical reactions and mass transfers occur as fluids circulate (Fig. 1.5). These interactions take place at low temperatures when the seawater enters the seafloor, then in the deepest portions of the circulation system at much higher temperatures and pressures, and finally when the hot, buoyant fluid rises to exit at the seafloor where it mixes with cold seawater. Both, the circulating fluid and seafloor lithologies, are altered by the reactions along this path. Lithologies affected by hydrothermal interactions at slow-spreading ridges are those, as described above, that form from partial melting of peridotite such as, e. g., troctolitic, gabbroic, basaltic, and—although volumetrically much less important—more evolved, felsic rocks (e. g., Koepke et al., 2005), as well as peridotite itself.

Tivey (2007) reviewed basalt-hosted hydrothermal systems (Fig. 1.5) to be characterized by the hydration and alteration of basaltic glass, olivine, and plagioclase to ferric micas, smectite, and Fe-oxyhydroxides at low temperatures, shortly after seawater entered the oceanic crust. Along the fluid's path towards greater depth, smectite and chlorite

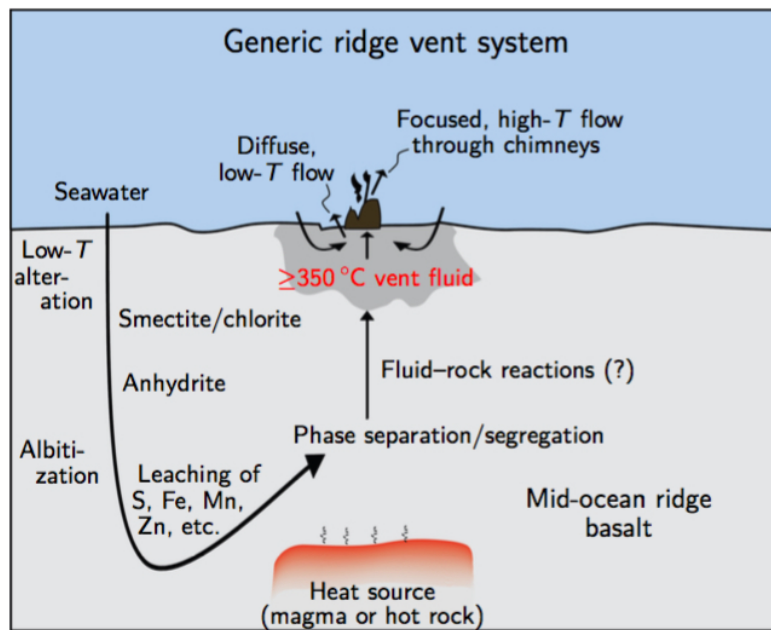
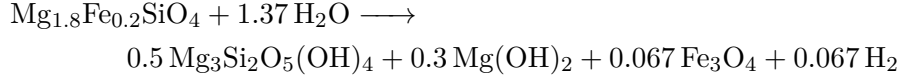


Figure 1.5 Schematic drawing of a hydrothermal system within oceanic crust. Depicted are the processes that contribute to the formation of vent fluids and to a net change of the fluid and rock chemistries. See text for details. Figure after Tivey (2007).

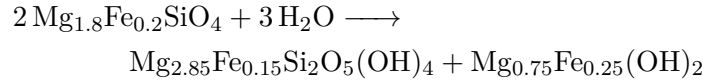
precipitation results in removal of Mg from the fluid in exchange for Ca^{2+} , H^+ , and Na^+ , and subsequently, in removal of Ca^{2+} and SO_4^{2-} during anhydrite precipitation. Content of volatiles (e. g., H_2O , Cl , CO_2) and trace elements such as K, Rb, Cs, U, Pb, Sr, As, and B are as well increased in the crust (e. g., Staudigel, 2003). At deeper crustal levels, the fluids loses Na^+ and Si^{4+} but gets enriched in Ca^{2+} during the alteration of anorthite to albite. These reactions produce a slightly acidic, anoxic, alkali-rich, Mg-poor fluid that leaches S and metals from the rock at high temperatures. Heat sources initiating the hydrothermal system are newly formed basalt or its plutonic equivalent and/or underlying magma chambers. During the buoyant rise of this hot fluid back to the seafloor, precipitation and/or dissolution of sulfide phases may occur. Eventually, the fluid is modified close to the seafloor by mixing with entraining seawater, or it vents directly in the oceans via diffuse or focused flow, the latter of which is commonly marked by chimney structures that form when the hot metal- and sulfide-rich fluids come in contact with seawater.

Lower crustal rocks alter to assemblages that include sodic plagioclase + actinolite \pm diopside clinopyroxene \pm epidote \pm chlorite \pm prehnite \pm quartz at ~ 300 to 500°C and plagioclase + hornblende \pm diopside \pm chlorite at ~ 500 to 700°C , respectively, during interaction with seawater-derived fluids (e. g., McCollom and Shock, 1998).

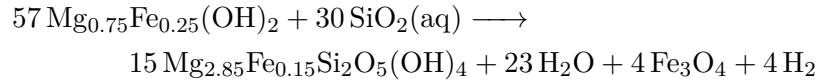
Serpentinization Serpentine-rich assemblages form during the widespread interaction of peridotite with seawater. The serpentinization of peridotite can be represented by the generalized reaction of olivine ($X_{\text{Mg}} = \text{Mg}/(\text{Mg} + \text{Fe}^{2+}) = 0.90$) to serpentine, brucite, magnetite, and hydrogen (e. g., McCollom and Bach, 2009):



The exact mineral assemblage produced, however, depends on several factors as noted above. For instance, reaction path models predict olivine to be a stable member of the equilibrium mineral assemblage when harzburgite reacts with seawater at temperatures of $>315^\circ\text{C}$ and a water/rock ratio of 1; in contrast, the harzburgite is completely altered to serpentine, brucite, and magnetite at lower temperatures (Fig. 2a of McCollom and Bach, 2009). At temperatures below the stability field of olivine, serpentinization may proceed through the following sequence of reactions, as proposed by Bach et al. (2006) on the basis of mineral chemical investigations. At an early stage with low fluid flux, olivine ($X_{\text{Mg}} = 0.90$) quasi-isochemically reacts to serpentine ($X_{\text{Mg}} = 0.95$) and ferroan brucite ($X_{\text{Mg}} = 0.75$), similar to what is predicted by thermodynamic modeling (Fig. 2b of McCollom and Bach, 2009):



In the presence of aqueous silica, this Fe-rich brucite forms serpentine and magnetite at a later serpentinization stage that is more open-system:



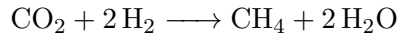
whereby aqueous silica can for instance be provided by the breakdown of the peridotite's orthopyroxene to serpentine:



The upper temperature limit under which serpentinization occurs is estimated at ~ 400 to 425°C (e. g., Früh-Green et al., 2004). Heat is provided by magmatic activity, by the highly exothermic serpentinization reactions (e. g., Lowell and Rona, 2002) or by a combination of these two.

The transformation of peridotite into serpentinite has drastic effects on the rock's physical properties. Whereas peridotite is a dense, mechanically strong, poorly magnetic, dry rock, serpentinite is a low-density, mechanically weak, and highly magnetic rock that comprises $>10\%$ H_2O . These physical changes have severe implications on the geotectonic environments where serpentinization occurs. Escartín et al. (1997, 2001), for instance, demonstrated that even slightly serpentinized peridotites significantly alter the rock's rheologic characteristics, namely reducing its strength and favoring strain localization in and deformation of the serpentinized portions of the rock.

Typical fluids produced during serpentinization are characterized by high concentrations of H₂, CH₄, and other hydrocarbons (Bach and Früh-Green, 2010, and references therein). The production of methane is attributed to Fischer–Tropsch type reactions (e. g., Berndt et al., 1996) such as



with CO₂ derived from the mantle (e. g., Proskurowski et al., 2008). Hydrogen and hydrocarbons are of great biologic importance in that they serve as geochemical energy for deep ocean ecosystems in which chemolithoautotrophic microorganisms derive metabolic energy from the catalysis of redox reactions (e. g., Kelley et al., 2005; Petersen et al., 2011). It has repeatedly been suggested that such hydrothermal systems may have played a role in the origin of life on Earth and perhaps elsewhere (e. g., Shock and Schulte, 1998; Martin et al., 2008).

Hydrothermal alteration assemblages rich in serpentine ± chlorite ± amphibole ± talc have been described from areas where gabbroic rocks occur together with peridotite—for instance at the above-mentioned detachment footwalls that are commonly intruded by gabbroic bodies (e. g., MacLeod et al., 2002; Schroeder and John, 2004; Dick et al., 2008; Harigane et al., 2008). These assemblages are interpreted to have formed from hybrid mafic and ultramafic protoliths during fluid–rock interactions (e. g., Picazo et al., 2012), or from intense metasomatism that lead to an enrichment of Si and Ca in the fluid during interaction with gabbroic rocks and the subsequent precipitation of the above mentioned phases in peridotite (e. g., Boschi et al., 2006; Früh-Green et al., 2018). Strong deformation of these weak secondary assemblages is common and zones where they occur are suggested to be loci of strong strain localization, deformation and/or active faulting (see references above).

15°20' N Fracture Zone area, Mid-Atlantic Ridge

The exhumed footwalls of several detachment faults are exposed on the seafloor near the 15°20' N Fracture Zone at the Mid-Atlantic Ridge. This prominent fracture zone offsets by ~180 km the spreading center (Fig. 1.6), which diverges at a mean full rate of ~25 mm a⁻¹ in this area (Fujiwara et al., 2003). The seafloor to the north and south of the transform is characterized by rugged and blocky topography with an asymmetric morphology across the spreading axis (Escartín et al., 2003). Bordered by magmatic segment centers with thick igneous crust at ~14° N and 16° N, respectively, the region is interpreted as magma-starved (e. g., Cannat et al., 1997; Fujiwara et al., 2003). In line with this are frequent exposures of mantle peridotite and gabbroic rocks at both walls of the rift valley for more than 100 km (e. g., Shipboard Scientific Party, 2004a). Schroeder et al. (2007) assigned the infrequency of volcanism to the presence of a 10 to 20 km thick lithosphere that inhibits magma from erupting at the seafloor. Extensional faulting rather than magmatism consequently accommodates plate accretion. Mantle denudation and spreading is accounted for by high-displacement, rolling-hinge normal faults and secondary lower-displacement normal faults (Schroeder et al., 2007).

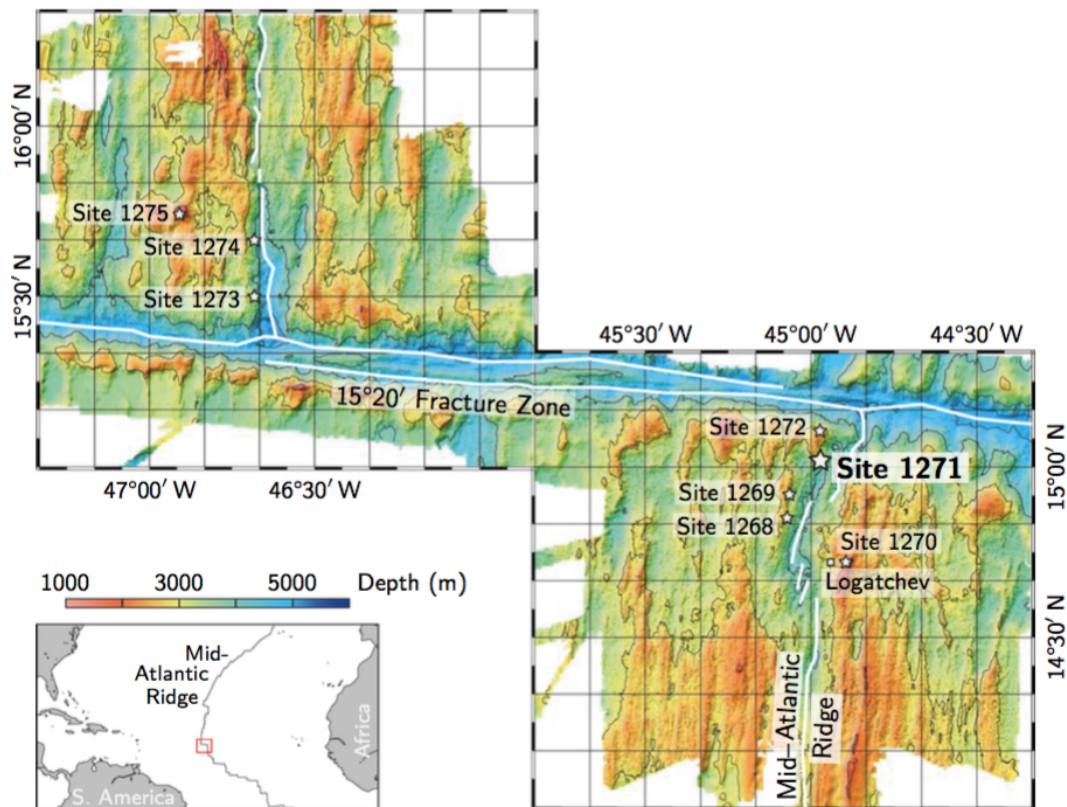


Figure 1.6 Bathymetry map of the 15°20' N Fracture Zone area and locations of sites drilled during ODP Leg 209. The Logatchev hydrothermal field is also indicated. Thick contour intervals are 1000 m, thick white lines locate bathymetric lows within the axial valley and the fracture zone. After Fujiwara et al. (2003).

During Ocean Drilling Program (ODP) Leg 209, 19 holes at 8 sites were drilled into the MAR axial valley and on the immediate valley walls in the 15°20' N Fracture Zone area (Fig. 1.6; Shipboard Scientific Party, 2004a). Recovered core primarily consists of peridotite that has, at most sites, been modified by late melt impregnation and alteration processes, respectively (e. g., Shipboard Scientific Party, 2004a; Paulick et al., 2006; Bach et al., 2004). Melt impregnations are mostly gabbroic in composition and are present in core from Sites 1268, 1270, 1271, and 1275 (Shipboard Scientific Party, 2004a).

Rocks recovered from Site 1271 were investigated in the course of this PhD project. Two holes were drilled at this site that is located at the inner corner high along the south wall of the 15°20' N Fracture Zone. Recovered core from Hole 1271A (44.8 m deep, 12.9% recovery) is mainly dunitic with minor amounts of orthopyroxene. Core from the deeper Hole 1271B (103.8 m deep, 15.3% recovery) consists of rock dominated by dunite, followed by gabbroic rocks, troctolite, minor harzburgite, and gabbroic rocks (Shipboard Scientific Party, 2004b). Gabbroic material in the form of plagioclase, clinopyroxene, and/or amphibole occurs interstitial to olivine or fills microfractures crosscutting the ultramafic

rocks. The Shipboard Scientific Party interpreted these impregnations to have resulted from (i) the migration of basaltic liquids along grain boundaries by porous flow during early stages of the mantle uplift; (ii) crystallization of plagioclase and clinopyroxene during a decrease in temperature, resulting in the incorporation of interstitial gabbroic material in the peridotite; (iii) local focused flow resulting in channels that produced hybrid rock composed of olivine and gabbro; and (iv) a switch to predominantly fracture flow during further cooling of the rock, resulting in the crystallization of gabbroic domains in small patches throughout the peridotite sequence.

The drill core from Site 1271 is strongly altered. Dunite at Hole 1271A is completely serpentinized, consisting of serpentine, magnetite, and locally abundant brucite; with minor altered gabbro and microgabbro (Shipboard Scientific Party, 2004b; Bach et al., 2004). Lithologies at Hole 1271B are variably altered—a great proportion of the recovered core is composed of serpentinized dunite, consisting of serpentine, magnetite, and brucite. Strongly altered gabbroic domains are dominated by secondary amphibole and chlorite with the local occurrence of secondary plagioclase and/or talc (Shipboard Scientific Party, 2004b). In the proximity to the contacts with mafic material, olivine is replaced by amphibole and orthopyroxene can be altered to talc. According to Bach et al. (2004), dunite in sections of the core with little or no mafic material is much more serpentinized than dunite in contact with mafic material.

Structural observations of the core recovered from Site 1271 highlight a deformation history that follows a general down-temperature path from high-temperature crystal-plastic to low-temperature brittle deformation (Shipboard Scientific Party, 2004b). Ductile-to-brittle fault rocks were interpreted by Schroeder et al. (2007) to represent a major, large-offset detachment fault that led to the denudation of the mantle rocks.

The nearby active Logatchev black smoker field and CH₄- and H₂-rich hydrothermal plume signatures in the water column indicate extensive serpentinization of ultramafic rocks in the sub-seafloor of the 15°20' N Fracture Zone area (e.g., Charlou et al., 1991; Bogdanov et al., 1997).

1.2.2 Convergent plate boundaries

Oceanic lithosphere is cycled back into the Earth's mantle at subduction zones. Subduction takes place along the more than 50 000 km of convergent margins; about 35% of these are intra-oceanic subduction systems, i.e., margins where two oceanic plates collide (Fig. 1.2; e.g., Bird, 2003). Most of these are located in the Western Pacific where they form part of the 'Ring of Fire' (Fig. 1.1). Intra-oceanic subduction zones are characterized by the presence of oceanic trenches that mark the position at which the subducting slab begins to descend. It is usually the older and hence cooler and more dense lithospheric plate that subducts underneath the younger, less dense plate. These age-related physical properties are among the key parameters that determine a subduction zone's geometry: old, dense plates subduct with steeper angles as compared to younger lithosphere. Steepest dip angles of up to 90° (e.g., Katsumata and Sykes, 1969) result from the subduction of the worldwide oldest portions of oceanic crust east of the Mariana trench in the western Pacific (>150 Ma old; e.g., Müller et al., 2008).

High subduction angles are frequently accompanied by tensional forces in the backarc, which can result in active seafloor spreading Uyeda and Kanamori (1979). Further, the position of the volcanic arc depends on the subduction angle, since magma generation and volcanism take place as a function of pressure and temperature in the downgoing slab (e. g., Cross and Pilger, 1982; see below and next section). Other factors that influence the geometries of subduction zones include convergence rates, absolute motions of the upper plates, and the presence of seamounts or other heterogeneities on the incoming plate (e. g., Molnar and Atwater, 1978; Cross and Pilger, 1982; Dominguez et al., 1998). Convergence rates, for instance, may vary from $\sim 20 \text{ mm a}^{-1}$ at the Lesser Antilles to $\sim 240 \text{ mm a}^{-1}$ at the northern Tonga arc Sykes et al. (1982); Bevis et al. (1995). The variability of these key parameters results in a high diversity in the structure of convergent margins worldwide.

Inputs into subduction zones are the lithospheric plate including upper mantle, altered oceanic crust, and sediments. As pointed out in Section ‘**Divergent plate boundaries,**’ the composition of the upper mantle and crust can substantially vary—and so do the thickness as well as lithological and chemical composition of the sediments. Where thick layers of sediments arrive at convergent margins, accretionary prisms typically form. Here, a portion of the incoming sediment is scraped off the downgoing slab and accumulates onto the forearc (e. g., Hilde, 1983; Clift et al., 2009). Where sediment supply is low, sediments are subducted and non-accretionary forearcs form. These subduction zones are commonly associated with subduction erosion, whereby material is eroded from the bottom of the hanging wall and carried down with the subducting plate (e. g., von Huene and Scholl, 1991). Such erosion of the overriding plate’s basal plane may continue to great depth and causes mechanical mixing with materials from the downgoing plate and the formation of a subduction mélange in the subduction channel (e. g., Cloos and Shreve, 1988; Gerya et al., 2002; Federico et al., 2007). Materials are thereby exposed to increasing temperatures and, in particular, increasing pressures with progressive burial. These cause prograde metamorphic reactions to take place in the downgoing plate. Reactions include the destabilization of H_2O -bearing minerals at depth, which leads to the release of large amounts of fluids (Fig. 1.7a; e. g., Peacock, 1996). These fluids hydrate the overriding plate and cause serpentinization of the mantle wedge at forearc depth (e. g., Fryer et al., 1985), and at greater depth a lowering of the solidus of the overlying mantle that triggers concomitant melting, formation of magma, and arc volcanism (Fig. 1.7b; e. g., Gill, 1981b). Ultimately, subducted materials re-equilibrate with the Earth’s mantle—except for a portion of the material that is returned to the exosphere. This cycling of materials as well as interactions between fluids released from the incoming plate and the lithologies of the hanging wall are discussed in greater detail in the next section.

Fluids, fluid–rock interactions, and element cycling

Large amounts of fluids enter subduction zones stored in pore spaces of sediments and bound in H_2O -bearing sediments and hydrated oceanic crust (*cf.* Section ‘**Hydrothermal fluid–rock interactions**’). A portion of the fluids is released by the compaction of sediments with incipient subduction, and some is directly expelled back to the ocean (e. g., Moore

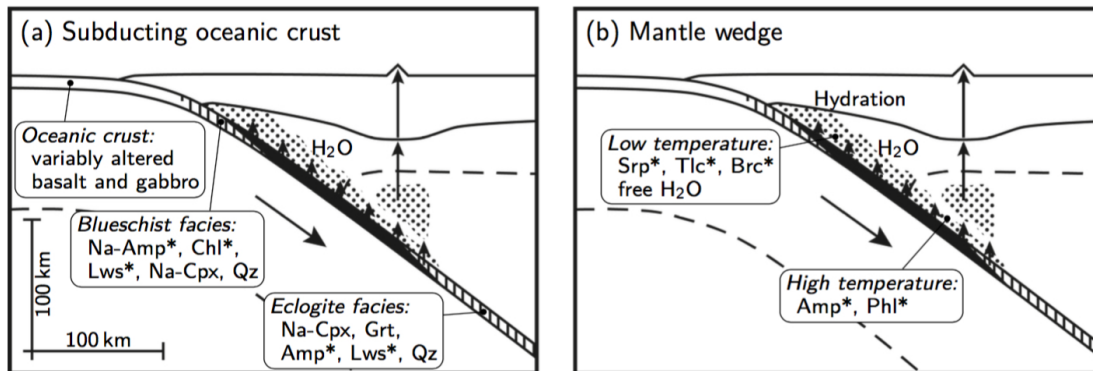


Figure 1.7 Petrologic model of a mature intra-oceanic subduction zone. (a) With ongoing subduction, increasing pressure and temperature conditions cause dehydration reactions that lead to the release of large amounts of H_2O from the subducting hydrated oceanic crust. Proposed mineralogy of the subducting slab is shown in boxes. (b) Aqueous fluids released from the subducting slab cause extensive hydration of the overlying mantle wedge and concomitant mineralogic changes (possible minerals are shown in boxes) and may trigger partial melting in the core of the convecting mantle. Abbreviations: Amp, amphibole; Brc, brucite; Chl, chlorite; Cpx, clinopyroxene; Grt, garnet; Lws, lawsonite; Phl, phlogopite; Qz, quartz; Srp, serpentine; Tlc, talc. Asterisks mark hydrous minerals. Figure after Peacock (1996).

and Vrolijk, 1992). Fluids released at greater depths, by contrast, interact with rocks of both, the downgoing and the overriding plates (e. g., Peacock, 1990). More precisely, fluids originate from, e. g., sediment pore waters and dehydration of opal at forearc depths and from the breakdown of clay-rich sediment and hydrous phases within the altered oceanic crust at intermediate to subarc depths and temperatures (e. g., Kastner, 1981; Nichols et al., 1996; Peacock, 1990). Altered basalt may contain up to 5 wt.% H_2O —the bulk of this is released during the breakdown of hydrous phases as subduction metamorphism causes the transformation to blueschist (~ 3 wt.% H_2O) and amphibolite (~ 1 – 2 wt.% H_2O) facies assemblages (Fig. 1.7a; e. g., Poli and Schmidt, 1995). Minerals that dehydrate during progressive burial are, for instance, prehnite, chlorite, amphibole, or lawsonite (e. g., Schmidt and Poli, 1998). Fluid liberated during these reactions hydrate the mantle wedge, which leads to the formation of lithologies rich in serpentine, talc, and brucite underneath the forearc and to amphibole- and phlogopite-containing assemblages at greater depth (Fig. 1.7b; e. g., Peacock, 1996). Portions of the hydrated mantle wedge may mechanically couple with the subducting plate and be dragged downward with the slab, thereby transporting H_2O -bearing minerals to greater depth (e. g., Tatsumi, 1989; Savov et al., 2007; Stern, 2011). A major role in terms of fluid transport to great depths is attributed to serpentine (Fig. 1.8).

Serpentinized ultramafic portions of the oceanic crust carry large amounts of water into subduction zones. Serpentinization of oceanic crust mainly occurs at or close to mid-ocean ridges (*cf.* Section ‘Serpentinization’); it may, however, as well take place at the outer rise of subduction zones. Here, the oceanic plate bends before it enters the trench and extensional faults, that form in response to the bending, enable seawater to penetrate deep into the lithosphere and interact with the ultramafic rocks (e. g., Ranero

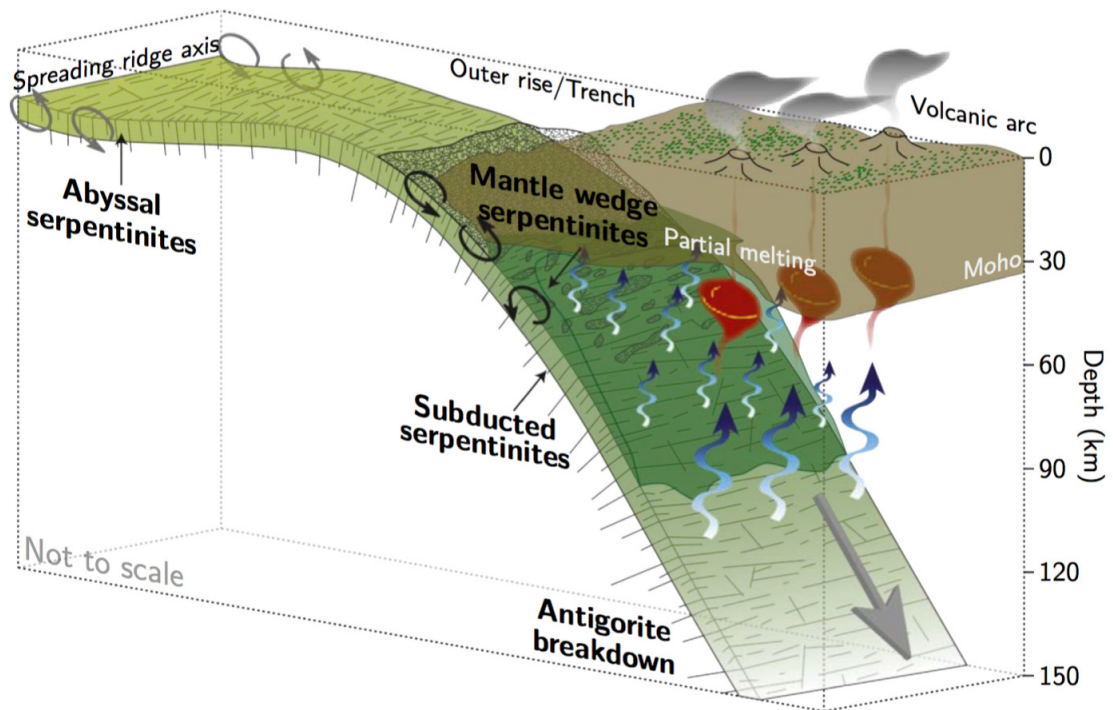


Figure 1.8 Schematic illustration highlighting the significance of serpentinites and serpentinization in the subduction context. Seafloor hydrothermal activity and seawater alteration cause hydration of oceanic peridotites. At convergent margins, these are subducted together with hydrated upper lithospheric rocks and H_2O -rich sediments. Release of fluids from the subducted slab starts at shallow portions of the subduction zone, where the fluids cause serpentinization of mantle wedge peridotites, and continues to great depth, where antigorite breakdown contributes to partial melting of the convecting mantle and thus to arc volcanism. Figure after Deschamps et al. (2013).

et al., 2003). In a recent study, Cai et al. (2018) showed that mantle hydration may extend to depths of ~ 30 km below the seafloor in the case of the slab subducting at the Mariana trench. Within the subduction zone, the massive release of fluids from the slab causes serpentinization of the mantle wedge at shallow to intermediate subduction levels. Such wedge hydration is observed worldwide (Hyndman and Peacock, 2003) and particularly well exemplified in the case of the Mariana forearc (e.g., Fryer et al., 1985). Here, some of the serpentine diapirically rises to the seafloor through the deeply hydrated forearc (*cf.* Section ‘[Mariana serpentinite mud volcanism](#)’). The serpentinization of the mantle wedge occurs at relatively low temperatures of $< 80^\circ\text{C}$ with lizardite and chrysotile as the dominant serpentine varieties (e.g., Bonatti et al., 1984; D’Antonio and Kristensen, 2004). Antigorite joins the assemblage at greater depth—either formed directly by hydration or from the transformation of lizardite and chrysotile that formed at shallower levels but become increasingly unstable with ongoing subduction (Fig. 1.9; Hattori and Guillot, 2007). Antigorite, however, is stable up to ~ 600 to 700°C and

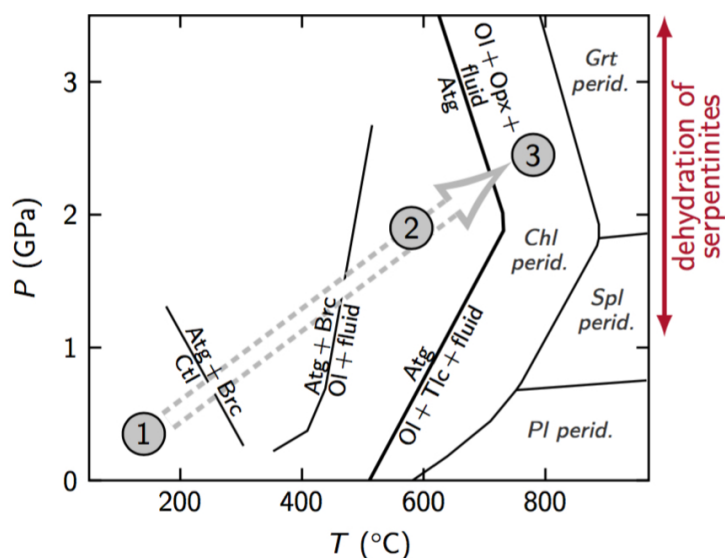


Figure 1.9 Pressure–temperature diagram showing the stability field of serpentinite. Antigorite is stable up to temperatures of $>600\text{ }^{\circ}\text{C}$ and pressures of several GPa (left of thick black line). The evolutionary path of oceanic serpentinite (1) to high-pressure antigorite serpentinite (2), to olivine–orthopyroxene–lithologies (3) is also indicated. Antigorite breakdown occurs via the reactions $\text{Atg} + \text{Brc} \rightarrow \text{Ol} + \text{fluid}$ and $\text{Atg} \rightarrow \text{Ol} + \text{Opx} + \text{fluid}$. Abbreviations: Atg, antigorite; Brc, brucite; Chl, chlorite; Ctl, chrysotile; Grt, garnet; Ol, olivine; Opx, orthopyroxene; perid., peridotite; Pl, plagioclase; Spl, spinel; Tlc, talc. After Scambelluri et al. (2004); Hermann et al. (2000); Deschamps et al. (2013); reactions after Scambelluri et al. (1995); Trommsdorff et al. (1998).

several GPa (e.g., Ulmer and Trommsdorff, 1995; Evans, 2004). Beyond these limits, typically within the range of ~ 70 to 120 km, the breakdown of antigorite again releases fluids into the mantle wedge (Fig. 1.9; e.g., Schmidt and Poli, 1998).

Fluids released during these high-temperature, high-pressure metamorphic reactions migrate upward into the anhydrous upper plate where they trigger partial melting, that in turn leads to the formation of arc magmas and volcanism (e.g., Gill, 1981a; Bebout, 1991; John et al., 2011). Eruptives at island arcs commonly belong to the calc-alkaline magma series and often exhibit H_2O contents of 4 to 6 wt.% (e.g., Sisson and Grove, 1993). Eventually, some of the water is hence returned to the surface. Residual fluids within the downgoing plate are cycled back into the asthenosphere where they impact the long-term chemical evolution of the deep mantle (e.g., Kerrick and Connolly, 2001). Old slabs may retain up to 40% of their initial water (e.g., Rüpke et al., 2004).

Along with high volatile contents, arc eruptives commonly exhibit a trace elemental signal indicative of sources that include metasomatized slab-derived components (e.g., Manning, 2004). The eruptives are, among other elements, particularly rich in the incompatible elements B, K, Sr, Cs, Ba, U, and Pb (e.g., Perfit et al., 1980). These elements are traditionally interpreted to originate from sediments and altered oceanic basement and are known as the ‘slab signature’ Tatsumi and Eggins (1995). With

progressive burial of the slab the elements are mobilized during mineral dehydration, and transported within the subduction channel or into the mantle wedge by H₂O, which acts as a primary transport agent for mass in subduction systems (e. g., Bebout et al., 1999; Scambelluri and Philippot, 2001; Ulmer, 2001). Accordingly, fluids essentially mediate material transfers and element cycling (e. g., Manning, 2004, and references therein).

Besides originating from the devolatilization of sediments and altered oceanic crust at great depth (e. g., Bebout et al., 1999; Marschall et al., 2007), it has more recently been proposed that trace elements are as well liberated from serpentinite during the breakdown of antigorite (e. g., Tenthorey and Hermann, 2004; Straub and Layne, 2003; John et al., 2011). Serpentine is capable of incorporating high concentrations of trace elements that were present in the serpentinizing fluids. Serpentinites hence act as reservoirs for, e. g., fluid-mobile elements such as Li, B, As, Sr, Sb, Cs, Ba, Pb, and U (e. g., Scambelluri et al., 2004; Deschamps et al., 2011, and references therein). Both, abyssal serpentinites formed near spreading centers and forearc serpentinites carry these high concentrations (e. g., Peters et al., 2017). In the latter case, serpentine incorporates fluid-mobile elements that are liberated from the subducted sediment and crust during progressive metamorphism, as for instance evidenced by rock samples from the basal plane of the Mariana forearc that were brought to the seafloor by serpentinite mud volcanism (e. g., Savov et al., 2007; Kahl et al., 2015; see also next section). During the eventual breakdown of antigorite deep within the subduction zone, the fluid-mobile elements are once again released into liberated fluids since they are not compatible with the newly formed olivine Tenthorey and Hermann (2004). From here, a portion of the subducted material is cycled back up, the other portion is carried to deeper mantle levels. Over longer timescales, however, ancient subducted material may be expelled to the surface via deeply-sourced intraplate volcanism (e. g., Hofmann, 1997).

Together with the H₂O, mass is hence transferred between the Earth's surface, lithosphere, and asthenosphere at subduction zones together with the fluids. This mass represents materials that were initially subducted as sediments, oceanic crust, or upper mantle. Tatsumi and Kogiso (2003) termed this cycling of materials in subduction zones 'subduction factory.'

Cycling of carbon Carbon played a crucial role in Earth's history owing to its importance for processes such as the differentiation of the mantle and core or for the long-term evolution of climate (e. g., Blundy and Dalton, 2000; Franks et al., 2014). Understanding cycling of C at convergent margins as well as fluxes between subducting lithosphere and the oceans and atmosphere has hence been of particular interest in the recent past. Inputs to and outputs from the Earth's mantle, the largest of all C reservoirs, are to a large degree mediated by subduction zone processes (e. g., Sleep and Zahnle, 2001). Carbon fluxes into subduction zones can be derived by examining the compositions of lithospheric plates before they subduct, as for instance implemented by ocean research drilling campaigns east of the Izu-Bonin-Mariana arc (e. g., Shipboard Scientific Party, 2000). Bulk sediment and rock analyses provide estimates on the total subducted C (e. g., Kelemen and Manning, 2015). The fate of C after subduction is more difficult to

constrain; in situ sampling is not possible with modern techniques once the lithosphere has entered the subduction zone. Some insight is derived from studying magmatic products of arc volcanism or from parts of ancient subduction zones that have been obducted. It could be shown that C is mobilized in the downgoing slab below the volcanic arcs and transported into the upper plate's mantle (e. g., Kerrick and Connolly, 2001). A fraction of the C is subsequently returned to the Earth's exosphere together with the H₂O- and fluid-mobile element-rich arc magmas (e. g., Blundy et al., 2010). At shallower depth, it has been proposed that only small amounts of C are mobilized (e. g., Kerrick and Connolly, 2001). However, evidence from ophiolitic sections that has not undergone deep burial implies that carbonic fluids also exist at subduction depth of ~40 km (e. g., Schwarzenbach et al., 2018). Similarly, reports on slab-derived fluids rich in dissolved inorganic C, CH₄, and other light hydrocarbons, which upwell in the forearc of the active Mariana subduction system, as well as on listvenites from the Oman ophiolite provide evidence for C mobilization at even lower pressures and temperatures (e. g., Mottl et al., 2004; Falk and Kelemen, 2015).

Based on these and similar data, budgets for fluxes of C in subduction zones were compiled. But estimates on the amount of C that is ultimately returned to the deep mantle vary strongly (e. g., Gorman et al., 2006; Dasgupta and Hirschmann, 2010; Kelemen and Manning, 2015) so that these budgets are rather inconclusive. Budgeting C fluxes in shallow portions of subduction zones remains particularly difficult since the processes affecting the cycling of C have gained little attention in the past.

Mariana serpentinite mud volcanism

Serpentinite mud volcanism at the outer Mariana forearc in the western Pacific serves as a natural window into processes at depths far too deep to be accessed by any known technology. Here, the >150 Ma old Pacific plate subducts below the Philippine Sea plate (Fig. 1.10). The convergent margin is marked by the crescent-shaped Mariana Trench. As reviewed by Leat and Larter (2003), the tectonic plates converge with ~70 mm a⁻¹ in the central parts of the Mariana subduction system. The system is non-accretionary—the thin sedimentary cover (~460 m) atop the incoming plate, composed of siliceous ooze, volcanoclastic deposits and pelagic clays, is entirely being subducted. The forearc is subject to tectonic erosion by the subducting plate. Arc volcanism is well developed as apparent from the presence of the Mariana Islands, situated ~200 km westward of the trench. Backarc rifting of the subduction system is currently well developed but its history is complex. Subduction at the Mariana convergent margin is thought to have initiated ~40 to 50 Ma ago (e. g., Bloomer et al., 1995).

The forearc region of the Mariana subduction system exhibits a rough bathymetry. The forearc itself is tectonically active as indicated by the presence of abundant normal faults; this trench-parallel faulting has been linked to the spreading in the backarc (e. g., Mrozowski and Hayes, 1980). Sets of northeast-orientated conjugate faults, potentially resulting from an increase of the arc–trench curvature, also cross the forearc (e. g., Wessel et al., 1994; Stern and Smoot, 1998). In addition, the subduction of seamounts, which

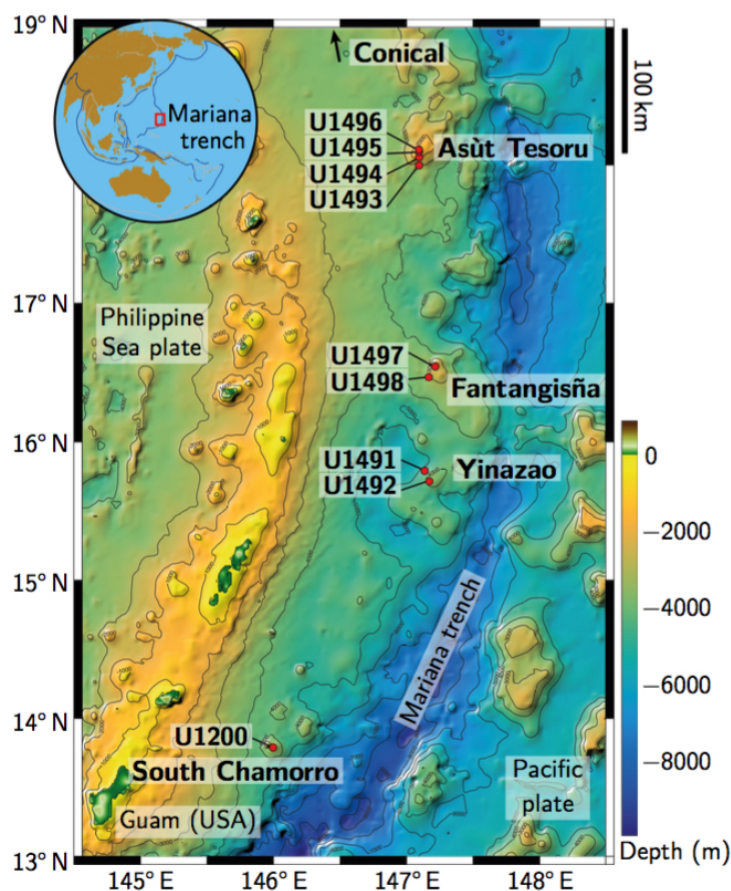


Figure 1.10 Map of the Mariana forearc region and locations of sites drilled during IODP Expedition 366 at the Yinazao, Asùt Tesoru and Fantangisña serpentinite mud volcanoes. Conical and South Chamorro (Site U1200) seamounts were targets of ODP Legs 125 and 195, respectively. Map after Fryer et al. (2018a).

are abundant on the incoming Pacific plate, causes vertical tectonic movements (e. g., Hussong and Fryer, 1986).

A widespread low-velocity zone in the Mariana forearc is evident from seismic studies and suggests the abundant presence of serpentinite within the mantle wedge (e. g., Tibi et al., 2008). This is in line with the hypothesis that fluid fluxes from the slab would, over several tens of millions of years, be sufficient to serpentinite the entire forearc mantle wedge Hyndman and Peacock (2003). Indeed, large volumes of serpentinite have been discovered in the forearc area: more than a dozen seamounts consisting of serpentinite mudflows are situated on its outer half (Fig. 1.10; Fryer et al., 1985). These edifices formed by the extrusion of diapirically upwelling serpentinite materials that originate from the basal plane of the mantle wedge (Fryer and Fryer, 1987). They are situated along tectonic faults that are interpreted as sites where it is most likely that conduits for fluid and mud release will develop (Fryer, 1992). The seamounts exist in varying

distance, from ~50 to 120 km, from the trench axis and reach heights of ~2.5 km and basal diameters of up to ~50 km (Fryer et al., 1985). They likely formed over tens of millions of years (Fryer, 2012).

In greater detail, the serpentinite mudflows contain both finely comminuted serpentinite matrix and rock clasts of variably serpentinitized mantle peridotite. The ultramafic mud and clasts originate from the mantle wedge that was hydrated by fluids liberated from the downgoing slab. The variably serpentinitized ultramafic rock is sheared and mylonized by tectonic movements along the abundant faults and buoyantly rises towards the seafloor, where it erupts in series of episodic flows (Fig. 1.11). The mudflows mainly consist of lizardite, chrysotile, minor antigorite, and accessory minerals such as brucite or magnetite. Larger peridotite clasts, up to a meter or more in diameter, are variably serpentinitized harzburgites or dunites. The mudflows contain few percent of other lithologies, including (i) chunks of material from the slab such as metasediments and greenschist to blueschist facies metabasalts originating from ocean island and mid-ocean ridge settings, (ii) island arc tholeiite and boninite from the forearc crust, and (iii) authigenic minerals such as aragonite and calcite (see review by Fryer, 2012, and references therein).

Together with the serpentinite muds, slab-derived fluids rise through the mud volcanoes towards the seafloor. The chemistries of these fluids systematically change across the forearc as a function of prograde metamorphic and associated dehydration reactions taking place in the subducting slab, i. e., with increasing depth to the slab (Fig. 1.11; e. g., Mottl et al., 2004; Hulme et al., 2010). Upwelling fluids at the shallow-sourced mud volcanoes are thought to emanate from sediment compaction and the dehydration of opal, whereas intermediate- and deep-sourced mud volcanoes are fed by fluids released during the dehydration of H₂O-rich sediments and the altered oceanic crust (e. g., Mottl et al., 2004; Hulme et al., 2010; Fryer et al., 2018a). The increasing influence of the dehydration of the oceanic crust is, for instance, mirrored in increasing B, K, Rb, and Cs concentrations in pore waters sampled from the mud volcanoes across the forearc Mottl et al. (2004). However, the compositions of the fluids are altered after their release due to interactions with rocks in the subduction channel or during their rise towards the seafloor. For instance, Ca and Sr concentrations in pore waters are markedly enriched relative to seawater at Yinazao serpentinite mud volcano (previously known as Blue Moon; ~13 km above the subducting slab) and Fantangisña (previously known as Celestial; ~14 km above the slab) but heavily depleted at Asùt Tesoru (previously known as Big Blue; ~18 km above the slab) and other, deeper-sourced mud volcanoes (Mottl et al., 2004; Fryer et al., 2018a; Oakley et al., 2007, 2008). Mottl et al. (2004) suggested that this drop may be ascribed to the formation of calcium carbonates at depth, incorporating large quantities of Ca and Sr, and hence affecting the composition of the upwelling fluids. They argue that fluids below the deeper-sourced mud volcanoes are likely saturated with CaCO₃, since enrichments in carbonate alkalinity in upwelling fluids as well as in dissolved inorganic carbon, CH₄, and more evolved hydrocarbons (see also Fryer et al., 2018a) imply that decarbonation of sediments and altered oceanic crust has joined the metamorphic reactions within the subducted slab.

Based on fluid trace element inventories as well as on metamorphic assemblages in the mud and clasts, temperatures at the top of the slab were estimated (Fig. 1.11; e. g.,

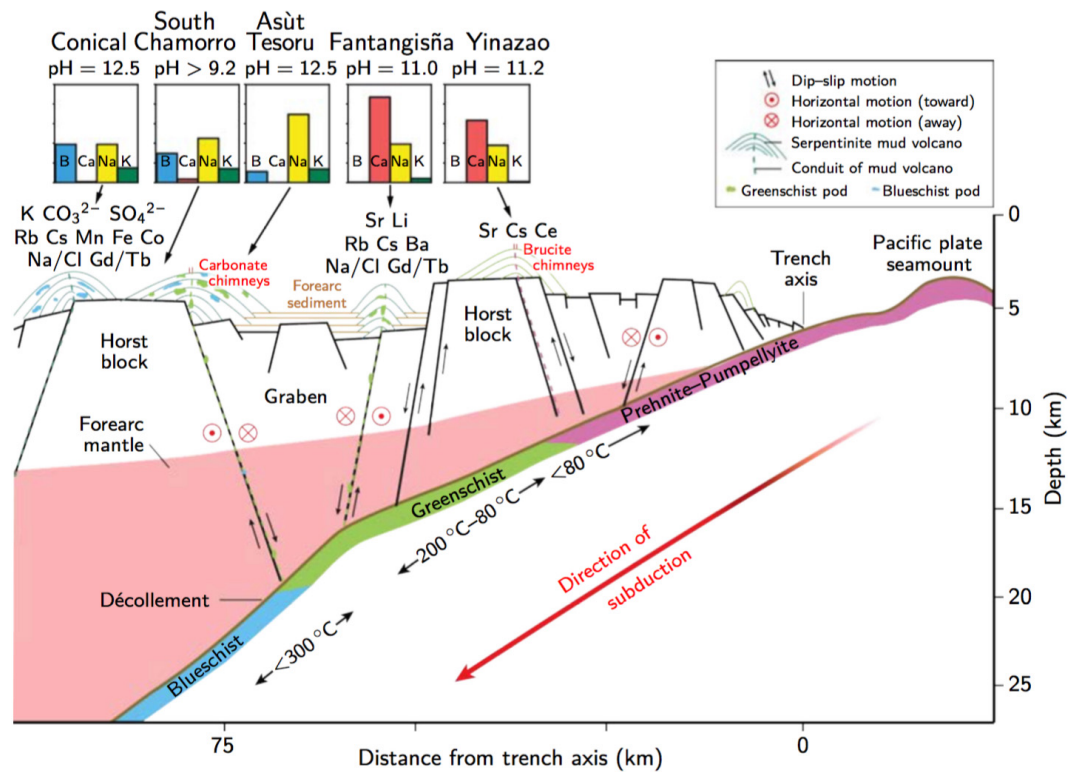


Figure 1.11 Schematic cross-section through the Mariana forearc. Extensive faulting creates conduits and permits slab-derived fluids and serpentinitized fault gouge of forearc lithospheric mantle to rise towards the seafloor where they eventually erupt and form serpentinite mud volcanoes. The chemistry of serpentinite mud pore waters varies with the depth to the décollement with respect to metamorphic processes occurring in the slab (all elemental concentrations in mM, but B was multiplied by 10 and Na was divided by 10). Figure after Fryer et al. (2018a), including data from Hulme et al. (2010).

Maekawa et al., 1993; Oakley et al., 2008; Hulme et al., 2010): these vary between $\sim 80^{\circ}\text{C}$ at Yinazao ($\sim 13\text{ km}$ depth to slab) and 250 to 350°C at Conical ($\sim 19\text{ km}$ depth to slab). Lower blueschist facies conditions hence prevail underneath the deeper-sourced mud volcanoes.

The serpentinite mud volcanoes are regarded as direct window into geologic processes taking place at shallow depth in a subduction zone. Serpentinite mud volcanism is unique in the modern World Ocean but it likely occurred in the geologic past, at least since the Archean (e. g., Lockwood, 1972; Pons et al., 2011). The presence of serpentinization-fueled microbial communities inhabiting the mud volcanoes led to the suggestion that the origin of life on Earth may be linked to such serpentinization environments (e. g., Fryer, 2012, and references therein).

The serpentinite mud volcanoes Yinazao, Fantangisña, and Asùt Tesoru were drilled during International Ocean Discovery Program (IODP) Expedition 366. Recovery from summits and flanks of the mud volcanoes, including ultramafic, metavolcanic,

and metasedimentary rock clasts as well as pore waters and authigenic minerals, were investigated within this PhD project.

1.3 Motivation for this thesis and scientific questions

Mass transfers during fluid–rock interactions in the World Ocean impact major geologic processes, such as plate tectonics or the Earth’s chemical and long-term climatic evolution, and can have direct implications for, e. g., biogeochemical processes such as those related to the origin of life. Many of these interactions occur when oceanic lithosphere is formed along mid-ocean ridges or during its destruction in subduction zones. The understanding of these interactions has improved much over the last decades, as outlined above. Many questions yet remain open. With the aim to contribute to furthering our understanding of interactions between fluids and rock in the marine realm, I worked on rock samples from the Mid-Atlantic Ridge, a divergent plate boundary, and from the Mariana forearc, a convergent plate boundary.

Divergent plate boundaries

Tectonic seafloor spreading contributes to a great extent to plate separation at slow-spreading mid-ocean ridges. Understanding the initiation and evolution of detachment faults is key for determining the mechanisms that accommodate plate separation.

Ultramafic and mafic lithologies are frequently observed in association with detachment faults (e. g., Ildefonse et al., 2007). A relation between magmatism and detachment faulting has hence been postulated (e. g., MacLeod et al., 2009; Olive et al., 2010). Likewise, the presence of minerals such as chlorite, tremolite, talc, and serpentine, or mixtures thereof, is common in detachment faults (e. g., Boschi et al., 2006; MacLeod et al., 2002). These phases are mechanically weak and lower the shear strength of rocks; this weakening ultimately facilitates slip and faulting to initiate (e. g., Escartín et al., 2003; Boschi et al., 2006).

The reasons for the common association of ultramafic–mafic rocks and mechanically weak minerals with detachment faults are not well understood. Jöns et al. (2009, 2010), and Picazo et al. (2012) suggested a mechanism that assigns a key role to the impregnation of ultramafic rocks with melt at deep lithospheric levels. Jöns et al. (2009) and Jöns et al. (2010) studied fault rocks from a detachment fault at the Mid-Atlantic Ridge, 15°20' N Fracture Zone area, and proposed a feedback mechanism between silicic melt impregnation, hydrothermal alteration, and detachment faulting. Hydrothermal alteration of the impregnated areas thereby results in the formation of mechanically weak talc–chlorite–tremolite-rich lithologies. Strain localizing within these zones ultimately leads to deformation and faulting; faulting, in turn, causes further hydration, promoting further weakening of the rock. This mechanism, induced by the impregnation of mantle rocks, takes place at temperatures $>200\text{ °C}$ higher than where unimpregnated mantle peridotite would hydrate and weaken. Likewise, Picazo et al. (2012) demonstrated the hydrothermal weakening of ultramafic rocks that were intruded by gabbroic melts. These

authors provided evidence that chlorite–tremolite-rich domains have localized deformation at temperatures above the main serpentinization window of $\sim 400^\circ\text{C}$. The samples were recovered from detachment faults at 13 to 15°N , Mid-Atlantic Ridge.

The interplay between melt impregnation and hydrothermal alteration hence appears to provide a mechanism for substantial weakening and faulting. Aim of the first part of my PhD project was to test the hypothesis that metamorphic weakening of melt-impregnated domains plays a key role in the evolution of detachments. In particular, I wanted to systematically examine

- the dependence of hydrothermal alteration assemblages on the precursor lithology, i. e., purely ultramafic and gabbroic rocks, and mixtures thereof;
- the dependence of hydrothermal alteration assemblages after these precursors on hydration at varying temperatures;
- the potential effect of the secondary assemblages on weakening of the rock.

These questions were approached by combining natural observations on fault rock samples from the $15^\circ 20' \text{N}$ Fracture Zone area, Mid-Atlantic Ridge, with geochemical reaction path modeling. This strategy was designed to also take account of the question whether the addition of Si, on which the formation of the chlorite–tremolite–talc-assemblages relies, needs to take place via fluid metasomatism or if the melt impregnations provide sufficient Si.

Convergent plate boundaries

Geologic processes that affect the fate of the downgoing slab set in at very shallow portions of subduction zones. A throughout comprehension of these processes is crucial to classify their role in the Earth's geochemical evolution.

The cycling of C in subduction zones has gained much attention in the recent past, since it directly connects the long-term with the short-term C cycle (e. g., Sleep and Zahnle, 2001). A portion of the subducting C, stored in sediments and altered oceanic crust, is cycled back to the surface by arc volcanism—but this does by far not balance the amount of initially subducted C (e. g., Blundy et al., 2010). The fate of subducted C at shallower subduction levels remains much less well understood. The serpentinite mud volcanoes in the Mariana forearc provide insight into processes affecting the C cycle at shallow depth. Mottl et al. (2004) and Fryer et al. (2018b) emphasized high concentrations of dissolved inorganic C, CH_4 , and lighter hydrocarbons in the slab-derived fluids that upwell in intermediate- to deep-sourced mud volcanoes (~ 18 to 19 km depth to the slab). These concentrations are interpreted to originate from the subducting slab, implying that C is efficiently mobilized at relatively low pressures and temperatures. This is in agreement with, e. g., Kelemen and Manning (2015), who budgeted the global C loss in forearcs to up to 12 Mt C a^{-1} , but it stands in stark contrast to computed phase equilibria predicting minor C mobilization at forearc pressures and temperatures (e. g., Kerrick and Connolly, 2001).

Drill core recovery from IODP Expedition 366 potentially offers an opportunity to discover new contexts of the fate of C at shallow portions of subduction zones. Among

the recovery are clasts of metavolcanic and metasedimentary material from the slab that contain mm-wide carbonate–silicate–sulfate veins, and also authigenic calcium carbonate crystals that grew in the mud matrix of the serpentinite mud volcanoes. During the second part of my PhD, I intended to study the processes that led to the formation of these carbonate to extend the knowledge on potential C mobilization at shallow subduction zones. In greater detail, the scientific questions were:

- Under which conditions of fluid–rock interactions did the carbonate-rich veins form and where did this happen?
- How does the formation of carbonates in veins differ from that of authigenic precipitates?
- What are the C sources?
- If any, which implications can be drawn from the findings for the global C cycle?

I further worked on variably serpentinitized clasts from the serpentinite mud volcanoes that were also drilled during IODP Expedition 366. These clasts exhibit a polyphase serpentinitization history and likely attest the mobilization of fluid-mobile elements at subduction depths of ~13 to 18 km.

During progressive dehydration reactions at shallow subduction levels, large amounts of fluid are released from the incoming plate’s sediments and altered oceanic crust. Fluid-mobile elements are lost from the slab during early subduction as well, since fluids are a primary transport agent for many of these elements (e. g., Bebout et al., 1999). The slab-derived fluids that are sampled as pore waters in the Mariana forearc serpentinite mud volcanoes carry signals that are the geochemical signals of metamorphic processes at depth (e. g., Mottl et al., 2004; Hulme et al., 2010). For instance, across-forearc increases in pore water concentrations of B and Cs were interpreted to represent the advancing dehydration of altered oceanic crust (Mottl et al., 2004). However, the chemistry of the upwelling fluids is altered during fluid–rock interactions within the subduction channel and mantle wedge. The pore fluids sampled from the mud volcanoes hence do not mirror pristine fluid compositions. The work by Kahl et al. (2015) confirms this assumption: these authors studied fluid-mobile elements contained in several generations of serpentine in ultramafic clasts from deep-sourced South Chamorro (~19 km depth to slab). Concentrations of B, Rb, Sr, Cs, and Ba are considerably higher in early veins and pervasive serpentinitization stages as compared to late-stage serpentine veins and brucite formed during late fluid–rock interactions. Kahl et al. interpreted these distinctions to result from a resetting of the fluids caused by an *en route* loss of the fluid-mobile elements due to their incorporation into hydration products in the subduction channel.

The study by Kahl et al. (2015) emphasizes the necessity to investigate materials from the hydrated forearc lithosphere in order to better understand the fluid release and fluxes from the slab and related mass transfers to the mantle wedge. To contribute to a better understanding of these processes, I focused on

- the reconstruction of conditions during the polyphase serpentinitization history of mantle wedge material below the serpentinite mud volcanoes;

- tracking the incorporation of fluid-mobile elements released from the slab throughout the distinct generations of serpentine;
- potential changes in fluid-mobile element contents in serpentine linked to the slab depths of the individual mud volcanoes;
- compiling an overview on (changing) dehydration reactions affecting the subducting slab with progressive subduction.

These questions were addressed by investigating serpentinite clasts from the three serpentinite mud volcanoes that were targeted by IODP Expedition 366. *In situ* concentrations of Li, B, Rb, Sr, Cs, and Ba in serpentine veins provided insight into the abundance of these species within the serpentinizing fluids across the forearc.

1.4 Outline and scientific contributions

I. High-temperature hybrid rock hydration

<i>Full title</i>	Melt-impregnation of mantle peridotite facilitates high-temperature hydration and mechanical weakening: implications for oceanic detachment faults
<i>Authors</i>	Elmar Albers, Tim Schroeder, Wolfgang Bach
<i>Publication status</i>	Published in <i>Geochem., Geophys., Geosys.</i> 20, doi: 10.1029/2018GC007783

This study investigates the occurrence of mixed peridotite–gabbro lithologies at a detachment fault setting at the Mid-Atlantic Ridge. The hybrid rocks alter to amphibole- and phyllosilicate-rich secondary mineral assemblages during interaction with seawater-derived fluids at temperatures $>500^{\circ}\text{C}$. Strain, deformation, and faulting localize in these now mechanically weak zones, indicating that hybrid lithologies may play a key role in the evolution of detachment faults. Comparable hybrid rocks are described from detachment faults worldwide, implying that this process contributes to seafloor generation worldwide.

Author’s contributions

E. Albers	Sampling, sample preparation, petrographic and geochemical analyses of the samples, data processing and evaluation, implementation of geochemical models (in continuous dialogue with W. Bach), generation of figures, drafting of the manuscript.
T. Schroeder	Microstructural investigations and evaluation.
W. Bach	Assistance in modeling and model evaluation, supervision of the project.

Both co-authors further contributed by discussing and interpreting data and results and by improving earlier versions of the manuscript.

II. Clues on carbon cycling

<i>Full title</i>	Carbon cycling in the Mariana forearc
<i>Authors</i>	Elmar Albers, Frieder Klein, Wolfgang Bach, Catriona D. Menzies, Friedrich Lucassen
<i>Publication status</i>	To be submitted to <i>Solid Earth</i>

This manuscript reports on the occurrence of carbonate-rich veins in metavolcanic clast that have been recycled via serpentinite mud volcanism in the forearc of the Mariana subduction zone. The carbonates are interpreted to have formed under oxic conditions within the subduction channel. Their existence implies that CO₂ is effectively mobilized at shallow subduction levels and trapped in the form of carbonate mineralizations; these mineralizations represent a previously undescribed sink for carbon and may be significant for budgeting the long-term carbon cycle.

Author's contributions

E. Albers	Sampling, sample preparation, mineralogical and geochemical sample characterization and analyses, data processing and evaluation, generation of figures, drafting of the manuscript.
W. Bach	Supervision of the project, implementation of geochemical modeling, contribution to interpretation and discussion of data and results.
F. Klein	Supervision of and help with Raman work.
C.D. Menzies	Sampling of pore fluids, analyses of fluid Sr geochemistry.
F. Lucassen	Analyses of carbonate Sr isotopic compositions.

W. Bach and F. Klein further contributed by discussing data and results, and all co-authors helped to improve earlier versions of the manuscript. Harald Strauß (University of Münster) analyzed S isotopes.

III. Shallow subduction zone serpentinitization

<i>Full title</i>	Shallow subduction zone serpentinitization traps fluid-mobile elements: implications for element mobilization from serpentinite mud volcanism (Mariana forearc)
<i>Authors</i>	Elmar Albers, Wolf-Achim Kahl, Lena Beyer, Wolfgang Bach
<i>Publication status</i>	In preparation for submission to <i>Lithos</i>

This manuscript describes the incorporation of fluid-mobile elements (FMEs) in serpentinite clasts recovered from different serpentinite mud volcanoes at the Mariana forearc. The clasts originate from the basal plane of the mantle wedge and record geochemical signatures of fluids present in the subduction channel. FME concentrations within the serpentinites vary as a function of progressive subduction and associated prograde metamorphic reactions within the downgoing slab, leading to the release of FMEs from

different sources. We present a dataset that gives insight into the mobilization and cycling of FMEs at subduction levels of ~13 to 18 km.

Author's contributions

E. Albers	Sampling, sample preparation, petrographic characterization, EPMA and LA-ICP-MS analyses, data processing and evaluation, generation of figures, drafting of the manuscript.
W.-A. Kahl	Interpretation and discussion of data and results.
L. Beyer	EPMA and LA-ICP-MS analyses of three samples.
W. Bach	Supervision of the project.
W.-A. Kahl	further contributed by improving earlier versions of the manuscript.

References

- Anderson, R. N., Hobart, M. A., 1976. The relation between heat flow, sediment thickness, and age in the eastern Pacific. *J. Geophys. Res.* 81 (17), 2968–2989, doi:[10.1029/jb081i017p02968](https://doi.org/10.1029/jb081i017p02968).
- Bach, W., Banerjee, N. R., Dick, H. J. B., Baker, E. T., 2002. Discovery of ancient and active hydrothermal systems along the ultra-slow spreading Southwest Indian Ridge 10°–16° E. *Geochem. Geophys. Geosyst.* 3 (7), 1–14, doi:[10.1029/2001gc000279](https://doi.org/10.1029/2001gc000279).
- Bach, W., Früh-Green, G. L., 2010. Alteration of the oceanic lithosphere and implications for seafloor processes. *Elements* 6 (3), 173–178, doi:[10.2113/gselements.6.3.173](https://doi.org/10.2113/gselements.6.3.173).
- Bach, W., Garrido, C. J., Paulick, H., Harvey, J., Rosner, M., 2004. Seawater–peridotite interactions: first insights from ODP Leg 209, MAR 15° N. *Geochem. Geophys. Geosyst.* 5 (9), Q09F26, doi:[10.1029/2004gc000744](https://doi.org/10.1029/2004gc000744).
- Bach, W., Paulick, H., Garrido, C. J., Ildefonse, B., Meurer, W. P., Humphris, S. E., 2006. Unraveling the sequence of serpentinization reactions: petrography, mineral chemistry, and petrophysics of serpentinites from MAR 15° N (ODP Leg 209, Site 1274). *Geophys. Res. Lett.* 33 (13), L13306, doi:[10.1029/2006gl025681](https://doi.org/10.1029/2006gl025681).
- Bebout, G. E., 1991. Field-based evidence for devolatilization in subduction zones: implications for arc magmatism. *Science* 251 (4992), 413–416, doi:[10.1126/science.251.4992.413](https://doi.org/10.1126/science.251.4992.413).
- Bebout, G. E., Ryan, J. G., Leeman, W. P., Bebout, A. E., 1999. Fractionation of trace elements by subduction-zone metamorphism — effect of convergent-margin thermal evolution. *Earth Planet. Sci. Lett.* 171 (1), 63–81, doi:[10.1016/s0012-821x\(99\)00135-1](https://doi.org/10.1016/s0012-821x(99)00135-1).
- Berndt, M. E., Allen, D. E., Seyfried, W. E., 1996. Reduction of CO₂ during serpentinization of olivine at 300 °C and 500 bar. *Geology* 24 (4), 351, doi:[10.1130/0091-7613\(1996\)024<0351:rocdso>2.3.co;2](https://doi.org/10.1130/0091-7613(1996)024<0351:rocdso>2.3.co;2).
- Bevis, M., Taylor, F. W., Schutz, B. E., Recy, J., Isacks, B. L., Helu, S., Singh, R., Kendrick, E., Stowell, J., Taylor, B., Calmantli, S., 1995. Geodetic observations of very rapid convergence and back-arc extension at the Tonga arc. *Nature* 374 (6519), 249–251, doi:[10.1038/374249a0](https://doi.org/10.1038/374249a0).
- Bird, P., 2003. An updated digital model of plate boundaries. *Geochem. Geophys. Geosyst.* 4 (3), 1027, doi:[10.1029/2001gc000252](https://doi.org/10.1029/2001gc000252).
- Blackman, D. K., Ildefonse, B., John, B. E., Ohara, Y., Miller, D. J., MacLeod, C. J., the Expedition 304/305 Scientists (Eds.), 2006. Oceanic core complex formation, Atlantis Massif. Vol. 304/305 of Proc. IODP. Integrated Ocean Drilling Program, College Station (TX).
- Bloomer, S. H., Taylor, B., MacLeod, C. J., Stern, R. J., Fryer, P., Hawkins, J. W., Johnson, L., 1995. Early arc volcanism and the ophiolite problem: a perspective from drilling in the western Pacific. *Geoph. Monog. Series* 88, 1–30, doi:[10.1029/gm088p0001](https://doi.org/10.1029/gm088p0001).
- Blundy, J., Cashman, K. V., Rust, A., Witham, F., 2010. A case for CO₂-rich arc magmas. *Earth Planet. Sci. Lett.* 290 (3–4), 289–301, doi:[10.1016/j.epsl.2009.12.013](https://doi.org/10.1016/j.epsl.2009.12.013).

- Blundy, J., Dalton, J., 2000. Experimental comparison of trace element partitioning between clinopyroxene and melt in carbonate and silicate systems, and implications for mantle metasomatism. *Contrib. Mineral. Petrol.* 139 (3), 356–371, doi:[10.1007/s004100000139](https://doi.org/10.1007/s004100000139).
- Bogdanov, Y. A., Bortnikov, N. S., Vikent'ev, I. V., Gurvich, E. G., Sagalevich, A. M., 1997. A new type of modern mineral-forming system: black smokers of the hydrothermal field at 14°45' N latitude, Mid-Atlantic Ridge. *Geol. Ore Deposits* 39, 58–78.
- Bonatti, E., Lawrence, J. R., Morandi, N., 1984. Serpentinization of oceanic peridotites: temperature dependence of mineralogy and boron content. *Earth Planet. Sci. Lett.* 70 (1), 88–94, doi:[10.1016/0012-821x\(84\)90211-5](https://doi.org/10.1016/0012-821x(84)90211-5).
- Boschi, C., Früh-Green, G. L., Delacour, A., Karson, J. A., Kelley, D. S., 2006. Mass transfer and fluid flow during detachment faulting and development of an oceanic core complex, Atlantis Massif (MAR 30° N). *Geochem. Geophys. Geosyst.* 7 (1), Q01004, doi:[10.1029/2005gc001074](https://doi.org/10.1029/2005gc001074).
- Buck, W. R., 1988. Flexural rotation of normal faults. *Tectonics* 7 (5), 959–973, doi:[10.1029/TC007i005p00959](https://doi.org/10.1029/TC007i005p00959).
- Buck, W. R., Lavier, L. L., Poliakov, A. N. B., 2005. Modes of faulting at mid-ocean ridges. *Nature* 434, 719–723, doi:[10.1038/nature03358](https://doi.org/10.1038/nature03358).
- Cai, C., Wiens, D. A., Shen, W., Eimer, M., 2018. Water input into the Mariana subduction zone estimated from ocean-bottom seismic data. *Nature* 563 (7731), 389–392, doi:[10.1038/s41586-018-0655-4](https://doi.org/10.1038/s41586-018-0655-4).
- Cann, J. R., Blackman, D. K., Smith, D. K., McAllister, E., Janssen, B., Mello, S., Avgerinos, E., Pascoe, A. R., Escartín, J., 1997. Corrugated slip surfaces formed at ridge-transform intersections on the Mid-Atlantic Ridge. *Nature* 385, 329–332, doi:[10.1038/385329a0](https://doi.org/10.1038/385329a0).
- Cannat, M., Lagabrielle, Y., Bougault, H., Casey, J., de Coutures, N., Dmitriev, L., Fouquet, Y., 1997. Ultramafic and gabbroic exposures at the Mid-Atlantic Ridge: geological mapping in the 15° N region. *Tectonophysics* 279, 193–213, doi:[10.1016/S0040-1951\(97\)00113-3](https://doi.org/10.1016/S0040-1951(97)00113-3).
- Cannat, M., Sauter, D., Mendel, V., Ruellan, E., Okino, K., Escartín, J., Combiér, V., Baala, M., 2006. Modes of seafloor generation at a melt-poor ultraslow-spreading ridge. *Geology* 34 (7), 605–608, doi:[10.1130/g22486.1](https://doi.org/10.1130/g22486.1).
- Charlou, J. L., Bougault, H., Appriou, P., Nelsen, T., Rona, P., 1991. Different TDM/CH₄ hydrothermal plume signatures: TAG site at 26° N and serpentinized ultrabasic diapir at 15°05' N on the Mid-Atlantic Ridge. *Geochim. Cosmochim. Acta* 55 (11), 3209–3222, doi:[10.1016/0016-7037\(91\)90484-m](https://doi.org/10.1016/0016-7037(91)90484-m).
- Chase, C. G., 1972. The N plate problem of plate tectonics. *Geophys. J. Int.* 29 (2), 117–122, doi:[10.1111/j.1365-246x.1972.tb02202.x](https://doi.org/10.1111/j.1365-246x.1972.tb02202.x).
- Clift, P. D., Vannucchi, P., Morgan, J. P., 2009. Crustal redistribution, crust–mantle recycling and Phanerozoic evolution of the continental crust. *Earth Sci. Rev.* 97 (1–4), 80–104, doi:[10.1016/j.earscirev.2009.10.003](https://doi.org/10.1016/j.earscirev.2009.10.003).
- Cloos, M., Shreve, R. L., 1988. Subduction-channel model of prism accretion, melange formation, sediment subduction, and subduction erosion at convergent plate margins: 1. Background and description. *Pure Appl. Geophys.* 128 (3–4), 455–500, doi:[10.1007/bf00874548](https://doi.org/10.1007/bf00874548).
- Conrad, C. P., Lithgow-Bertelloni, C., 2002. How mantle slabs drive plate tectonics. *Science* 298 (5591), 207–209, doi:[10.1126/science.1074161](https://doi.org/10.1126/science.1074161).
- Cross, T. A., Pilger, R. H., 1982. Controls of subduction geometry, location of magmatic arcs, and tectonics of arc and back-arc regions. *Geol. Soc. Am. Bull.* 93 (6), 545–562, doi:[10.1130/0016-7606\(1982\)93<545:cosglo>2.0.co;2](https://doi.org/10.1130/0016-7606(1982)93<545:cosglo>2.0.co;2).
- D'Antonio, M., Kristensen, M. B., 2004. Serpentine and brucite of ultramafic clasts from the South Chamorro seamount (Ocean Drilling Program Leg 195, Site 1200): inferences for the serpentinization of the Mariana forearc mantle. *Mineralog. Mag.* 68 (6), 887–904, doi:[10.1180/0026461046860229](https://doi.org/10.1180/0026461046860229).
- Dasgupta, R., Hirschmann, M. M., 2010. The deep carbon cycle and melting in Earth's interior. *Earth Planet. Sci. Lett.* 298 (1–2), 1–13, doi:[10.1016/j.epsl.2010.06.039](https://doi.org/10.1016/j.epsl.2010.06.039).
- deMartin, B. J., Sohn, R. A., Canales, J. P., Humphris, S. E., 2007. Kinematics and geometry of active detachment faulting beneath the Trans-Atlantic Geotraverse (TAG) hydrothermal field on the Mid-Atlantic Ridge. *Geology* 35 (8), 711–714, doi:[10.1130/g23718a.1](https://doi.org/10.1130/g23718a.1).
- Deschamps, F., Godard, M., Guillot, S., Hattori, K., 2013. Geochemistry of subduction zone serpentinites:

- a review. *Lithos* 178, 96–127, doi:[10.1016/j.lithos.2013.05.019](https://doi.org/10.1016/j.lithos.2013.05.019).
- Deschamps, F., Guillot, S., Godard, M., Andreani, M., Hattori, K., 2011. Serpentinites act as sponges for fluid-mobile elements in abyssal and subduction zone environments. *Terra Nova* 23 (3), 171–178, doi:[10.1111/j.1365-3121.2011.00995.x](https://doi.org/10.1111/j.1365-3121.2011.00995.x).
- Dick, H. J. B., Lin, J., Schouten, H., 2003. An ultraslow-spreading class of ocean ridge. *Nature* 426, 405–412, doi:[10.1038/nature02128](https://doi.org/10.1038/nature02128).
- Dick, H. J. B., Natland, J., Ildefonse, B., 2006. Past and future impact of deep drilling in the oceanic crust and mantle. *Oceanography* 19 (4), 72–80, doi:[10.5670/oceanog.2006.06](https://doi.org/10.5670/oceanog.2006.06).
- Dick, H. J. B., Tivey, M. A., Tucholke, B. E., 2008. Plutonic foundation of a slow-spreading ridge segment: oceanic core complex at KANE Megamullion, 23°30' N, 45°20' W. *Geochem. Geophys. Geosyst.* 9 (5), Q05014, doi:[10.1029/2007GC001645](https://doi.org/10.1029/2007GC001645).
- Dominguez, S., Lallemand, S. E., Malavieille, J., von Huene, R., 1998. Upper plate deformation associated with seamount subduction. *Tectonophysics* 293 (3–4), 207–224, doi:[10.1016/s0040-1951\(98\)00086-9](https://doi.org/10.1016/s0040-1951(98)00086-9).
- Elderfield, H., Schultz, A., 1996. Mid-ocean ridge hydrothermal fluxes and the chemical composition of the ocean. *Annu. Rev. Earth Planet. Sci.* 24 (1), 191–224, doi:[10.1146/annurev.earth.24.1.191](https://doi.org/10.1146/annurev.earth.24.1.191).
- Escartín, J., Hirth, G., Evans, B., 1997. Effects of serpentinization on the lithospheric strength and the style of normal faulting at slow-spreading ridges. *Earth Planet. Sci. Lett.* 151 (3–4), 181–189, doi:[10.1016/s0012-821x\(97\)81847-x](https://doi.org/10.1016/s0012-821x(97)81847-x).
- Escartín, J., Hirth, G., Evans, B., 2001. Strength of slightly serpentinized peridotites: implications for the tectonics of oceanic lithosphere. *Geology* 29 (11), 1023–1026, doi:[10.1130/0091-7613\(2001\)029<1023:sosspi>2.0.co;2](https://doi.org/10.1130/0091-7613(2001)029<1023:sosspi>2.0.co;2).
- Escartín, J., Mével, C., MacLeod, C. J., McCaig, A. M., 2003. Constraints on deformation conditions and the origin of oceanic detachments: the Mid-Atlantic Ridge core complex at 15°45' N. *Geochem. Geophys. Geosyst.* 4 (8), 1067, doi:[10.1029/2002gc000472](https://doi.org/10.1029/2002gc000472).
- Escartín, J., Mevel, C., Petersen, S., Bonnemains, D., Cannat, M., Andreani, M., Augustin, N., Bezos, A., Chavagnac, V., Choi, Y., Godard, M., Haaga, K., Hamelin, C., Ildefonse, B., Jamieson, J., John, B., Laleu, T., MacLeod, C. J., Massot-Campos, M., Nomikou, P., Olive, J. A., Paquet, M., Rommevaux, C., Rothenbeck, M., Steinfuhrer, A., Tominaga, M., Triebe, L., Campos, R., Gracias, N., Garcia, R., 2017. Tectonic structure, evolution, and the nature of oceanic core complexes and their detachment fault zones (13°20' N and 13°30' N, Mid Atlantic Ridge). *Geochem. Geophys. Geosyst.* 18 (4), 1451–1482, doi:[10.1002/2016gc006775](https://doi.org/10.1002/2016gc006775).
- Evans, B. W., 2004. The serpentinite multisystem revisited: chrysotile is metastable. *Int. Geol. Rev.* 46 (6), 479–506, doi:[10.2747/0020-6814.46.6.479](https://doi.org/10.2747/0020-6814.46.6.479).
- Falk, E. S., Kelemen, P. B., 2015. Geochemistry and petrology of listvenite in the Samail ophiolite, Sultanate of Oman: complete carbonation of peridotite during ophiolite emplacement. *Geochim. Cosmochim. Acta* 160, 70–90, doi:[10.1016/j.gca.2015.03.014](https://doi.org/10.1016/j.gca.2015.03.014).
- Federico, L., Crispini, L., Scambelluri, M., Capponi, G., 2007. Ophiolite mélange zone records exhumation in a fossil subduction channel. *Geology* 35 (6), 499–502, doi:[10.1130/g23190a.1](https://doi.org/10.1130/g23190a.1).
- Fowler, C. M. R., 2004. *The solid Earth: an introduction to global geophysics*, 2nd Edition. Cambridge University Press, Cambridge.
- Franks, P. J., Royer, D. L., Beerling, D. J., Van de Water, P. K., Cantrill, D. J., Barbour, M. M., Berry, J. A., 2014. New constraints on atmospheric CO₂ concentration for the Phanerozoic. *Geophys. Res. Lett.* 41 (13), 4685–4694, doi:[10.1002/2014gl060457](https://doi.org/10.1002/2014gl060457).
- Früh-Green, G. L., Connolly, A. D., Plas, A., Kelley, D. S., Grobéty, B., 2004. Serpentinization of oceanic peridotites: implications for geochemical cycles and biological activity. *Geoph. Monog. Series* 144, 119–136, doi:[10.1029/144gm08](https://doi.org/10.1029/144gm08).
- Früh-Green, G. L., Orcutt, B. N., Rouméjon, S., Lilley, M. D., Morono, Y., Cotterill, C., Green, S., Escartín, J., John, B. E., McCaig, A. M., Cannat, M., Ménez, B., Schwarzenbach, E. M., Williams, M. J., Morgan, S., Lang, S. Q., Schrenk, M. O., Brazelton, W. J., Akizawa, N., Boschi, C., Dunkel, K. G., Quéméneur, M., Wattam, S. A., Mayhew, L., Harris, M., Bayrakci, G., Behrmann, J.-H., Herrero-Bervera, E., Hesse, K., Liz, H.-Q., Ratnayake, A. S., Twing, K., Weis, D., Zhao, R., Bilenker, L., 2018. Magmatism, serpentinization and life: insights through drilling the Atlantis Massif (IODP

- Expedition 357). *Lithos* 323, 137–155, doi:[10.1016/j.lithos.2018.09.012](https://doi.org/10.1016/j.lithos.2018.09.012).
- Fryer, P., Ambos, E. L., Hussong, D. M., 1985. Origin and emplacement of Mariana forearc seamounts. *Geology* 13 (11), 774–777, doi:[10.1130/0091-7613\(1985\)13<774:oeomf>2.0.co;2](https://doi.org/10.1130/0091-7613(1985)13<774:oeomf>2.0.co;2).
- Fryer, P., Fryer, G. J., 1987. Origins of nonvolcanic seamounts in a forearc environment. *Seamounts, Islands, and Atolls* 43, 61–69, doi:[10.1029/gm043p0061](https://doi.org/10.1029/gm043p0061).
- Fryer, P., Wheat, C. G., Williams, T., Albers, E., Bekins, B., Debret, B. P. R., Deng, J., Dong, Y., Eickenbusch, P., Frery, E. A., Ichiyama, Y., Jonson, K., Jonston, R. M., Kevorkian, R. T., Kurz, W., Magalhaes, V., Mantovanelli, S. S., Menapace, W., Menzies, C. D., Michibayashi, K., Moyer, C. L., Mullane, K. K., Park, J.-W., Price, R. E., Ryan, J. G., Shervais, J. W., Sissmann, O. J., Suzuki, S., Takai, K., Walter, B., Zhang, R., 2018a. Expedition 366 summary. Vol. 366 of Proc. IODP. International Ocean Discovery Program, College Station (TX). doi:[10.14379/iodp.proc.366.101.2018](https://doi.org/10.14379/iodp.proc.366.101.2018).
- Fryer, P., Wheat, C. G., Williams, T., the Expedition 366 Scientists (Eds.), 2018b. Mariana convergent margin and South Chamorro seamount. Vol. 366 of Proc. IODP. International Ocean Discovery Program, College Station (TX).
- Fryer, P. B., 1992. A synthesis of Leg 125 drilling of serpentinite seamounts on the Mariana and Izu-Bonin forearcs. In: Fryer, P., Pearce, J. A., Stokking, L. B. (Eds.), *Scientific Results*. Vol. 125 of Proc. ODP. Ocean Drilling Program, College Station (TX), pp. 593–614. doi:[10.2973/odp.proc.sr.125.168.1992](https://doi.org/10.2973/odp.proc.sr.125.168.1992).
- Fryer, P. B., 2012. Serpentinite mud volcanism: observations, processes, and implications. *Ann. Rev. Mar. Sci.* 4 (1), 345–373, doi:[10.1146/annurev-marine-120710-100922](https://doi.org/10.1146/annurev-marine-120710-100922).
- Fujiwara, T., Lin, J., Matsumoto, T., Kelemen, P. B., Tucholke, B. E., Casey, J. F., 2003. Crustal evolution of the Mid-Atlantic Ridge near the Fifteen-Twenty Fracture Zone in the last 5 Ma. *Geochem. Geophys. Geosyst.* 4 (3), 1024, doi:[10.1029/2002gc000364](https://doi.org/10.1029/2002gc000364).
- Furnes, H., Staudigel, H., 1999. Biological mediation in ocean crust alteration: how deep is the deep biosphere? *Earth Planet. Sci. Lett.* 166 (3–4), 97–103, doi:[10.1016/s0012-821x\(99\)00005-9](https://doi.org/10.1016/s0012-821x(99)00005-9).
- German, C. E., Seyfried, W. E., 2014. Hydrothermal processes. In: Holland, H. D., Turekian, K. K. (Eds.), *Treatise on geochemistry*, 2nd Edition. Vol. 8: The oceans and marine geochemistry. Elsevier, pp. 191–233. doi:[10.1016/b978-0-08-095975-7.00607-0](https://doi.org/10.1016/b978-0-08-095975-7.00607-0).
- German, C. R., Thurnherr, A. M., Knoery, J., Charlou, J.-L., Jean-Baptiste, P., Edmonds, H. N., 2010. Heat, volume and chemical fluxes from submarine venting: a synthesis of results from the Rainbow hydrothermal field, 36°N MAR. *Deep Sea Res. Part I* 57 (4), 518–527, doi:[10.1016/j.dsr.2009.12.011](https://doi.org/10.1016/j.dsr.2009.12.011).
- Gerya, T. V., Stöckhert, B., Perchuk, A. L., 2002. Exhumation of high-pressure metamorphic rocks in a subduction channel: a numerical simulation. *Tectonics* 21 (6), 1056, doi:[10.1029/2002tc001406](https://doi.org/10.1029/2002tc001406).
- Gill, J. B., 1981a. *Orogenic andesites and plate tectonics*. Springer, Berlin, Heidelberg. doi:[10.1007/978-3-642-68012-0](https://doi.org/10.1007/978-3-642-68012-0).
- Gill, J. B., 1981b. The role of subducted ocean crust in the genesis of orogenic andesite. In: *Orogenic andesites and plate tectonics*. Springer, Berlin, Heidelberg, pp. 230–247. doi:[10.1007/978-3-642-68012-0_8](https://doi.org/10.1007/978-3-642-68012-0_8).
- Gille, S., Metzger, J., Tokmakian, R., 2004. Seafloor topography and ocean circulation. *Oceanography* 17 (1), 47–54, doi:[10.5670/oceanog.2004.66](https://doi.org/10.5670/oceanog.2004.66).
- Gorman, P. J., Kerrick, D. M., Connolly, J. A. D., 2006. Modeling open system metamorphic decarbonation of subducting slabs. *Geochem. Geophys. Geosyst.* 7 (4), Q04007, doi:[10.1029/2005gc001125](https://doi.org/10.1029/2005gc001125).
- Harigane, Y., Michibayashi, K., Ohara, Y., 2008. Shearing within lower crust during progressive retrogression: structural analysis of gabbroic rocks from the Godzilla Mullion, an oceanic core complex in the Parece Vela backarc basin. *Tectonophysics* 457 (3), 183–196, doi:[10.1016/j.tecto.2008.06.009](https://doi.org/10.1016/j.tecto.2008.06.009).
- Harper, J. F., 1975. On the driving forces of plate tectonics. *Geophys. J. Int.* 40 (3), 465–474, doi:[10.1111/j.1365-246x.1975.tb04143.x](https://doi.org/10.1111/j.1365-246x.1975.tb04143.x).
- Hattori, K. H., Guillot, S., 2007. Geochemical character of serpentinites associated with high- to ultrahigh-pressure metamorphic rocks in the Alps, Cuba, and the Himalayas: recycling of elements in subduction zones. *Geochem. Geophys. Geosyst.* 8 (9), Q09010, doi:[10.1029/2007gc001594](https://doi.org/10.1029/2007gc001594).
- Hermann, J., Müntener, O., Scambelluri, M., 2000. The importance of serpentinite mylonites for subduction and exhumation of oceanic crust. *Tectonophysics* 327 (3–4), 225–238, doi:[10.1016/s0040-1951\(00\)00171-2](https://doi.org/10.1016/s0040-1951(00)00171-2).

- Hilde, T. W. C., 1983. Sediment subduction versus accretion around the Pacific. *Tectonophysics* 99 (2–4), 381–397, doi:[10.1016/0040-1951\(83\)90114-2](https://doi.org/10.1016/0040-1951(83)90114-2).
- Hofmann, A. W., 1988. Chemical differentiation of the Earth: the relationship between mantle, continental crust, and oceanic crust. *Earth Planet. Sci. Lett.* 90 (3), 297–314, doi:[10.1016/0012-821x\(88\)90132-x](https://doi.org/10.1016/0012-821x(88)90132-x).
- Hofmann, A. W., 1997. Mantle geochemistry: the message from oceanic volcanism. *Nature* 385 (6613), 219–229, doi:[10.1038/385219a0](https://doi.org/10.1038/385219a0).
- Hulme, S. M., Wheat, C. G., Fryer, P. B., Mottl, M. J., 2010. Pore water chemistry of the Mariana serpentinite mud volcanoes: a window to the seismogenic zone. *Geochem. Geophys. Geosyst.* 11 (1), Q01X09, doi:[10.1029/2009gc002674](https://doi.org/10.1029/2009gc002674).
- Hussong, D. M., Fryer, P., 1986. Forearc tectonics in the northern Mariana arc. In: Nasu, N., Uyeda, S., Kobayashi, K., Kushiro, I., Kagami, H. (Eds.), *Formation of active ocean margins. Advances in Earth and Planetary Sciences*. Terra Scientific Publishing Co., Tokyo, pp. 273–290.
- Hyndman, R. D., Peacock, S. M., 2003. Serpentinization of the forearc mantle. *Earth Planet. Sci. Lett.* 212 (3–4), 417–432, doi:[10.1016/s0012-821x\(03\)00263-2](https://doi.org/10.1016/s0012-821x(03)00263-2).
- Ildefonse, B., Blackman, D. K., John, B. E., Ohara, Y., Miller, D. J., MacLeod, C. J., 2007. Oceanic core complexes and crustal accretion at slow-spreading ridges. *Geology* 35 (7), 623–626, doi:[10.1130/g23531a.1](https://doi.org/10.1130/g23531a.1).
- Jannasch, H. W., Mottl, M. J., 1985. Geomicrobiology of deep-sea hydrothermal vents. *Science* 229 (4715), 717–725, doi:[10.1126/science.229.4715.717](https://doi.org/10.1126/science.229.4715.717).
- John, B. E., Cheadle, M. J., 2010. Deformation and alteration associated with oceanic and continental detachment fault systems: are they similar? *Geoph. Monog. Series* 188, 175–205, doi:[10.1029/2008gm000772](https://doi.org/10.1029/2008gm000772).
- John, T., Scambelluri, M., Frische, M., Barnes, J. D., Bach, W., 2011. Dehydration of subducting serpentinite: implications for halogen mobility in subduction zones and the deep halogen cycle. *Earth Planet. Sci. Lett.* 308 (1–2), 65–76, doi:[10.1016/j.epsl.2011.05.038](https://doi.org/10.1016/j.epsl.2011.05.038).
- Jöns, N., Bach, W., Klein, F., 2010. Magmatic influence on reaction paths and element transport during serpentinization. *Chem. Geol.* 274 (3–4), 196–211, doi:[10.1016/j.chemgeo.2010.04.009](https://doi.org/10.1016/j.chemgeo.2010.04.009).
- Jöns, N., Bach, W., Schroeder, T., 2009. Formation and alteration of plagiogranites in an ultramafic-hosted detachment fault at the Mid-Atlantic Ridge (ODP Leg 209). *Contrib. Mineral. Petrol.* 157 (5), 625–639, doi:[10.1007/s00410-008-0357-2](https://doi.org/10.1007/s00410-008-0357-2).
- Kadko, D., 1993. An assessment of the effect of chemical scavenging within submarine hydrothermal plumes upon ocean geochemistry. *Earth Planet. Sci. Lett.* 120 (3–4), 361–374, doi:[10.1016/0012-821x\(93\)90250-d](https://doi.org/10.1016/0012-821x(93)90250-d).
- Kahl, W.-A., Jöns, N., Bach, W., Klein, F., Alt, J. C., 2015. Ultramafic clasts from the South Chamorro serpentinite mud volcano reveal a polyphase serpentinization history of the Mariana forearc mantle. *Lithos* 227, 1–20, doi:[10.1016/j.lithos.2015.03.015](https://doi.org/10.1016/j.lithos.2015.03.015).
- Karson, J. A., 1998. Internal structure of oceanic lithosphere: a perspective from tectonic windows. *Geoph. Monog. Series* 106, 177–218, doi:[10.1029/gm106p0177](https://doi.org/10.1029/gm106p0177).
- Karson, J. A., 1999. Geological investigation of a lineated massif at the Kane transform fault: implications for oceanic core complexes. *Phil. Trans. R. Soc. A* 357, 713–740, doi:[10.1098/rsta.1999.0350](https://doi.org/10.1098/rsta.1999.0350).
- Karson, J. A., Thompson, G., Humphris, S. E., Edmond, J. M., Bryan, W. B., Brown, J. R., Winters, A. T., Pockalny, R. A., Casey, J. F., Campbell, A. C., Klinkhammer, G., Palmer, M. R., Kinzler, R. J., Sulanowska, M. M., 1987. Along-axis variations in seafloor spreading in the MARK area. *Nature* 328, 681–685, doi:[10.1038/328681a0](https://doi.org/10.1038/328681a0).
- Kastner, M., 1981. Authigenic silicates in deep-sea sediments: formation and diagenesis. In: Emiliani, C. (Ed.), *The sea*, vol. 7: the oceanic lithosphere. Wiley, London, pp. 515–980.
- Katsumata, M., Sykes, L. R., 1969. Seismicity and tectonics of the western Pacific: Izu-Mariana-Caroline and Ryukyu-Taiwan regions. *J. Geophys. Res.* 74 (25), 5923–5948, doi:[10.1029/jb074i025p05923](https://doi.org/10.1029/jb074i025p05923).
- Kelemen, P., Kikawa, E., Miller, D. J., the Leg 209 Scientific Party, 2004. ODP Leg 209 drills into mantle peridotite along the Mid-Atlantic Ridge from 14° N to 16° N. *JOIDES Journal* 30 (1), 14–19.
- Kelemen, P. B., Manning, C. E., 2015. Reevaluating carbon fluxes in subduction zones, what goes down, mostly comes up. *Proc. Natl. Acad. Sci.* 112 (30), E3997–E4006, doi:[10.1073/pnas.1507889112](https://doi.org/10.1073/pnas.1507889112).

- Kelley, D. S., Karson, J. A., Früh-Green, G. L., Yoerger, D. R., Shank, T. M., Butterfield, D. A., Hayes, J. M., Schrenk, M. O., Olson, E. J., Proskurowski, G., Jakuba, M., Bradley, A., Larson, B., Ludwig, K., Glickson, D., Buckman, K., Bradley, A. S., Brazelton, W. J., Roa, K., Elend, M. J., Delacour, A., Bernasconi, A. M., Lilley, M. D., Baross, J. A., Summons, R. E., Sylva, S. P., 2005. A serpentinite-hosted ecosystem: the Lost City hydrothermal field. *Science* 307, 1428–1434, doi:[10.1126/science.1102556](https://doi.org/10.1126/science.1102556).
- Kerrick, D. M., Connolly, J. A. D., 2001. Metamorphic devolatilization of subducted marine sediments and the transport of volatiles into the Earth's mantle. *Nature* 411 (6835), 293–296, doi:[10.1038/35077056](https://doi.org/10.1038/35077056).
- Koepke, J., Feig, S. T., Snow, J., 2005. Hydrous partial melting within the lower oceanic crust. *Terra Nova* 17 (3), 286–291, doi:[10.1111/j.1365-3121.2005.00613.x](https://doi.org/10.1111/j.1365-3121.2005.00613.x).
- Kumagai, H., Nakamura, K., Toki, T., Morishita, T., Okino, K., Ishibashi, J.-i., Tsunogai, U., Kawagucci, S., Gamo, T., Shibuya, T., Sawaguchi, T., Neo, N., Joshima, M., Sato, T., Takai, K., 2008. Geological background of the Kairei and Edmond hydrothermal fields along the Central Indian Ridge: implications of their vent fluids' distinct chemistry. *Geofluids* 8, 239–251, doi:[10.1111/j.1468-8123.2008.00223.x](https://doi.org/10.1111/j.1468-8123.2008.00223.x).
- Langmuir, C. H., Klein, E. M., Plank, T., 1992. Petrological systematics of mid-ocean ridge basalts: constraints on melt generation beneath ocean ridges. *Geoph. Monog. Series* 71, 183–280, doi:[10.1029/gm071p0183](https://doi.org/10.1029/gm071p0183).
- Leat, P. T., Larter, R. D., 2003. Intra-oceanic subduction systems: introduction. *Geol. Soc. Spec. Pub.* 219 (1), 1–17, doi:[10.1144/gsl.sp.2003.219.01.01](https://doi.org/10.1144/gsl.sp.2003.219.01.01).
- Lockwood, J. P., 1972. Possible mechanisms for the emplacement of alpine-type serpentinite. *Geol. Soc. Am. Mem.* 132, 273–288, doi:[10.1130/mem132-p273](https://doi.org/10.1130/mem132-p273).
- Lowell, R. P., Rona, P. A., 2002. Seafloor hydrothermal systems driven by the serpentinization of peridotite. *Geophys. Res. Lett.* 29 (11), 26, doi:[10.1029/2001gl014411](https://doi.org/10.1029/2001gl014411).
- MacLeod, C. J., Escartín, J., Banerji, D., Banks, G. J., Gleeson, M., Irving, D. H. B., Lilly, R. M., McCaig, A. M., Niu, Y., Allerton, S., Smith, D. K., 2002. Direct geological evidence for oceanic detachment faulting: the Mid-Atlantic Ridge, 15°45' N. *Geology* 30 (10), 879–882, doi:[10.1130/0091-7613\(2002\)030<0879:dgefod>2.0.co;2](https://doi.org/10.1130/0091-7613(2002)030<0879:dgefod>2.0.co;2).
- MacLeod, C. J., Searle, R. C., Murton, B. J., Casey, J. F., Mallows, C., Unsworth, S. C., Schenbach, K. L., Harris, M., 2009. Life cycle of oceanic core complexes. *Earth Planet. Sci. Lett.* 287 (3–4), 333–344, doi:[10.1016/j.epsl.2009.08.016](https://doi.org/10.1016/j.epsl.2009.08.016).
- Maekawa, H., Masaya, S., Ishill, T., Fryer, P., Pearce, J. A., 1993. Blueschist metamorphism in an active subduction zone. *Nature* 364, 520–523, doi:[10.1038/364520a0](https://doi.org/10.1038/364520a0).
- Manning, C. E., 2004. The chemistry of subduction-zone fluids. *Earth Planet. Sci. Lett.* 223 (1–2), 1–16, doi:[10.1016/j.epsl.2004.04.030](https://doi.org/10.1016/j.epsl.2004.04.030).
- Marschall, H. R., Altherr, R., Rüpke, L., 2007. Squeezing out the slab — modelling the release of Li, Be and B during progressive high-pressure metamorphism. *Chem. Geol.* 239 (3–4), 323–335, doi:[10.1016/j.chemgeo.2006.08.008](https://doi.org/10.1016/j.chemgeo.2006.08.008).
- Martin, W., Baross, J., Kelley, D., Russell, M. J., 2008. Hydrothermal vents and the origin of life. *Nat. Rev. Microbiol.* 6, 805–814, doi:[10.1038/nrmicro1991](https://doi.org/10.1038/nrmicro1991).
- McCaig, A. M., Cliff, R. A., Escartín, J., Fallick, A. E., MacLeod, C. J., 2007. Oceanic detachment faults focus very large volumes of black smoker fluids. *Geology* 35 (10), 935–938, doi:[10.1130/g23657a.1](https://doi.org/10.1130/g23657a.1).
- McCullom, T. M., Bach, W., 2009. Thermodynamic constraints on hydrogen generation during serpentinization of ultramafic rocks. *Geochim. Cosmochim. Acta* 73 (3), 856–875, doi:[10.1016/j.gca.2008.10.032](https://doi.org/10.1016/j.gca.2008.10.032).
- McCullom, T. M., Shock, E. L., 1998. Fluid-rock interactions in the lower oceanic crust: thermodynamic models of hydrothermal alteration. *J. Geophys. Res. Solid Earth* 103 (B1), 547–575, doi:[10.1029/97jb02603](https://doi.org/10.1029/97jb02603).
- Michael, P. J., Langmuir, C. H., Dick, H. J. B., Snow, J. E., Goldstein, S. L., Graham, D. W., Lehnert, K., Kurras, G., Jokat, W., Mühe, R., Edmonds, H. N., 2003. Magmatic and amagmatic seafloor generation at the ultraslow-spreading Gakkel Ridge, Arctic Ocean. *Nature* 423, 956–961, doi:[10.1038/nature01704](https://doi.org/10.1038/nature01704).
- Molnar, P., Atwater, T., 1978. Interarc spreading and Cordilleran tectonics as alternates related to the age of subducted oceanic lithosphere. *Earth Planet. Sci. Lett.* 41 (3), 330–340, doi:[10.1016/0012-821x\(78\)90187-5](https://doi.org/10.1016/0012-821x(78)90187-5).

- Moore, J. C., Vrolijk, P., 1992. Fluids in accretionary prisms. *Rev. Geophys.* 30 (2), 113–135, doi:[10.1029/92rg00201](https://doi.org/10.1029/92rg00201).
- Mottl, M. J., Wheat, C. G., Fryer, P. B., Gharib, J., Martin, J. B., 2004. Chemistry of springs across the Mariana forearc shows progressive devolatilization of the subducting plate. *Geochim. Cosmochim. Acta* 68 (23), 4915–4933, doi:[10.1016/j.gca.2004.05.037](https://doi.org/10.1016/j.gca.2004.05.037).
- Mrozowski, C. L., Hayes, D. E., 1980. A seismic reflection study of faulting in the Mariana fore arc. *Geoph. Monog. Series* 23, 223–234, doi:[10.1029/gm023p0223](https://doi.org/10.1029/gm023p0223).
- Müller, R. D., Sdrolias, M., Gaina, C., Roest, W. R., 2008. Age, spreading rates, and spreading asymmetry of the world's ocean crust. *Geochem. Geophys. Geosyst.* 9 (4), Q04006, doi:[10.1029/2007gc001743](https://doi.org/10.1029/2007gc001743).
- Nichols, G. T., Wyllie, P. J., Stern, C. R., 1996. Experimental melting of pelagic sediment, constraints relevant to subduction. *Geoph. Monog. Series* 96, 293–298, doi:[10.1029/gm096p0293](https://doi.org/10.1029/gm096p0293).
- Oakley, A. J., Taylor, B., Fryer, P. B., Moore, G. F., Goodliffe, A. M., Morgan, J. K., 2007. Emplacement, growth, and gravitational deformation of serpentinite seamounts on the Mariana forearc. *Geophys. J. Int.* 170 (2), 615–634, doi:[10.1111/j.1365-246x.2007.03451.x](https://doi.org/10.1111/j.1365-246x.2007.03451.x).
- Oakley, A. J., Taylor, B., Moore, G. F., 2008. Pacific plate subduction beneath the central Mariana and Izu-Bonin fore arcs: new insights from an old margin. *Geochem. Geophys. Geosyst.* 9 (6), Q06003, doi:[10.1029/2007gc001820](https://doi.org/10.1029/2007gc001820).
- Olive, J.-A., Behn, M. D., Tucholke, B. E., 2010. The structure of oceanic core complexes controlled by the depth distribution of magma emplacement. *Nat. Geosci.* 3 (7), 491–495, doi:[10.1038/ngeo888](https://doi.org/10.1038/ngeo888).
- Paulick, H., Bach, W., Godard, M., de Hoog, J. C. M., Suhr, G., Harvey, J., 2006. Geochemistry of abyssal peridotites (Mid-Atlantic Ridge, 15°20' N, ODP Leg 209): implications for fluid/rock interaction in slow spreading environments. *Chem. Geol.* 234, 179–210, doi:[10.1016/j.chemgeo.2006.04.011](https://doi.org/10.1016/j.chemgeo.2006.04.011).
- Peacock, S. A., 1990. Fluid processes in subduction zones. *Science* 248 (4953), 329–337, doi:[10.1126/science.248.4953.329](https://doi.org/10.1126/science.248.4953.329).
- Peacock, S. M., 1996. Thermal and petrologic structure of subduction zones. *Geoph. Monog. Series* 96, 119–133, doi:[10.1029/gm096p0119](https://doi.org/10.1029/gm096p0119).
- Perfit, M. R., Gust, D. A., Bence, A. E., Arculus, R. J., Taylor, S. R., 1980. Chemical characteristics of island-arc basalts: implications for mantle sources. *Chem. Geol.* 30 (3), 227–256, doi:[10.1016/0009-2541\(80\)90107-2](https://doi.org/10.1016/0009-2541(80)90107-2).
- Peters, D., Bretscher, A., John, T., Scambelluri, M., Pettke, T., 2017. Fluid-mobile elements in serpentinites: constraints on serpentinitisation environments and element cycling in subduction zones. *Chem. Geol.* 466, 654–666, doi:[10.1016/j.chemgeo.2017.07.017](https://doi.org/10.1016/j.chemgeo.2017.07.017).
- Petersen, J. M., Zielinski, F. U., Pape, T., Seifert, R., Moraru, C., Amann, R., Hourdez, S., Girguis, P. R., Wankel, S. D., Barbe, V., Pelletier, E., Fink, D., Borowski, C., Bach, W., Dubilier, N., 2011. Hydrogen is an energy source for hydrothermal vent symbioses. *Nature* 476, 176–180, doi:[10.1038/nature10325](https://doi.org/10.1038/nature10325).
- Picazo, S., Cannat, M., Delacour, A., Escartín, J., Rouméjon, S., Silantyev, S., 2012. Deformation associated with the denudation of mantle-derived rocks at the Mid-Atlantic Ridge 13°–15° N: the role of magmatic injections and hydrothermal alteration. *Geochem. Geophys. Geosyst.* 13 (9), 3306–3313, doi:[10.1029/2012gc004121](https://doi.org/10.1029/2012gc004121).
- Poli, S., Schmidt, M. W., 1995. H₂O transport and release in subduction zones: experimental constraints on basaltic and andesitic systems. *J. Geophys. Res. Solid Earth* 100 (B11), 22299–22314, doi:[10.1029/95jb01570](https://doi.org/10.1029/95jb01570).
- Pons, M.-L., Quitté, G., Fujii, T., Rosing, M. T., Reynard, B., Moynier, C. D., Albarède, F., 2011. Early Archean serpentinite mud volcanoes at Isua, Greenland, as a niche for early life. *Proc. Natl. Acad. Sci.* 108 (43), 17639–17643, doi:[10.1073/pnas.1108061108](https://doi.org/10.1073/pnas.1108061108).
- Proskurowski, G., Lilley, M. D., Seewald, J. S., Früh-Green, G. L., Olson, E. J., Lupton, J. E., Sylva, S. P., Kelley, D. S., 2008. Abiogenic hydrocarbon production at Lost City hydrothermal field. *Science* 319, 604–607, doi:[10.1126/science.1151194](https://doi.org/10.1126/science.1151194).
- Rahmstorf, S., 2002. Ocean circulation and climate during the past 120,000 years. *Nature* 419 (6903), 207–214, doi:[10.1038/nature01090](https://doi.org/10.1038/nature01090).
- Ranero, C. R., Phipps Morgan, J., McIntosh, K., Reichert, C., 2003. Bending-related faulting and mantle serpentinitization at the Middle America trench. *Nature* 425 (6956), 367–373, doi:[10.1038/nature01961](https://doi.org/10.1038/nature01961).

- Reynolds, S. J., Richard, S. M., Haxel, G. M., Tosdal, R. M., Laubach, S. E., 1988. Geologic setting of Mesozoic and Cenozoic metamorphism in Arizona. In: Ernst, W. G. (Ed.), *Metamorphism and crustal evolution of the Western United States*. Prentice Hall, Englewood Cliffs (NJ), pp. 446–501.
- Ringwood, A. E., 1969. Composition and evolution of the upper mantle. *Geoph. Monog. Series* 13, 1–17, doi:[10.1029/gm013p0001](https://doi.org/10.1029/gm013p0001).
- Rüpke, L. H., Morgan, J. P., Hort, M., Connolly, J. A. D., 2004. Serpentine and the subduction zone water cycle. *Earth Planet. Sci. Lett.* 223 (1–2), 17–34, doi:[10.1016/j.epsl.2004.04.018](https://doi.org/10.1016/j.epsl.2004.04.018).
- Savov, I. P., Ryan, J. G., Antonio, M. D., Fryer, P., 2007. Shallow slab fluid release across and along the Mariana arc-basin system: insights from geochemistry of serpentinized peridotites from the Mariana fore arc. *J. Geophys. Res.* 112 (B9), B09205, doi:[10.1029/2006jb004749](https://doi.org/10.1029/2006jb004749).
- Scambelluri, M., Fiebig, J., Malaspina, N., Müntener, O., Pettke, T., 2004. Serpentinite subduction: implications for fluid processes and trace-element recycling. *Int. Geol. Rev.* 46 (7), 595–613, doi:[10.2747/0020-6814.46.7.595](https://doi.org/10.2747/0020-6814.46.7.595).
- Scambelluri, M., Müntener, O., Hermann, J., Piccardo, G. B., Trommsdorff, V., 1995. Subduction of water into the mantle: history of an Alpine peridotite. *Geology* 23 (5), 459–462, doi:[10.1130/0091-7613\(1995\)023<0459:sowitm>2.3.co;2](https://doi.org/10.1130/0091-7613(1995)023<0459:sowitm>2.3.co;2).
- Scambelluri, M., Philippot, P., 2001. Deep fluids in subduction zones. *Lithos* 55 (1–4), 213–227, doi:[10.1016/s0024-4937\(00\)00046-3](https://doi.org/10.1016/s0024-4937(00)00046-3).
- Schmidt, M. W., Poli, S., 1998. Experimentally based water budgets for dehydrating slabs and consequences for arc magma generation. *Earth Planet. Sci. Lett.* 163 (1–4), 361–379, doi:[10.1016/s0012-821x\(98\)00142-3](https://doi.org/10.1016/s0012-821x(98)00142-3).
- Schmidt, M. W., Poli, S., 2014. Devolatilization during subduction. In: Holland, H. D., Turekian, K. K. (Eds.), *Treatise on geochemistry*, 2nd Edition. Vol. 8: The oceans and marine geochemistry. Elsevier, pp. 669–701. doi:[10.1016/b978-0-08-095975-7.00321-1](https://doi.org/10.1016/b978-0-08-095975-7.00321-1).
- Schroeder, T., Cheadle, M. J., Dick, H. J. B., Faul, U., Casey, J. F., Kelemen, P. B., 2007. Nonvolcanic seafloor spreading and corner-flow rotation accommodated by extensional faulting at 15° N on the Mid-Atlantic Ridge: a structural synthesis of ODP Leg 209. *Geochem. Geophys. Geosyst.* 8 (6), Q06015, doi:[10.1029/2006gc001567](https://doi.org/10.1029/2006gc001567).
- Schroeder, T., John, B. E., 2004. Strain localization on an oceanic detachment fault system, Atlantis Massif, 30° N, Mid-Atlantic Ridge. *Geochem. Geophys. Geosyst.* 5 (11), Q11007, doi:[10.1029/2004gc000728](https://doi.org/10.1029/2004gc000728).
- Schwarzenbach, E. M., Caddick, M. J., Petroff, M., Gill, B. C., Cooperdock, E. H. G., Barnes, J. D., 2018. Sulphur and carbon cycling in the subduction zone mélange. *Sci. Rep.* 8 (1), 15517, doi:[10.1038/s41598-018-33610-9](https://doi.org/10.1038/s41598-018-33610-9).
- Shiklomanov, I. A., 1993. World fresh water resources. In: Gleick, P. H. (Ed.), *Water in crisis: a guide to the world's fresh water resources*. Oxford University Press, New York (NY)/Oxford, Ch. 2, pp. 13–24.
- Shipboard Scientific Party, 2000. Leg 185 summary: inputs to the Izu-Mariana subduction system. In: Plank, T., Ludden, J. N., Escutia, C. (Eds.), *Init. Rep. Vol. 185 of Proc. ODP. Ocean Drilling Program, College Station (TX)*, pp. 1–63. doi:[10.2973/odp.proc.ir.185.101.2000](https://doi.org/10.2973/odp.proc.ir.185.101.2000).
- Shipboard Scientific Party, 2004a. Leg 209 summary. In: Kelemen, P. B., Kikawa, E., Miller, D. J. (Eds.), *Init. Res. Vol. 209 of Proc. ODP. Integrated Ocean Drilling Program, College Station (TX)*, pp. 0–139. doi:[10.2973/odp.proc.ir.209.101.2004](https://doi.org/10.2973/odp.proc.ir.209.101.2004).
- Shipboard Scientific Party, 2004b. Site 1271. In: Kelemen, P. B., Kikawa, E., Miller, D. J. (Eds.), *Initial Reports. Vol. 209 of Proc. ODP. Integrated Ocean Drilling Program, College Station (TX)*. doi:[10.2973/odp.proc.ir.209.110.2004](https://doi.org/10.2973/odp.proc.ir.209.110.2004).
- Shock, E. L., Schulte, M. D., 1998. Organic synthesis during fluid mixing in hydrothermal systems. *J. Geophys. Res. Planets* 103 (E12), 28513–28527, doi:[10.1029/98je02142](https://doi.org/10.1029/98je02142).
- Sisson, T. W., Grove, T. L., 1993. Temperatures and H₂O contents of low-MgO high-alumina basalts. *Contrib. Mineral. Petrol.* 113 (2), 167–184, doi:[10.1007/bf00283226](https://doi.org/10.1007/bf00283226).
- Sleep, N. H., Zahnle, K., 2001. Carbon dioxide cycling and implications for climate on ancient Earth. *J. Geophys. Res.* 106 (E1), 1373–1399, doi:[10.1029/2000je001247](https://doi.org/10.1029/2000je001247).
- Smith, D. K., Escartín, J., Schouten, H., Cann, J. R., 2008. Fault rotation and core complex formation: significant processes in seafloor formation at slow-spreading mid-ocean ridges (Mid-Atlantic Ridge,

- 13°–15° N). *Geochem. Geophys. Geosyst.* 9 (3), Q03003, doi:[10.1029/2007gc001699](https://doi.org/10.1029/2007gc001699).
- Staudigel, H., 2003. Hydrothermal alteration processes in the oceanic crust. In: Holland, H. D., Turekian, K. K. (Eds.), *Treatise on geochemistry*. Vol. 3. Elsevier, Amsterdam, pp. 511–535. doi:[10.1016/b0-08-043751-6/03032-2](https://doi.org/10.1016/b0-08-043751-6/03032-2).
- Stein, C. A., Stein, S., 1994. Constraints on hydrothermal heat flux through the oceanic lithosphere from global heat flow. *J. Geophys. Res. Solid Earth* 99 (B2), 3081–3095, doi:[10.1029/93jb02222](https://doi.org/10.1029/93jb02222).
- Stern, C. R., 2011. Subduction erosion: rates, mechanisms, and its role in arc magmatism and the evolution of the continental crust and mantle. *Gondwana Res.* 20 (2–3), 284–308, doi:[10.1016/j.gr.2011.03.006](https://doi.org/10.1016/j.gr.2011.03.006).
- Stern, R. J., 2002. Subduction zones. *Rev. Geophys.* 40 (4), 3, doi:[10.1029/2001rg000108](https://doi.org/10.1029/2001rg000108).
- Stern, R. J., Smoot, N. C., 1998. A bathymetric overview of the Mariana forearc. *The Island Arc* 7 (3), 525–540, doi:[10.1111/j.1440-1738.1998.00208.x](https://doi.org/10.1111/j.1440-1738.1998.00208.x).
- Straub, S. M., Layne, G. D., 2003. Decoupling of fluids and fluid-mobile elements during shallow subduction: evidence from halogen-rich andesite melt inclusions from the Izu arc volcanic front. *Geochem. Geophys. Geosyst.* 4 (7), 9003, doi:[10.1029/2002gc000349](https://doi.org/10.1029/2002gc000349).
- Sykes, L. R., McCann, W. R., Kafka, A. L., 1982. Motion of Caribbean plate during last 7 million years and implications for earlier Cenozoic movements. *J. Geophys. Res. Solid Earth* 87 (B13), 10656–10676, doi:[10.1029/jb0871b13p10656](https://doi.org/10.1029/jb0871b13p10656).
- Tatsumi, Y., 1989. Migration of fluid phases and genesis of basalt magmas in subduction zones. *J. Geophys. Res. Solid Earth* 94 (B4), 4697–4707, doi:[10.1029/jb094ib04p04697](https://doi.org/10.1029/jb094ib04p04697).
- Tatsumi, Y., Eggins, S., 1995. Subduction zone magmatism. *Frontiers in Earth Sciences*. John Wiley & Sons, Cambridge.
- Tatsumi, Y., Kogiso, T., 2003. The subduction factory: its role in the evolution of the earth's crust and mantle. *Geol. Soc. Spec. Pub.* 219 (1), 55–80, doi:[10.1144/gsl.sp.2003.219.01.03](https://doi.org/10.1144/gsl.sp.2003.219.01.03).
- Taylor, S. R., McLennan, S. M., 1995. The geochemical evolution of the continental crust. *Rev. Geophys.* 33 (2), 241–265, doi:[10.1029/95rg00262](https://doi.org/10.1029/95rg00262).
- Tenthorey, E., Hermann, J., 2004. Composition of fluids during serpentinite breakdown in subduction zones: evidence for limited boron mobility. *Geology* 32 (10), 865–868, doi:[10.1130/g20610.1](https://doi.org/10.1130/g20610.1).
- Thompson, A. B., 2010. Perspectives on metamorphic processes and fluids. *Elements* 6 (3), 142–143.
- Tibi, R., Wiens, D. A., Yuan, X., 2008. Seismic evidence for widespread serpentinized forearc mantle along the Mariana convergence margin. *Geophys. Res. Lett.* 35 (13), L13303, doi:[10.1029/2008gl034163](https://doi.org/10.1029/2008gl034163).
- Tivey, M. K., 2007. Generation of seafloor hydrothermal vent fluids and associated mineral deposits. *Oceanography* 20 (1), 50–65, doi:[10.5670/oceanog.2007.80](https://doi.org/10.5670/oceanog.2007.80).
- Trommsdorff, V., López Sánchez-Vizcaíno, V., Gómez-Pugnaire, M. T., Müntener, O., 1998. High pressure breakdown of antigorite to spinifex-textured olivine and orthopyroxene, SE Spain. *Contrib. Mineral. Petrol.* 132 (2), 139–148, doi:[10.1007/s004100050412](https://doi.org/10.1007/s004100050412).
- Tucholke, B. E., Behn, M. D., Buck, W. R., Lin, J., 2008. Role of melt supply in oceanic detachment faulting and formation of megamullions. *Geology* 36 (6), 455–458, doi:[10.1130/g24639a.1](https://doi.org/10.1130/g24639a.1).
- Tucholke, B. E., Lin, J., Kleinrock, M. C., 1998. Megamullions and mullion structure defining oceanic metamorphic core complexes on the Mid-Atlantic Ridge. *J. Geophys. Res.* 103 (B5), 9857–9866, doi:[10.1029/98jb00167](https://doi.org/10.1029/98jb00167).
- Ulmer, P., 2001. Partial melting in the mantle wedge — the role of H₂O in the genesis of mantle-derived ‘arc-related’ magmas. *Phys. Earth Planet. Inter.* 127 (1–4), 215–232, doi:[10.1016/s0031-9201\(01\)00229-1](https://doi.org/10.1016/s0031-9201(01)00229-1).
- Ulmer, P., Trommsdorff, V., 1995. Serpentine stability to mantle depths and subduction-related magmatism. *Science* 268 (5212), 858–861, doi:[10.1126/science.268.5212.858](https://doi.org/10.1126/science.268.5212.858).
- Uyeda, S., Kanamori, H., 1979. Back-arc opening and the mode of subduction. *J. Geophys. Res.* 84 (B3), 1049, doi:[10.1029/jb084ib03p01049](https://doi.org/10.1029/jb084ib03p01049).
- von Huene, R., Scholl, D. W., 1991. Observations at convergent margins concerning sediment subduction, subduction erosion, and the growth of continental crust. *Rev. Geophys.* 29 (3), 279, doi:[10.1029/91rg00969](https://doi.org/10.1029/91rg00969).
- Wessel, J. K., Fryer, P., Wessel, P., Taylor, B., 1994. Extension in the northern Mariana inner forearc. *J. Geophys. Res.* 99 (B8), 15181, doi:[10.1029/94jb00692](https://doi.org/10.1029/94jb00692).

2 High-temperature hybrid rock hydration

<i>Full title</i>	Melt-impregnation of mantle peridotite facilitates high-temperature hydration and mechanical weakening: implications for oceanic detachment faults
<i>Authors</i>	Elmar Albers,* Tim Schroeder,† Wolfgang Bach*
<i>Affiliations</i>	*Department of Geosciences and MARUM – Center for Marine Environmental Sciences, University of Bremen, Germany; †Natural Sciences Division, Bennington College, Vermont, USA
<i>Publication status</i>	Published as Albers, E., Schroeder, T., Bach, W., 2019. Melt-impregnation of mantle peridotite facilitates high-temperature hydration and mechanical weakening: implications for oceanic detachment faults. <i>Geochem. Geophys. Geosys.</i> 20, doi: 10.1029/2018GC007783

Abstract

The footwalls of oceanic detachment faults commonly expose shear zone rocks that appear to have compositions intermediate between those of mantle peridotite and magmatic rocks. These compositions either reflect metasomatic mass transfers or they relate to the impregnation of lithospheric mantle with basaltic or more evolved melts. We studied chlorite–amphibole-rich shear zone rocks from a detachment fault zone in the 15°20' N Fracture Zone area, Mid-Atlantic Ridge, to examine their origin and role in strain localization. Geochemical compositions of these rocks imply that they formed by mixing between peridotite and gabbro. Textural observations indicate a strong contrast between the deformation intensity of these hybrid peridotite–gabbro rocks and the host serpentinized peridotite. Geothermometry data give formation temperatures of >500 °C for synkinematic amphibole, zircon, rutile, and titanite. Chlorite appears intergrown with these phases and likely grew at similar temperatures. These results are compliant to thermodynamic computations that predict comparable mechanically weak mineralogies when hydrating hybrid rocks at 500 to 600 °C, whereas secondary assemblages after pure peridotite or gabbro are considerably stronger. Consequently, metamorphic weakening takes place to a much greater extent in rocks with a hybrid ultramafic–mafic composition than in purely ultramafic or gabbroic lithologies. Deformation may enhance fluid flow, which will in turn increase the extent of hydration and mechanical weakening. A positive feedback loop between hydration and strain localization may hence develop and facilitate the concentration of extensional tectonics into long-lived, high-displacement

faults. We suggest that hybrid lithologies may play a key role in detachment faulting at slow-spreading ridges worldwide.

2.1 Introduction

Long-lived detachment faults are present in many areas along the Mid-Atlantic Ridge (MAR), Southwest Indian Ridge (SWIR), Central Indian Ridge (CIR), and other slow- or ultraslow-spreading ridges, where they significantly contribute to lithospheric accretion and the generation of new seafloor (e.g., Blackman et al., 1998; Cann et al., 1997; Tucholke et al., 2001; Cannat et al., 2009; Escartín et al., 2008). At the MAR, detachment faulting has been suggested to occur along as much as half of the spreading axis between 12° and 35° N (Escartín et al., 2008). Detachment faulting is characterized by lithospheric extension on a single, shallow-dipping (10 to 30°) fault with 10 to 50 km of total displacement (Cann et al., 1997). Significant flexural rotation of the footwall beneath the shallow-dipping fault leads to formation of oceanic core complexes, in which lower lithospheric rocks, mainly mantle peridotite and gabbroic rocks, are exposed as a domal seafloor massif (e.g., Ildefonse et al., 2007; Smith et al., 2006; Tucholke et al., 1998).

In earlier studies, researchers have suggested that oceanic detachment faults form when roughly half of the plate separation is accommodated by extensional faulting rather than magmatic accretion, as based on observational evidence (Ildefonse et al., 2007; MacLeod et al., 2009) and numerical modeling (Olive et al., 2010; Tucholke et al., 2008). It is generally thought that detachment faults initiate as high-angle (~60° dip) faults, which then remain active for >1 Ma and flexurally rotate to gentle angles as the footwall is progressively unloaded (e.g., Garcés and Gee, 2007; MacLeod et al., 2009). Whereas high magma flux leads to the termination of detachment faults (e.g., Loocke et al., 2013; MacLeod et al., 2009), some presence of magmatic intrusions seems to facilitate initial strain localization and deformation in the lithosphere (e.g., Cannat et al., 2009; Ildefonse et al., 2007). Different mechanisms for the critical mechanical weakening in the initiation of detachment faults have been proposed, including the presence of plagioclase (e.g., Loocke et al., 2013), metamorphic reactions at the gabbro–peridotite interface (e.g., Cannat et al., 2009), and serpentinization of the mantle around the intrusions (e.g., Ildefonse et al., 2007).

Oceanic detachment faults may act as conduits for hydrothermal fluid, and thereby facilitate the development of hydrothermal vent fields far away from magmatically active zones (deMartin et al., 2007; McCaig et al., 2007; Tivey, 2007; Tucholke et al., 2013). Seawater infiltrates through hanging walls and allows hydrothermal fluids to reach the detachment fault at several kilometers depth, where they interact with rocks of ultramafic to mafic composition. At temperatures greater 400 to 500 °C, peridotite shows little alteration and olivine remains stable (Früh-Green et al., 2004; Mével, 2003); at or below greenschist-grades peridotite alters to mainly serpentine + brucite + magnetite (e.g., Bach et al., 2006). In gabbroic rocks, pyroxenes are commonly replaced by hornblende whereas

plagioclase and olivine alter to tremolitic amphibole and chlorite at amphibolite-grade temperatures (Blackman et al., 2011; Nozaka and Fryer, 2011).

Oceanic detachment faults around the world have been observed to contain highly sheared rocks with schistose and/or cataclastic textures and mineral assemblages of chlorite \pm amphibole \pm talc \pm serpentine (e. g., Blackman et al., 2011; Boschi et al., 2006a; Escartín et al., 2003; MacLeod et al., 2002; McCaig et al., 2007; Picazo et al., 2012; Schroeder and John, 2004). We term these ‘hybrid rocks,’ as they generally have bulk compositions between those of mafic and ultramafic rocks, and are similar to the ‘blackwall’ rocks that commonly form the border between ultramafic ophiolite bodies and continental crust (e. g., Frost, 1975). The phyllosilicate-rich assemblages of hybrid rocks make detachment faults frictionally weak and allow them to remain active with highly localized strain at inopportune slip angles; these zones are usually loci of intense deformation and/or active faulting.

Hybrid rocks have been interpreted by some investigators to mainly result from chemical exchange between ultramafic and mafic lithologies via metasomatic fluid flow (Boschi et al., 2006a; Escartín et al., 2003; Früh-Green et al., 2017; McCaig et al., 2007). For instance, Boschi et al. (2006a) suggest that seawater compositions of the circulating hydrothermal fluids were locally modified by interaction with gabbroic rocks to produce oxidizing, Si–Al–Ca-rich fluids. These, in turn, are thought to have caused talc \pm amphibole \pm chlorite metasomatism after ultramafic protoliths.

Another possible explanation for the formation of hybrid rocks in detachment faults is mechanical mixing of melt impregnations with host peridotite during seawater infiltration and hydrothermal alteration. Jöns et al. (2009, 2010) and (Picazo et al., 2012) showed that mechanically weak amphibole- \pm chlorite-bearing mineral assemblages are developed when hydrothermal fluids interact with melt-impregnated peridotite in detachment faults from 13°N and the 15°20' N Fracture Zone area, both MAR. In these hybrid rocks, mechanically weak minerals may form at temperatures >200 °C higher than at which unimpregnated mantle rocks would be hydrated (i. e., serpentinization at greenschist-facies conditions), leading to strain localization at higher temperatures than would have occurred otherwise. Jöns et al. (2009, 2010) argue that deformation may open fluid pathways, leading to further hydration and weakening of the rock.

The above studies highlight the importance of addressing the protolith composition and to demonstrate that the presence of magmatic intrusions may control the nature of secondary mineral assemblages at the onset of hydrothermal alteration. Here we show that deformation of hydrothermally altered peridotite with gabbroic melt impregnations from the 15°20' N Fracture Zone area, MAR, occurred before the onset of serpentinization. We present petrographic textures and results of thermodynamic computations indicating that hybrid peridotite–gabbro lithologies hydrate to mineral assemblages rich in mechanically weak, hydrous phases at amphibolite grade temperatures. Such metamorphic weakening does not occur when endmember peridotitic or gabbroic lithologies are being altered at similar conditions. These findings strongly support the idea of a positive feedback between melt impregnation, hydration at elevated temperatures, resulting metamorphic weakening and strain localization, active faulting and enhanced fluid flow.

Geological background The samples investigated here were recovered at Site 1271B of Ocean Drilling Program (ODP) Leg 209 at the MAR. Site 1271 penetrated into the footwall of a detachment fault (Kelemen et al., 2004; Shipboard Scientific Party, 2004b), located at an inside corner high of the prominent 15°20' N Fracture Zone (Fig. 2.1a). Variably serpentinized and gabbroic melt-impregnated abyssal peridotites are exposed on both flanks of the MAR in this area (Kelemen et al., 2004; Lagabrielle et al., 1998). Based on structural and lithological observations, Schroeder et al. (2007) interpreted the MAR in the 15°20' N Fracture Zone area as a non-volcanic ridge with abundant large-displacement faults. Widespread fluid-peridotite interaction in the sub-seafloor is indicated by extensive CH₄ and H₂ anomalies in the water column as well as by the nearby active Logatchev black smoker field (Bogdanov et al., 1997; Charlou et al., 1991, 1998).

At Site 1271 two holes were drilled into a smooth, sedimented slope that has been interpreted to be part of an exposed long-lived detachment fault (Fig. 2.1b; Schroeder et al., 2007; Shipboard Scientific Party, 2004b; Smith et al., 2008). The dominant rock type of Holes 1271A and B is serpentinized dunite (Shipboard Scientific Party, 2004b), with—despite the area's scarce volcanic activity—abundant gabbroic intrusions in Hole 1271B. Both peridotite and melt intrusions are variably altered by metasomatic processes. A complex tectonic history, probably related to the exhumation of the mantle along a detachment fault, is suggested by the numerous intensely deformed shear zones in the recovered core (Bach et al., 2004; Kelemen et al., 2004; Paulick et al., 2006; Schroeder et al., 2007). The age of the seafloor at Site 1271 is estimated at 1.5 Ma (Bach et al., 2011).

2.2 Analytical procedures

Core material available from Hole 1271B was examined macroscopically at the IODP (International Ocean Discovery Program) Bremen Core Repository. Representative samples of the main types of melt-impregnated and deformed ultramafic rocks developed throughout the hole were collected for microtextural, petrological, and geochemical studies.

2.2.1 Rock alteration and deformation textures

Magmatic, alteration, and deformation fabrics were visually classified in hand specimen and further documented in thin sections using a standard polarized light microscope and from backscattered electron imaging. Mineral phase assemblages with respect to alteration fabrics and cross-cutting relations were observed and noted in all of these mediums. Semi-quantitative deformation fabric in individual samples were rated following procedures that are typically followed on ODP/IODP hard-rock expeditions (see Shipboard Scientific Party, 2004a), and conform with the fabric intensity scales of Cannat (1991) and Dick et al. (1991). Ductile and brittle deformation fabrics are rated separately, and scales range from no apparent deformation (zero) to ultramylonite/ultracataclasite (5).

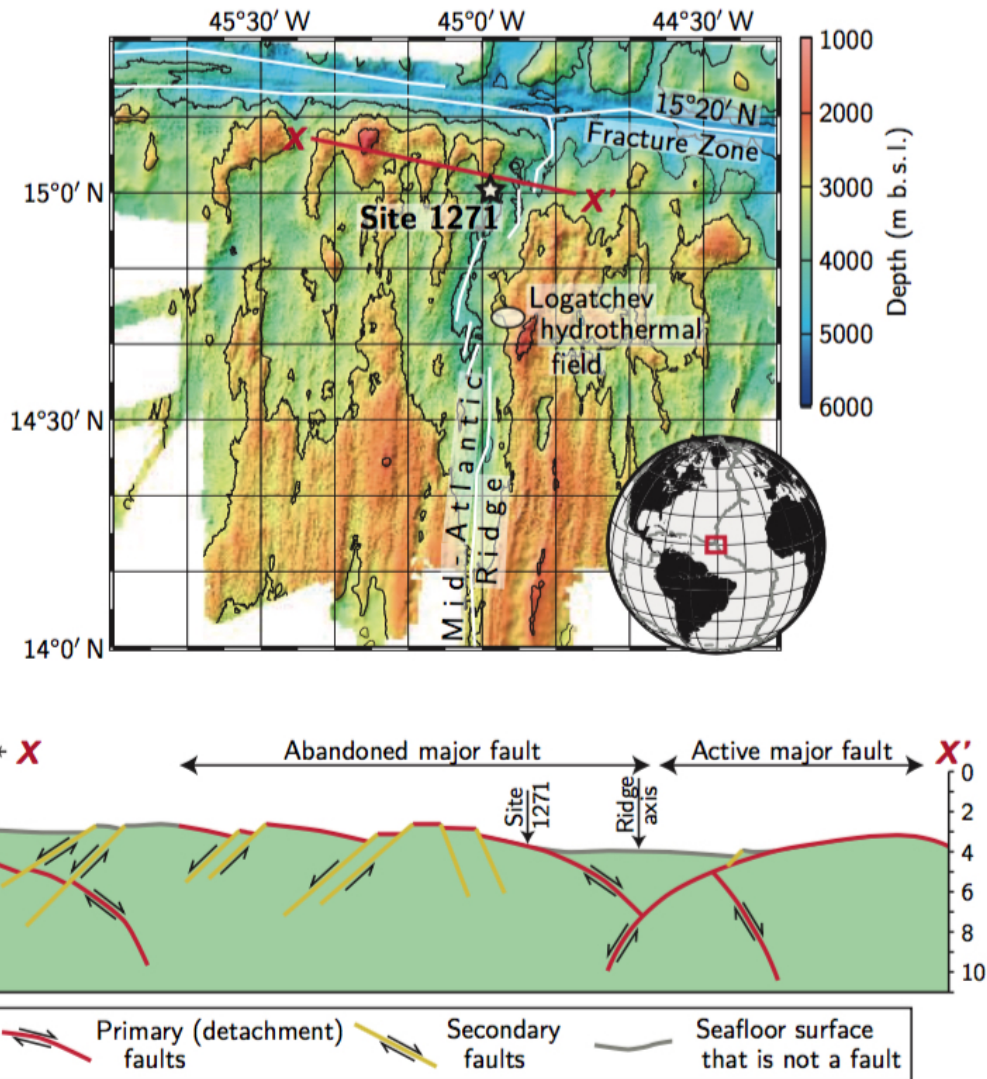


Figure 2.1 Study area on the Mid-Atlantic Ridge. **(Top)** Bathymetric map of the study area south of the 15°20' N Fracture Zone with the locations of ODP Site 1271 and the Logatchev hydrothermal 162 vent field. After Fujiwara et al. (2003). **(Bottom)** Bathymetric profile with interpreted fault patterns. Position indicated by line X-X' in (a). Cross section after Schroeder et al. (2007). Abbreviations: b.s.l., below sealevel.

2.2.2 Whole-rock analyses

Sample preparation for whole-rock analyses included cutting with a rock saw, removing saw marks by grinding with SiC powder, and subsequent cleaning with deionized water in an ultrasonic bath. Samples were dried at 60 °C and pulverized using a planetary agate ball mill. Fused glass beads were prepared at the Institute for Chemistry and Biology of the Marine Environment at the University of Oldenburg. Weighed portions of

sample, lithium borate, and ammonium nitrate were pre-oxidizing at 500 °C and melted at 1450 °C (following Eckert et al., 2013). Concentrations of major and minor elements (Si, Ti, Al, Fe, Mn, Ca, S, Cr, Co, Ni, Zn, Zr) were measured at the Institute for Chemistry and Biology of the Marine Environment with a wavelength dispersive PANalytical Axios mAX X-ray fluorescence spectrometer.

Na₂O and K₂O were analyzed using a Varian Vista Pro ICP-OES and trace element contents (Ba, Nb, Rb, Sr, Y, Ta, Th, Hf, REE, etc.) were measured using a Thermo Finnigan Element2 ICP-MS at the University of Bremen. In the ICP-MS analyses, all elements were measured in low resolution, except Hf and Sm to Lu, which were measured in high-resolution mode; In and Tl were used as internal standards. Fifty mg of sample powder were given in 30 mL Savillex PTFE beakers and heated at 145 °C for 12 h after a mixture of Hf (2 mL, 48%, suprapur®, Merck, Germany), HCl (1 mL, 32%, subboiled) and HNO₃ (2 mL, 65%, subboiled) had been added. The sample solutions were then evaporated at 110 °C in a closed EvapoClean heating block system, and residuals (100 µL) were re-dissolved in 0.5 mL HNO₃ (65%, subboiled) and 4 mL ultrapure (18.2 MΩ) water. These solutions were heated at 110 °C in closed beakers for another six hours to achieve total digestion and were diluted to 25 mL afterwards. United States Geological Survey reference materials (BCR-2G and BHVO-2G) and in-house standards were measured to monitor analytical quality (reported in Tab 2.2).

2.2.3 Electron microprobe analyses

Elemental compositions of minerals were obtained with a CAMECA SX100 EPMA at the University of Bremen, equipped with four wavelength dispersive spectrometers. Accelerating voltages of 15 kV and beam currents of 10 to 15 nA for silicates and 15 nA for oxides were used. Peak counting times varied between 20 to 40 s per element and all analyses were carried out with a focused beam. The built-in PAP correction was applied for data reduction/correction. Repeated analyses of natural silicate and oxide standards were used to check data quality. Averaged precision and accuracy are better than 3% for element oxides with concentrations <1 wt.%, except for Na₂O (5.7%).

2.2.4 Laser ablation ICP-MS analyses

In situ analyses of trace elemental concentrations in zircon, rutile, and titanite were carried out using a Thermo Finnigan Element2 ICP-MS coupled to a New Wave UP193 solid-state laser ablation system at the University of Bremen. Analytical conditions included an irradiance of ~1 GW cm⁻² for ablation, spot sizes of 15 to 50 µm and a laser pulse rate of 5 Hz. Helium (0.7 L min⁻¹) and Ar (0.9 L min⁻¹) were used as sample and make-up gases, respectively. All isotopes were analyzed at low resolution with five samples in a 20% mass window and a total dwell time of 25 ms per isotope. After every four to eight samples the glass standard NIST 610 was measured for external calibration using the values from Jochum et al. (2011). Depending on the mineral composition, ²⁹Si, ⁴³Ca, or ⁴⁷Ti were used as internal standards and concentrations were calculated with the Cetac GeoPro™ software. A detection limit of 0.001 µg g⁻¹ was tentatively assigned

and analytical quality was controlled by repeated analyses of USGS reference materials BCR-2G and BHVO-2G and comparison of our data with the geoREM database (as of April 2017). Averaged precisions are better than 8%, averaged accuracies are better than 5%.

2.3 Results

2.3.1 Petrography and mineral chemistry

Drill core from Hole 1271B consists of a complex mixture of serpentinized dunite and minor harzburgite with abundant gabbro, amphibole gabbro, and troctolite intrusions in the form of dikelets and veins (e. g., Bach et al., 2004; Kelemen et al., 2004; Paulick et al., 2006). It also features intensely deformed ductile shear zones, ductile to brittle, and brittle faults (Schroeder et al., 2007). The here studied samples (Tab. 2.1) are representative of all three types of deformation.

Host peridotite Host rock to the magmatic intrusions is variably serpentinized residual mantle dunite or harzburgite with protogranular to porphyroclastic textures (Fig. 2.2a,b). Primary olivine is preserved in few samples that exhibit little serpentinization or, more commonly, as relics in the centers of cells in serpentine mesh textures of serpentinized domains. Olivine has $X_{\text{Mg}} = \text{Mg}/(\text{Mg} + \text{Fe}^{2+})$ of 0.87 to 0.90. No unaltered primary orthopyroxene was observed in the samples. Primary clinopyroxene is present in small amounts in less serpentinized samples or occurs as exsolution lamellae in now altered orthopyroxene ($X_{\text{Mg}} = 0.90\text{--}0.94$, $\text{CaO} = 22.1\text{--}24.9$ wt.%, $\text{TiO}_2 = 0.1\text{--}0.6$ wt.%). Cr-spinel has intermediate $\text{Cr}/(\text{Cr}+\text{Al})$ of 0.39 to 0.52 and shows local alteration to ferritchromite.

The degree of alteration is generally 80 to 100 vol.% of the original mineral assemblage. Altered samples show evidence of pervasive serpentinization and mesh texture serpentine with compositions of X_{Mg} of 0.83 to 0.99. Magnetite occurs within the mesh serpentine to a small degree. Serpentine after orthopyroxene is present in bastite textures and has X_{Mg} of 0.81 to 0.98 and Al_2O_3 of 1.1 to 8.2 wt.%. Several generations of serpentine \pm magnetite veins are present throughout the altered samples.

The bulk of host peridotite displays little or no crystal-plastic or cataclastic deformation textures; remnant olivine grains are large and mostly strain-free (Fig. 2.2a,b). In few cases, they contain dislocation walls and/or subgrains, appearing dominantly near margins of melt-impregnated domains. Several small (~1–5 mm) localized shear zones in host peridotite are present, usually adjacent to magmatic intrusions. Within these shear zones, olivine is locally recrystallized and displays protomylonitic to mylonitic textures (Fig. 2.2c,d). In some fully serpentinized samples relict olivine porphyroclast–neoblast textures are still visible.

Melt-impregnated domains Melt impregnations in cores from Site 1271 occur mainly as millimeter- to several centimeter-wide veins (Fig. 2.2a). Minor amounts of primary pyroxene and magmatic amphibole (see below) are preserved; plagioclase is absent. The

Table 2.1 List of investigated samples.

Sample	Depth (m b. s. f.)	Lithology	Degree of melt impregn. ^a	Mineral assemblage	Fault type ^b	Plastic deform.	Clastic deform.
1271B-1R-1, 8-13 cm	0.01	Chl-poor amphibolite	all-hybrid	Amp, Chl, Cb, clay minerals	Ductile to brittle	4.5	3
1271B-2R-1, 12-16 cm	12.12	Impregn. Spl-rich serp. Du	~25%	Amp, Srp, Spl, Chl, Cb, clay minerals	Ductile to brittle	2	0.5
1271B-3R-1, 17-20 cm	17.17	Chl-poor amphibolite	all-hybrid	Amp, Chl, clay minerals	Ductile to brittle	4	3
1271B-3R-1, 93-99 cm	17.93	Chl-poor amphibolite	all-hybrid	Amp, Rtl, Zrc, Qz	Ductile to brittle	2	2
1271B-5R-1, 12-14 cm	27.82	Chl-rich amphibolite	all-hybrid	Amp, Rtl, Ttn	n/a	1	1.5
1271B-10R-1, 59-65 cm	51.09	Chl-poor amphibolite	all-hybrid	Amp, Chl, Srp, Spl, clay minerals	Ductile to brittle	4	2
1271B-10R-1, 67-70 cm	51.17	Impregn. Hz	~45%	Srp, Amp, Ol, Chl, Mt, Spl, Zrc	Ductile to brittle	3.5	2
1271B-11R-1, 88-91 cm	56.38	Chl-poor amphibolite	~85%	Amp, Zrc	Ductile to brittle	4.5	2
1271B-13R-1, 20-24 cm	65.30	Impregn. Du	~35%	Srp, Ol, Amp, Chl, Mt, Spl	n/a	2.5	1.5
1271B-13R-1, 27-31 cm	65.37	Impregn. Du	~50%	Ol, Srp, Amp, Chl, Mt	n/a	3.5	2
1271B-13R-1, 52-59 cm	65.61	Spl-rich serp. Du	10-15%	Amp, Srp, Chl, Mt, Spl	n/a	3.5	3
1271B-13R-1, 98-102 cm	66.08	Chl-rich amphibolite	all-hybrid	Chl, Amp, Cb, Srp, Mel	n/a	1	3.5
1271B-14R-1, 21-24 cm	70.01	Impregn. Spl-rich serp. Du	15-20%	Srp, Chl, Amp, Spl, Mt, Zrc	Ductile	2	2
1271B-14R-1, 32-35 cm	70.12	Chl-poor amphibolite	all-hybrid	Amp, Chl, Cpx, Spl, Grs, Ttn	Ductile	4.5	0
1271B-14R-1, 45-48 cm	70.25	Chl-poor amphibolite	all-hybrid	Amp, Chl, Spl	Ductile	3	1
1271B-17R-1, 17-19 cm	84.67	Chl-poor amphibolite	all-hybrid	Amp, Chl, Cpx, Ttn, Ilm	n/a	3	1
1271B-18R-1, 27-31 cm	89.37	Impregn. Du	~35%	Ol, Cpx, Amp, Srp, Cb, Spl, Mt, Grs	Ductile	1.5	0
1271B-18R-1, 33-36 cm	89.43	Chl-rich amphibolite	all-hybrid	Srp, Chl, Mt, Cb	Ductile	3	3
1271B-18R-1, 38-42 cm	89.48	Impregn. Du	~5%	Srp, Mt, Chl	Ductile	3	2
1271B-18R-1, 44-47 cm	89.54	Impregn. Du	15-20%	Srp, Chl, Cb, Mt	Ductile	0	0
1271B-18R-1, 49-51 cm	89.59	Serp. Hz	<5%	Mt, Srp, Spl	Ductile	0	1.5
1271B-18R-1, 81-84 cm	89.91	Chl-poor amphibolite	all-hybrid	Amp	Ductile	4	3.5
1271B-18R-1, 85-87 cm	89.95	Chl-rich amphibolite	>90%	Srp, Spl, Mt	Ductile	4	2
1271B-18R-1, 93-96 cm	90.03	Chl-rich amphibolite	all-hybrid	Cpx, Srp, Spl, Mt, Chl	Ductile	4	3
1271B-18R-1, 104-107 cm	90.14	Impregn. Du	~5%	Spl, Chl, Srp, Mt	Ductile	0	1
1271B-18R-1, 109-112 cm	90.19	Impregn. Du	~25%	Ol, Srp, Spl, Chl, Amp, Ttn	Ductile	1	1
1271B-20R-1, 0-2 cm	98.81	Impregn. serp. Du	~25%	Ol, Srp, Amp, Chl, Mt	Brittle	3.5	3.5

^a Degrees of melt impregnation estimated by point-counting; all-hybrid describes hydrated rocks of which the primary lithologies cannot be discriminated.

^b Fault type according to Schroeder et al. (2007); samples marked 'n/a' originate from core sections that were not described by these authors.

Abbreviations: impregn., impregnated; serp., serpentinitized; Amp, amphibole; Cb, carbonate; Chl, chlorite; Cpx, clinopyroxene; Du, dumite; Grs, grossular; Hz, harzburgite; m b. s. l., m below seafloor; Mel, melanite; Mt, magnetite; n/a, not available; Ol, olivine; Qz, quartz; Rtl, rutile; Spl, spinel; Srp, serpentine; Ttn, titanite; Zrc, zircon.

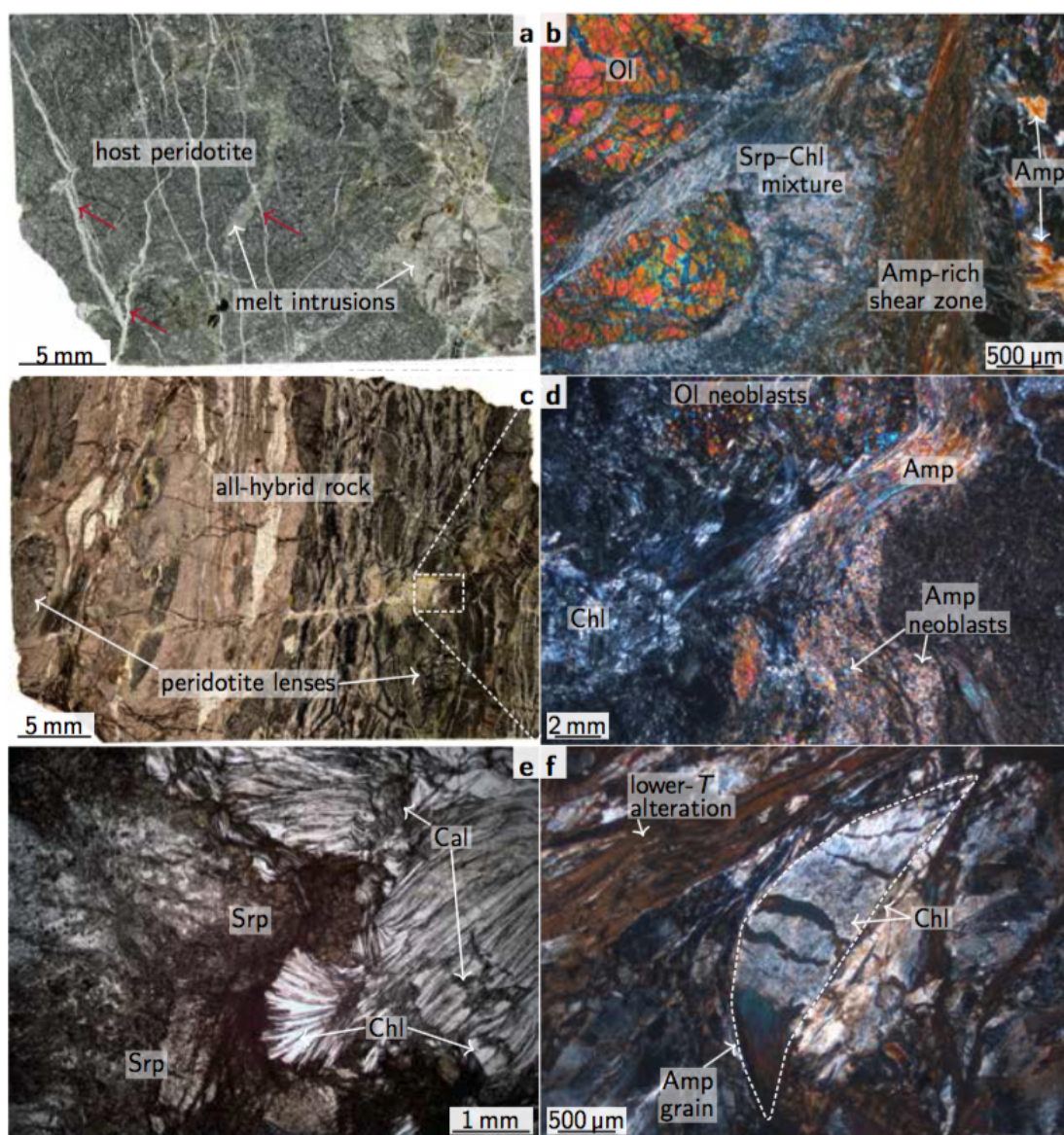


Figure 2.2 Photomicrographs depicting lithologic and textural features. (a) Undeformed peridotite with narrow gabbroic melt intrusions. High-temperature intrusion textures are well preserved, but overprinted by static alteration of primary minerals to low-Ti amphibole and chlorite; peridotite is only partly serpentinized. Late-stage serpentine veins (red arrows) crosscut both, host peridotite and melt impregnations. Sample 1271B-18R-1, 109–112 cm, PPL. (b) Undeformed, unserpentinized olivine adjacent to an amphibole-rich shear zone with highly deformed porphyroclasts, illustrating amphibolite-grade deformation. Sample 1271B-10R-1, 67–70 cm, XPL. (c, d) Strongly altered and deformed hybrid rock, consisting primarily of amphibole and chlorite. Amphibole locally exhibits mylonitic textures and neoblast growth resulting from high-temperature strain (d). Unaltered olivine is present in elongated lenses (c) but may as well display neoblasts (d). Sample 1271B-11R-1, 88–91 cm, PPL and XPL, respectively. (e, f) Low-temperature deformation textures. (e) Intergrown schistous chlorite and calcite; the peridotite (left hand side) is fully serpentinized. Sample 1271B-13R-1, 98–102 cm. (f) Strongly deformed amphibole statically overprinted by chlorite, presumably during lower-temperature fluid-rock interaction. Sample 1271B-18R-1, 93–96 cm, XPL. Abbreviations: Amp, amphibole; Cal, calcite; Chl, chlorite; Ol, olivine; PPL, plane polarized light; Srp, serpentine; *T*, temperature; XPL, crossed polarized light.

intrusions have been altered by extensive water–rock interaction and consist mainly of secondary mineral assemblages. Secondary phases include Ca-amphiboles and chlorite with accessory zircon, rutile, apatite, titanite, grossular, and talc.

A small number of Site 1271 impregnations are weakly or not deformed (e. g., 1271B-18R-1, 109–112 cm; Fig. 2.2a). These vein-like features are up to several cm in width and filled with clinopyroxene grains several mm in diameter, and with hornblende or tremolite, and chlorite, which presumably altered from pyroxene and plagioclase, respectively. Grains lack a preferred orientation, are euhedral to subhedral in shape, and are generally strain free. These veins are present along olivine grain boundaries or crosscut large olivine grains. For the latter, vein contacts towards the peridotite are irregular, suggesting that the impregnating melts have filled voids in the host rock from where they percolated along grain boundaries into the peridotite. The presence of olivine next to hornblende and chlorite (Fig. 2.3a) attests impregnation and hydrous mineral reactions within the olivine stability field; well-developed chlorite–hornblende grain boundaries may indicate equilibrium between the two phases.

Most impregnations are highly deformed and consist of mineral assemblages that likely grew from a mixture of mafic melt and peridotite host. These hybrid rock shear zones were deformed dominantly under amphibolite-facies conditions (e. g., 1271B-14R-1, 32–35 cm, or 17R-1, 17–19 cm) and consist almost entirely (>90 vol.%) of schistose amphibole with minor chlorite and accessory titanite (Figs. 2.2c,d, 2.3b). Some shear zones consist of interlocking, aligned grains of columnar amphiboles, forming aggregates with phacoidal shapes within a groundmass of fibrous amphiboles intergrown with chlorite (Supplementary Information Fig. A.1.1). Some amphiboles within these shear zones display mylonitic textures, with sub-grain formation and dynamic recrystallization (neoblast growth; Fig. 2.2d). Deformation continued after crystallization in few samples, evident from plastically deformed neoblasts (sample 1271B-11R-1, 88–91 cm). Chlorite appears to have crystallized in voids with accessory titanite, and may be a secondary product formed post-deformation (Fig. 2.3b,c,e). Hybrid rock shear zones formed after peridotites with lower fractions of melt intrusions exhibit assemblages of schistose amphibole, chlorite, serpentine, and calcite with accessory titanite (e. g., 1271B-13R-1, 98–102 cm, or 18R-1, 33–36 cm). In these samples, chlorite is intergrown with and displays equilibrium textures with all other phases. In other areas, fibrous chlorite is intergrown with amphibole, serpentine, and calcite in anastomosing shear zones (Fig. 2.2e). Some amphibolite shear zones further contain patches of chlorite that presumably represent former plagioclase. The contacts between the shear zones and the host rocks are commonly straight, unlike the very irregular margins of the undeformed impregnations (Fig. 2.2a). Amphibole and chlorite also commonly exhibit cataclastic textures. Larger tabular amphibole grains are fractured along their margins and angular fragments, intergrown with chlorite, string into the margins of schistose shear zones. Deformation at temperatures below the brittle–ductile transition caused the fracturing of grains into fine aggregates along the margins of schistose shear zones. Several generations of amphibole may have replaced pyroxene, olivine, or earlier amphibole (Fig. 2.3f). It exhibits various grain sizes and textural relationships with other minerals. Amphibole, in turn, may statically be replaced by chlorite

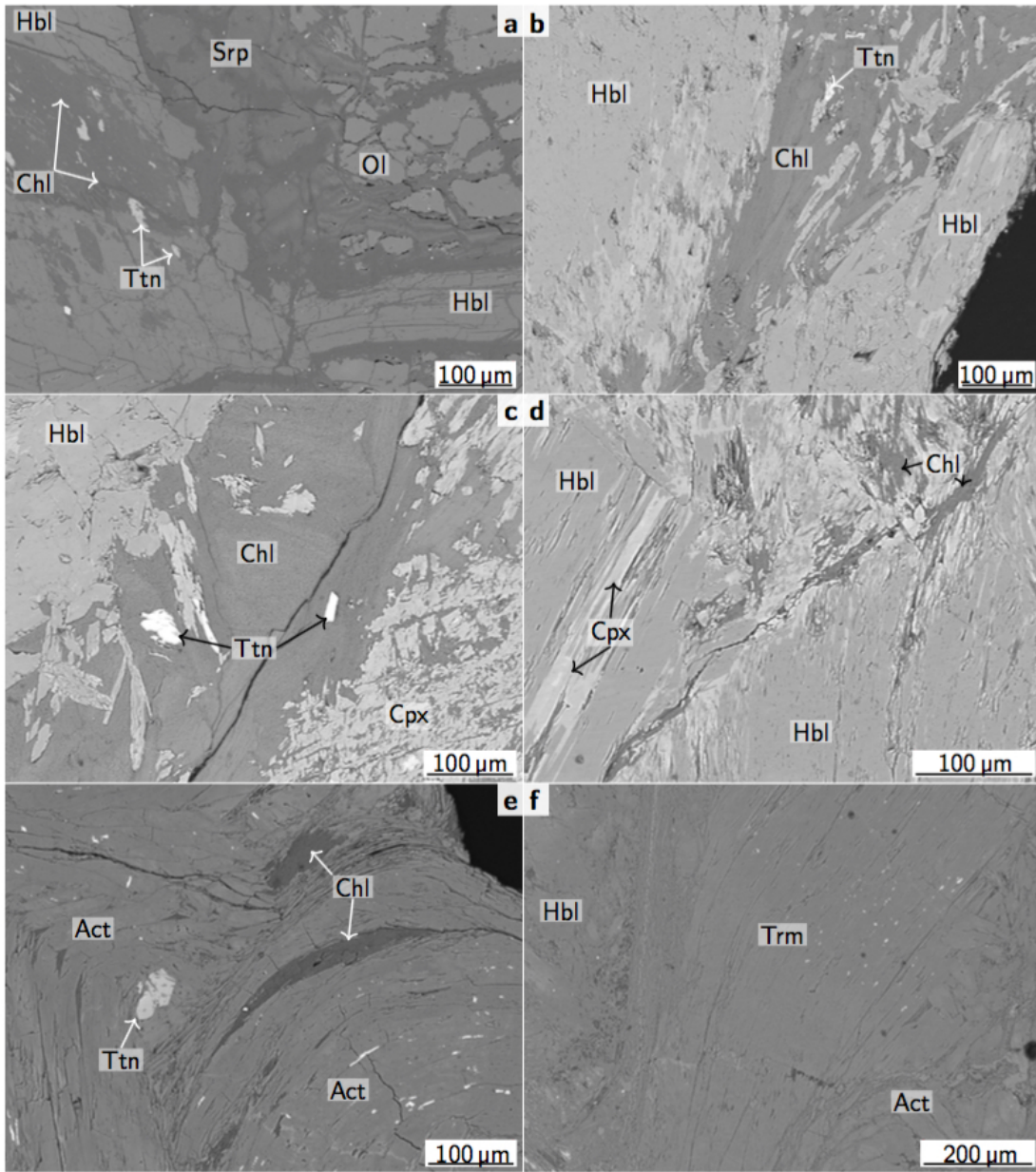


Figure 2.3 Backscattered electron images of mineral associations and textures. (a) Coexisting olivine, hornblende, and chlorite demonstrate melt impregnation and the formation of hydrous minerals within the olivine stability field. Sample 1271B-18R-1, 109–112 cm. (b, c, d) Hybrid rock alteration assemblages consist primarily of hornblende with minor chlorite and accessory titanite. Note the lighter gray hornblende that is slightly less Mg-rich as compared to the darker gray areas. Remnant clinopyroxene is present in (c) and (d); in (d) it has, however, mostly been hydrated and altered to hornblende. Sample 1271B-14R-1, 32–35 cm. (e, f) Alteration assemblage consisting of hornblende and tremolitic to actinolitic amphibole and minor titanite. Crystal-plastic deformation of amphibole points to deformation at amphibolite-facies temperatures. Later chlorite has filled void space that opened during amphibole deformation. Sample 1271B-17R-1, 17–19 cm. Abbreviations: Act, actinolite; Chl, chlorite; Cpx, clinopyroxene; Hbl, hornblende; Ol, olivine; Srp, serpentine; Trm, tremolite; Ttn, titanite.

during lower-temperature water–rock interaction (Fig. 2.2f). Alteration assemblages point to pyroxene- and plagioclase-rich, presumably basaltic, parental melts that were injected into the host peridotite, consistent with earlier-published results (e. g., Kelemen et al., 2004; Shipboard Scientific Party, 2004b; Schroeder et al., 2007).

Two groups of amphibole can be distinguished based on their textural characteristics and geochemistry. High-Ti amphibole has TiO_2 of up to 3.0 wt.% and is pargasitic, edenitic, or magnesiohornblende in composition ($X_{\text{Mg}} > 0.86$). It is rich in Al_2O_3 and Na_2O (up to 13.6 wt.% and 3.3 wt.%, respectively), and low in SiO_2 (≤ 50.6 wt.%). It is fine- to medium-grained, subhedral, light to dark brown in color, often with distinct cleavage (e. g., sample 1271B-3R-1, 93–99 cm). We consider this high-Ti amphibole to be magmatic. Low-Ti amphibole occurs in veins (e. g., sample 1271B-14R-1, 32–35 cm), where it forms euhedral crystals. These amphiboles have, compared to high-Ti amphibole, lower TiO_2 , Al_2O_3 , and Na_2O (as low as <0.1 wt.%, 3.9 wt.%, and 0.8 wt.%, respectively), but higher SiO_2 (≤ 53.9 wt.%). Some are Fe-rich (X_{Mg} as low as 0.53). This low-Ti endmember is clearly hydrothermal. Amphibole with intermediate contents of TiO_2 , SiO_2 , Al_2O_3 , and alkalis likely represents higher-temperature metamorphic amphibole that grew from magmatic amphibole. Amphibole further occurs as micrographic, in parts fibrous, crystals throughout the samples and frequently as an alteration product of magmatic or hydrothermal amphibole, often together with ilmenite and chlorite. Less frequent is pseudomorphic replacement of pyroxene by amphibole. This replacive amphibole is colorless to greenish or light brown in color with tschermakitic to actinolitic or tremolitic composition. It usually has considerably lower TiO_2 than magmatic amphibole, and contents of SiO_2 , Al_2O_3 , and alkalis considerable scatter around mixing lines of the precursor minerals. Amphibole chemical compositions and stoichiometric recalculations are provided in Supplementary Information Fig. A.1.2.

Bluish colored, fibrous chlorite is abundant in most impregnated areas. Deformed chlorite is co-located with high-Ti amphibole (e. g., Fig. 2.3a). It has variable X_{Mg} of 0.46 to 0.93 that correlates with generally low contents of SiO_2 , whereas Al_2O_3 is high and anticorrelates with X_{Mg} ($\text{SiO}_2 = 24.5\text{--}37.9$ wt.%, $\text{Al}_2\text{O}_3 = 11.5\text{--}24.6$ wt.% for high-temperature chlorite; $\text{SiO}_2 = 24.7\text{--}40.0$ wt.%, $\text{Al}_2\text{O}_3 = 11.0\text{--}20.0$ wt.% for chlorite after amphibole). In contrast, chlorite that formed in voids or statically replaces earlier metamorphic phases, commonly occurring together with serpentine (e. g., Fig. 2e,f), is usually Mg-rich ($X_{\text{Mg}} = 0.83\text{--}0.94$, median = 0.94). SiO_2 (30.0–37.0 wt.%) correlates and Al_2O_3 (10.4–18.8 wt.%) contents anticorrelate with X_{Mg} . Chlorite chemical compositions are presented in Supplementary Information Fig. A.1.3.

Zircon is present in three samples where it occurs embedded in secondary amphibole and/or chlorite as subhedral to anhedral, partly corroded crystals with sizes of up to 130 μm in size. Titanium contents in zircon are $<28 \mu\text{g g}^{-1}$, Y ranges from ~ 250 to $5610 \mu\text{g g}^{-1}$. Rare earth element (REE) patterns of zircon suggest a magmatic origin (Supplementary Information Fig. A.1.4). Rutile and titanite are present as accessory phases in the altered melt impregnations of one and of three samples, respectively. Rutile is sub- to anhedral and commonly 200 to 350 μm in size. It occurs together with ilmenite and titanite embedded in high-Ti hornblende; the rutile and ilmenite crystallized in

apparent equilibrium whereas titanite appears to overgrow rutile. Titanite may hence be a product of hydrothermal alteration, whereas rutile could be magmatic. Titanite is also present as subhedral crystals, $<40\ \mu\text{m}$ in size, within amphibole and/or chlorite in two further samples. Analyzed rutile grains contain Zr contents between ~ 500 and $1990\ \mu\text{g g}^{-1}$; titanite has ~ 6 to $570\ \mu\text{g g}^{-1}$ Zr and ~ 8 to $230\ \mu\text{g g}^{-1}$ Y.

Late stage veining and related alteration High-temperature assemblages were partly overprinted by lower-temperature alteration. Static chlorite replacement of metamorphic amphibole occurs locally but former processes and textures can still be recognized (Fig. 2.2f). Late-stage veins occasionally crosscut the shear zones or undeformed melt impregnations (Fig. 2.2a). These veins commonly consist of serpentine and are usually free of magnetite. Intergrowth of serpentine with brucite at microscale seems restricted to few local occurrences, as indicated by the lack of general correlation between serpentine SiO_2 and MgO and total oxides, respectively. Dunite sample 1271B-18R-1, 33–36 cm, depicts greenschist-grade alteration and deformation in the form of schistose serpentine and chlorite. Small shear zones cross the sample. Minor amounts of talc occur intergrown with serpentine in few (e. g., in sample 1271B-13R-1, 98–102 cm) but is absent in most samples. If present, talc is undeformed. Quartz \pm rutile veins in sample 1271B-5R-1, 12–14 cm, or 3R-1, 93–99 cm, are undeformed and crosscut all previous textures, thus representing a late stage of the fluid-related alteration history.

2.3.2 Whole-rock geochemistry

Eight samples were analyzed for their whole-rock geochemical composition (Figs. 2.4 and 2.5, Tab. 2.1). When compared to unimpregnated peridotite or serpentinite, the melt-impregnated samples are enriched in SiO_2 (35.02–46.97 wt.%), Al_2O_3 (2.44–8.49 wt.%), CaO (0.30–10.68 wt.%), and TiO_2 (0.07–1.16 wt.%) and depleted with respect to MgO (23.02–32.92 wt.%) and $\text{FeO}^{\text{total}}$ (3.60–9.30 wt.%, with all iron calculated as ferrous). $\text{Mg}\# = 100 \times \text{Mg}/(\text{Mg} + \text{Fe}^{\text{total}})$ range from 86.7 to 93.9; lower Mg-number samples have higher degrees of melt impregnation. Contents of alkali metals are up to 0.54 wt.% for Na_2O , <0.02 wt.% for K_2O , and $<0.6\ \mu\text{g g}^{-1}$ for Rb; contents of other fluid-mobile elements are 2.46 to $12.80\ \mu\text{g g}^{-1}$ for Sr, 1.24 to $5.65\ \mu\text{g g}^{-1}$ for Ba, and 8 to $87\ \mu\text{g g}^{-1}$ for Zr. The compositions of the shear zone rocks plot between those of peridotite and gabbro and are likely mixtures thereof (Figs. 2.4 and 2.5).

Chondrite-normalized REEs show flat patterns with values ~ 5 to 20-fold chondritic (Fig. 2.6). Light REE contents are slightly less enriched than heavy REEs. Most samples show negative Eu anomalies, the degree of which increases with the overall REE concentration. The sample with the lowest REE concentration (heavy REEs about 5 times chondritic) has $\text{Eu}/\text{Eu}^* = \text{Eu}/\text{Sm} \times \text{Gd}^{0.5}$ of 0.64 whereas higher REE concentrations (heavy REEs about 20 times chondritic) correspond to Eu/Eu^* of 0.30 or lower.

Major and trace element geochemistry implies impregnation of the peridotites by mafic melts. Our data overlap well with other melt-impregnated peridotite from ODP Leg 209 (Kelemen et al., 2007; Paulick et al., 2006) and with published data for gabbro and mid-ocean ridge basalt recovered during Leg 209 and other ocean drilling campaigns (Fig. 5

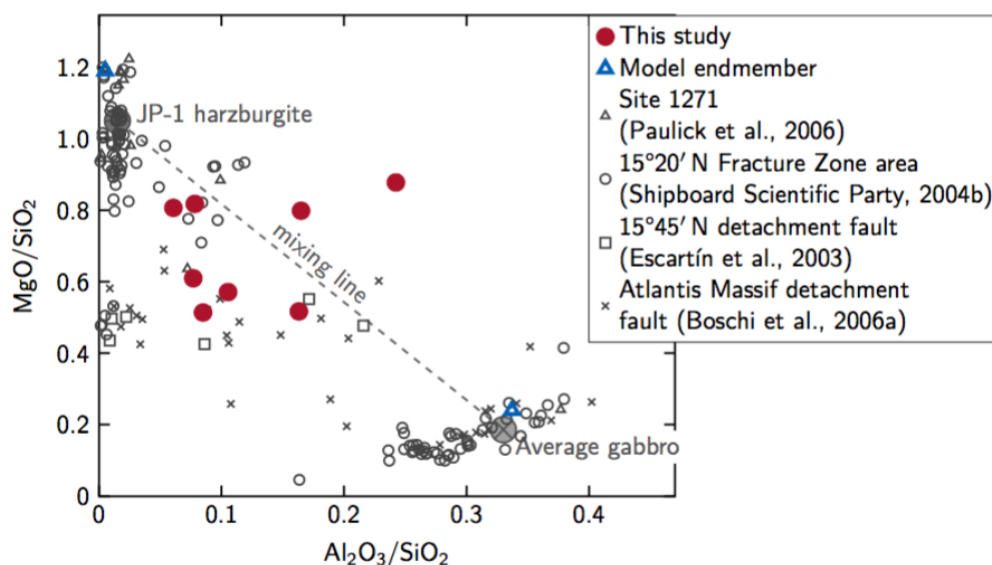


Figure 2.4 Whole-rock $\text{Al}_2\text{O}_3/\text{SiO}_2$ vs. MgO/SiO_2 of hybrid rocks. For comparison, published data of samples from the $15^\circ20'$ N Fracture Zone area and from the Atlantis Massif south wall as well as average gabbro composition (Coogan, 2014) and JP-1 harzburgite (Imai et al., 1995) are shown. Many samples scatter around harzburgite and gabbro compositions, or along the mixing line between the two. Model endmember compositions (Paulick et al., 2006) are also plotted.

of Kelemen et al., 2007). All samples exhibit REE enrichments or are within the range of unimpregnated samples drilled during Leg 209 (Kelemen et al., 2007; Paulick et al., 2006). Smooth, elevated REE patterns are similar to those of gabbroic rocks, indicating interaction of the host peridotite with a respective melt phase (see Paulick et al., 2006, for discussion). Negative Eu anomalies reflect the fractionation of plagioclase (Weill and Drake, 1973). Major elemental metasomatic mass transfers during post-impregnation fluid–rock interactions appear to be minor, except for some of the more fluid-mobile elements such as Si and Ca (see below).

Estimations of the degrees of melt impregnation were derived by using the ‘least squares’ method to calculate the best fit between two endmember whole-rock compositions. We chose the most primitive serpentinized dunite (sample 1271B-17R-1, 61–69 cm) and the most evolved amphibole gabbro (1271B-17R-1, 8–15 cm) of the Site 1271 samples from the Paulick et al. (2006) dataset as model endmembers (Tab. 2.1). The estimated degrees of melt impregnation range from less than 30% to almost 60%, with highly varying sums of the squared residuals between the actual and predicted compositions (Supplementary Information Tab. A.1.1). Substantial misfits of Si and Ca may be explained by their mobile behavior during metasomatic reactions and related mass transfers across the interface between mafic and ultramafic rocks (Bach and Klein, 2009). In contrast, varying misfits for fluid-immobile elements, in particular Al for which the squared residuals vary from 0 to 42, suggest that the model endmembers may be accurate endmember choices for some but inaccurate for other samples. The composition of the impregnating melt

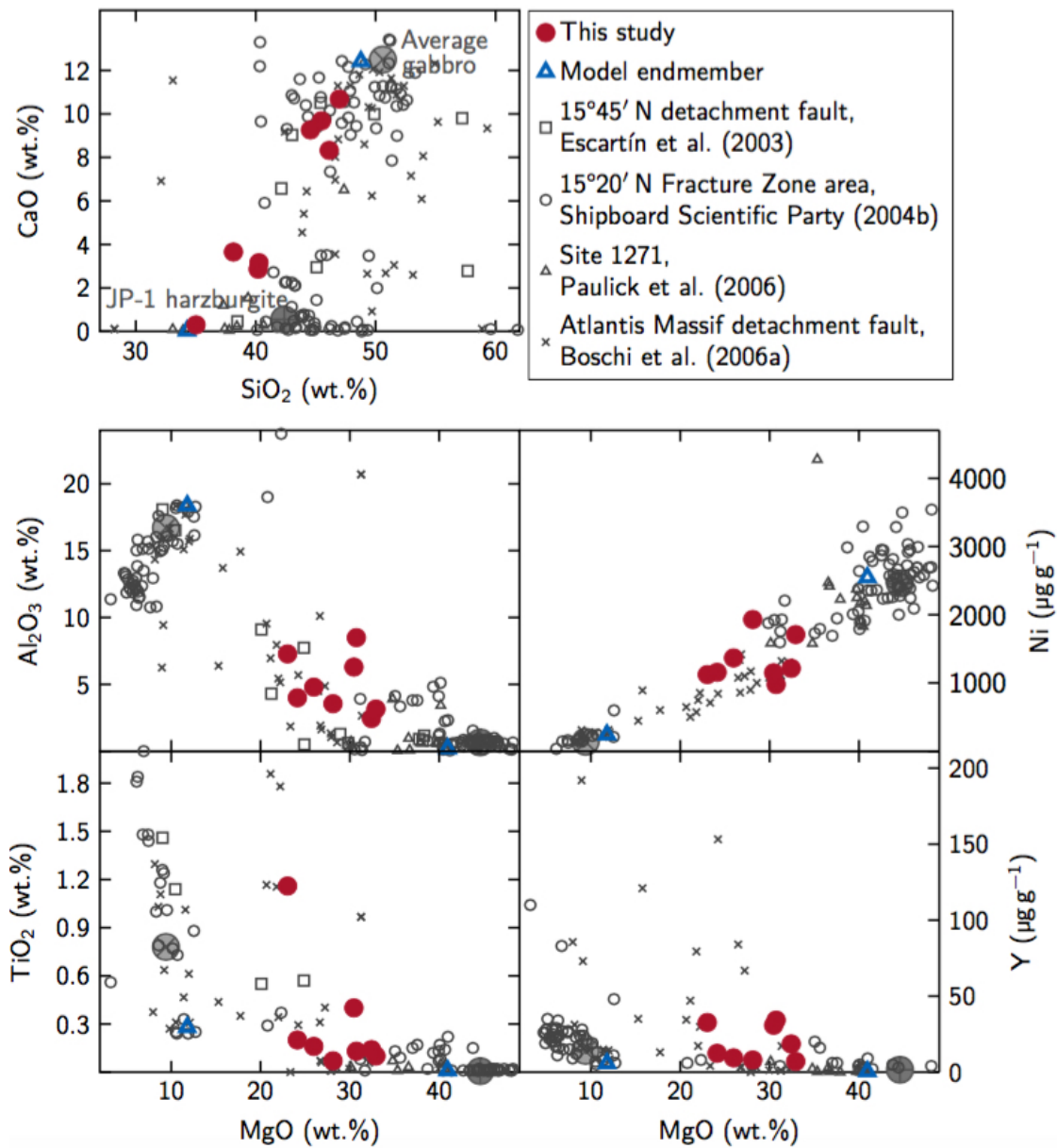


Figure 2.5 Whole-rock geochemical data of hybrid rocks. For comparison, published data of samples from the 15°20' N Fracture Zone area and the Atlantis Massif south wall as well as average gabbro composition (Coogan, 2014) and JP-1 harzburgite (Imai et al., 1995) are shown. Silicon and Ca are fluid-mobile elements that may easily be influenced by metasomatism; MgO and Al₂O₃, TiO₂, and Ni are considered fluid-immobile. MgO vs. Ni nicely depicts mixing trends from ultramafic to gabbroic. Yttrium concentrations indicate the degree of fractionation of impregnating melts. Model endmember compositions (Paulick et al., 2006) are also plotted.

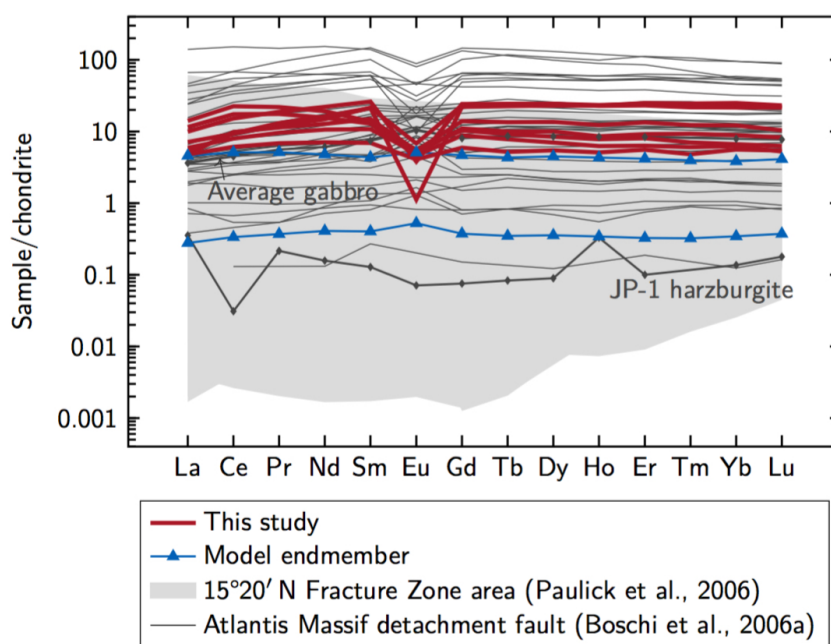


Figure 2.6 Chondrite-normalized whole-rock REEs of hybrid rock samples (chondrite after McDonough and Sun, 1995). Samples studied here show enrichments of REEs when compared to pure ultramafic rock. Similar trends are seen in hybrid rocks from the 15°20' N Fracture Zone area and the Atlantis Massif south wall. Samples with stronger REE enrichments represent more evolved impregnating melts. For comparison, average gabbro (Coogan, 2014) and JP-1 harzburgite (Imai et al., 1995) are shown. Model endmember compositions (Paulick et al., 2006) are also plotted.

must hence have been variable, even on a small scale. This assumption is in line with considerable scatter around simple mixing lines of trace elemental concentrations (e. g., Ni, Y, REEs; Figs. 2.5 and 2.6).

2.3.3 Temperature estimates

Ti-in-hornblende Otten (1984) formulated a titanium-in-hornblende geothermometer based on the temperature dependence of TiO_2 contents in Ca-amphiboles. The thermometer requires the input of the total amount of Ti p. f. u. (per formula unit) in the hornblende, which itself depends, among others, on the oxidation state of iron. Here, ferrous and ferric iron contents were estimated following Leake et al. (1997). These yield minimum and maximum estimates for ferric iron and with it for most other elements in the particular hornblende, including Ti. Minimum and maximum values for Ti, however, only vary in the third decimal place which would affect resultant temperature estimates by $\leq 4^\circ\text{C}$. This range is negligible for our purposes and we based our final temperature calculations on average Ti estimates; this ranges from <0.001 to 0.321 cations p. f. u. Further, an implicit assumption for the thermometer is that, for amphiboles formed from subsolidus alteration of cumulus minerals, all available Ti is consumed by the amphibole

(Otten, 1984). If other Ti-bearing phases (e. g., rutile, ilmenite) are present, hornblende may not contain the total amount of Ti available in the system. Calculated temperatures must hence be considered as minimum estimates. This is the case for the here-studied samples (*cf.* Sections 2.3.1 and 2.3.3).

Formation temperatures were estimated for both, deformed and undeformed amphibole grains. Derived temperatures mirror the two amphibole populations, i. e., high-Ti *vs.* low-Ti amphibole, and show a bivariate pattern within 545 to 931 °C, with 84.6% ($n = 110$) in the range of 545 to 700 °C and 6.2% ($n = 8$) within 825 to 900 °C (Fig. 2.7). Amphiboles temperature estimates are given in Tab. 2.2.

Ti-in-zircon Several geothermometers have been developed based on increasing Ti contents in zircon with temperature. The calibration by Ferry and Watson (2007) may be applied to rocks without quartz and/or rutile, provided $a\text{SiO}_2$ and $a\text{TiO}_2$ are known. We estimated $a\text{SiO}_2$ at 0.9 and $a\text{TiO}_2$ at 1.0, the latter of which is a higher-than-conservative estimate (Ferry and Watson, 2007) but reasonable as rutile appears to be present in some samples. Titanium contents in zircon vary from 2 to 28 $\mu\text{g g}^{-1}$. Estimated temperatures range from 585 to 820 °C for a pressure of 0.2 GPa. Estimates for the individual samples range from 585 to 662 °C ($n = 2$), 630 to 820 °C ($n = 2$), and 741 to 786 °C ($n = 11$), respectively (Fig. 2.7, Tab. 2.3). The pressure dependence of the thermometer is small at 50 °C GPa^{-1} (Ferry and Watson, 2007). Ferriss et al. (2008) estimated the pressure-sensitivity to be 100 °C GPa^{-1} which would lower the estimated temperatures by 10 °C if pressure was 0.1 instead of 0.2 GPa.

Recent studies (Fu et al., 2008; Tailby et al., 2011) revealed complexities in the substitution of Ti in zircon and larger uncertainties in the Ti-in-zircon thermometry. Our estimates are thus to be treated with caution.

Zr-in-rutile The temperature-dependence of the substitution of Zr for Ti in rutile was determined in several studies (Watson et al., 2006; Tomkins et al., 2007; Ferry and Watson, 2007; Shulaker et al., 2015). We found rutile in one sample (1271B-5R-1, 12–14 cm); its Zr contents range from 505 to 1987 $\mu\text{g g}^{-1}$. The calibration by Ferry and Watson (2007) yields temperature estimates of 663 to 799 °C after correcting for pressure ($P = 0.2$ GPa; Fig. 2.7, Tab. 2.3). This calibration does not require quartz to be present in the samples, but $a\text{SiO}_2$ relative to quartz ($a\text{SiO}_2 = 1$) has to be known. Since we observed quartz in some of the samples (e. g., sample 1271B-3R-1, 93–99 cm) we assumed a reasonably high silica activity of 0.9. In a system with lower silica activity, temperature estimates would be somewhat lower. However, at 700 °C and 0.2 GPa, the silica activity of the forsterite–enstatite buffer is only 0.25 log units below that of quartz (Fig. 9 in Klein et al., 2009), so even in ultramafic rocks, silica activity is fairly high. In a system that is saturated in quartz, temperature estimates would be ~ 10 °C higher. Estimates after Tomkins et al. (2007), who developed a calibration for rutile coexisting with zircon and quartz, are within the same range (658–791 °C).

Table 2.2 Whole-rock geochemical compositions of hybrid rocks.

Sample	1271B-1R-1, 8–13 cm	1271B-3R-1, 17–20 cm	1271B-13R-1, 27–31 cm	1271B-13R-1, 52–59 cm	1271B-14R-1, 45–48 cm	1271B-18R-1, 81–84 cm	1271B-18R-1, 93–96 cm	1271B-20R-1, 0–2 cm	1271B-17R-1, 61–69 cm	1271B-17R-1, 8–16 cm
Lithology	Chl-poor amphibolite	Chl-poor amphibolite	Impr. dunite, weakly serp.	Spl-rich serp. dunite	Chl-poor amphibolite	Chl-poor amphibolite	Chl-rich amphibolite	Impr. dunite, weakly serp.	Serp. dunite, MRI	Ampgabbro
Depth (m b. s. f.)	0.01	17.17	65.37	65.61	70.25	89.91	90.03	98.81	85.11	84.58
wt. %										
SiO ₂ ^a	45.5	46.1	40.3	35.0	44.6	40.2	38.1	47.0	34.3	48.8
TiO ₂ ^a	0.16	0.07	0.10	0.13	1.16	0.14	0.40	0.20	0.01	0.28
Al ₂ O ₃ ^a	4.79	3.55	3.15	8.49	7.27	2.44	6.29	3.99	0.19	18.38
Fe ₂ O ₃ ^a	4.06	3.60	9.30	9.05	7.02	7.00	6.86	5.40	8.08	4.98
MnO ^a	0.13	0.14	0.13	0.22	0.11	0.20	0.25	0.11	0.10	0.17
MgO ^a	26.0	28.1	32.9	30.7	23.0	32.4	30.5	24.1	41.0	11.8
CaO ^a	9.68	8.32	3.16	0.30	9.26	2.86	3.65	10.68	0.03	12.42
Na ₂ O ^b	0.20	0.09	0.47	0.14	0.35	0.10	0.04	0.54	0.06	1.10
K ₂ O ^b	b. d. l.	b. d. l.	0.01	0.02	0.01	0.01	b. d. l.	0.01	0.01	0.31
Total	90.4	90.0	89.8	84.1	92.8	85.4	86.1	92.1	83.7	98.2
LOI	n. d.	n. d.	n. d.	n. d.	n. d.	n. d.	n. d.	n. d.	14.55	2.77
µg g⁻¹										
S ^a	0.0	40.1	1001.3	80.1	0.0	360.5	120.2	200.3	0.2	0.0
Cr ^a	3556	2760	5412	13 122	2607	2232	4347	5060	1813	113
Co ^a	38	33	103	67	68	59	62	63	n. d.	n. d.
Ni ^a	1366	1930	1709	977	1122	1214	1149	1156	2549	242
Zn ^a	43	33	44	87	27	31	36	38	n. d.	n. d.
Rb	0.287	0.262	0.414	0.602	0.260	0.269	0.234	0.213	0.081	5.094
Sr	4.11	3.20	4.45	4.50	5.28	3.01	2.46	12.80	0.39	466.52
Y	9.37	7.98	7.01	34.20	32.63	18.50	30.77	12.35	0.47	5.76
Zr ^a	17	8	16	81	87	29	69	31	0.84	7.40
Nb	2.34	1.45	0.73	3.68	8.85	1.24	3.66	1.46	0.06	0.39

(continued on the following page)

(continued from the previous page)

Sample	1271B-1R- 1, 8–13 cm	1271B-3R- 1, 17–20 cm	1271B- 13R-1, 27–31 cm	1271B- 13R-1, 52–59 cm	1271B- 14R-1, 45–48 cm	1271B- 18R-1, 81–84 cm	1271B- 18R-1, 93–96 cm	1271B- 20R-1, 0–2 cm	<i>1271B- 17R-1, 61–69 cm</i>	<i>1271B- 17R-1, 8–16 cm</i>
Ba	3.78	2.67	1.65	1.96	2.72	5.11	1.24	5.65	<i>0.13</i>	<i>418.21</i>
La	3.34	2.73	1.13	1.21	1.69	1.14	2.36	1.40	<i>0.07</i>	<i>1.08</i>
Ce	13.80	10.69	3.74	5.75	5.71	6.02	9.30	4.89	<i>0.21</i>	<i>3.13</i>
Pr	2.03	1.63	0.64	1.22	1.13	1.05	1.75	0.89	<i>0.03</i>	<i>0.48</i>
Nd	8.78	7.11	3.23	7.43	6.79	5.82	10.07	4.85	<i>0.19</i>	<i>2.19</i>
Sm	2.03	1.90	1.02	3.15	3.19	2.21	3.86	1.59	<i>0.06</i>	<i>0.64</i>
Eu	0.30	0.26	0.23	0.06	0.38	0.30	0.21	0.28	<i>0.03</i>	<i>0.29</i>
Gd	2.06	1.75	1.18	4.39	4.61	2.77	4.82	2.19	<i>0.07</i>	<i>0.93</i>
Tb	0.33	0.28	0.19	0.82	0.87	0.49	0.88	0.36	<i>0.01</i>	<i>0.16</i>
Dy	2.08	1.72	1.34	5.63	6.00	3.35	5.98	2.47	<i>0.09</i>	<i>1.10</i>
Ho	0.43	0.34	0.28	1.25	1.28	0.67	1.24	0.47	<i>0.02</i>	<i>0.24</i>
Er	1.29	1.01	0.89	3.99	3.88	2.14	3.69	1.47	<i>0.05</i>	<i>0.67</i>
Tm	0.17	0.15	0.12	0.61	0.56	0.30	0.54	0.23	<i>0.01</i>	<i>0.10</i>
Yb	1.07	1.01	0.90	4.02	3.69	1.96	3.48	1.43	<i>0.06</i>	<i>0.62</i>
Lu	0.15	0.13	0.13	0.57	0.54	0.26	0.53	0.20	<i>0.01</i>	<i>0.10</i>
Hf	0.62	0.22	0.50	2.05	0.89	1.08	2.09	0.74	<i>0.02</i>	<i>0.24</i>
Ta	0.12	0.07	0.07	0.48	0.64	0.14	0.34	0.11	b. d. l.	<i>0.02</i>
Th	0.50	0.39	0.12	0.39	0.18	0.22	0.35	0.17	<i>0.01</i>	<i>0.04</i>
U	0.66	0.87	0.04	0.28	0.24	2.39	0.97	0.05	<i>0.01</i>	<i>0.03</i>

Included are data from Paulick et al. (2006; in *italic*) here used as endmember compositions for geochemical modeling.

^a marks XRF measurements; ^b marks ICP-OES; all other elements analyzed by ICP-MS.

Mean analytical accuracies are better than 3% for most elements analyzed by XRF; mean accuracies for ICP-OES analyses are better than 6%, except for K (13.9%); precisions of ICP-MS analyses are better than 3%, except for Tm (4.3%) and Lu (6.5%).

Abbreviations: m b. s. f., m below seafloor; Amp, amphibole; Chl, chlorite; LOI, loss on ignition; MRI, melt–rock interaction REE signature; n. d., not detected; serp., serpentized.

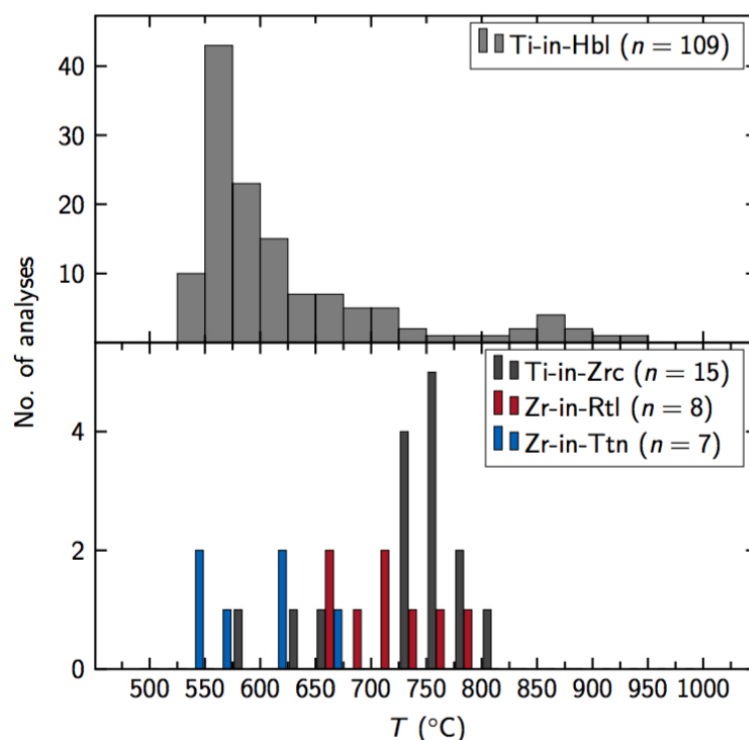


Figure 2.7 Geothermometric results. The estimates vary but all indicate temperatures of amphibolite-grade or higher. Abbreviations: Hbl, hornblende; Rtl, rutile; Ttn, titanite; Zrc, zircon.

Zr-in-titanite Hayden et al. (2008) developed a robust and precise geothermometer based on the replacement of Zr for Ti in titanite. Only three of our samples contain titanite crystals large enough to be ablated with the laser; Zr concentrations are 6 to $104 \mu\text{g g}^{-1}$. Temperature estimates are 533 to 558°C ($n=3$), 621 to 623°C ($n=2$), and 651 to 738°C ($n=2$), assuming $a\text{SiO}_2$ of 0.9, $a\text{TiO}_2$ of 1.0, and P of 0.2 GPa (Fig. 2.7, Tab. 2.3). These estimates are consistently lower than temperatures estimated by Zr-in-rutile thermometry, in agreement with a down-temperature progression in metamorphism and alteration and the observed overgrowth of titanite over rutile.

2.4 Thermodynamic calculations

2.4.1 Reaction path modeling with EQ3/6

Model parameters To simulate seawater influx into a peridotite-hosted detachment fault and subsequent alteration of hybrid rock varieties within the fault system, we performed reaction path modeling using the EQ3/6 software package (Wolery and Jarek, 2003). The database from Jöns et al. (2009) was used for all calculations. It contains $\log K$ values for minerals and aqueous species, calculated with SUPCRT92

Table 2.3 Zircon, rutile, and titanite compositions and thermometric estimates

Sample	Comment	Conc. ($\mu\text{g g}^{-1}$)	T ($^{\circ}\text{C}$)
Zircon		Ti	F&W'07
1271B-10R-1, 67–70 cm	Grain A	3.6	630
1271B-10R-1, 67–70 cm	Grain A	27.8	820
1271B-11R-1, 88–91 cm	Grain B	20.3	786
1271B-11R-1, 88–91 cm	Grain E	16.0	761
1271B-11R-1, 88–91 cm	Grain E	17.2	769
1271B-11R-1, 88–91 cm	Grain F	15.2	756
1271B-11R-1, 88–91 cm	Grain F	18.1	774
1271B-11R-1, 88–91 cm	Grain G	14.9	754
1271B-11R-1, 88–91 cm	Grain G	13.8	746
1271B-11R-1, 88–91 cm	Grain I	18.9	778
1271B-11R-1, 88–91 cm	Grain K	13.0	741
1271B-11R-1, 88–91 cm	Grain K	14.2	750
1271B-11R-1, 88–91 cm	Grain M	13.9	747
1271B-14R-1, 21–24 cm	Grain A	2.0	585
1271B-14R-1, 21–24 cm	Grain A	5.4	662
Rutile		Zr	F&W'07
1271B-5R-1, 12–14 cm	Grain A	1496	768
1271B-5R-1, 12–14 cm	Grain A	1144	740
1271B-5R-1, 12–14 cm	Grain A	1987	799
1271B-5R-1, 12–14 cm	Grain A	691	691
1271B-5R-1, 12–14 cm	Grain B	802	705
1271B-5R-1, 12–14 cm	Grain C	577	675
1271B-5R-1, 12–14 cm	Grain D	505	663
1271B-5R-1, 12–14 cm	Grain E	861	712
Titanite		Zr	Hayden'08
1271B-5R-1, 12–14 cm	Grain A	104.4	651
1271B-14R-1, 32–35 cm	Grain A	11.4	558
1271B-14R-1, 32–35 cm	Grain A	5.8	533
1271B-14R-1, 32–35 cm	Grain B	7.8	543
1271B-17R-1, 17–19 cm	Grain A	55.8	623
1271B-17R-1, 17–19 cm	Grain A	53.4	621

Zircon thermometric estimates after Ferry and Watson (2007; abbreviated F&W'07), with $\rho = 3300 \text{ kg m}^{-3}$, $P = 0.2 \text{ GPa}$, and a pressure correction of $50 \text{ }^{\circ}\text{C MPa}^{-1}$; rutile thermometric estimates after Ferry and Watson (2007; abbreviated F&W'07), with $a_{\text{SiO}_2} = 0.9$ and a pressure correction for 0.2 GPa ; titanite thermometric estimates after Hayden et al. (2008; abbreviated Hayden'08), with $\rho = 3300 \text{ kg m}^{-3}$, $P = 0.2 \text{ GPa}$, $a_{\text{TiO}_2} = 1$, $a_{\text{SiO}_2} = 0.9$.

(Johnson et al., 1992), along a geothermal gradient with the temperature (°C)/pressure (MPa) pairs: 2/25, 50/27, 100/33, 150/40, 200/50, 250/60, 300/72.5, 350/86, 400/97, 450/110, 500/125, 550/140, 600/160, 650/180, 700/200, 750/225, 800/250, 850/280, 900/315. As stated by Jöns et al. (2009), such a pressure–temperature gradient is slightly hotter than that expected for a normal oceanic crust, but may account for the large volumes of gabbroic intrusions seen in the Leg 209 drill holes. We considered solid solutions for serpentine (chrysotile–greenalite), brucite (brucite–Fe-brucite), olivine (forsterite–fayalite), clinopyroxene (diopside–hedenbergite), chlorite (clinochlore–daphnite), talc (talc–minnesotaite), garnet (andradite–grossular), actinolite (tremolite–ferrotremolite), pargasite (pargasite–ferropargasite), amphibole (tremolite–ferrotremolite–pargasite–ferropargasite), epidote (clinozoisite–epidote), and plagioclase (albite–anorthite), alkalifeldspar (albite–microcline), white mica (muscovite–paragonite), and biotite (phlogopite–annite). EQ3/6 can handle ideal solutions only; all mineral compositions in our calculations are, however, Mg-rich and thus reduce the effect of errors due to the mixing model. Minerals that were not observed in any of the samples were suppressed during the model runs (i. e., analcime, andalusite, antigorite, corundum, wuestite, kyanite, margarite, monticellite, nepheline, sillimanite). Modeling was performed in two steps: First, the reaction of seawater (composition after McCollom and Bach, 2009) with the most primitive dunite of the Paulick et al. (2006) dataset (Tab. 2.2) was computed with a final water/rock ratio of 10 while heating to temperatures of 300 °C, 400 °C, 500 °C, and 600 °C. This step simulates the recharge of seawater into the lithosphere and the compositional changes seawater-derived fluids are expected to undergo upon interaction with mantle peridotite. In a second step, these fluids were reacted with fresh dunite or gabbro (Paulick et al.; Tab. 2.2) or a mixture of both (peridotite–gabbro proportions of 80:20, 60:40, 40:60, 20:80). Water/rock (w/r) ratios were varied to simulate the change from a fluid dominated (w/r = 50, reaction progress $\xi = 0.01$) to a rock dominated system (w/r = 0.5, $\xi = 1$). These reaction path computations simulate interactions between recharged seawater-derived fluids with different lithologies in the lithosphere. Model runs were performed at 300 °C, 400 °C, 500 °C, and 600 °C—these temperatures allow comparison of processes at conditions where peridotite usually turns into serpentinite and higher temperatures indicated by our geothermometric estimates.

Results Predicted secondary assemblages change with temperature, w/r ratio, and primary lithology, i. e., the fraction of gabbro mimicking varying degrees of melt impregnation observed in the samples. At 300 °C, the main phases predicted to form by hydrating pure peridotite or gabbro are serpentine, brucite, chlorite, muscovite, epidote, and tremolitic amphibole (Supplementary Information Fig. A.1.5). Hybrid rock varieties will alter to assemblages rich in serpentine, chlorite, talc, tremolite, and epidote. In model runs at 400 °C, the predicted extent of serpentinization of the peridotitic endmember is low, and the gabbroic endmember alters to mainly plagioclase, tremolitic amphibole, and chlorite (Supplementary Information Fig. A.1.5). Hybrid rocks are predicted to form olivine, chlorite, serpentine, and tremolitic amphibole for rather peridotitic precursors, and assemblages rich in chlorite, tremolite, and plagioclase if gabbro was predominant.

At 500 °C and 600 °C, olivine is predicted to be stable for purely peridotitic precursors (Fig. 2.8). Adding gabbroic melt to the model at these temperatures results in assemblages rich in olivine and chlorite, with tremolitic amphibole and hornblende present at intermediate or low w/r ratios and talc at high w/r ratios. Magnetite contributes to the alteration assemblage at 600 °C and high w/r ratios. At all w/r ratios, olivine is predicted to disappear in hybrids with high proportions of gabbro ($\geq 60\%$). In these runs, chlorite is predominant, followed by tremolitic amphibole, magnetite, and pargasitic amphibole. Minor talc is predicted to form at high w/r ratios at 500 °C. Precursor assemblages with $\geq 80\%$ gabbro should alter to chlorite, tremolite, plagioclase, and magnetite with minor talc.

The expected fractions of phyllosilicates change with temperature and w/r ratio (Fig. 2.9). At 500 °C and 600 °C and w/r > 10, peridotite will form only minor amounts of phyllosilicates. This is similar for the gabbroic endmember at 600 °C but up to about 30 vol.% phyllosilicates will form at 500 °C. Hybrid rocks, however, may form up to 60 vol.% phyllosilicates at either temperature, most of which is chlorite. At lower temperatures, peridotitic lithologies alter to >80 vol.% phyllosilicates, most of which is serpentine. Serpentine disappears at a 40:60 peridotite–gabbro ratio, but chlorite (and minor talc and muscovite) still accounts for up to ~60 vol.% of the reaction products.

Hybrid rock precursors with 60% gabbro are expected to form highest amounts of phyllosilicates when hydrated at high temperatures (Supplementary Information Fig. A.1.6). Model runs predict almost pure phyllosilicate-assemblages for high w/r ratios at 500 °C, quickly declining to about 60 vol.% with decreasing w/r ratio.

Types and proportions of phyllosilicates vary over the different model runs; these variations are depicted in Fig. 2.8 and Supplementary Information Fig. A.1.5.

2.4.2 *T–X* sections with Theriak/Domino

Model parameters To further examine compositional dependencies of phase relations we calculated equilibrium assemblages in the pseudo-binary system of ultramafite–maficite applying Theriak/Domino (de Capitani and Petrakakis, 2010). The tcdb55c2d-database, which is to a great part based on (Holland and Powell, 1998), was used. Endmembers for the binary system were the same whole rock compositions by Paulick et al. (2006) used for the EQ3/6 modeling, which were recalculated to Si 33.73, Al 10.22, Fe 5.98, Mg 60.09, Ca 0.03, Na 0.11, H 60 and Si 51.17, Al 22.73, Fe 3.93, Mg 18.44, Ca 13.96, Na 2.24, H 60, respectively, to use as input for Theriak/Domino. Hydrogen was set to the arbitrary high number of 60 to account for excess water in the system. The modeling temperature range was set to 200 to 700 °C and pressure to 0.2 GPa, which represents lithostatic pressure at a depth of ~6 km below the seafloor. In contrast to EQ3/6, the interacting fluid cannot be speciated in Theriak/Domino and it does not take account of varying w/r ratios. Theriak/Domino, on the other hand, allows for a more sophisticated treatment of solid solution thermodynamic properties. Both modeling codes hence have strengths and weaknesses. Yet, the results yielded by both models are very similar which lends credit to the major conclusion drawn about the higher state of hydration in the mixed lithologies.

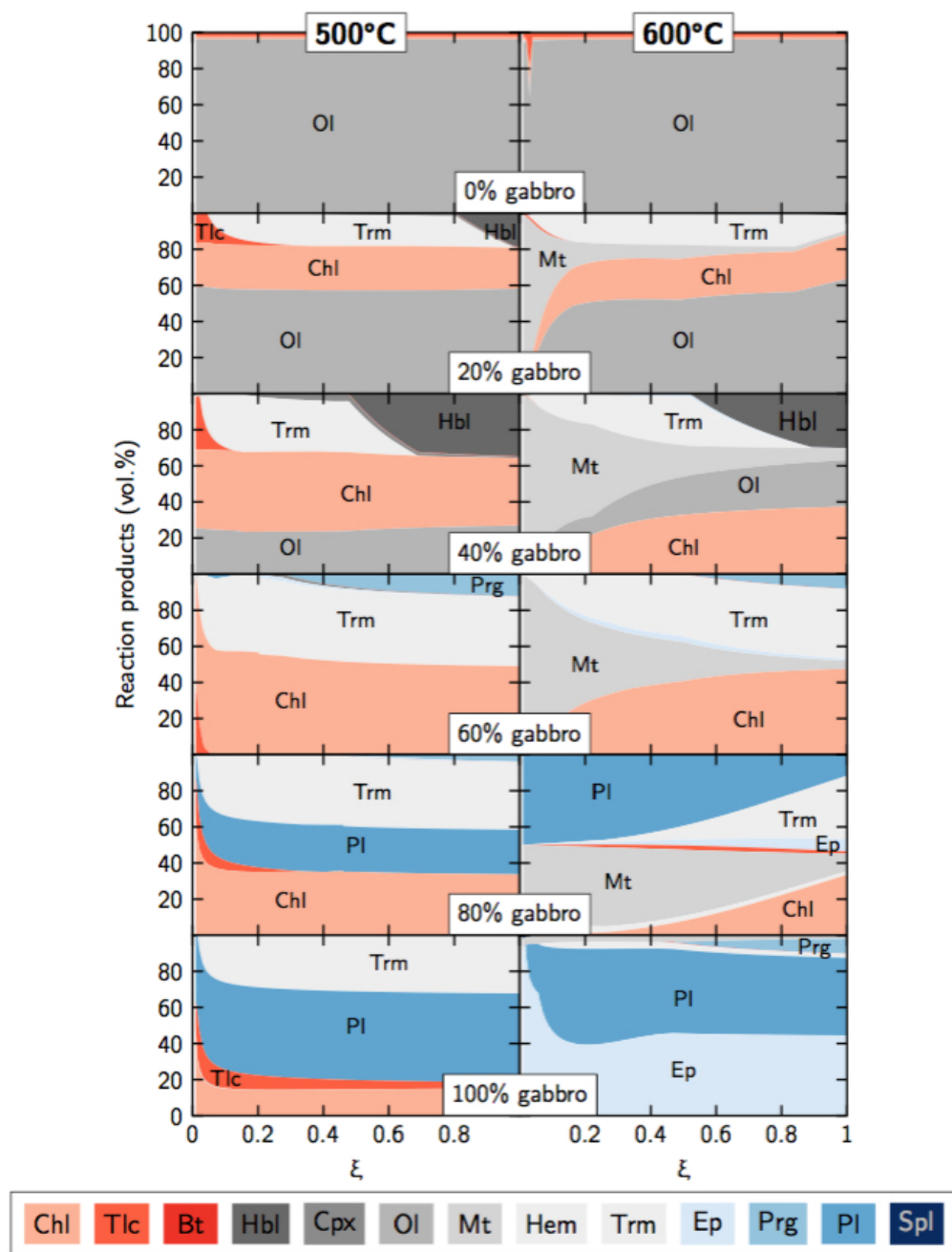


Figure 2.8 EQ3/6 modeling results for 500°C and 600°C and different peridotite–gabbro mixing ratios. The x-axis depicts w/r ratios, changing from fluid-dominated (towards left) to rock-dominated (towards right). Note that the y-axis corresponds to vol.% reaction product, i. e., high abundances of a mineral in fluid-dominated systems depict little absolute volume (e. g., 90 vol.% of 0.02 kg rock for $\xi = 0.01$). Endmember lithologies alter to assemblages lacking significant amounts of mechanically weak minerals, whereas hybrid protoliths turn into assemblages rich in weak minerals. Abbreviations: Bt, biotite; Chl, chlorite; Cpx, clinopyroxene; Ep, epidote; Hbl, hornblende; Hem, hematite; Mt, magnetite; Ol, olivine; Pl, plagioclase; Prg, pargasite; Spl, spinel; Tlc, talc; Trm, tremolite.

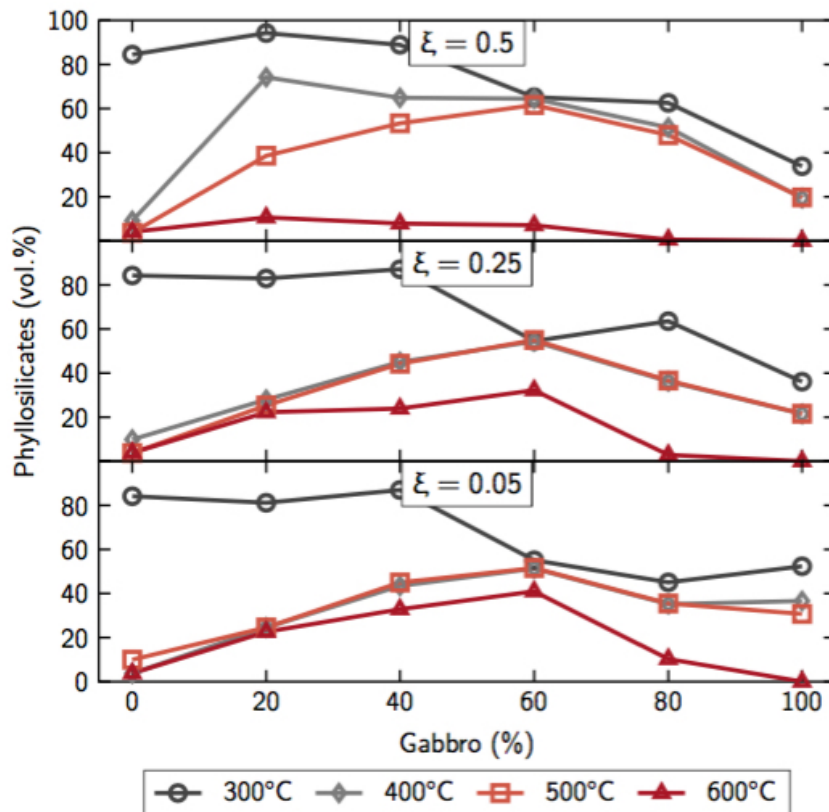


Figure 2.9 EQ3/6 modeling results. Varying amounts of phyllosilicates are predicted to form as a function of protolith composition, temperature, and w/r ratio. Hybrid rock compositions are predicted to alter to phyllosilicate-rich assemblages at high temperatures. Serpentinization of olivine-rich protoliths is reflected in highest amounts phyllosilicates at model runs ≤ 400 °C.

Results Modeling results (Fig. 2.10 and Supplementary Information Fig. A.1.7) predict alteration assemblages after peridotitic precursor rocks to be rich in olivine at high and in serpentine at low temperatures, whereas gabbroic precursors will form high volumes of plagioclase at high and of epidote (clinzoisite) and prehnite at lower temperatures. For hybrid precursor rocks with similar proportions of dunite and gabbro, the T - X sections display alteration assemblages rich in amphibole at high temperatures and, over the complete temperature range, in chlorite (clinocllore; >50 vol.%). At temperatures below ~ 350 °C, higher proportions of chlorite are predicted for rocks with greater proportions of gabbro. The total amount of H_2O bound in secondary minerals reflects this prediction of chlorite-rich hybrid rock alteration assemblages. In addition, it displays large amounts of H_2O stored in serpentine formed from peridotite-rich lithologies below ~ 400 °C.

The results of the Theriak/Domino computations hence corroborate the results of the reaction path model calculations in that much increased abundances of phyllosilicates are predicted to form from hybrid rock hydration. In contrast, purely peridotitic or gabbroic lithologies will not form high amounts of phyllosilicates under the same pressure/temperature conditions.

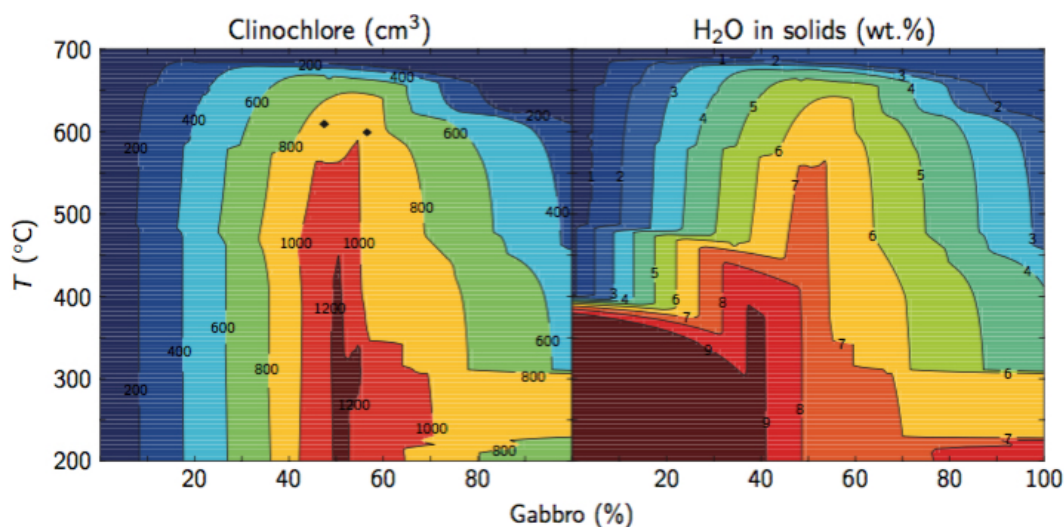


Figure 2.10 Theriak/Domino modeling results. Highest amounts of clinocllore are predicted to form from hybrid peridotite–gabbro precursors, in particular at temperatures $>350^{\circ}\text{C}$. This hydration of hybrid rock at elevated temperatures is mirrored in the total amount of H_2O bound in the alteration assemblage. Serpentinization of ultramafic rocks absorbs high amounts of H_2O below $\sim 400^{\circ}\text{C}$.

2.5 Discussion

2.5.1 Fluid-induced metasomatism versus magmatic impregnation

The whole-rock compositions of Site 1271B shear zone rocks are intermediate to peridotite and gabbro (Figs. 2.4 and 2.5), strongly suggesting that they represent hybrids of the two. Textural evidence implies that this hybridization is caused by impregnations of the peridotites with basaltic melts. Remnant primary phases, secondary mineral assemblages, and whole-rock geochemical data are consistent with mixed ultramafic–mafic precursor rock compositions from other ODP Leg 209 sites and detachment fault sites on the MAR (e.g., Boschi et al., 2006a; Escartín et al., 2003; Früh-Green et al., 2017; Godard et al., 2009; Kelemen et al., 2007; Paulick et al., 2006; Schroeder and John, 2004; *cf.* Figs. 2.4 and 2.5) and along other slow-spreading ridges (e.g., Morishita et al., 2009; Yi et al., 2014). We hence conclude that detachment fault rocks commonly represent mantle peridotite impregnated by mainly mafic melts.

It is, however, not generally accepted that these now altered hybrid rocks represent melt-impregnated peridotite. Boschi et al. (2006a) and Früh-Green et al. (2017), who studied deformed amphibole- and/or talc-rich lithologies recovered from detachment shear zones at the south wall of the Atlantis Massif, MAR, ascribe few of these rocks to result from the alteration of hybrid peridotite–gabbro protoliths. Instead, they assign most samples to represent metasomatism induced by localized oxidizing, Si–Al–Ca-rich fluids during deformation. The amphibole-dominated rocks are thought to have gabbroic protoliths that were altered during interaction with seawater-derived fluids whereas the

serpentinites formed talc-rich rocks during alteration by gabbro-derived, Si-rich fluids. Likewise, Escartín et al. (2003) invoked channeled fluid flow forming talc- and amphibole-schists after an ultramafic protolith in the detachment fault zone at the 15°45' N core complex. The formation of the talc-schists clearly involves Si-metasomatism, but the interpretation of metasomatic mass transfers as the major cause for the bulk compositions of fault rocks may be problematic. Calcium and Si are both highly fluid-mobile during metasomatic reactions between ultramafic and mafic lithologies (Bach and Klein, 2009). Expectedly, the fault rocks—having been affected by diffusive mass transfers driven by steep chemical potential gradients between ultramafic and mafic rocks—do not plot between serpentinitized mantle peridotites and magmatic intrusions, but scatter markedly in the Ca–Si compositional plane (Fig. 2.5; see also Fig. 9 of Boschi et al., 2006a). Scattering of elements with exceedingly low solubilities in intergranular aqueous solutions such as Mg, Al, Ti, and many trace elements like Cr, Ni, and REEs (Figs. 2.5 and 2.6; Figs. 9–11 of Boschi et al., 2006a) cannot, however, easily be explained by metasomatism. These elements instead show tight relations expected for hybrid rocks (which underwent subsequent hydrothermal alteration and deformation). In particular the relationships between Mg and Al, Ti, or Ni demonstrate direct mixing trends between peridotites and gabbroic melts. Similarly, the whole-rock geochemical data presented by Escartín et al. (2003) are consistent with a predominance of hybrid ultramafic–mafic protoliths. Metasomatic mass transfers did not appear to play a major role in setting whole-rock compositions of the shear zone rocks.

We suggest that hybrid rocks may be distinguished from metasomatically altered lithologies by examining whole-rock geochemical data, particularly concentrations of fluid-immobile elements, e. g., Mg, Al, Ti, Cr, Ni, or REEs. Obvious mixing trends between ultramafic and pure gabbroic compositions strongly argue for melt impregnation instead of metasomatism. This geochemical approach is particularly helpful when studying samples heavily affected by alteration, where only few primary features are preserved.

Some rocks have trace element contents higher than expected from peridotite–gabbro mixing. These enrichments are likely caused by the local occurrence of more evolved melts that have higher contents of trace elements, notably REEs. Such REE-rich impregnations in peridotite were, for instance, observed in the form of oxide gabbro-norite or plagiogranite veins at ODP Site 1270 (Jöns et al., 2009, 2010; Shipboard Scientific Party, 2003) nearby our study site in the 15°20' N Fracture Zone area.

The nature of the impregnating melts can be inferred by considering elements that exhibit highly variable concentrations in magmatic rocks and are at the same time not soluble in aqueous solutions. Yttrium and REEs are generally low in mafic melts but increase with progressive fractionation; samples enriched in Y or REEs may hence represent peridotites impregnated by more evolved melts. The general existence of highly fractionated melt impregnations in oceanic core complexes has been documented by, e. g., Godard et al. (2009) and Jöns et al. (2009), who described leucocratic to plagiogranitic dikes and veins drilled at IODP Site U1309, Atlantis Massif, and at ODP Site 1270, 15°20' N Fracture Zone area, respectively. In each case, REE concentrations show a multifold enrichment with respect to gabbroic rocks and to chondrite (up to ~200 times for the latter).

2.5.2 Alteration of hybrid lithologies at elevated temperatures

The melt-impregnated peridotites studied here display evidence for interaction with seawater alteration to hydrous assemblages including chlorite at amphibolite-grade temperatures. We base this interpretation on the combination of textural, thermometric, and modeling results, namely on (i) amphibolite-facies alteration assemblages, i. e., Ca-amphiboles and chlorite; (ii) fresh olivine occurring next to altered mafic veins, indicating hydration at above-serpentinization temperatures; (iii) geothermometric estimates of temperatures above 530 °C for secondary minerals; and on (iv) mineral assemblages that are in agreement with model runs at 500 °C and 600 °C (EQ3/6) and >400 °C (Theriak/Domino).

High-temperature assemblages in the hybrid rocks include hornblende co-occurring with olivine and chlorite as in impregnated-dunite sample 1271B-18R-1, 109–112 cm. Geothermometers indicate that this hornblende formed at 566 to 677 °C, which agrees well with EQ3/6 model runs at 500 °C and 600 °C, predicting this same mineral assemblage to be stable for hybrid rocks (20–40 vol.% impregnation) and low w/r ratios. Hornblende in fault schists (e. g., sample 1271B-17R-1, 17–19 cm) is estimated to have grown at 557 to 748 °C from Ti-in-Hbl thermometry. Hornblende is overgrown by actinolite, which is in apparent equilibrium with titanite that is estimated to have formed at ~620 °C. Hybrid rocks with mylonitic textures (e. g., hybrid rock sample 1271B-11R-1, 88–91 cm) locally show similar alteration patterns of hornblende to actinolite and tremolite. These samples also contain areas of both primary minerals and secondary amphibole recrystallized into fine neoblasts. Ti-in-hornblende thermometric estimates from porphyroclastic amphibole in mylonitic zones are 577 to 711 °C. Ti-in-zircon temperature estimates of crystals that co-occur with the mylonitic hornblende indicate similar temperatures (741–786 °C). Replacement textures of primary clinopyroxene by hornblende and chlorite (e. g., sample 1271B-14R, 32–35 cm) indicate the instability of clinopyroxene during later phases of deformation. Chlorite shows local crystal-plastic deformation, but statically fills tension gashes and other void spaces in other areas. Formation temperatures of hornblende are 572 to 606 °C, those of chlorite are inferred from euhedral titanite, enclosed within the chlorite, indicating formation at 533 to 558 °C. Required Ti needed to crystallize titanite presumably originates from the breakdown of clinopyroxene or Ti-rich hornblende, which is not stable below 500 °C, as indicated by EQ3/6 model runs. Model results predict the assemblage hornblende–chlorite to occur at low w/r ratios for 20 to 40% gabbro impregnation at 500 °C and 600 °C. Replacement of amphibole by high-temperature chlorite is as well seen in sample 1271B-18R, 38–42 cm.

Noteworthy is the presence of the actinolite–chlorite assemblage at >500 °C, since the appearance of these minerals in mafic rocks is typically considered to represent alteration at greenschist facies conditions (e. g., Fletcher et al., 1997). Our textural, geochemical, and modeling data demonstrate that, in this setting, they form at amphibolite-facies conditions leading to the proposed rock weakening (see below) at these elevated temperatures. Similarly, Nozaka and Fryer (2011) assigned secondary amphibole–chlorite assemblages from IODP Site 1309, Atlantis Massif, to amphibolite-facies conditions.

We anticipate that fluid–rock interactions initiated close to the ridge axis, where the upwelling asthenospheric mantle and infrequent melt injections provided sufficient heat.

Hydrothermal alteration at high temperatures is not uncommon at slow-spreading MORs, where tectonic processes predominate and brittle faulting allows seawater to penetrate deep into the lithosphere (e. g., deMartin et al., 2007; Escartín et al., 2008; Grevemeyer et al., 2013; McCaig et al., 2010). Indeed, microseismic events occurring down to 7 to 8 km below seafloor at asymmetric-spreading portions along the MAR, led these and other authors to anticipate that the entire crust supports brittle failure and hence faulting. In the vicinity of our study site, seismicity patterns suggest that temperatures below 600 °C, which approximately defines the highest temperature at which earthquakes occur at MORs (Golden et al., 2003; Wilcock et al., 2002), exist at depth of 5 to 6 km below the seafloor (Grevemeyer et al., 2013). In line with our conclusions, Grevemeyer et al. state that faulting likely supports seawater migration down to these depths.

Purely gabbroic precursor lithologies do not have sufficiently high MgO-contents to form high amounts of chlorite. The formation of Ca-amphibole- and chlorite-rich lithologies after peridotite, particularly after dunite, on the other hand requires additional availability of Si, Al, and Ca. These elements, in particular Si and Ca, appear to be mobile in the system as indicated by discrepancies in our mixing models. It would be possible that they are added by fluids that earlier interacted with gabbroic rocks, whereby the fluids got enriched in these elements. Yet, our thermodynamic computations show that the chlorite–amphibole assemblages form only during interaction of seawater-derived fluids with hybrid lithologies. Since we observe this alteration assemblage mainly in the vicinity of melt impregnations, we conclude that fluid-induced metasomatic mass transfer was minor. This, in turn, is indicative of fairly low time-integrated fluid fluxes, i. e., low w/r ratios. The lack of significant amounts of talc in the studied samples seems to confirm this interpretation, since reaction path models predict talc to form only at high w/r ratios (Fig. 2.8).

2.5.3 High-temperature deformation of altered hybrid lithologies

Hybrid rocks, including hornblende-bearing assemblages, display evidence of intense deformation at amphibolite-grade conditions in the form of crystal-plastic deformation textures, dynamic crystallization, and neoblast formation in amphiboles (Fig. 2.2c,d). Some hornblende neoblasts in mylonitic shear zones show intracrystalline deformation (Fig. 2.2d) evidencing continued deformation even after recrystallization. This interpretation is consistent with rheologic studies that demonstrated that hornblende may display intracrystalline deformation at temperatures of, e. g., 600 to 750 °C (Brodie and Rutter, 1985; Dollinger and Blacic, 1975) or >585 °C (Cao et al., 2010), whereas it commonly deforms by cataclasis and concomitant breakdown reactions at or below lower amphibolite-facies conditions (e. g., Allison and La Tour, 1977; Brodie and Rutter, 1985).

Amphibole-rich mylonites are cut by mylonitic and schistose shear zones with assemblages of chlorite and hornblende occurring in apparent equilibrium. Chlorite, in contrast to amphibole, is particularly liable to crystal-plastic deformation as it exhibits, like all phyllosilicates, a layered crystal structure and weak interlayer bonds (e. g., Moore and Lockner, 2008). Deformation of phyllosilicates can thus occur over a large temperature range; in our samples we can connect the deformation of chlorite, at least partly, to the

amphibolite-grade temperature field since it locally appears intergrown with schistous hornblende.

The existence of unserpentinized peridotite next to altered, strongly deformed domains of melt impregnation further supports the conclusion that alteration to hydrous assemblages and deformation has occurred at temperatures above the main serpentinization window, i. e., above $\sim 400^\circ\text{C}$ (*cf.* Fig. 2.10). Deformation likely localized into the zone of fluid infiltration as concluded from the lack of petrographic evidence for static replacement of already deformed primary minerals. We hence infer that metamorphic weakening induced by hydrothermal alteration of hybrid rocks is the probable mechanism for strain localization in the detachment fault, and that this localization was enhanced by formation of phyllosilicate-bearing assemblages at amphibolite-grade conditions in the hybrid rocks.

However, earlier and thus hotter deformation of the impregnated rocks, i. e., at granulite-facies temperatures, is not unlikely. The impregnated zones may be weakened by the presence of impregnating melt or, after its full crystallization, by the presence of plagioclase. Strong rheological contrast between plagioclase-rich lithologies and peridotite would lead to strain localization within the plagioclase-rich veins (*cf.* Homburg et al., 2010). Resultant plastic deformation in the already weakened impregnated zones would (i) lead to mechanical mixing of the two lithologies, which is a requirement for our proposed feedback (see next Section) to kick in, (ii) presumably remain active down-temperature, thus opening pathways for fluids that could, penetrated to deep lithospheric levels, induce the here investigated water–rock interactions. Earlier (deformation) textures may thereby easily be overprinted and explain the absence of such in our sample suite.

Petrographic and textural observations are in agreement with Schroeder et al. (2007) who proposed that the ductile shear zones, localized in gabbroic veins throughout the Site 1271B recovered core, were initiated as ductile faults under at least amphibolite-grade temperatures (700°C). Many of the narrow ($<2\text{ cm}$ wide) gabbro veins experienced continuous, down-temperature deformation through the brittle–ductile transition to greenschist grade ($\sim 300^\circ\text{C}$) conditions. Schroeder et al. interpreted the ductile-to-brittle fault rocks as one major, large-offset fault that is believed to have been responsible for the denudation of the mantle rocks during asymmetric seafloor spreading. The authors describe similar deformation textures and histories for the other ODP Leg 209 sites.

Since much of the metamorphic evolution has apparently taken place under amphibolite facies conditions, one may wonder why the gabbroic precursor domains do not exhibit plagioclase—a mineral stable in metagabbros under these pressure–temperature conditions. We argue that the absence of plagioclase in our samples can be reconciled with high metamorphic grades, when the actual compositions of the hybrid rocks are considered. The computed T – X sections (Supplementary Information Fig. A.1.7) indicate that plagioclase is not expected to form in hybrid ultramafic–mafic rocks that have the intermediate fractions of gabbroic material indicated by the mass balance results (30–60%). Hybrid rocks with these compositions are instead predicted to form chlorite and tremolite over a wide temperature range from amphibolite- to greenschist-facies conditions (Fig. 2.10). This means that the rocks where hybridized to an extent that had the ultramafic and mafic domains in the rock small enough for the metamorphic reactions to remove all

initial chemical potential differences. This requires efficient mechanical mixing either in the form of anastomosing small-scale basaltic melt impregnations or by deformation prior to rock hydration.

Our conclusions are consistent with the occurrence of talc-, chlorite-, serpentine-, and other phyllosilicate-containing assemblages in association with major fault zones, including continental faults, subduction zones, and long-lived oceanic transform and detachment faults in various geotectonic settings worldwide (e.g., Boschi et al., 2006b; D’Orazio et al., 2004; Escartín et al., 2003; Escartín et al., 2008; Floyd et al., 2001; Ikari et al., 2009; MacLeod et al., 2002; Schroeder and John, 2004). Even small amounts (few wt.%) of phyllosilicates can initiate substantial weakening of fault rocks (e.g., Escartín et al., 1997; Escartín et al., 2008; Niemeijer et al., 2010).

2.5.4 Prevailing static alteration at low temperatures

Most samples experienced down-temperature alteration and overprinting by continued fluid–rock interaction. This includes mostly static serpentinization of the host peridotite and limited deformation through the brittle–ductile transition to and below greenschist-facies conditions. Strain at these lower temperatures may result in deformation that is partitioned into endmember or close-to-endmember precursor rocks. Cataclastic deformation prevails but schistose serpentine and chlorite are locally present in small-scale shear zones. The serpentine–chlorite assemblage matches model predictions for low-grade hydrothermal alteration of peridotite with gabbro proportions $\leq 20\%$. The computational results also suggest that $\sim 380^\circ\text{C}$ can be considered as the upper temperature limit at which serpentine-rich assemblages are formed.

2.5.5 Implications for oceanic detachment faults

Highly deformed ultramafic–mafic hybrid rocks have been observed at numerous other oceanic core complex sites, including the MARK area, the Kane Megamullion, the $15^\circ 20' \text{N}$ Fracture Zone area, Atlantis Massif, and other locations along the MAR (e.g., Cannat et al., 1997; Dick et al., 2008; Picazo et al., 2012; Schroeder and John, 2004), at the Atlantis Bank, SWIR (Cannat, 1991; Miranda and John, 2010), and at the Godzilla Megamullion, Philippine Sea (Harigane et al., 2008, 2011). Picazo et al. (2012) described an assemblage and deformation textures in hybrid rocks from core complexes at 13° and $14^\circ 45' \text{N}$, MAR, similar to what we observe at Site 1271. These include hybrid ultramafic–mafic rocks that display several stages of deformation, including crystal-plastic deformation of amphibole-rich lithologies interpreted as hydrothermal alteration products after (evolved) mafic melts intruded into the host peridotite. The alteration occurred at above-serpentinization temperatures but probably below $\sim 700^\circ\text{C}$. The authors further depict a down-temperature path of deformation including late strain localization in and brittle fracturing of serpentine–talc assemblages, whereby they allocate talc formation to the influx of Si-rich hydrothermal fluids. The deformation–alteration history in the temperature range of ~ 700 to 400°C is complementary to our results. Greenschist-grade deformation, on the other hand, is less pronounced in our samples and talc is rare,

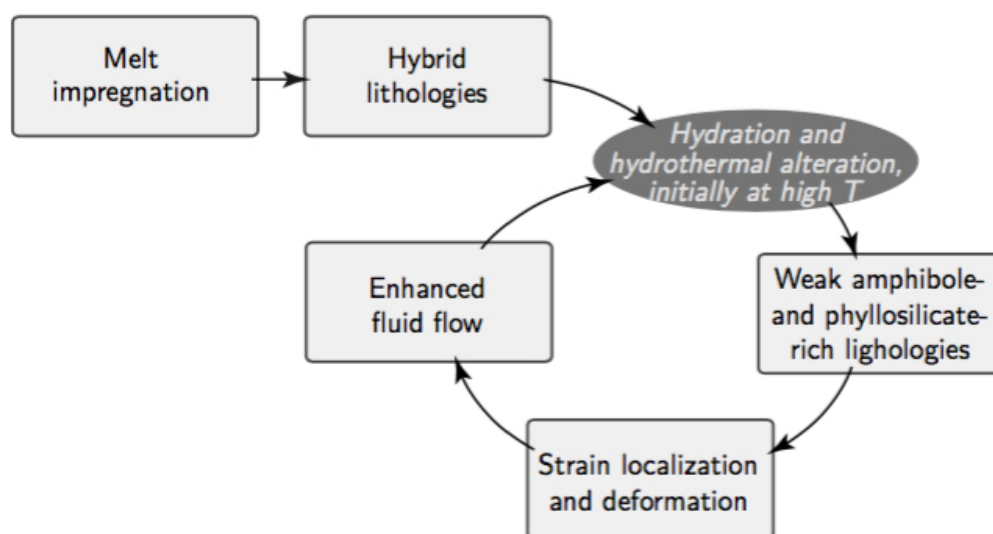


Figure 2.11 Feedback leading to the stabilization of detachment faults. Strain initially localizes in the impregnations, allowing hydration of these hybrid rocks by deeply circulating hydrothermal fluids. Interactions between fluids and hybrid rock cause the formation of weak amphibole- and phyllosilicate-rich secondary assemblages in which strain and deformation localizes and, eventually, faulting occurs. Faulting, in turn, may favor enhanced fluid flow and further hydration of the lithosphere, potentially stabilizing the fault zone.

suggesting that not all detachment faults seem to record this stage of high fluid flux under low-grade metamorphic conditions (*cf.* Bach et al., 2011).

As demonstrated here, secondary mineral assemblages formed during the reaction with seawater-derived fluids strongly depend on the presence (and nature) of melt impregnations. Gabbro-impregnated hybrid rocks likely hydrate to weak amphibole- and phyllosilicate-rich assemblages more readily and at higher temperatures than either pure endmember. This facilitates strain localization deeper in the crust than settings where pure peridotite or gabbro prevail. Fluid infiltration into localized deformation zones (*cf.* Grevemeyer et al., 2013; Jöns et al., 2009) may create a feedback loop that facilitates further hydration and strain localization (Fig. 2.11). Such a positive feedback loop may play a general role in the initiation and evolution of detachment faults at slow-spreading ridges. Given the ubiquitous presence of hybrid mafic–ultramafic fault rocks at oceanic core complexes, we propose that melt impregnation of peridotite may be a primary mechanism for oceanic detachment fault strain localization. A similar metamorphic weakening effect is caused by the impregnation with more evolved melts, as demonstrated by Jöns et al. (2009). These authors showed that strain was localized into chlorite–amphibole-assemblages that developed from hydrothermal alteration of plagiogranite veins and their host peridotite. Shearing preferentially occurred in these zones.

2.6 Summary and conclusions

Our samples from an exposed detachment fault south of the 15°20' N Fracture Zone, MAR, provide new evidence for the impregnation of peridotites with more silicic melts and the role of such, now hybrid, lithologies for the destabilization of the lithosphere. Whole-rock geochemistry indicates the impregnating melts to be of gabbroic compositions, even though metasomatism may have added or removed fluid-mobile elements, e. g., Ca and/or Si. Both, host peridotite and impregnations are now mostly metamorphosed due to hydrothermal alteration that set in at temperatures of ~500 to 600 °C. Secondary mineral assemblages in the vicinity of magmatic impregnations are rich in amphibole and chlorite and show frequent but variable deformation fabric intensities, ranging from a weak alignment of crystals to mylonitic textures with the common formation of neoblasts. Pure peridotite by contrast generally displays static serpentinization textures. These differences strongly suggest strain localization and deformation in areas where strength contrasts were induced by the alteration of hybrid lithologies by seawater. This metamorphic weakening occurred at temperatures above the main serpentine stability field, i. e., above ~400 °C, and hence deeper in the crust compared to where common serpentinization-related weakening occurs.

Based on these data and on reports on deformed hybrid lithologies from oceanic detachment faults worldwide, we propose that detachment fault stabilization is facilitated at deeper lithospheric depth when melt intrusions are present and seawater circulates deeply through the crust, causing its hydration. Much of the strain at slow-spreading ridges may hence localize in such weak zones, eventually causing active faulting. Secondary mineral assemblages formed during reaction with seawater are strongly dependent on the presence and composition of magmas intruded into the peridotites and are further a function of temperature, pressure, water/rock ratio, and local variations in bulk composition that result from different degrees of mixing between host peridotite and impregnating melt. Since faults in extensional settings commonly act as fluid conduits, they potentially enhance further hydration of the lithosphere that leads to further phyllosilicate formation and possibly to a long-term localization of strain along the shear zone.

We conclude that the processes described here, triggered by the interaction of magmatic activity and hydrothermal alteration at depth, may play a general role in the stabilization and evolution of detachment faults at slow-spreading ridges.

Acknowledgements

We are grateful to the captain and crew of *JOIDES Resolution* and the members of the Science Party. We thank Walter Hale for assistance during sampling, Bastian Bieseler and Bernhard Schnetger for help with whole-rock analyses, and Stefan Sopke, Andreas Klügel, and Patrick Monien for help with EPMA and LA-ICP-MS. Reviews by Matthew Loocke and two additional anonymous reviewers helped to improve the quality of this paper. E. A. received financial support from GLOMAR – Bremen International Graduate School for

Marine Sciences. W. B. acknowledges funding by the Deutsche Forschungsgemeinschaft (German Research Foundation), project number BA 1605/13. This research project was further supported by the Hanse-Wissenschaftskolleg Institute for Advanced Study. Data presented in this contribution are available in the main text, in the Supplementary Information, or at PANGAEA (doi:[10.1594/PANGAEA.895069](https://doi.org/10.1594/PANGAEA.895069)).

References

- Allison, I., La Tour, T. E., 1977. Brittle deformation of hornblende in a mylonite: a direct geometrical analogue of ductile deformation by translation gliding. *Can. J. Earth Sci.* 14 (8), 1953–1958, doi:[10.1139/e77-166](https://doi.org/10.1139/e77-166).
- Bach, W., Garrido, C. J., Paulick, H., Harvey, J., Rosner, M., 2004. Seawater–peridotite interactions: first insights from ODP Leg 209, MAR 15° N. *Geochem. Geophys. Geosyst.* 5 (9), Q09F26, doi:[10.1029/2004gc000744](https://doi.org/10.1029/2004gc000744).
- Bach, W., Klein, F., 2009. The petrology of seafloor rodingites: insights from geochemical reaction path modeling. *Lithos* 112 (1–2), 103–117, doi:[10.1016/j.lithos.2008.10.022](https://doi.org/10.1016/j.lithos.2008.10.022).
- Bach, W., Paulick, H., Garrido, C. J., Ildefonse, B., Meurer, W. P., Humphris, S. E., 2006. Unraveling the sequence of serpentinization reactions: petrography, mineral chemistry, and petrophysics of serpentinites from MAR 15° N (ODP Leg 209, Site 1274). *Geophys. Res. Lett.* 33 (13), L13306, doi:[10.1029/2006gl025681](https://doi.org/10.1029/2006gl025681).
- Bach, W., Rosner, M., Jöns, N., Rausch, S., Robinson, L. F., Paulick, H., Erzinger, J., 2011. Carbonate veins trace seawater circulation during exhumation and uplift of mantle rock: results from ODP Leg 209. *Earth Planet. Sci. Lett.* 311 (3–4), 242–252, doi:[10.1016/j.epsl.2011.09.021](https://doi.org/10.1016/j.epsl.2011.09.021).
- Blackman, D. K., Cann, J. R., Janssen, B., Smith, D. K., 1998. Origin of extensional core complexes: evidence from the Mid-Atlantic Ridge at Atlantis Fracture Zone. *J. Geophys. Res.* 103 (B9), 21315–21333, doi:[10.1029/98JB01756](https://doi.org/10.1029/98JB01756).
- Blackman, D. K., Ildefonse, B., John, B. E., Ohara, Y., Miller, D. J., Abe, N., Abratis, M., Andal, E. S., Andreani, M., Awaji, S., Beard, J. S., Brunelli, D., Charney, A. B., Christie, D. M., Collins, J., Delacour, A. G., Delius, H., Drouin, M., Einaudi, F., Escartín, J., Frost, B. R., Früh-Green, G., Fryer, P. B., Gee, J. S., Godard, M., Grimes, C. B., Halfpenny, A., Hansen, H.-E., Harris, A. C., Tamura, A., Hayman, N. W., Hellebrand, E., Hirose, T., Hirth, J. G., Ishimaru, S., Johnson, K. T. M., Karner, G. D., Linek, M., MacLeod, C. J., Maeda, J., Mason, O. U., McCaig, A. M., Michibayashi, K., Morris, A., Nakagawa, T., Nozaka, T., Rosner, M., Searle, R. C., Suhr, G., Tominaga, M., von der Handt, A., Yamasaki, T., Zhao, X., 2011. Drilling constraints on lithospheric accretion and evolution at Atlantis Massif, Mid-Atlantic Ridge 30° N. *J. Geophys. Res.* 116 (B7), doi:[10.1029/2010jb007931](https://doi.org/10.1029/2010jb007931).
- Bogdanov, Y. A., Bortnikov, N. S., Vikent'ev, I. V., Gurchich, E. G., Sagalevich, A. M., 1997. A new type of modern mineral-forming system: black smokers of the hydrothermal field at 14°45' N latitude, Mid-Atlantic Ridge. *Geol. Ore Deposits* 39, 58–78.
- Boschi, C., Früh-Green, G. L., Delacour, A., Karson, J. A., Kelley, D. S., 2006a. Mass transfer and fluid flow during detachment faulting and development of an oceanic core complex, Atlantis Massif (MAR 30° N). *Geochem. Geophys. Geosyst.* 7 (1), Q01004, doi:[10.1029/2005gc001074](https://doi.org/10.1029/2005gc001074).
- Boschi, C., Früh-Green, G. L., Escartín, J., 2006b. Occurrence and significance of serpentinite-hosted, talc- and amphibole-rich fault rocks in modern oceanic settings and ophiolite complexes: an overview. *Ofioliti* 31 (2), 129–140.
- Brodie, K. H., Rutter, E. H., 1985. On the relationship between deformation and metamorphism, with special reference to the behavior of basic rocks. In: Thompson, A. B., Rubie, D. C. (Eds.), *Metamorphic reactions. Advances in physical geochemistry*. Springer, New York (NY), pp. 138–179. doi:[10.1007/978-1-4612-5066-1_6](https://doi.org/10.1007/978-1-4612-5066-1_6).
- Cann, J. R., Blackman, D. K., Smith, D. K., McAllister, E., Janssen, B., Mello, S., Avgerinos, E., Pascoe,

- A. R., Escartín, J., 1997. Corrugated slip surfaces formed at ridge–transform intersections on the Mid-Atlantic Ridge. *Nature* 385, 329–332, doi:[10.1038/385329a0](https://doi.org/10.1038/385329a0).
- Cannat, M., 1991. Plastic deformation at an oceanic spreading ridge: a microstructural study of the Site 735 gabbros (Southwest Indian Ocean). In: von Herzen, R., Robinson, P. T., et al. (Eds.), *Proceedings of the Ocean Drilling Program. Vol. 118 of Scientific Results. Ocean Drilling Program*, pp. 399–408. doi:[10.2973/odp.proc.sr.118.134.1991](https://doi.org/10.2973/odp.proc.sr.118.134.1991).
- Cannat, M., Lagabrielle, Y., Bougault, H., Casey, J., de Coutures, N., Dmitriev, L., Fouquet, Y., 1997. Ultramafic and gabbroic exposures at the Mid-Atlantic Ridge: geological mapping in the 15°N region. *Tectonophysics* 279, 193–213, doi:[10.1016/S0040-1951\(97\)00113-3](https://doi.org/10.1016/S0040-1951(97)00113-3).
- Cannat, M., Sauter, D., Escartín, J., Lavier, L., Picazo, S., 2009. Oceanic corrugated surfaces and the strength of the axial lithosphere at slow spreading ridges. *Earth Planet. Sci. Lett.* 288 (1–2), 174–183, doi:[10.1016/j.epsl.2009.09.020](https://doi.org/10.1016/j.epsl.2009.09.020).
- Cao, S., Liu, J., Leiss, B., 2010. Orientation-related deformation mechanisms of naturally deformed amphibole in amphibolite mylonites from the Diancang Shan, SW Yunnan, China. *J. Struct. Geol.* 32 (5), 606–622, doi:[10.1016/j.jsg.2010.03.012](https://doi.org/10.1016/j.jsg.2010.03.012).
- Charlou, J. L., Bougault, H., Appriou, P., Nelsen, T., Rona, P., 1991. Different TDM/CH₄ hydrothermal plume signatures: TAG site at 26°N and serpentinized ultrabasic diapir at 15°05'N on the Mid-Atlantic Ridge. *Geochim. Cosmochim. Acta* 55 (11), 3209–3222, doi:[10.1016/0016-7037\(91\)90484-m](https://doi.org/10.1016/0016-7037(91)90484-m).
- Charlou, J. L., Fouquet, Y., Bougault, H., Donval, J. P., Etoubleau, J., Jean-Baptiste, P., Dapoigny, A., Appriou, P., Rona, P. A., 1998. Intense CH₄ plumes generated by serpentinization of ultramafic rocks at the intersection of the 15°20'N Fracture Zone and the Mid-Atlantic Ridge. *Geochim. Cosmochim. Acta* 62 (13), 2323–2333, doi:[10.1016/s0016-7037\(98\)00138-0](https://doi.org/10.1016/s0016-7037(98)00138-0).
- Coogan, L. A., 2014. The lower oceanic crust. In: Holland, H., Turekian, K. (Eds.), *Treatise on geochemistry*, 2nd Edition. Vol. 4. Elsevier Ltd., Amsterdam, Ch. 4.14, pp. 497–541. doi:[10.1016/B978-0-08-095975-7.00316-8](https://doi.org/10.1016/B978-0-08-095975-7.00316-8).
- de Capitani, C., Petrakakis, K., 2010. The computation of equilibrium assemblage diagrams with Theriak/Domino software. *Am. Mineral.* 95 (7), 1006–1016, doi:[10.2138/am.2010.3354](https://doi.org/10.2138/am.2010.3354).
- deMartin, B. J., Sohn, R. A., Canales, J. P., Humphris, S. E., 2007. Kinematics and geometry of active detachment faulting beneath the Trans-Atlantic Geotraverse (TAG) hydrothermal field on the Mid-Atlantic Ridge. *Geology* 35 (8), 711–714, doi:[10.1130/g23718a.1](https://doi.org/10.1130/g23718a.1).
- Dick, H. J. B., Meyer, P. S., Bloomer, S., Kirby, S., Stakes, D., Mawer, C., 1991. Lithostratigraphic evolution of an *in-situ* section of oceanic layer 3. In: Von Herzen, T., Robinson, P. T., et al. (Eds.), *Scientific Results. Ocean Drilling Program*, pp. 439–538. doi:[10.2973/odp.proc.sr.118.128.1991](https://doi.org/10.2973/odp.proc.sr.118.128.1991).
- Dick, H. J. B., Tivey, M. A., Tucholke, B. E., 2008. Plutonic foundation of a slow-spreading ridge segment: oceanic core complex at KANE Megamullion, 23°30'N, 45°20'W. *Geochem. Geophys. Geosyst.* 9 (5), Q05014, doi:[10.1029/2007GC001645](https://doi.org/10.1029/2007GC001645).
- Dollinger, G., Blacic, J. D., 1975. Deformation mechanisms in experimentally and naturally deformed amphiboles. *Earth Planet. Sci. Lett.* 26 (3), 409–416, doi:[10.1016/0012-821x\(75\)90016-3](https://doi.org/10.1016/0012-821x(75)90016-3).
- D'Orazio, M., Boschi, C., Brunelli, D., 2004. Talc-rich hydrothermal rocks from the St. Paul and Conrad Fracture Zones in the Atlantic Ocean. *Eur. J. Mineral.* 16, 73–83, doi:[10.1127/0935-1221/2004/0016-0073](https://doi.org/10.1127/0935-1221/2004/0016-0073).
- Eckert, S., Brumsack, H.-J., Severmann, S., Schnetger, B., März, C., Fröllje, H., 2013. Establishment of euxinic conditions in the Holocene Black Sea. *Geology* 41 (4), 431–434, doi:[10.1130/g33826.1](https://doi.org/10.1130/g33826.1).
- Escartín, J., Andreani, M., Hirth, G., Evans, B., 2008. Relationships between the microstructural evolution and the rheology of talc at elevated pressures and temperatures. *Earth Planet. Sci. Lett.* 268 (3–4), 463–475, doi:[10.1016/j.epsl.2008.02.004](https://doi.org/10.1016/j.epsl.2008.02.004).
- Escartín, J., Hirth, G., Evans, B., 1997. Nondilatant brittle deformation of serpentinites: implications for Mohr–Coulomb theory and the strength of faults. *J. Geophys. Res.* 102 (B2), 2897–2913, doi:[10.1029/96jb02792](https://doi.org/10.1029/96jb02792).
- Escartín, J., Mével, C., MacLeod, C. J., McCaig, A. M., 2003. Constraints on deformation conditions and the origin of oceanic detachments: the Mid-Atlantic Ridge core complex at 15°45'N. *Geochem. Geophys. Geosyst.* 4 (8), 1067, doi:[10.1029/2002gc000472](https://doi.org/10.1029/2002gc000472).

- Escartín, J., Smith, D. K., Cann, J., Schouten, H., Langmuir, C. H., Escrig, S., 2008. Central role of detachment faults in accretion of slow-spreading oceanic lithosphere. *Nature* 455 (7214), 790–794, doi:[10.1038/nature07333](https://doi.org/10.1038/nature07333).
- Ferriss, E. D. A., Essene, E. J., Becker, U., 2008. Computational study of the effect of pressure on the Ti-in-zircon geothermometer. *Eur. J. Mineral.* 20, 745–755, doi:[10.1127/0935-1221/2008/0020-1860](https://doi.org/10.1127/0935-1221/2008/0020-1860).
- Ferry, J. M., Watson, E. B., 2007. New thermodynamic models and revised calibrations for the Ti-in-zircon and Zr-in-rutile thermometers. *Contrib. Mineral. Petrol.* 154 (4), 429–437, doi:[10.1007/s00410-007-0201-0](https://doi.org/10.1007/s00410-007-0201-0).
- Fletcher, J. M., Stephens, C. J., Petersen, E. U., Skerl, L., 1997. Greenschist facies hydrothermal alteration of oceanic gabbros: a case study of element mobility and reaction paths. In: Karson, J. A., Cannat, M., Miller, D. J., Elthon, D. (Eds.), *Sci. Res. Vol. 153 of Proc. ODP. Ocean Drilling Program, College Station (TX)*, pp. 389–398. doi:[10.2973/odp.proc.sr.153.036.1997](https://doi.org/10.2973/odp.proc.sr.153.036.1997).
- Floyd, J. S., Mutter, J. C., Goodliffe, A. M., Taylor, B., 2001. Evidence for fault weakness and fluid flow within an active low-angle normal fault. *Nature* 411, 779–783, doi:[10.1038/35081040](https://doi.org/10.1038/35081040).
- Frost, R., 1975. Contact metamorphism of serpentinite, chloritic blackwall and rodingite at Paddy-Go-Easy Pass, Central Cascades, Washington. *J. Petrol.* 16 (2), doi:[10.1093/petrology/16.1.272](https://doi.org/10.1093/petrology/16.1.272).
- Früh-Green, G. L., Connolly, A. D., Plas, A., Kelley, D. S., Grobéty, B., 2004. Serpentinization of oceanic peridotites: implications for geochemical cycles and biological activity. *Geoph. Monog. Series 144*, 119–136, doi:[10.1029/144gm08](https://doi.org/10.1029/144gm08).
- Früh-Green, G. L., Orcutt, B. N., Green, S. L., Cotterill, C., the Expedition 357 Scientists (Eds.), 2017. Atlantis Massif serpentinization and life. Vol. 357 of *Proc. IODP. International Ocean Discovery Program, College Station (TX)*.
- Fu, B., Page, F. Z., Cavosie, A. J., Fournelle, J., Kita, N. T., Lackey, J. S., Wilde, S. A., Valley, J. W., 2008. Ti-in-zircon thermometry: applications and limitations. *Contrib. Mineral. Petrol.* 156 (2), 197–215, doi:[10.1007/s00410-008-0281-5](https://doi.org/10.1007/s00410-008-0281-5).
- Fujiwara, T., Lin, J., Matsumoto, T., Kelemen, P. B., Tucholke, B. E., Casey, J. F., 2003. Crustal evolution of the Mid-Atlantic Ridge near the Fifteen-Twenty Fracture Zone in the last 5 Ma. *Geochem. Geophys. Geosyst.* 4 (3), 1024, doi:[10.1029/2002gc000364](https://doi.org/10.1029/2002gc000364).
- Garcés, M., Gee, J. S., 2007. Paleomagnetic evidence of large footwall rotations associated with low-angle faults at the Mid-Atlantic Ridge. *Geology* 35 (3), 279–282, doi:[10.1130/g23165a.1](https://doi.org/10.1130/g23165a.1).
- Godard, M., Awaji, S., Hansen, H., Hellebrand, E., Brunelli, D., Johnson, K., Yamasaki, T., Maeda, J., Abratis, M., Christie, D., Kato, Y., Mariet, C., Rosner, M., 2009. Geochemistry of a long in-situ section of intrusive slow-spread oceanic lithosphere: results from IODP Site U1309 (Atlantis Massif, 30° N Mid-Atlantic-Ridge). *Earth Planet. Sci. Lett.* 279 (1–2), 110–122, doi:[10.1016/j.epsl.2008.12.034](https://doi.org/10.1016/j.epsl.2008.12.034).
- Golden, C. E., Webb, S. C., Sohn, R. A., 2003. Hydrothermal microearthquake swarms beneath active vents at Middle Valley, northern Juan de Fuca Ridge. *J. Geophys. Res.* 108 (B1), 2027, doi:[10.1029/2001jb000226](https://doi.org/10.1029/2001jb000226).
- Grevemeyer, I., Reston, T. J., Moeller, S., 2013. Microseismicity of the Mid-Atlantic Ridge at 7° S–8° 15' S and at the Logatchev Massif oceanic core complex at 14° 40' N–14° 50' N. *Geochem. Geophys. Geosyst.* 14 (9), 3532–3554, doi:[10.1002/ggge.20197](https://doi.org/10.1002/ggge.20197).
- Harigane, Y., Michibayashi, K., Ohara, Y., 2008. Shearing within lower crust during progressive retrogression: structural analysis of gabbroic rocks from the Godzilla Mullion, an oceanic core complex in the Parece Vela backarc basin. *Tectonophysics* 457 (3), 183–196, doi:[10.1016/j.tecto.2008.06.009](https://doi.org/10.1016/j.tecto.2008.06.009).
- Harigane, Y., Michibayashi, K., Ohara, Y., 2011. Deformation and hydrothermal metamorphism of gabbroic rocks within the Godzilla Megamullion, Parece Vela Basin, Philippine Sea. *Lithos* 124 (3), 185–199, doi:[10.1016/j.lithos.2011.02.001](https://doi.org/10.1016/j.lithos.2011.02.001).
- Hayden, L. A., Watson, E. B., Wark, D. A., 2008. A thermobarometer for sphene (titanite). *Contrib. Mineral. Petrol.* 155 (4), 529–540, doi:[10.1007/s00410-007-0256-y](https://doi.org/10.1007/s00410-007-0256-y).
- Holland, T. J. B., Powell, R., 1998. An internally consistent thermodynamic data set for phases of petrological interest. *J. Metamorph. Geol.* 16 (3), 309–343, doi:[10.1111/j.1525-1314.1998.00140.x](https://doi.org/10.1111/j.1525-1314.1998.00140.x).
- Homburg, J. M., Hirth, G., Kelemen, P. B., 2010. Investigation of the strength contrast at the Moho: a case study from the Oman ophiolite. *Geology* 38 (8), 679–682, doi:[10.1130/g30880.1](https://doi.org/10.1130/g30880.1).

- Ikari, M. J., Saffer, D. M., Marone, C., 2009. Frictional and hydrologic properties of a major splay fault system, Nankai subduction zone. *Geophys. Res. Lett.* 36 (20), L20313, doi:[10.1029/2009gl040009](https://doi.org/10.1029/2009gl040009).
- Ildefonse, B., Blackman, D. K., John, B. E., Ohara, Y., Miller, D. J., MacLeod, C. J., 2007. Oceanic core complexes and crustal accretion at slow-spreading ridges. *Geology* 35 (7), 623–626, doi:[10.1130/g23531a.1](https://doi.org/10.1130/g23531a.1).
- Imai, N., Terashima, S., Itoh, S., Ando, A., 1995. 1994 compilation values for GSJ reference samples, "Igneous rock series". *Geochem. J.* 29 (1), 91–95, doi:[10.2343/geochemj.29.91](https://doi.org/10.2343/geochemj.29.91).
- Jochum, K. P., Weis, U., Stoll, B., Kuzmin, D., Yang, Q., Raczek, I., Jacob, D. E., Stracke, A., Birbaum, K., Frick, D. A., Günther, D., Enzweiler, J., 2011. Determination of reference values for NIST SRM 610–617 glasses following ISO guidelines. *Geostand. Geoanal. Res.* 35 (4), 397–429, doi:[10.1111/j.1751-908x.2011.00120.x](https://doi.org/10.1111/j.1751-908x.2011.00120.x).
- Johnson, J. W., Oelkers, E. H., Helgeson, H. C., 1992. SUPCRT92: a software package for calculating the standard molal thermodynamic properties of minerals, gases, aqueous species, and reactions from 1 to 5000 bar and 0 to 1000 °C. *Comput. Geosci.* 18 (7), 899–947, doi:[10.1016/0098-3004\(92\)90029-q](https://doi.org/10.1016/0098-3004(92)90029-q).
- Jöns, N., Bach, W., Klein, F., 2010. Magmatic influence on reaction paths and element transport during serpentinization. *Chem. Geol.* 274 (3–4), 196–211, doi:[10.1016/j.chemgeo.2010.04.009](https://doi.org/10.1016/j.chemgeo.2010.04.009).
- Jöns, N., Bach, W., Schroeder, T., 2009. Formation and alteration of plagiogranites in an ultramafic-hosted detachment fault at the Mid-Atlantic Ridge (ODP Leg 209). *Contrib. Mineral. Petrol.* 157 (5), 625–639, doi:[10.1007/s00410-008-0357-2](https://doi.org/10.1007/s00410-008-0357-2).
- Kelemen, P., Kikawa, E., Miller, D. J., the Leg 209 Scientific Party, 2004. ODP Leg 209 drills into mantle peridotite along the Mid-Atlantic Ridge from 14° N to 16° N. *JOIDES Journal* 30 (1), 14–19.
- Kelemen, P. B., Kikawa, E., Miller, D. (Eds.), 2007. Scientific Results. Vol. 209 of Proc. ODP. Ocean Drilling Program, College Station (TX).
- Klein, F., Bach, W., Jöns, N., McCollom, T., Moskowicz, B., Berquó, T. S., 2009. Iron partitioning and hydrogen generation during serpentinization of abyssal peridotites from 15° N on the Mid-Atlantic Ridge. *Geochim. Cosmochim. Acta* 73 (22), 6868–6893, doi:[10.1016/j.gca.2009.08.021](https://doi.org/10.1016/j.gca.2009.08.021).
- Lagabriele, Y., Bideau, D., Cannat, M., Karson, J. A., Mével, C., 1998. Ultramafic-mafic plutonic rock suites exposed along the Mid-Atlantic Ridge (10° N–30° N): symmetrical-asymmetrical distribution and implications for seafloor spreading processes. *Geoph. Monog. Series* 106, 153–176, doi:[10.1029/gm106p0153](https://doi.org/10.1029/gm106p0153).
- Leake, B. E., Woolley, A. R., Arps, C. E. S., Birch, W. D., Gilbert, M. C., Grice, J. D., Hawthorne, F. C., Kato, A., Kisch, H. J., Krivovichev, V. G., Linthout, K., Laird, J., Mandarino, J. A., Maresch, W. V., Nickel, E. H., Rock, N. M. S., Schumacher, J. C., Smith, D. C., Stephenson, N. C. N., Ungaretti, L., Whittaker, J. W., Youzhi, G., 1997. Nomenclature of amphiboles: report of the Subcommittee on Amphiboles of the International Mineralogical Association, Commission on New Minerals and Mineral Names. *Mineral. Mag.* 35, 1019–1037.
- Loocke, M., Snow, J. E., Ohara, Y., 2013. Melt stagnation in peridotites from the Godzilla Megamullion oceanic core complex, Parece Vela Basin, Philippine Sea. *Lithos* 182–183, 1–10, doi:[10.1016/j.lithos.2013.09.005](https://doi.org/10.1016/j.lithos.2013.09.005).
- MacLeod, C. J., Escartín, J., Banerji, D., Banks, G. J., Gleeson, M., Irving, D. H. B., Lilly, R. M., McCaig, A. M., Niu, Y., Allerton, S., Smith, D. K., 2002. Direct geological evidence for oceanic detachment faulting: the Mid-Atlantic Ridge, 15°45' N. *Geology* 30 (10), 879–882, doi:[10.1130/0091-7613\(2002\)030<0879:dgefod>2.0.co;2](https://doi.org/10.1130/0091-7613(2002)030<0879:dgefod>2.0.co;2).
- MacLeod, C. J., Searle, R. C., Murton, B. J., Casey, J. F., Mallows, C., Unsworth, S. C., Schenbach, K. L., Harris, M., 2009. Life cycle of oceanic core complexes. *Earth Planet. Sci. Lett.* 287 (3–4), 333–344, doi:[10.1016/j.epsl.2009.08.016](https://doi.org/10.1016/j.epsl.2009.08.016).
- McCaig, A. M., Cliff, R. A., Escartín, J., Fallick, A. E., MacLeod, C. J., 2007. Oceanic detachment faults focus very large volumes of black smoker fluids. *Geology* 35 (10), 935–938, doi:[10.1130/g23657a.1](https://doi.org/10.1130/g23657a.1).
- McCaig, A. M., Delacour, A., Fallick, A. E., Castelain, T., Früh-Green, G. L., 2010. Detachment fault control on hydrothermal circulation systems: interpreting the subsurface beneath the TAG hydrothermal field using the isotopic and geological evolution of oceanic core complexes in the Atlantic. *Geoph. Monog. Series* 188, 207–239, doi:[10.1029/2008gm000729](https://doi.org/10.1029/2008gm000729).

- McCollom, T. M., Bach, W., 2009. Thermodynamic constraints on hydrogen generation during serpentinization of ultramafic rocks. *Geochim. Cosmochim. Acta* 73 (3), 856–875, doi:[10.1016/j.gca.2008.10.032](https://doi.org/10.1016/j.gca.2008.10.032).
- McDonough, W. F., Sun, S., 1995. The composition of the Earth. *Chem. Geol.* 120 (3–4), 223–253, doi:[10.1016/0009-2541\(94\)00140-4](https://doi.org/10.1016/0009-2541(94)00140-4).
- Mével, C., 2003. Serpentinization of abyssal peridotites at mid-ocean ridges. *C. R. Geosci.* 335 (10–11), 825–852, doi:[10.1016/j.crte.2003.08.006](https://doi.org/10.1016/j.crte.2003.08.006).
- Miranda, E. A., John, B. E., 2010. Strain localization along the Atlantis Bank oceanic detachment fault system, Southwest Indian Ridge. *Geochem. Geophys. Geosyst.* 11 (4), Q04002, doi:[10.1029/2009gc002646](https://doi.org/10.1029/2009gc002646).
- Moore, D. E., Lockner, D. A., 2008. Talc friction in the temperature range 25 °–400 °C: relevance for fault-zone weakening. *Tectonophysics* 449 (1), 120–132, doi:[10.1016/j.tecto.2007.11.039](https://doi.org/10.1016/j.tecto.2007.11.039).
- Morishita, T., Hara, K., Nakamura, K., Sawaguchi, T., Tamura, A., Arai, S., Okino, K., Takai, K., Kumagai, H., 2009. Igneous, alteration and exhumation processes recorded in abyssal peridotites and related fault rocks from an oceanic core complex along the Central Indian Ridge. *J. Petrol.* 50 (7), 1299–1325, doi:[10.1093/petrology/egp025](https://doi.org/10.1093/petrology/egp025).
- Niemeijer, A., Marone, C., Elsworth, D., 2010. Fabric induced weakness of tectonic faults. *Geophys. Res. Lett.* 37 (3), L03304, doi:[10.1029/2009gl041689](https://doi.org/10.1029/2009gl041689).
- Nozaka, T., Fryer, P. B., 2011. Alteration of the oceanic lower crust at a slow-spreading axis: insight from vein-related zoned halos in olivine gabbro from Atlantis Massif, Mid-Atlantic Ridge. *J. Petrol.* 52 (4), 643–664, doi:[10.1093/petrology/egq098](https://doi.org/10.1093/petrology/egq098).
- Olive, J.-A., Behn, M. D., Tucholke, B. E., 2010. The structure of oceanic core complexes controlled by the depth distribution of magma emplacement. *Nat. Geosci.* 3 (7), 491–495, doi:[10.1038/ngeo888](https://doi.org/10.1038/ngeo888).
- Otten, M. T., 1984. The origin of brown hornblende in the Artfjället gabbro and dolerites. *Contrib. Mineral. Petrol.* 86, 189–199, doi:[10.1007/BF00381846](https://doi.org/10.1007/BF00381846).
- Paulick, H., Bach, W., Godard, M., de Hoog, J. C. M., Suhr, G., Harvey, J., 2006. Geochemistry of abyssal peridotites (Mid-Atlantic Ridge, 15°20' N, ODP Leg 209): implications for fluid/rock interaction in slow spreading environments. *Chem. Geol.* 234, 179–210, doi:[10.1016/j.chemgeo.2006.04.011](https://doi.org/10.1016/j.chemgeo.2006.04.011).
- Picazo, S., Cannat, M., Delacour, A., Escartín, J., Rouméjon, S., Silantyev, S., 2012. Deformation associated with the denudation of mantle-derived rocks at the Mid-Atlantic Ridge 13°–15° N: the role of magmatic injections and hydrothermal alteration. *Geochem. Geophys. Geosyst.* 13 (9), 3306–3313, doi:[10.1029/2012gc004121](https://doi.org/10.1029/2012gc004121).
- Schroeder, T., Cheadle, M. J., Dick, H. J. B., Faul, U., Casey, J. F., Kelemen, P. B., 2007. Nonvolcanic seafloor spreading and corner-flow rotation accommodated by extensional faulting at 15° N on the Mid-Atlantic Ridge: a structural synthesis of ODP Leg 209. *Geochem. Geophys. Geosyst.* 8 (6), Q06015, doi:[10.1029/2006gc001567](https://doi.org/10.1029/2006gc001567).
- Schroeder, T., John, B. E., 2004. Strain localization on an oceanic detachment fault system, Atlantis Massif, 30° N, Mid-Atlantic Ridge. *Geochem. Geophys. Geosyst.* 5 (11), Q11007, doi:[10.1029/2004gc000728](https://doi.org/10.1029/2004gc000728).
- Shipboard Scientific Party (Ed.), 2003. Preliminary Report: drilling mantle peridotite along the Mid-Atlantic Ridge from 14° to 16° N. Vol. 209 of Proc. ODP. Ocean Drilling Program, College Station (TX).
- Shipboard Scientific Party, 2004a. Explanatory notes. In: Kelemen, P. B., Kikawa, E., Miller, D. J. (Eds.), *Init. Rep. Vol. 209 of Proc. ODP. Ocean Drilling Program, College Station (TX)*, pp. 1–75. doi:[10.2973/odp.proc.ir.209.102.2004](https://doi.org/10.2973/odp.proc.ir.209.102.2004).
- Shipboard Scientific Party, 2004b. Site 1271. In: Kelemen, P. B., Kikawa, E., Miller, D. J. (Eds.), *Initial Reports. Vol. 209 of Proc. ODP. Integrated Ocean Drilling Program, College Station (TX)*. doi:[10.2973/odp.proc.ir.209.110.2004](https://doi.org/10.2973/odp.proc.ir.209.110.2004).
- Shulaker, D. Z., Schmitt, A. K., Zack, T., Bindeman, I., 2015. In-situ oxygen isotope and trace element geothermometry of rutilated quartz from Alpine fissures. *Am. Mineral.* 100 (4), 915–925, doi:[10.2138/am-2015-4961](https://doi.org/10.2138/am-2015-4961).
- Smith, D. K., Cann, J. R., Escartín, J., 2006. Widespread active detachment faulting and core complex formation near 13° N on the Mid-Atlantic Ridge. *Nature* 442 (7101), 440–443, doi:[10.1038/nature04950](https://doi.org/10.1038/nature04950).
- Smith, D. K., Escartín, J., Schouten, H., Cann, J. R., 2008. Fault rotation and core complex formation:

- significant processes in seafloor formation at slow-spreading mid-ocean ridges (Mid-Atlantic Ridge, 13°–15° N). *Geochem. Geophys. Geosyst.* 9 (3), Q03003, doi:[10.1029/2007gc001699](https://doi.org/10.1029/2007gc001699).
- Tailby, N. D., Walker, A. M., Berry, A. J., Hermann, J., Evans, K. A., Mavrogenes, J. A., O'Neill, H. S. C., Rodina, I. S., Soldatov, A. V., Rubatto, D., Sutton, S. R., 2011. Ti site occupancy in zircon. *Geochim. Cosmochim. Acta* 75 (3), 905–921, doi:[10.1016/j.gca.2010.11.004](https://doi.org/10.1016/j.gca.2010.11.004).
- Tivey, M. K., 2007. Generation of seafloor hydrothermal vent fluids and associated mineral deposits. *Oceanography* 20 (1), 50–65, doi:[10.5670/oceanog.2007.80](https://doi.org/10.5670/oceanog.2007.80).
- Tomkins, H. S., Powell, R., Ellis, D. J., 2007. The pressure dependence of the zirconium-in-rutile thermometer. *J. Metamorph. Geol.* 25 (6), 703–713, doi:[10.1111/j.1525-1314.2007.00724.x](https://doi.org/10.1111/j.1525-1314.2007.00724.x).
- Tucholke, B. E., Behn, M. D., Buck, W. R., Lin, J., 2008. Role of melt supply in oceanic detachment faulting and formation of megamullions. *Geology* 36 (6), 455–458, doi:[10.1130/g24639a.1](https://doi.org/10.1130/g24639a.1).
- Tucholke, B. E., Fujioka, K., Ishihara, T., Hirth, G., Kinoshita, M., 2001. Submersible study of an oceanic megamullion in the central North Atlantic. *J. Geophys. Res.* 106 (B8), 16145–16161, doi:[10.1029/2001jb000373](https://doi.org/10.1029/2001jb000373).
- Tucholke, B. E., Humphris, S. E., Dick, H. J. B., 2013. Cemented mounds and hydrothermal sediments on the detachment surface at Kane Megamullion: a new manifestation of hydrothermal venting. *Geochem. Geophys. Geosyst.* 14 (9), 3352–3378, doi:[10.1002/ggge.20186](https://doi.org/10.1002/ggge.20186).
- Tucholke, B. E., Lin, J., Kleinrock, M. C., 1998. Megamullions and mullion structure defining oceanic metamorphic core complexes on the Mid-Atlantic Ridge. *J. Geophys. Res.* 103 (B5), 9857–9866, doi:[10.1029/98jb00167](https://doi.org/10.1029/98jb00167).
- Watson, E. B., Wark, D. A., Thomas, J. B., 2006. Crystallization thermometers for zircon and rutile. *Contrib. Mineral. Petrol.* 151 (4), 413–433, doi:[10.1007/s00410-006-0068-5](https://doi.org/10.1007/s00410-006-0068-5).
- Weill, D. F., Drake, M. J., 1973. Europium anomaly in plagioclase feldspar: experimental results and semiquantitative model. *Science* 180, 1059–1060, doi:[10.1126/science.180.4090.1059](https://doi.org/10.1126/science.180.4090.1059).
- Wilcock, W. S. D., Archer, S. D., Purdy, G. M., 2002. Microearthquakes on the Endeavour segment of the Juan de Fuca Ridge. *J. Geophys. Res.* 107 (B12), 2027, doi:[10.1029/2001jb000505](https://doi.org/10.1029/2001jb000505).
- Wolery, T. J., Jarek, R. L., 2003. Software user's manual EQ3/6, version 8.0. Sandia National Laboratories, Albuquerque (NM).
- Yi, S.-B., Oh, C.-W., Pak, S. J., Kim, J., Moon, J.-W., 2014. Geochemistry and petrogenesis of mafic-ultramafic rocks from the Central Indian Ridge, latitude 8°–17° S: denudation of mantle harzburgites and gabbroic rocks and compositional variation of basalts. *Int. Geol. Rev.* 56 (14), 1691–1719, doi:[10.1080/00206814.2014.955539](https://doi.org/10.1080/00206814.2014.955539).

3 Clues on carbon cycling

Full title Carbon cycling in the shallow Mariana forearc
Authors Elmar Albers,* Wolfgang Bach,* Frieder Klein,† Catriona D. Menzies,‡§ Friedrich Lucassen*
Affiliations *Department of Geosciences and MARUM – Center for Marine Environmental Sciences, Bremen, Germany; †Department of Marine Chemistry and Geochemistry, Woods Hole Oceanographic Institution, Woods Hole (MA), USA; ‡Ocean and Earth Science, National Oceanography Centre, University of Southampton, UK; §now at Department of Geology and Petroleum Geology, University of Aberdeen, UK
Publication status To be submitted to *Solid Earth*

Abstract

Few data exist that provide insight into processes affecting the long-term carbon cycle at shallow forearc depths. To better understand the mobilization of C in sediments and crust of the subducting slab, we investigated carbonate materials originating from the subduction channel below the Mariana forearc (<20 km slab depth). The calcium carbonates exist in the form of vein precipitates within metavolcanic and metasedimentary clasts. The clasts represent portions of the subducting lithosphere that were altered at up to lower blueschist facies conditions and were subsequently transported to the forearc seafloor by serpentinite mud volcanism. Euhedral aragonite and calcite crystal faces and the lack of deformation within the veins suggest carbonate formation in a strain-free environment, that is, after peak metamorphism affected their hosts. Intergrowth with barite and marked negative Ce anomalies in carbonate attest the precipitation within a generally oxic environment that was not controlled by serpentinization. Carbonate isotopic compositions ($^{87}\text{Sr}/^{86}\text{Sr} = 0.7052$ to 0.7054 , $\delta^{18}\text{O}_{\text{VSMOW}} = 20$ to 24‰) imply precipitation from slab-derived fluids at temperatures within the range of ~ 130 to 300 °C . These temperature estimates are consistent with the presence of blueschist facies phases, such as lawsonite, co-occurring with the carbonates in some veins. Incorporated C is inorganic ($\delta^{13}\text{C}_{\text{VPDB}} = -1$ to $+4\text{‰}$) and likely derived from the decarbonation of carbonaceous sediment and/or oceanic crust. The mineralizations provide evidence for the mobilization of C in the downgoing slab at depths of ~ 14 to 18 km. Our study for the first time shows in detail that a portion of this C is bound in carbonate precipitates in the subduction channel of an active convergent margin. This process may be an important

asset in understanding the deep carbon cycle since it highlights that C is lost from the subducting lithosphere before reaching greater depth.

3.1 Introduction

Subduction of oceanic lithosphere plays a crucial role in geochemical cycling on Earth, as subduction zones are the primary locus of transfers between the exosphere and the mantle. During the progressive subduction of H₂O-rich sediments as well as hydrated and carbonated lithosphere, a continuum of prograde diagenetic and metamorphic reactions in the downgoing slab drive dehydration and devolatilization. The nature and extent of these processes control whether subducted materials are mobilized and transported into the suprasubduction lithosphere/back to the atmosphere or are carried into the deeply convecting mantle.

The greatest portion of C on Earth is stored in the crust and mantle—a profound comprehension of processes in subduction zones is hence crucial to understanding C cycling on Earth (e.g., Sleep and Zahnle, 2001). Geochemical fluxes of C in convergent plate boundary settings have thus gained much attention in the recent past (e.g., Ague and Nicolescu, 2014; Frezzotti et al., 2011; Gorman et al., 2006; Newton and Manning, 2002; Piccoli et al., 2016; Sverjensky et al., 2014; Kerrick and Connolly, 2001; Füre et al., 2010; Dasgupta and Hirschmann, 2010). Yet, despite being subject of many investigations, its fate in subduction zones remains poorly understood. Most recent mass balances on the cycling of subducted C estimate that 0.0001 to 52 Mt, translating to <1 to 80% of the initially subducted 40 to 66 Mt C a⁻¹, are transported back into the convecting mantle (Kelemen and Manning, 2015).

Much insight into the deep C cycle is derived from studying magmatic products of backarc volcanism. It has been shown that C is mobilized below the volcanic arcs and transported into the upper plate's mantle or lithosphere and/or back into the atmosphere in the form of CO₂ (e.g., Blundy et al., 2010; Sleep and Zahnle, 2001; Kerrick and Connolly, 1998). These insights, however, only reflect processes at deep subduction levels, i.e., at depths of 70 km or more, and the amount of CO₂ emitted from arc volcanoes does not balance the amount of C initially being subducted (e.g., Kelemen and Manning, 2015; Dasgupta and Hirschmann, 2010). A significant portion of subducted C must hence either be released from the downgoing slab before reaching these great depths or it is transported to even greater depths (discussed in greater detail by, e.g., Kelemen and Manning, 2015). Geologic processes at both shallower and greater depths remain largely unknown since obtaining natural samples from these portions is not possible with current technology. Insight into the shallow system, however, come from the investigation of ophiolite sequences that commonly include obducted forearc materials (e.g., Piccoli et al., 2016; Schwarzenbach et al., 2018; ?; Frezzotti et al., 2011). The Oman ophiolite, for instance, exhibits extensive outcrops of listvenites, rocks rich in magnesite ± dolomite ± quartz (Falk and Kelemen, 2015). Carbon bound in these rocks is derived from carbonate dissolution of subducted sediments (Falk and Kelemen, 2015); Kelemen and Manning (2015) hence proposed that the transfer of CO₂ to the leading

edge of the mantle wedge, where the listvenites were formed, could depict an important process in forearc regions of convergent margins and that ‘substantial carbon transfer at low temperatures’ occurs here. These observations are in line with experiments that demonstrated the increase in solubility of calcite minerals in aqueous fluids with increasing pressure and temperature (Caciagli and Manning, 2003), suggesting that an efficient release of C from the downgoing slab could occur even at relatively shallow levels.

Fluids that upwell through serpentinite mud volcanoes at the Mariana forearc affirm the suggestion of carbonate breakdown at shallow portions of convergent margins. The chemical compositions of these slab-derived fluids reflect prograde metamorphic processes in the subducting lithosphere (e.g., Mottl et al., 2004; Wheat et al., 2018). The mud volcanoes sample the slab–wedge interface at different depths, and they provide a direct, natural window into the shallow portions of an active subduction system (e.g., Fryer et al., 1985, 1995; Hulme et al., 2010). Fluids upwelling at relatively deep-rooted mud volcanoes exhibit high carbonate alkalinities (CO_3^{2-}) and elevated concentrations of dissolved hydrocarbons (CH_4 and C_2H_6), indicative of decarbonation reactions in the downgoing plate at depths of <30 km (Mottl et al., 2003; Hulme et al., 2010; Fryer et al., 2018a).

In other alkaline ultramafic-hosted hydrothermal systems, carbonic fluids commonly lead to carbonate precipitation within the host peridotite (e.g., Klein and Garrido, 2011; Bach et al., 2011; Klein and McCollom, 2013; Schroeder et al., 2015). Results from recent laboratory experiments indicate that significant carbonation of peridotite may also occur at 1 to 2 GPa and 500 to 600 °C, i.e., under conditions similar to those at intermediate depths of forearc regions (Sieber et al., 2018). But no such carbonates have been described from the serpentinite mud volcanoes in the Mariana forearc. Carbonate precipitates described from serpentinite mud volcanoes to date appear to have mostly formed where upwelling fluids mixed with seawater near/at the seafloor (Haggerty, 1991; Gharib, 2006; Tran et al., 2014), except for few samples that are thought to have formed at higher temperatures from venting fluids (Alt and Shanks III, 2006). The latter have not been studied in detail.

We studied rock xenoliths brought to the seafloor along with fluids and muds in the Mariana serpentinite mud volcanoes, which were recovered during International Ocean Discovery Program (IODP) Expedition 366. The clasts originate from the downgoing oceanic crust and from the upper plate’s lithosphere, respectively. They contain carbonate \pm silicate \pm sulfate veins, the genesis of which expand the knowledge into the subduction channel conditions and into the cycling of C in the shallow portions of the Mariana convergent margin. Metavolcanic-hosted carbonate geochemical and isotopic signatures attest to mobilization of C in the downgoing plate and its mineralization in the form of Ca carbonates. Such carbonate precipitation below the ‘cold nose’ of a convergent margin represents a potential sink for C in the deep carbon cycle that remains unconstrained. Across-forearc trends in the geochemistry of pore waters in the mud volcanoes (e.g., Mottl et al., 2004; Fryer et al., 2018a) imply that the carbonation at depth may be widespread in the Mariana subduction system.

3.2 Study area and materials

Deep-rooted faults in the forearc of the non-accretionary Mariana subduction system act as pathways for upwelling fluids released from the subducting Pacific plate (Fig. 3.1; e.g., Uyeda and Kanamori, 1979; Fryer, 1992, 1996; Fryer et al., 1990). Together with mobilized serpentinite fault gouge these fluids rise through the Philippine Sea plate to the seafloor, where they form more than a dozen active serpentinite mud volcanoes typically tens of km in diameter and up to 2.5 km high (Fryer and Fryer, 1987; Fryer, 1992). These are composed principally of unconsolidated flows of serpentinite muds, containing clasts of serpentinitized forearc mantle peridotite and rare other lithologies including sediments and mafic crust derived from the subducted Pacific plate (e.g., Maekawa et al., 1995; Fryer et al., 1999; Fryer et al., 2018a). The mud volcanoes exist at varying distances from to the trench, i.e., the depth to the subducting slab varies and so do the pressure and temperature conditions at the location of fluid release (e.g., Oakley et al., 2007; Hulme et al., 2010). The serpentinite mud volcanism hence provides direct access to deep-sourced fluids and materials from the subduction channel and suprasubduction zone and unique insight into shallow subduction zone processes. There is evidence that serpentinite mud volcanism has occurred at least as early as the Archean (e.g., Pons et al., 2011).

Five serpentinite mud volcanoes have been targeted by three ocean drilling campaigns: Yinazao (55 km distance from the trench, ~13 km slab depth, slab temperature ~80 °C), Fantangisña (62 km from the trench, ~14 km slab depth, ~150 °C), Asùt Tesoru (72 km from the trench, ~18 km slab depth, ~250 °C), South Chamorro (78 km from the trench, ~18 km slab depth, ~250–350 °C), and Conical (86 km distance from the trench, ~18 km slab depth, ~250–350 °C; Oakley et al., 2007, 2008; Hulme et al., 2010; Maekawa et al., 1993; Fryer et al., 2006; Gharib, 2006). We studied drill core materials recovered from Yinazao, Fantangisña, and Asùt Tesoru during IODP Expedition 366 (Fig. 3.1). Our samples include (i) rock clasts of serpentinitized peridotite, altered mafic rock, and lithified metasediment, (ii) authigenic carbonate precipitates, and (iii) serpentinite mud pore waters. Veins composed of carbonate \pm silicate \pm sulfate phases crosscut the clasts.

3.3 Methodology

Visual observations were conducted on thin sections with both a standard petrographic microscope and a scanning electron microscope. Detailed mineralogical and geochemical analyses of mineral assemblages were carried out on thin sections; isotope ratios were determined on hand-picked mineral separates of vein materials.

3.3.1 *In situ* analyses

Raman Mineral assemblages were analyzed with a computer controlled Horiba LabRAM HR confocal Raman microscope at the Woods Hole Oceanographic Institution. The device is equipped with three lasers (473 nm, 532 nm, and 633 nm), two

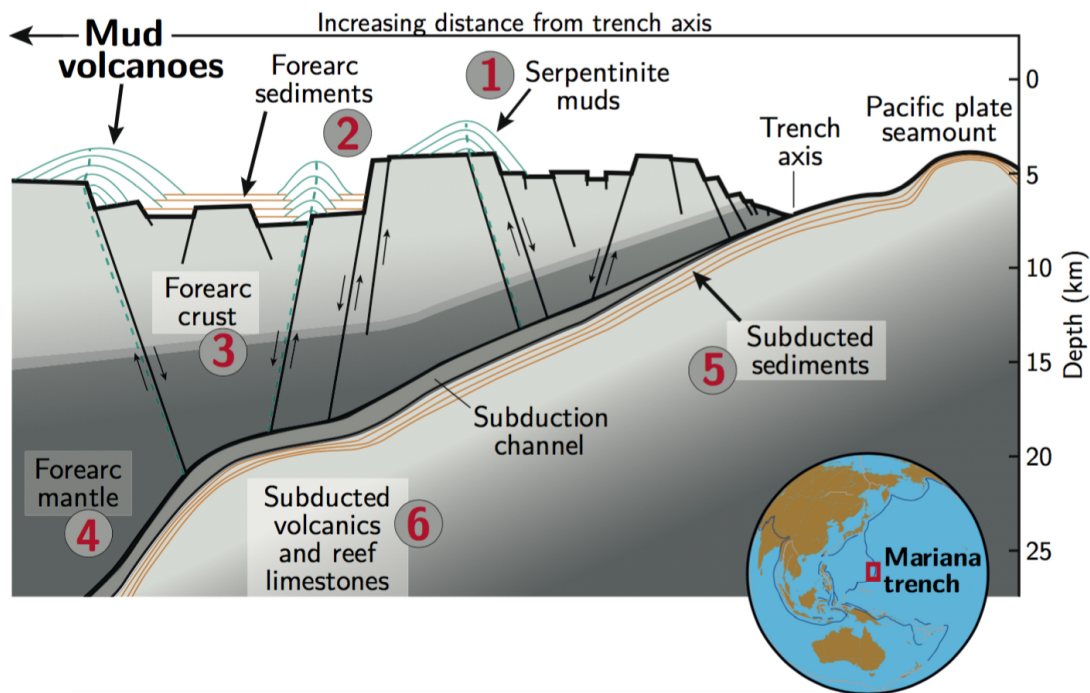


Figure 3.1 Geotectonic setting of the study area. Idealized cross-section of the Mariana forearc, including the relative positioning of serpentinite mud volcanoes drilled during IODP Expedition 366. Sediments (5) and crustal rocks (6) from the downgoing plate are reworked in the shallow subduction zone and are, together with materials from the forearc lithosphere (2–4), erupted within the serpentinite mudflows (1). Figure modified after Fryer et al. (2018a).

gratings (600 and 1800 grooves mm^{-1}), a thermoelectric cooled ($-70\text{ }^{\circ}\text{C}$) CCD detector, $50\times$ and $100\times$ objectives, a x - y - z motorized stage, and automated mapping options. Spectra were collected for 5 to 10 s with three to five accumulations between 100 and 1280 cm^{-1} . The LabSpec 6 software suite was used for post-processing of acquired spectra. The instrument was calibrated before each session using a silicon wafer and the RRUFF Raman database (Lafuente et al., 2016) was used for identification of unknown phases.

Electron microprobe Elemental compositions of minerals were obtained with a CAMECA SX100 electron microprobe at the University of Bremen. The device is equipped with four wavelength dispersive spectrometers. Analytical conditions included accelerating voltages of 15 kV and beam currents of 10 nA for silicates and 8 nA for carbonates. Peak counting times varied between 20 to 40 s per element and analyses were carried out with a focused beam (silicates) and defocused beam (carbonates). The built-in PAP correction was applied for data reduction and correction. Repeated analyses of natural silicate and carbonate standards guaranteed data quality. For most elements with concentrations $>1\text{ wt.}\%$, averaged precision is better than 2% and averaged accuracy is better than 5%.

Laser ablation ICP-MS Analyses of trace elements (B, Sr, Y, and rare earth elements) were carried out using a Thermo Finnigan Element2 ICP-MS coupled to a New Wave UP193 solid-state laser ablation system at the University of Bremen. Analytical conditions included an irradiance of $\sim 1 \text{ GW cm}^{-2}$ for ablation, spot sizes of 75 to 100 μm and a laser pulse rate of 5 Hz. Helium (0.7 L min^{-1}) and Ar (0.9 L min^{-1}) were used as sample and make-up gases, respectively. All isotopes were analyzed at low resolution with five samples in a 20% mass window and a total dwell time of 25 ms per isotope. After every 4 to 8 samples the glass standard NIST 610 was measured for external calibration using the values from (Jochum et al., 2011). To correct for interferences between ^{43}Ca and $^{86}\text{Sr}^{2+}$ we determined the quantitative relationship between $^{86}\text{Sr}^{2+}$ and ^{88}Sr in an in-house Ca-free but Sr-containing glass standard; the abundance of $^{86}\text{Sr}^{2+}$ is about 1.7% of that of ^{88}Sr , which is considered to mirror its natural isotopic existence. For all analyses we hence subtracted 1.7% of the intensity counts per second of ^{88}Sr from that of ^{43}Ca . The ^{43}Ca isotope was used as internal standard and concentrations were calculated with the Cetac GeoPro™ software. We tentatively assigned a detection limit of $0.001 \mu\text{g g}^{-1}$ for all trace elements as their detection limits are not well defined due to low blanks. Such low contents correspond to few counts per second for some elements, which results in relative standard deviations as high as 50%. Analytical quality was controlled by repeated analyses of United States Geological Survey reference materials BCR-2G, BHVO-2G, and MACS-3 and comparison of our data with the GeoReM database (as of February 2018). For the three reference materials, averaged precisions are better than 7.5% except for Ho and Tm (better than 10%). Averaged accuracies of BCR-2G and BHVO-2G are better than 6% except for Tm and Yb (up to 10.5%), averaged accuracy of MACS-3 is better than 10% except for Gd, Dy, Ho, Er, and Lu (all better than 15%).

3.3.2 Isotope analyses

Carbonate For the analyses of C and O isotopes, hand-picked vein carbonate samples were measured on a Thermo Scientific MAT 253 connected to a Kiel IV and authigenic carbonate samples on a Finnigan™ MAT 251 gas isotope ratio mass spectrometer connected to a Kiel I automated carbonate preparation device at MARUM. Carbon isotopes are reported in the usual delta notation versus VPDB, O isotopes are reported versus VSMOW. The instrument was calibrated against the house standard (ground Solnhofen limestone), which in turn was calibrated against the NBS 19 standard reference material. Over the measurement periods the standard deviations of the house standard were 0.06‰ for $\delta^{13}\text{C}$ values and 0.11‰ for $\delta^{18}\text{O}$ values for the Thermo Fischer and 0.04‰ for $\delta^{13}\text{C}$ and 0.03‰ for $\delta^{18}\text{O}$ for the Finnigan instrument.

For Sr isotope analyses, approximately 2 mg of homogenized carbonate powder were dissolved in 2 M HNO_3 , dried, and re-dissolved in 500 μL of 2 M HNO_3 in preparation for the chemical separation of Sr from unwanted matrix elements. Strontium was extracted using columns loaded with $\sim 70 \mu\text{L}$ of Sr-spec ion exchange resin (Triskem International) following a procedure adapted from Deniel and Pin (2001). The Sr was loaded on single Re filaments with Ta-oxide emitter, and analyzed with a Triton™ TIMS (Thermo Fisher Scientific) in the multidynamic acquisition mode at MARUM. The $^{87}\text{Sr}/^{86}\text{Sr}$

ratios were normalized to a $^{86}\text{Sr}/^{88}\text{Sr}$ ratio of 0.1194 to correct for instrumental mass fractionation. The long-term external reproducibility of the NIST 987 standard material is 0.710249 ± 0.000014 (2σ , $n = 220$) and falls within the range of 0.710250 ± 0.000034 (2σ , $n = 1245$, data <0.7102 and >0.7103 are discarded) of published NIST 987 values analyzed by TIMS (GeoReM data base, as of September 2017).

Sulfate The S and O isotope compositions of barite were analyzed at the University of Münster. Prior to the analyses, the barite was treated with HCl (10%) to remove intergrown carbonate, cleaned, and dried. For traditional S isotope measurements ($^{34}\text{S}/^{32}\text{S}$), an aliquot of 400 μg of barite was homogeneously mixed with 400 to 600 μg vanadium pentoxide (V_2O_5) in a tin capsule. $\delta^{34}\text{S}$ was measured with an EA-IRMS (element analyzer-IRMS) with a combination of EA IsoLinkTM and ThermoScientific Delta V Advantage mass spectrometer. For $\delta^{18}\text{O}$, 200 μg barite was weighted into an Ag capsule. Analyses were carried out with a temperature conversion/EA interfaced with a ThermoScientific Delta V Plus mass spectrometer. Results are reported in the common delta notation, for O isotopic compositions versus VSMOW. Replicates were measured for both $\delta^{34}\text{S}$ and $\delta^{18}\text{O}$ and the accuracy of the measurements was monitored using the international reference materials IAEA-S1, IAEA-S2, IAEA-S3, and NBS 127 for S, and IAEA-SO5, IAEA-SO6, and NBS 127 for O as well as internal reference materials Ag_2S and CdS for S, and BaSO_4 for O. Reproducibility as determined from replicate analyses was better than $\pm 0.3\text{‰}$ for S and $\pm 0.5\text{‰}$ for O isotope measurements.

Pore waters Pore waters from the serpentinite mud volcanoes were sampled during IODP Expedition 366; treatment of the pore waters onboard is described in Fryer et al. (2018b). Preparation for the analysis of Sr isotopes were undertaken in the University of Southampton's Class 100 clean laboratories. Strontium was separated from dissolved whole rocks using Sr-spec resin following Harris et al. (2015). Strontium isotopes were measured on a Thermo Scientific TRITON Plus TIMS. Precision and accuracy were assessed using international reference material NBS 987. Average values for $^{87}\text{Sr}/^{86}\text{Sr}$ of NBS 987 are 0.710244 ± 0.000019 (2σ , $n = 135$).

3.4 Results

3.4.1 Host rocks

Host rocks of the carbonate \pm silicate \pm sulfate veins are ultramafic clasts, metavolcanic clasts, and metasediment. Metavolcanic and metasedimentary clasts originate exclusively from the deeper-sourced mud volcanoes Fantangisña and Asùt Tesoru, whereas ultramafic hosts were as well sampled at Yinazao (Tab. 3.1).

Studied peridotites include two samples of dunite and one sample of harzburgite. One of the dunitites is about 30% serpentized, whereas the other peridotites are fully serpentized and characterized by mesh textures and distinct generations of crosscutting serpentine \pm iowaite \pm magnetite veins (Supplementary Information Fig. A.2.1). The

Table 3.1 Overview on samples and vein mineralogies.

Sample	Seamount	Type	Vein mineralogy
U1491B-5H-CC, 0–3 cm	Yinazao	Serp. dunite	Cal, Arg, Hem
U1492B-1H-3, 16–18 cm	Yinazao	Authigenic	Arg
U1492B-1H-4, 8–10 cm	Yinazao	Authigenic	Arg
U1492C-1H-2, 18–20 cm	Yinazao	Serp. harzburgite	Cal, Brc, Mt
U1497A-7X-CC, 29–31 cm	Fantangisña	Metasediment	Arg, Cal, Brt
U1497A-8F-1, 118–122 cm	Fantangisña	Metavolcanic	–
U1497A-12F-1, 93–95 cm	Fantangisña	Metavolcanic	Cal
U1498B-8R-1, 0–4 cm	Fantangisña	Metavolcanic	Cal, Nsq, Pct, Prh, Thm
U1498B-8R-1, 10–15 cm	Fantangisña	Metavolcanic	Arg, Cal, Pct
U1498B-8R-1, 32–34 cm	Fantangisña	Metavolcanic	Cal, Pct, Prh
U1495B-5G-CC, 1–3 cm	Asùt Tesoru	Serp. dunite	Cal, Arg
U1496A-10G-CC, 23–26 cm	Asùt Tesoru	Metavolcanic	Pct
U1496B-4F-3, 105–106 cm	Asùt Tesoru	Authigenic	Cal
U1496B-8X-CC, 33–41 cm	Asùt Tesoru	Metavolcanic	Arg, Ms, Lws, Ttn
U1496B-10F-2, 10–12 cm	Asùt Tesoru	Metavolcanic	Arg, Nsq

Abbreviations: Arg, aragonite; Brc, brucite; Brt, barite; Cal, calcite; Hem, hematite; Lws, lawsonite; Ms, muscovite; Mt, magnetite; Nsq, nesquehonite; Pct, pectolite; Prh, prehnite; serp., serpentized; Thm, thaumasite; Ttn, titanite; –, not applicable.

harzburgite contains hydroandradite intergrown within bastite serpentine after pyroxene (Supplementary Information Fig. A.2.1b), and scarce late veins that contain carbonate phases.

Seven samples represent volcanic rocks that are variably metamorphosed (Fig. 3.2a; Tab. 3.1). Remnant primary minerals include lath-shaped plagioclase and titaniferous clinopyroxene (Fig. 3.2a–c). The Ti-rich pyroxenes mostly plot in the field of alkali basalt, as classified by Leterrier et al. (1982; Fig. 3.2e). The clasts are altered to prehnite–pumpellyite and blueschist facies mineral assemblages, including chlorite, prehnite, pumpellyite, glaucophane, lawsonite, titanite, and vesuvianite (representative analyses available in Supplementary Information Tab. A.2.1). Complex networks of carbonate–silicate veins characterize the samples.

One sample is composed of quartzite that is brecciated into smaller fragments in a fine-grained matrix rich in hematite (Fig. 3.2d). Narrow calcite veins crosscut the quartz fragments; the breccia is crosscut by a cm-wide vein of Ca carbonate and barite.

3.4.2 Carbonate ± silicate ± sulfate veins

Petrography Distinct vein generations crosscut the clasts and comprise (i) carbonate–silicate, (ii) silicate-only, or (iii) carbonate–sulfate vein types (Tab. 3.1). Carbonate–silicate veins are hosted by variably serpentized peridotite and metavolcanic clasts. Veins in the serpentinites are <0.5 mm wide and crosscut most other textures, indicating a late formation. Carbonate phases are calcite and aragonite, the crystals of which are up to ~0.3 mm in size. Both phases can coexist in the same sample; in one clast they were observed in the same vein (Fig. 3.3a). Serpentine ± iowaite ± minor magnetite and

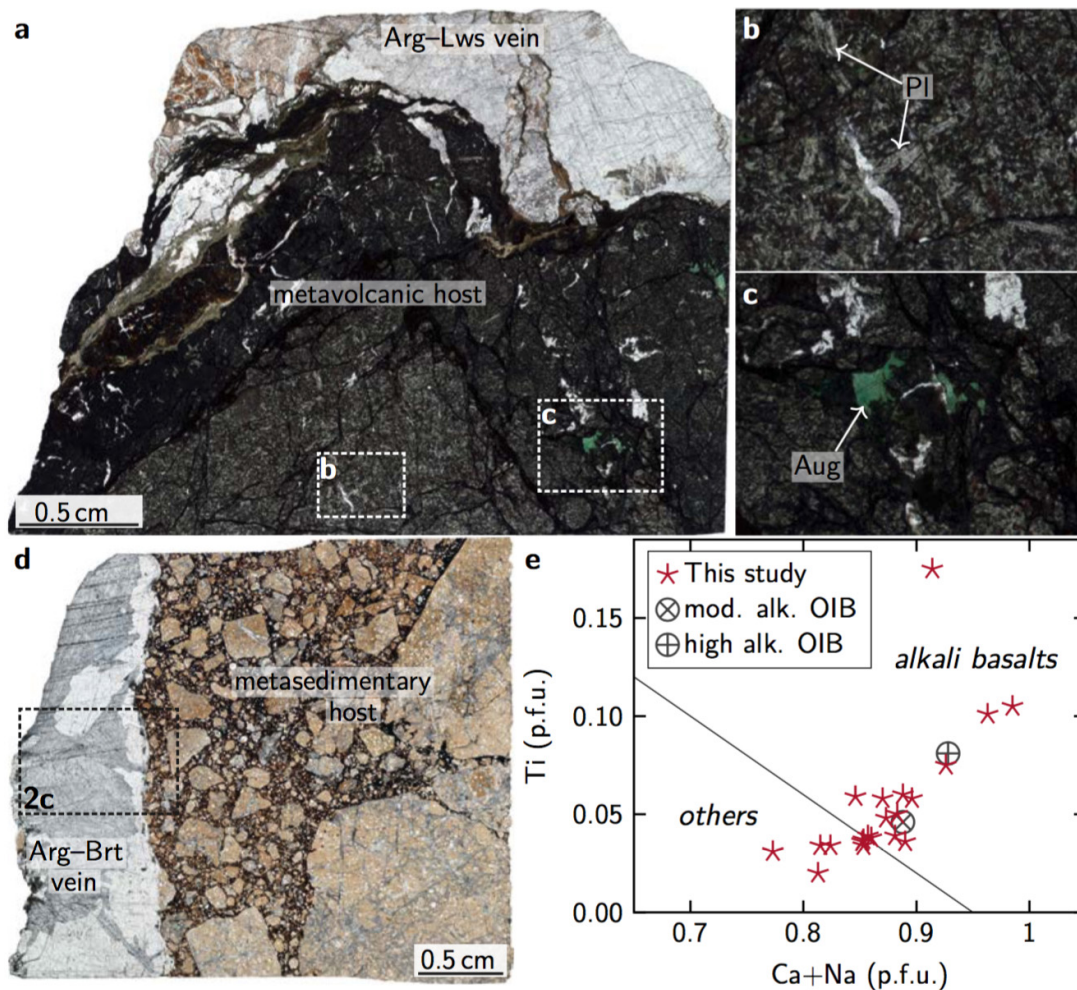


Figure 3.2 Thin section scans and photomicrographs showing host lithologies. (a) Thin section scan of a metavolcanic clast interpreted as subducted and recycled Pacific plate seamount material (sample U1496B-8X-CC, 33–41 cm). A carbonate–silicate vein crosscuts the clast. Close-ups show (b) remnant primary plagioclase lath textures and (c) titaniferous clinopyroxene inside the metavolcanic rock. (d) Thin section scan of a metasedimentary clast representing subducted and recycled Pacific plate sediment (sample U1497A-7X-CC, 29–31 cm). The sample is cut by a carbonate–sulfate vein (close-up in Fig. 3.3c). (e) Discrimination diagram for clinopyroxene phenocrysts (after Leterrier et al., 1982). Many clinopyroxenes from the metavolcanic samples plot in the field of alkali basalts (calculated on the basis of 6 O). Averaged basalt compositions are shown for comparison (as compiled by Leterrier et al., 1982). Abbreviations: alk., alkaline; Arg, aragonite; Aug, augite; Brt, barite; Lws, lawsonite; mod., moderately; OIB, ocean island basalt; Pl, plagioclase.

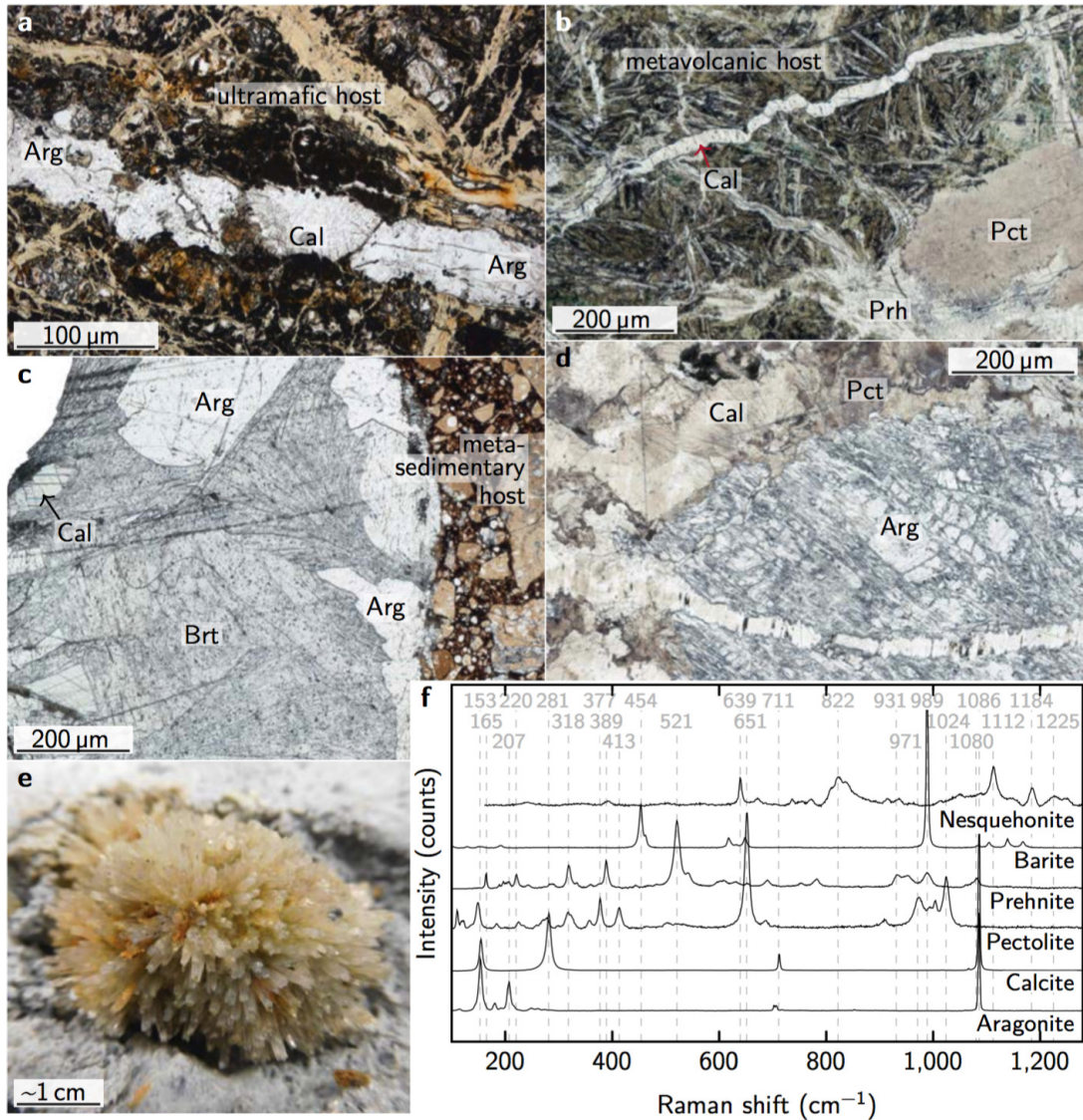


Figure 3.3 Thin section scans and photomicrographs depicting vein assemblages. (a) Late-stage calcite–aragonite vein in partially serpentinized ultramafic clast (sample U1491B-5H-CC, 1–3 cm). (b) Narrow late-stage calcite vein in metavolcanic host rock (sample U1498B-8R-1, 32–34 cm). (c) Wide barite–aragonite–calcite vein in a brecciated quartzite clast (sample U1497A-7X-CC, 29–31 cm). Euhedral crystal shapes imply a strain-free environment and chemical equilibrium during precipitation. (d) Wide vein inside metavolcanic clast with complex intergrowth of pectolite and microcrystalline calcite overgrowing earlier aragonite (sample U1498B-8R-1, 10–15 cm). (e) Authigenic aragonite with acicular growth within serpentinite mudflow (sample U1492B-1H-3, 16–18 cm). (f) Raman lines of the most common carbonate, silicate, and sulfate vein assemblages. Abbreviations: Arg, aragonite; Brt, barite; Cal, calcite; Pct, pectolite; Prh, prehnite.

hematite co-occur with the carbonates inside the veins. Iowaitite can show needle-like textures suggestive of growth in free space. The veins observed in metavolcanic clasts can be up to a cm in width and usually overprint earlier textures (Fig. 3.3b,d). The most abundant vein minerals are aragonite, calcite (less abundant than aragonite), pectolite, and prehnite; some samples contain minor lawsonite, nesquehonite, and phengite (see Fig. 3.3f for vein mineral Raman spectra). Aragonite crystals are up to a mm in size, often exhibiting euhedral crystal shapes. Calcite is generally <0.25 mm in size or microcrystalline. Several generations of carbonate are observed in some samples, e. g., sample U1498B-8R-1, 10–15 cm, where calcite and pectolite overgrow earlier aragonite (Fig. 3.3d). Carbonates and silicates generally occur intergrown or with straight crystal contacts indicating growth in chemical equilibrium. Silicates, particularly pectolite, in many cases show euhedral or radial textures (Fig. 3.3b,d); these crystallization patterns are indicative of free growth in open space. Veins in metavolcanic sample U1498B-8R-1, 32–34 cm, consist of pectolite and prehnite except for a narrow (<1 mm) vein of pure calcite, crosscutting all other textures (Fig. 3.3b). Metavolcanic sample U1498B-8R-1, 0–4 cm, contains veins of pectolite, prehnite, and minor mostly microcrystalline calcite as well as veinlets of late nesquehonite, $\text{Mg}(\text{HCO}_3)(\text{OH}) \cdot 2(\text{H}_2\text{O})$. Two metavolcanic clasts do not exhibit any carbonate-bearing veins. One of those has veins of pectolite in radiating crystal clusters; the other is not veined.

The quartzite sample has millimetric aragonite and barite crystals in a mm wide vein (Fig. 3.3c; Tab. 3.1). Euhedral shapes of aragonite and barite suggest co-crystallization in equilibrium with a fluid. The vein further hosts one ~ 150 μm long euhedral calcite crystal extending into the barite.

In addition to carbonates found in clasts, we sampled authigenic carbonates contained in the serpentinite mud matrix (Tab. 3.1). At Yinazao, acicular aragonite crystals up to 4 mm in length were scattered throughout the recovered drill core (sample U1492B-1H-4, 8–10 cm; Fig. 3.3e). At Asút Tesoru, calcite crystals with euhedral shapes and diameters of up to ~ 5 mm occurred disseminated in the mud matrix (sample U1496B-4F-3, 105–106 cm). The euhedral growth of both aragonite and calcite implies their in situ precipitation in the mud matrix, as previously interpreted by Fryer et al. (2018c,d,e).

Mineral chemistry Major and trace elemental compositions in the carbonates are highly variable. Magnesium and Fe concentrations vary from below detection to up to $\sim 14\,000$ $\mu\text{g g}^{-1}$ and ~ 1600 $\mu\text{g g}^{-1}$, respectively. Serpentinite-hosted calcites exhibit the highest Mg contents; concentrations in aragonites and calcites hosted by metavolcanic and the -sedimentary clasts are below 8500 $\mu\text{g g}^{-1}$ Mg. Mg/Ca ratios vary respectively, ranging up to 0.022 for the latter-mentioned *vs.* values up to 0.038 for carbonate in serpentinite. Strontium concentrations vary from <30 $\mu\text{g g}^{-1}$ to $\sim 15\,300$ $\mu\text{g g}^{-1}$, and Sr/Ca ratios from <0.001 to ~ 0.04 . Aragonites contain most Sr but concentrations can also be low (<1200 $\mu\text{g g}^{-1}$). Aragonites further reveal variable B concentrations (0.5 – 34 $\mu\text{g g}^{-1}$, mean = 4.9 $\mu\text{g g}^{-1}$). By comparison, B concentrations in calcite are much lower (0.3 – 6.2 $\mu\text{g g}^{-1}$, mean = 1.4 $\mu\text{g g}^{-1}$). Yttrium concentrations are low in aragonite (<0.1 – 4.4 $\mu\text{g g}^{-1}$, mean = 0.4 $\mu\text{g g}^{-1}$) but range up to 8.6 $\mu\text{g g}^{-1}$ in calcite (mean = 2.4 $\mu\text{g g}^{-1}$).

No distinctions between aragonites and calcites are apparent in their chondrite-normalized REE+Y patterns (chondrite composition from McDonough and Sun, 1995). Instead, distinct differences in REE+Y systematics are developed in the different host lithologies (Fig. 3.4). Chondrite-normalized REE+Y patterns of carbonates hosted by serpentinite clasts or the serpentinite mud are flat or slightly heavy-REE-enriched and concentrations are below chondritic (highest Lu value is <0.7 times chondritic). Chondrite-normalized La/Lu ratios range from 0.3 to 22.3. By contrast, carbonate phases hosted by metavolcanic clasts and the quartzite have generally higher REE+Y concentrations and show a strong depletion in heavy REEs (HREEs), with Lu depletion over La of <0.001 to 0.84. The patterns of these vein minerals commonly show negative Ce anomalies with $Ce/(La \times Pr)^{0.5}$ of 0.01 to 1.18. Because these carbonates are commonly associated with high-pressure phases, such as lawsonite, we will refer to the carbonates with high light REE (LREE) concentrations as ‘deep carbonates’ and to the REE-low carbonates as ‘shallow carbonates.’ Representative chemical analyses are presented in Tab. 3.2.

Isotopic compositions Strontium isotopic ratios ($^{87}\text{Sr}/^{86}\text{Sr}$) vary from 0.7052 to 0.7054 for deep carbonates and from 0.7049 to 0.7064 for shallow carbonates (Tab. 3.3). This clear distinction from modern seawater ($^{87}\text{Sr}/^{86}\text{Sr} = 0.70917$; McArthur et al., 2001) indicates that the precipitation of the studied carbonates is not due to precipitation from only seawater. Instead, a non-seawater source with low $^{87}\text{Sr}/^{86}\text{Sr}$ values is required. Pore water samples from Yinazao, Fantangisña, and Asùt Tesoru serpentinite mud volcanoes exhibit endmember $^{87}\text{Sr}/^{86}\text{Sr}$ of 0.70566, 0.70495, and 0.70510 (Fig. 3.5, Supplementary Information Tab. A.2.2), respectively, which indicates interactions with rocks that have low $^{87}\text{Sr}/^{86}\text{Sr}$. Accordingly, Sr isotopes indicate that deep carbonates likely precipitated from the slab-derived fluids, and shallow carbonates may have formed from a mixture of venting fluid and seawater (Fig. 3.5).

Carbonate $\delta^{13}\text{C}$ values range from -0.6 to $+3.3\text{‰}$ VPDB (Fig. 3.6; Tab. 3.3) with no distinction between deep and shallow carbonates. These isotopic signatures are characteristic of inorganic C. Similar C isotopic compositions were reported by Alt and Shanks III (2006; $\delta^{13}\text{C} = +0.07$ to $+2.5\text{‰}$) for aragonite veins in metabasalt and siltstone clasts within the serpentinite flows at South Chamorro and by Tran et al. (2014) for Ca carbonate chimneys on the summit of Conical seamount ($\delta^{13}\text{C} = -3.7$ to 0‰). Alt and Shanks III (2006) explained the vein carbonate data by their formation from venting fluids at depth; Tran et al. (2014) interpreted the chimneys to have formed from mixed vent fluid and seawater, as indicated by radiogenic Sr isotopes. Haggerty (1987); Haggerty (1991) and Gharib (2006) studied calcite and aragonite chimneys and authigenic carbonates from several Mariana serpentinite mud volcanoes; isotopic compositions are similar to those reported by Tran et al. (2014) for chimney carbonates ($\delta^{13}\text{C} = -2.9$ to -0.1‰) but vary greatly in authigenic precipitates from serpentinite clasts and muds ($\delta^{13}\text{C} = -27.4$ to $+10.2\text{‰}$).

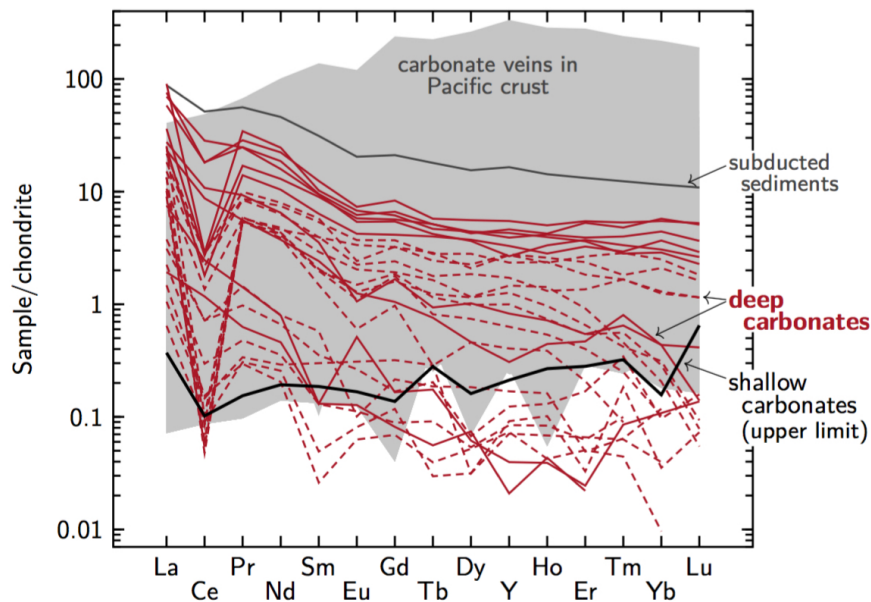


Figure 3.4 REE+Y compositions of vein carbonates normalized for chondrite (McDonough and Sun, 1995). Carbonates formed from deep fluids (red lines) are enriched in REEs and exhibit negative Ce anomalies. They are hosted by metavolcanic clasts and a quartzite breccia. Samples are from Fantangisña (dashed lines) and Asùt Tesoru (solid lines). Carbonates formed close to the seafloor have low REE contents (the black line marks the upper limit of REE contents) and likely precipitated from mixed venting fluid and seawater. These carbonates are hosted by serpentinite and one metavolcanic clast, and also include aragonite and calcite that grew in the mud matrix. For comparison, REE data of carbonate veins in the basaltic Pacific crust (ODP Sites 801 and 1149; Rausch, 2012) and of subducting sediments (ODP Sites 800 and 801; Plank and Langmuir, 1998) are shown.

Table 3.2 Representative carbonate geochemistry.

Sample	U1497A- 7X-CC, 29–31 cm	U1497A- 7X-CC, 29–31 cm	U1497A- 12F-1, 93–95 cm	U1496B- 8X-CC, 33–41 cm	U1496B- 8X-CC, 33–41 cm	U1496B- 10F-2, 10–12 cm	U1496B- 10F-2, 10–12 cm	U1492B- 5H-CC, 0–3 cm	U1492B- 1H-4, 8–10 cm	U1496B- 4F-3, 105– 106 cm
Seamount	Fantang- isña	Fantang- isña	Fantang- isña	Asùt Tesoru	Asùt Tesoru	Asùt Tesoru	Asùt Tesoru	Yinazao	Yinazao	Asùt Tesoru
Host rock	Meta- sediment	Meta- sediment	Meta- volcanic	Meta- volcanic	Meta- volcanic	Meta- volcanic	Meta- volcanic	Ultramafic	–	–
Phase Formation	Cal Deep	Arg Deep	Arg Deep	Arg Deep	Arg Deep	Cal Deep	Cal Deep	Cal Shallow	Arg Shallow	Cal Shallow
wt. %										
CaCO ₃	98.15	99.77	100.97	100.40	100.71	100.42	101.74	91.47	89.01	96.83
FeCO ₃	0.03	0.04	0.07	0.04	b. d. l.	0.15	b. d. l.	0.20	2.80	0.65
MnCO ₃	0.08	0.07	b. d. l.	0.06	b. d. l.	0.06	0.08	2.17	0.04	0.02
MgCO ₃	b. d. l.	0.02	0.06	b. d. l.	b. d. l.	b. d. l.	b. d. l.	4.86	8.09	2.48
Total	98.26	99.9	101.09	100.50	100.71	100.62	101.82	98.70	99.942	99.98
µg g⁻¹										
Sr	123	1086	2705	2660	1836	370	428	785	11 931	58
Y	1.30	0.14	0.48	0.26	4.29	1.57	0.99	0.01	0.081	b. d. l.
La	6.53	0.15	5.53	0.89	3.59	2.41	3.18	b. d. l.	b. d. l.	b. d. l.
Ce	6.62	0.06	5.35	0.44	1.34	0.03	0.04	b. d. l.	b. d. l.	b. d. l.
Pr	0.864	0.028	0.519	0.134	0.785	0.506	0.508	b. d. l.	b. d. l.	b. d. l.
Nd	2.97	0.12	1.71	0.37	2.88	1.93	1.88	0.002	0.015	b. d. l.
Sm	0.524	0.007	0.358	0.085	0.583	0.294	0.293	b. d. l.	0.004	b. d. l.
Eu	0.060	0.005	0.070	0.006	0.189	0.084	0.062	b. d. l.	0.003	b. d. l.
Gd	0.332	0.023	0.209	0.043	0.641	0.370	0.355	b. d. l.	0.003	b. d. l.
Tb	0.034	0.001	0.027	0.007	0.104	0.042	0.029	b. d. l.	b. d. l.	b. d. l.
Dy	0.251	0.008	0.113	0.045	0.513	0.243	0.183	0.004	0.010	b. d. l.
Ho	0.039	0.006	0.024	0.009	0.128	0.040	0.029	b. d. l.	b. d. l.	b. d. l.
Er	0.087	0.005	0.075	0.008	0.426	0.087	0.064	b. d. l.	0.001	b. d. l.
Tm	0.016	0.005	0.020	0.002	0.070	0.014	0.006	b. d. l.	0.001	b. d. l.
Yb	0.070	0.006	0.070	0.019	0.403	0.046	0.016	0.011	0.003	b. d. l.
Lu	0.010	0.002	0.003	b. d. l.	0.045	0.002	b. d. l.	0.002	b. d. l.	b. d. l.

Abbreviations: Arg, aragonite; b. d. l., below detection limit; Cal, calcite; –, not applicable.

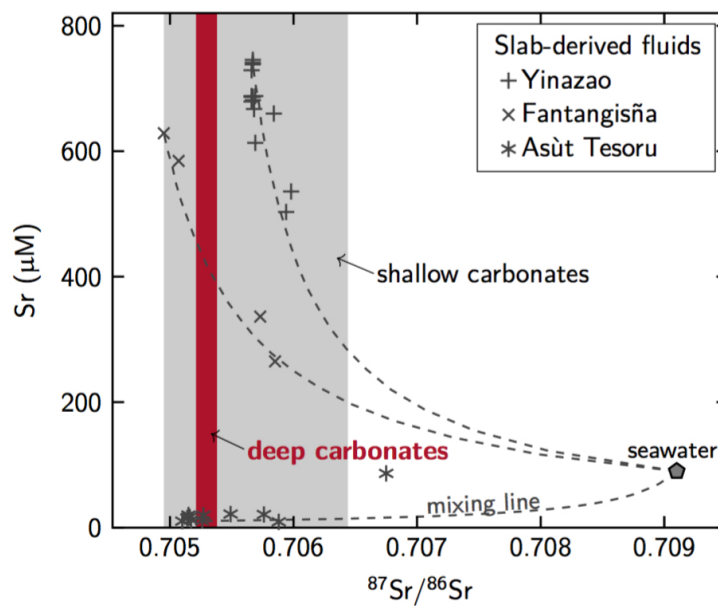


Figure 3.5 Strontium geochemistry of carbonates and serpentinite mud pore waters. Slab-derived fluids are unradiogenic but mix with seawater towards the core tops (*cf.* Supplementary Information Tab. A.2.2). Strontium isotopic values of deep carbonates well resemble those of slab-derived fluids, implying that they precipitated from these fluids at depth. Shallow carbonates exhibit a wider range of Sr isotopic compositions. They likely formed in the mixing zone of upwelling fluids and seawater. Note that even large amounts of seawater admixed into slab-derived fluids do not necessarily alter the Sr isotopic composition strongly. Bottom seawater composition from Mottl et al. (2004).

$\delta^{18}\text{O}$ values of shallow carbonates (33 to 36.3‰) fall in the range of authigenic carbonate literature data (Haggerty, 1987; Haggerty, 1991; Gharib, 2006; Tran et al., 2014), the deep carbonates $\delta^{18}\text{O}$ values between 20.2 and 23.5‰ are clearly different (Fig. 3.6; Tab. 3.3). These are in the range of aragonite data reported by Alt and Shanks III (2006) and are among the lowest $\delta^{18}\text{O}$ values reported for carbonates from the Mariana forearc.

Barite of the carbonate–sulfate vein hosted by the quartzite sample has a $\delta^{34}\text{S}$ value of 18.8‰ and a $\delta^{18}\text{O}$ value of 13.5‰. No barite has previously been described/studied in the eruptives of the serpentinite mud volcanoes.

3.5 Discussion

3.5.1 Recycling of Pacific crust through serpentinite mud volcanism

The serpentinitized peridotite clasts represent forearc mantle material; by contrast, the likely origin of the metavolcanic and metasedimentary lithologies is the subducting plate. For the latter, the presence of remnant Ti-rich pyroxene implies an ocean island provenance. This is in line with shipboard results of IODP Expedition 366 (Fryer et al.,

Table 3.3 Carbonate and sulfate stable isotope geochemistry.

Sample	Type	$^{87}\text{Sr}/^{86}\text{Sr}$	$\delta^{18}\text{O}$ (‰)	$\delta^{13}\text{C}$ (‰)	$\delta^{34}\text{S}$ (‰)	$\delta^{18}\text{O}_{\text{Brt}}$ (‰)
U1492B-1H-3, 16–18 cm	Authigenic	0.70644	36.3	−0.5	–	–
U1492B-1H-4, 8–10 cm	Authigenic	0.70524	36.2	−0.4	–	–
U1496B-4F-3, 105–106 cm	Authigenic	0.70495	33.0	2.4	–	–
U1496A-10G-CC, 23–26 cm	Metavolcanic	0.70523	21.2	0.9	–	–
U1497A-7X-CC, 29–31 cm	Metasediment	0.70525	20.2	−0.6	18.8	13.5
U1498B-8R-1, 0–4 cm	Metavolcanic	0.70526	20.4	2.2	–	–
U1498B-8R-1, 32–34 cm	Metavolcanic	0.70538	23.5	3.3	–	–

$\delta^{18}\text{O}$ in VSMOW, $\delta^{13}\text{C}$ in VPDB. Abbreviations: Brt, barite; –, not applicable.

2018a). The presence of the alteration phases demonstrates a high-pressure metamorphic overprint in accordance with peak temperature and pressure conditions at depth beneath Fantangisña (~14 km slab depth, ~150 °C slab temperature) and Asùt Tesoru (~18 km, ~250 °C; Oakley et al., 2007, 2008; Hulme et al., 2010). Glaucofane and lawsonite, present in samples from Asùt Tesoru, indicate beginning blueschist metamorphic conditions. Blueschist materials from the serpentinite mud volcanoes have previously been reported by, e. g., Maekawa et al. (1995); Fryer et al. (1999).

Quartzite breccias have not been previously described from the serpentinite mud volcanoes. We suggest that the sample represents lithified sedimentary siliceous ooze from the subducted Pacific plate. Such oozes cover large areas of the Western Pacific seafloor (*cf.* ODP Sites 801 and 1149; Shipboard Scientific Party, 2000), as the abyssal depth of the Western Pacific is in many places below the carbonate compensation depth (~4.5 km), which leads to the dissolution of large parts of otherwise frequent calcareous plankton (e. g., Pälike et al., 2012). With progressive metamorphism during subduction, the silica-rich sediments were likely transformed into quartzite (*cf.* Kastner, 1981). The brecciation indicates the exposure of the quartzite to strain at temperatures below that of the brittle–plastic transition zone (<300–350 °C; e. g., Stipp and Kunze, 2008), in agreement with estimated temperature of 150 °C for the subduction channel below Fantangisña (Hulme et al., 2010).

3.5.2 Carbonate formation in the subduction channel

Textural relationships and carbonate chemistry of the vein assemblages demonstrate that the veins formed after peak metamorphism and associated deformation. We base this interpretation on textural evidence: radial growth (e. g., Fig. 3.3d) and euhedral crystal shapes (e. g., Fig. 3.3c) of vein precipitates that indicate growth in strain-free environments. The host rocks show evidence of high-grade metamorphism as deformation and recrystallization to, e. g., pumpellyite or glaucofane; no such indications could be identified for the vein phases. Moreover, REE patterns of carbonates studied here substantially differ from those of carbonates formed during seawater circulation within the ocean crust where the formation of Ca carbonate veins in mafic portions of the

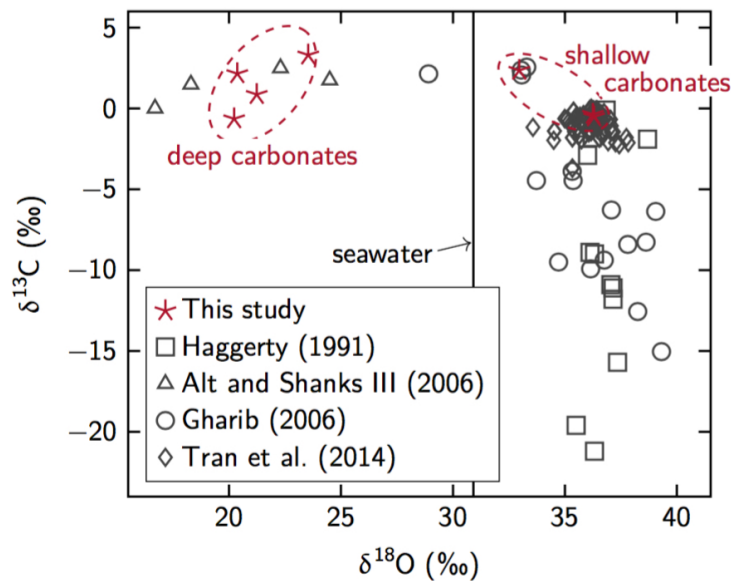


Figure 3.6 Carbonate C and O isotopic compositions. Carbonates from this study have slightly positive $\delta^{13}\text{C}$, suggesting an inorganic carbon source. $\delta^{18}\text{O}$ values of deep carbonates are considerably lower in comparison to authigenic carbonates since they precipitated at much higher temperatures. Literature data are shown for comparison, including data depicting carbonate chimneys from Conical (Haggerty, 1991), authigenic carbonates from several Mariana mud volcanoes (Gharib, 2006), and aragonite in metabasalt and siltstone clasts from Conical (Alt and Shanks III, 2006). The latter potentially had the same carbon source and formed at similar high temperatures; carbonates studied by Haggerty (1991) and Gharib (2006) are influenced by organic compounds and precipitated at ambient seawater conditions.

ocean crust is a common process (e.g., Alt and Teagle, 1999). Rausch (2012) studied carbonate veins in mafic lithologies from Sites 801 and 1149, ODP Leg 185, in the Western Pacific (gray shaded field in Fig. 3.4); these samples represent lithologies that are being subducted at the Izu-Bonin-Mariana convergent margin and could potentially be recycled via the mud volcanism. However, Site 801 and 1149 REE patterns generally exhibit higher REE concentrations and enrichments in HREEs as compared to the deep carbonates in this study, which are characterized by lower total REE concentrations, significant depletions in HREEs, and frequent negative Ce anomalies (Fig. 3.4). Only one sample (U1498B-8R-1, 10–15 cm) shows a slight HREE-enrichment similar to Pacific crust carbonates but total REE concentrations are considerably lower. Hence, we exclude the possibility that the vein precipitates represent portions of the subducted carbonated crust. In contrast, carbonates in veins hosted by ultramafic clasts exhibit patterns and low concentrations similar to those of carbonates from Sites 801 and 1149. But these veins are hosted by ultramafic clasts from the forearc mantle—they hence must have formed in the mantle wedge.

We conclude that the deep carbonates have formed during the interaction with fluids after peak metamorphism affecting their hosts. During and after vein assemblage

formation, relatively strain-free environments must have prevailed to form and preserve the observed undeformed mineral textures. The pressure–temperature conditions during vein formation were likely similar to the metamorphic conditions under which the host rocks recrystallized, as indicated by the intergrowth of carbonate with lawsonite and phengite. Lawsonite is characteristic of metamorphic alteration of mafic rocks under blueschist facies conditions (e. g., Black, 1977) at high pressures and temperatures ranging from 150 to 400 °C (Essene et al., 1965; Diessel et al., 1978). Intimate intergrowth of lawsonite with aragonite (Fig. 3.2a) hence clearly indicated that these veins formed at great depth. Furthermore, the uniform REE+Y patterns of those deep veins suggest that they have precipitated from fluids with alike compositions.

Temperatures of formation are difficult to constrain from metamorphic assemblages in subduction zones. But carbonate formation temperatures can be calculated from their $\delta^{18}\text{O}$ compositions, given that the O isotopic composition of the precipitating solution is known. Pore waters of the most deeply rooted of the mud volcanos targeted by IODP Expedition 366 (Asùt Tesoru) have $\delta^{18}\text{O}_{\text{fluid}}$ of +1.7 to +2‰ (Debret et al., 2019). Temperature estimates for deep carbonates based on these isotopic compositions range from ~60 to 95 °C (Fig. 3.7; estimates after O’Neil et al., 1969; Friedman and O’Neil, 1977). These values are much lower than the temperatures inferred for the depth of the slab interface underneath the serpentinite mud volcanoes. But it is unlikely that the $\delta^{18}\text{O}$ compositions of the pore waters of the mud volcanoes are representative for the slab-derived fluids from which the carbonates precipitated. The precipitation of the deep carbonates presumably occurred at (considerably) higher temperatures. Alt and Shanks III (2006) calculated isotopic compositions of fluids released at depth that are in equilibrium with the weighted mean of subducting sediment (their Tab. 4). These authors estimate the $\delta^{18}\text{O}$ value of such fluid to be +12‰ at 200 °C and to be +16‰ at 300 °C. Based on the assumption that the carbonates in basaltic clasts recovered from Conical ($\delta^{18}\text{O} = +16.7$ to 24.5‰; Fig. 3.6) had precipitated from slab-derived fluids, Alt and Shanks III suggested their formation at temperature up to 250 °C. Using the same approach as Alt and Shanks III, we calculated $\delta^{18}\text{O}_{\text{fluid}}$ in equilibrium with subducting sediment based on fractionation coefficients for calcite–water, quartz–water, albite–water, illite–water, and chlorite–water from Zheng (1993a,b), and Zheng (1999), respectively. For the inferred slab temperatures of 150 °C below Fantangisña and of 250 °C below Asùt Tesoru (Hulme et al., 2010) we obtain $\delta^{18}\text{O}_{\text{fluid}}$ compositions of 9.3‰ and 14.9‰, respectively. If the deep carbonates formed in equilibrium with these fluids, precipitation would be shifted to 130 to 175 °C and to 220 to 310 °C, respectively (Fig. 3.7). Fluids expelled from sediments at shallow depths in subduction zones may generally have high $\delta^{18}\text{O}$ values: for instance, Bebout and Barton (1989) estimated a $\delta^{18}\text{O}$ value of 13‰ for slab-derived fluids at 25 to 45 km depth in the Catalina Schist subduction complex.

Yet, incipient serpentinization in the subduction channel likely removes ^{18}O from the fluids into serpentine (e. g., Alt and Shanks III, 2006; Debret et al., 2019) so that the actual $\delta^{18}\text{O}_{\text{fluid}}$ in the subduction channel, which likely contains eroded variably serpentinized materials from the basal plane of the mantle wedge, may be somewhat lower. The temperatures estimated on the basis of calculated $\delta^{18}\text{O}_{\text{fluid}}$ should hence be considered

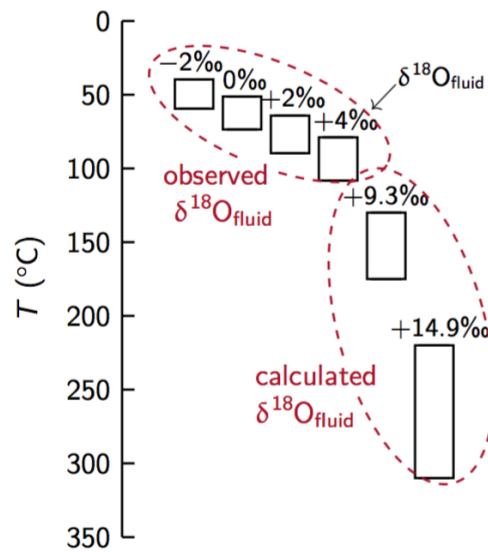


Figure 3.7 Estimated formation temperatures for deep carbonates. Oxygen isotopes suggest variable carbonate precipitation temperatures, depending on the isotope value of the fluid from which they formed. Pore water $\delta^{18}\text{O}$ compositions increase with depth-to-slab from negative values at Yinazao (-1.5‰) to positive values at Asùt Tesoru ($+2.5\text{‰}$) and Conical ($+4\text{‰}$). These would result in temperatures below 100 °C ; however, these fluids are not representative of fluid compositions at depth. In fact, calculated compositions of fluids being released from the subducting sediments have $\delta^{18}\text{O}$ ranging from 9.3 to 14.9‰ . Temperature estimates based on these values are 130 to 175 °C and 220 to 310 °C , respectively. Serpentinite mud pore water data from Debret et al. (2019) and Mottl et al. (2004); temperature calculation after O’Neil et al. (1969) and Friedman and O’Neil (1977).

maximum estimates. We suggest that the carbonates formed from dehydration fluids in the subduction channel soon after they were released from the downgoing slab. This idea is supported by the trace element composition of the deep carbonates, specifically the generally high concentrations of REEs and negative Ce anomalies. The low REE mobility and oxidizing conditions indicated by these REE compositions do not match the idea that the fluids had been modified significantly by serpentinization reactions.

Furthermore, prevailing serpentinization within the subduction channel would produce reducing conditions due to the release of H_2 to the aqueous solutions (e. g., McCollom and Bach, 2009). But the pronounced negative anomalies of Ce indicate that precipitation took place under fairly oxidizing conditions where Ce is tetravalent (Sverjensky, 1984). We calculated the predominant redox states of Ce and Eu in the $a\text{H}_2(\text{aq})$ vs. temperature plane to identify the low reduction potential under which the carbonates have formed (Fig. 3.8; see figure caption for details on the calculations). Within the estimated temperature range of ~ 130 to 310 °C , Ce^{4+} will be stable under fairly oxidizing conditions. Since not all carbonates exhibit Ce anomalies, the conditions presumably shifted towards slightly more reducing conditions, i. e., approaching the field of Ce^{3+} . Yet, the redox conditions under which tetravalent Ce is expected to predominate are clearly within

the stability region of SO_4^{2-} and CO_2 (Fig. 3.8). This result is consistent with the abundance of carbonate veins and the presence of barite in the quartzite sample. Our estimate puts the upper boundary of H_2 activity in the fluids well below levels imposed by serpentinization reactions, which would be $>\log -2$ for temperatures between 200 to 300 °C (McCollom and Bach, 2009). We hence suggest that the carbonate precipitation occurred in a system that was not dominated by serpentinization reactions.

It is hence likely that the deep carbonates formed within the subduction channel, where serpentinization of the mantle wedge contributes to a lower degree to the overall redox conditions. Instead, dehydration processes induced by prograde reactions in the subducting slab are thought to cause more oxic environments. These processes include the release of pore waters due to sediment compaction, dehydration of opal-CT, decomposition of clay, as well as decarbonation (e. g., Mottl et al., 2004; Fryer et al., 2018a). With the help of the textural relationships implying strain-free environments, we can further narrow down the carbonate precipitation to have occurred after the metavolcanics/metasediments got detached from the subducting lithosphere. These conclusions are summarized in Figure 3.9. Our isotope-based temperature estimates are in line with this interpretation as they well match inferred slab temperatures of ~ 150 °C beneath Fantangisña and ~ 250 °C beneath Asùt Tesoru.

3.5.3 Processes in the mud volcano conduits

Within the mantle wedge, excessive serpentinization is expected to become a dominant process and the redox conditions will turn highly reducing. The same can be expected for the conditions in the mud volcano conduits that are developed within the mantle wedge. Even intergranular fluids within larger serpentinite clasts within the subduction channel may be highly reduced. The reducing conditions are reflected by the presence of magnetite and awaruite in the serpentinite clasts (Kahl et al., 2015). These reducing conditions prevail all the way up: Kawagucci et al. (2018) suggested that the fluids venting at South Chamorro had as much as 40 mM H_2 , before most of the H_2 was consumed by microbial sulfate reduction.

The veined metavolcanic clasts were exposed to these reducing conditions imposed by serpentinization reactions, but the carbonate phases preserved a record of earlier oxidizing conditions in the subduction channel. However, evidence for late-stage reactions between the metavolcanic clasts and serpentinization fluids exists in the form of vein phases such as nesquehonite, $\text{Mg}(\text{HCO}_3)(\text{OH}) \cdot 2(\text{H}_2\text{O})$. This phase is stable only at temperatures of <100 °C (e. g., Davies and Bubela, 1973; Ballirano et al., 2010) and forms exclusively in alkaline environments (Wilson et al., 2009). Thaumasite, $\text{Ca}_3\text{Si}(\text{CO}_3)(\text{SO}_4)(\text{OH})_6 \cdot 12(\text{H}_2\text{O})$, is another low-temperature alteration phase in mafic rocks and forms preferentially in the presence of carbonate and sulfate at low temperatures at alkaline conditions (e. g., Karpoff et al., 1992; Schmidt et al., 2008). In deep-sea environments, the formation of thaumasite is assigned to temperatures of <100 °C (e. g., Noack, 1983; Karpoff et al., 1992). Nesquehonite and thaumasite are not directly intergrown with the deep carbonates but rather occur in, partly crosscutting, late veins. They

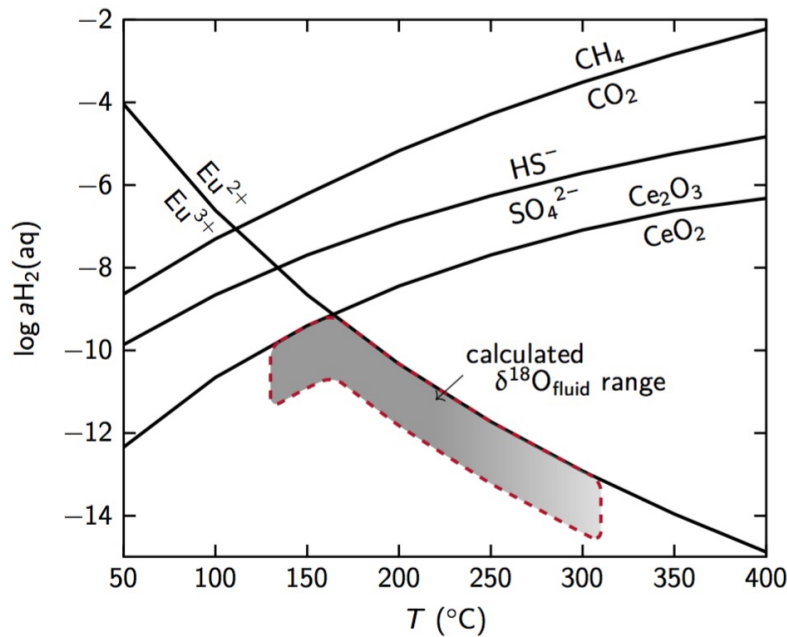


Figure 3.8 Predominance diagram showing the positions of redox reaction equilibria for equal activities of oxidized and reduced species. Over the entire temperature range, Ce^{4+} is only stable under conditions of low $\log a_{\text{H}_2(\text{aq})}$, i. e., in oxidizing environments. CO_2 and SO_4^{2-} co-occur with these oxidation states. The shaded field marks the here suggested conditions under which the deep carbonate Ce anomalies may have developed beneath Fantangisña and Asùt Tesoru, as based on temperature estimates relying on calculated $\delta^{18}\text{O}_{\text{fluid}}$. Europium anomalies are not developed, indicating Eu to be present in a trivalent state in the fluids from which the carbonates precipitated. The positions of the reaction lines were computed with SUPCRT92 (Johnson et al., 1992) for a pressure of 50 MPa, using thermodynamic data from Shock and Helgeson (1988), Shock et al. (1997), and Helgeson et al. (1998) for aqueous species and Robie et al. (1978) as well as Robie and Hemingway (1995) for Ce oxides.

likely formed during low-temperature alteration of the clasts below or within the mud volcanoes.

Other phases associated with calcite in some of the veins include pectolite and prehnite. These phases probably formed deeper in the system than nesquehonite and thaumasite. This is inferred from crosscutting relations and reflects the higher formation temperatures required for these phases. Pectolite may form at temperatures as high as 300 to 500 °C (e. g., Craw and Landis, 1980; Esteban et al., 2003). Similarly, prehnite may be stable in water–rock systems up to temperatures of ~300 °C (e. g., Bird and Spieler, 2004). Pectolite and prehnite are often associated with rodingitization (e. g., Austrheim and Prestvik, 2008), a process that has crustal rocks that interact with serpentinization fluids undergo Ca-metasomatism including the formation of Ca–Al silicates, such as hydrogarnet, prehnite, and vesuvianite (see, e. g., Bach and Klein, 2009, for details).

The precipitation of shallow carbonates within the mud volcanoes must have taken place under drastically different conditions in comparison to the deep carbonate formation,

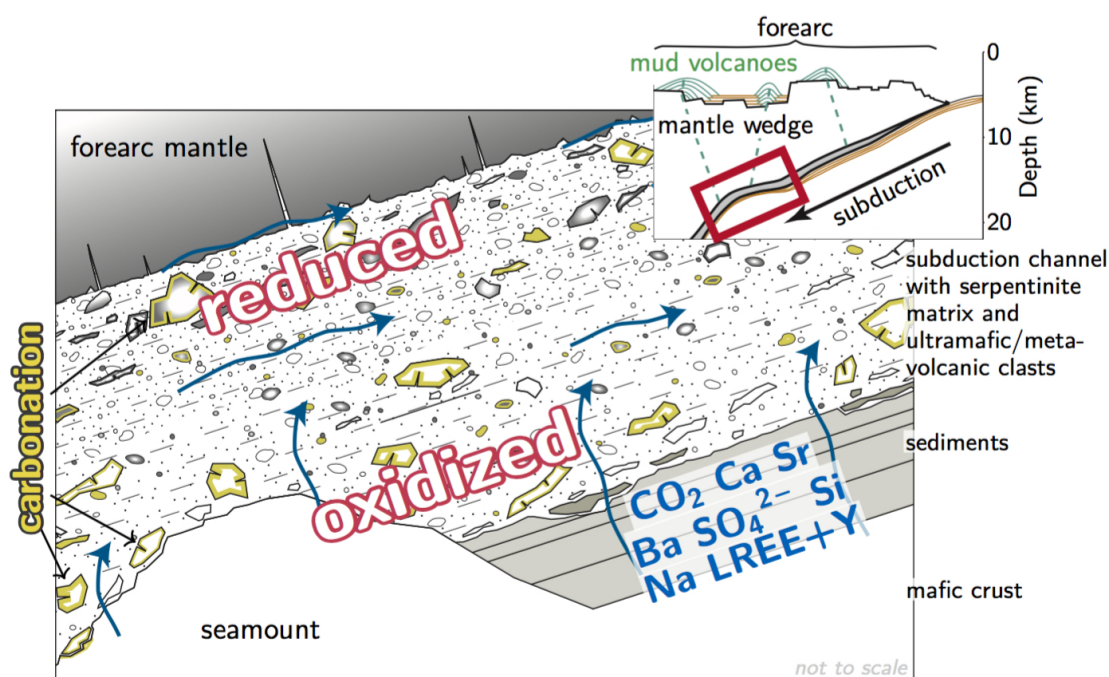


Figure 3.9 Interpretative conditions within the subduction channel below the Mariana forearc. Dehydration and decarbonation reactions release CO₂, SO₄²⁻, and other species into the subduction channel, where carbonation of metavolcanic clasts occurs under oxidizing conditions. Towards the mantle wedge, conditions turn progressively reducing. See text for further discussion. Figure in parts modified after Fryer et al. (2018a).

as indicated by their contrasting O isotope compositions. Radiating clusters of aragonite at Yinazao have exceptionally high $\delta^{18}\text{O}$ values ($\sim 36.6\text{‰}$), which leads to unrealistically low calculated formation temperatures (after Grossman and Ku, 1986) if the lowest $\delta^{18}\text{O}_{\text{fluid}}$ (-1.5‰ ; Debret et al., 2019) is assumed. Temperatures calculated for the highest values of $\delta^{18}\text{O}_{\text{fluid}}$ at Yinazao ($+0.6\text{‰}$) would be just below 1°C . Temperatures of 3.0°C and 15.6°C are computed for the calcite crystal ($\delta^{18}\text{O} = 33\text{‰}$) recovered from Asùt Tesoru (using Friedman and O'Neil, 1977) and the range of $\delta^{18}\text{O}_{\text{fluid}}$ values of pore water (-0.2 to $+2.5\text{‰}$; Debret et al., 2019). These estimates imply a formation of the shallow carbonates at low temperatures, which is in accordance with results of earlier work (Gharib, 2006; Tran et al., 2014).

The very low REE+Y contents of authigenic aragonite and calcite and of carbonate hosted in veins of the serpentinite clasts and one metavolcanic clast may point to a fluid source distinct from the slab-derived fluids. Low total REE+Y concentrations would be plausible if seawater was admixed in the shallow parts of the serpentinite mud volcanoes (REE concentrations in NW Pacific bottom water are $<60\text{ pM}$; e.g., Piepgras and Jacobsen, 1992). This interpretation is consistent with the similar $^{87}\text{Sr}/^{86}\text{Sr}$ isotopic compositions of the deep and shallow carbonates, indicating that entrainment of seawater in the shallow parts of the system were minimal. The lower REE+Y contents of the shallow carbonates may hence be more plausibly explained by (i) a loss of the REEs *en*

route to the surface (*cf.* Kahl et al., 2015; see also below), or (ii) lower precipitation temperatures that will favor crystal-chemical discrimination against REEs.

If the fluids in the pore waters of the mud volcanoes indeed represent cooled slab-derived fluids, then the oxygen isotopic composition must have been completely changed from high initial $\delta^{18}\text{O}$ values to overall seawater-like compositions near the seafloor. This shift in $\delta^{18}\text{O}$ may be explained by isotopic exchange in the mud between water and serpentine, which has higher $\delta^{18}\text{O}$ values than mantle wedge peridotites (e. g., Alt and Shanks III, 2006; Debret et al., 2019) and could hence explain the postulated decrease of $\delta^{18}\text{O}$ in the interacting fluids. The magnitude of the shift would indicate very low water/rock ratios.

3.5.4 Element transfers due to fluid release and subsequent fluid–mineral interactions

In addition to help constraining the temperature and redox conditions in the mud volcanoes' plumbing system, our results yield insights into the transport of elements from slab to seafloor. Barite intergrown with aragonite represents sulfate that was subducted with the downgoing slab. Sediment pore waters of the subducting lithosphere contain seawater with noticeable sulfate concentrations (D'Hondt et al., 2002). The isotopic composition of barite ($\delta^{34}\text{S} = 18.8\text{‰}$) is lower than that of modern seawater (21‰). In the Cretaceous and Cenozoic ocean water, $\delta^{34}\text{S}$ of sulfate has been as low $\sim 15\text{‰}$ in some periods (e. g., Paytan et al., 2004). Since the downgoing plate is inferred to have an age of >150 Ma (e. g., Müller et al., 2008), the isotopic composition of barite may represent Upper Mesozoic or Cenozoic seawater.

Ca-rich vein phases, namely aragonite, calcite, pectolite, and prehnite, derive their Ca either from slab-derived fluids or it is provided by the Ca-rich metavolcanic host rocks (ocean island basalts in the Pacific Ocean basin typically contain >8 wt.% CaO; e. g., Dasgupta et al., 2010). The latter could be particularly important at Asùt Tesoru, where Ca (and Sr) contents in the shallow pore waters and seep fluids are low (Mottl et al., 2004; Fryer et al., 2018a). If these low Ca and Sr concentrations were inherited from processes in the subduction channel, it would explain the presence of deep carbonate veins in basalt clasts and the quartzite breccia sample of Asùt Tesoru. In contrast, the very high concentrations of Ca and Sr in shallow fluids at Yinazao may indicate a lack of carbonate precipitation at depth. This idea is consistent with the absence of deep carbonates in the clasts at Yinazao. Calcium and Sr concentrations in pore waters at Fantangisña are intermediate, as is to be expected based on slab depths and inferred slab interface temperatures that are in-between Asùt Tesoru and Yinazao. The deep carbonate distribution hence appears to support the model by, e. g., Mottl et al. (2004) and Hulme et al. (2010), who suggested that the geochemical diversity of fluids seeping at the seafloor reflects differences in the compositions of the fluids liberated from the downgoing slab at different depths and temperatures as well as post-liberation fluid–rock interactions.

Strontium isotopic compositions of the deep carbonates provide additional evidence for mass transfer from the slab to the subduction channel and hanging wall. The unradiogenic values of $^{87}\text{Sr}/^{86}\text{Sr}$ ranging from 0.70495 to 0.70566 cannot be reconciled with simple

expulsion of seawater trapped in void space of the subducting sediment and basement. A fraction of the Sr must have also been released from slab minerals in the course of dehydration to explain the low $^{87}\text{Sr}/^{86}\text{Sr}$ numbers of the veins. Textural relations between the deep carbonates and silicates as well as barite imply that these phases grew simultaneously. We interpret the presence of silicates and barite as evidence for the release of SO_4^{2-} , Na, Si, Ba, and light REEs from sedimentary pore water and breakdown of opal and clay in subducted sediments and crust. The associations of carbonate with silicates or barite can be observed in the clasts of the intermediate-sourced Fantangisña and deep-sourced Asùt Tesoru, indicating an input of slab-derived dissolved inorganic carbon (DIC) in slab–interface depths of >14 km. For these mud volcanoes, the element release by dehydration of subducted clays and altered basalt has been suggested based on pore water compositions (Mottl et al., 2004; Hulme et al., 2010). These authors further proposed from the across-forearc comparison of pore waters that compositional differences are due to progressive slab dewatering and related element release (e. g., Mottl et al., 2004; Hulme et al., 2010; Fryer et al., 2018a). The Ca and Sr contents of the pore waters do reflect the distribution of vein carbonates in the clasts, indicating that deep slab-derived fluids are preserved in the mud volcano fluids all the way from the slab to the seafloor. It is, however, likely that the contents of elements less mobile than Ca and Sr are influenced by fluid–rock interactions. Geochemical studies of veined clasts show that these interactions do take place. Deep slab-derived fluid compositions are altered by interactions of these fluids by subsequent exchange processes with rocks in the subduction channel and forearc. Using trace element compositions of serpentine veins from South Chamorro, Kahl et al. (2015) showed that trace element and Si concentrations were high during early but low during later serpentinization stages of ultramafic clasts. This trend was interpreted to results from an *en route* loss of these elements from the fluids to the rocks within the subduction channel. Our results show that the highly immobile behavior of REEs likely resulted in rapid uptake by early precipitates. The depletion from the ascending fluids then gave rise to low concentrations of REEs in the shallow carbonates of the serpentinite mud volcanoes.

3.5.5 Element sources

Strontium isotope compositions of the deep carbonates attest to a formation from slab-derived fluids. All constituents needed to precipitate the vein carbonates as well as simultaneously grown silicate and sulfate minerals must consequently have been provided by the fluids (external source) or were present in the respective clasts that reacted with the fluids (internal source). This is particularly true for C, Na, Si, SO_4^{2-} , Ca, Sr, and Ba as well as trace elements, especially LREEs. Comparison of Sr isotopes of vein carbonates with that of upwelling fluids yet indicates that the vein minerals approximately formed in chemical equilibrium with ascending fluids. We argue that this is indicative of a fluid-dominated system, i. e., high water/rock ratios, and hence of external sources for the chemical species stated above. Even so, more rock-dominated interactions between fluids and clasts may have prevailed in narrow, sub-mm wide veinlets crosscutting the samples; internal element sources cannot be ruled out in these cases.

The compositions of venting fluids across the forearc fundamentally change in response to pressure and temperature conditions within the subduction channel (e.g., Mottl et al., 2004; Hulme et al., 2010; Fryer et al., 2018a). However, it is likely that fluid compositions at depth differ from what has been measured in seafloor samples (see above). Initial fluid compositions are altered by metamorphic, metasomatic, and mineral dissolution and precipitation processes occurring in the forearc (e.g., Kahl et al., 2015). Low measured pore water element concentrations at the serpentinite mud volcanoes may hence either indicate that no significant amounts of the respective species to have been released from the slab or that these were exhausted on their way to the seafloor.

3.5.6 Implications for carbon cycling

Based on the pore water compositions of the Mariana serpentinite mud volcanoes, it has been suggested that the decarbonation of the subducted slab initiates at depths of <30 km (e.g., Mottl et al., 2004; Hulme et al., 2010; Fryer et al., 2018a). The examination of the deep carbonate precipitates formed within the subduction channel provides information on geochemical conditions at depths of ~14 to 19 km and potential C sources. Samples from these shallow slab depths have not yet been described and hence shallow decarbonation processes have not been assessed. Geochemical modeling, experiments, and field evidence have focused on potential C mobilization at greater depths and temperatures of >300 °C (e.g., Ague and Nicolescu, 2014; Dasgupta et al., 2004; Frezzotti et al., 2011; Gorman et al., 2006; Molina and Poli, 2000; Newton and Manning, 2002; Piccoli et al., 2016; Schwarzenbach et al., 2018; Sieber et al., 2018; Sverjensky et al., 2014; Kerrick and Connolly, 2001). Budgets for the deep carbon cycle are hence plagued by very large uncertainties (e.g., Dasgupta and Hirschmann, 2010; Füre et al., 2010; Kelemen and Manning, 2015). Our data provide an important asset on understanding the transfer of carbonic fluids from the subducting slab and reactions of these fluids with rocks in the subduction channel. The data show that C is mobilized from the downgoing slab at subduction depths as low as ~14 km and lower blueschist facies temperatures within the Mariana subduction system. The mobilization of C at these low metamorphic grades is in accordance with experiments by Caciagli and Manning (2003), who showed that calcite solubility increases with pressure and temperature at pressures ≥ 0.3 GPa. Some of the mobilized C subsequently rises through the forearc with upwelling fluids and is either incorporated into carbonate precipitates within the serpentinite mud volcanoes or reduced to methane and transported back to the seafloor by serpentinite mud volcano activity (Mottl et al., 2004; Hulme et al., 2010; Fryer et al., 2018a). The abundance of carbonate veins in clasts from mud volcanoes with slab depths of ≥ 14 km reveal that the portion of C that is trapped by carbonate mineralization within the subduction channel is likely large. The REE characteristics of these carbonates indicate that the redox conditions within the subduction channel are oxic and within the stability field of DIC (and not methane). Carbon isotope compositions ($\delta^{13}\text{C} = -0.6$ to $+3.3\text{‰}$) also show that CO_2 reduction, which would deplete ^{12}C from the DIC pool, does not take place. Carbonate materials with similar isotopic compositions were described from South Chamorro ($\delta^{13}\text{C} = +0.07$ to $+2.5\text{‰}$; ~18 km depth to slab; Alt and Shanks III, 2006)

and carbonate veins in clasts of metasediment were also recovered from Conical (~19 km depth to slab; Shipboard Scientific Party, 1990). The presence of these attest that the mobilization of C continues at greater depths. The bulk of these carbonates presumably is not entrained into the serpentinite mud volcano conduits and remains at depth and may even be subducted further in the system.

The global significance of this process and its weight in the deep carbon cycle can, however, not yet be predicted reliably. Kelemen and Manning (2015) estimated the global C loss from forearcs to up to 12 Mt C a^{-1} . This budget includes C loss due to venting of carbonic fluids as it occurs in the Mariana forearc, but does not cover the solid storage of C within the shallow portions of subduction systems. Our study highlights that additional work is needed to better understand the shallow processes.

3.6 Conclusions

We studied clasts recovered from serpentinite mud volcanoes at the Mariana forearc that provide insight into shallow subduction zone processes. The clasts include serpentinite, metavolcanic, and metasedimentary lithologies that host carbonate \pm silicate \pm sulfate veins. The samples can be subdivided into two groups:

- (i) Veins comprising 'deep' carbonates are present in metavolcanic and -sedimentary clasts from the subducting Pacific plate. Phase assemblages, euhedral textures, and geochemical data suggest that these veins formed within the subduction channel after the clasts were detached from subducted lithosphere. Negative Ce anomalies in carbonate and the co-occurrence of sulfate imply precipitation under oxic conditions, and carbonate O isotopic compositions imply temperatures of ~130 to 300 °C. This is consistent with carbonate Sr isotopic compositions that indicate considerable exchange of Sr between seawater-derived fluids and rock within the slab and subduction channel. Mass transfers from the subducting Pacific slab to the subduction channel are particularly apparent for C, Sr, SO_4^{2-} , Ba, and REEs; C is inorganic and is likely derived from the decarbonation of carbonaceous sediment and/or oceanic crust.
- (ii) 'Shallow' carbonates are mainly hosted by ultramafic clasts from the forearc mantle of the Philippine Sea plate. Geochemical data and isotopic compositions indicate precipitation of these veins due to mixing between slab-derived fluids and seawater. REE+Y patterns are similar to those of acicular aragonite and calcite that formed at ambient seawater temperatures within the serpentinite mudflows. Carbon incorporated in these carbonates is inorganic; it may be slab-derived or from sourced from seawater.

Our data attest the mobilization of C from the downgoing slab at subduction depths of <20 km and low metamorphic grades (lower blueschist facies temperatures or below) within the Mariana subduction system. Some of the mobilized C subsequently rises through the forearc with upwelling fluids (e.g., Mottl et al., 2004; Hulme et al., 2010; Fryer et al., 2018a) and is either incorporated into carbonate precipitates within the serpentinite mud volcanoes or is transported back into the short-term carbon cycle as

the fluids vent at the seafloor. But another portion of the mobilized C is trapped in carbonate mineralizations that form under oxic conditions within the subduction channel. The bulk of these carbonates presumably remains at depth and may even be subducted further in the system.

Acknowledgements

We are grateful to the captain and crew of the *JOIDES Resolution*, to the co-chief scientists P. Fryer and G. Wheat and the members of the Science Party. Henning Kuhnert and Harald Strauß are thanked for the analyses of C, O, and S isotopes, respectively, and Patrick Monien for help with LA-ICP-MS analyses. This research used samples and data provided by IODP. E. A. received financial support by GLOMAR – Bremen International Graduate School for Marine Sciences. Funding was provided by the Deutsche Forschungsgemeinschaft (German Research Foundation), grant BA 1605/18-1, to W. B.

References

- Ague, J. J., Nicolescu, S., 2014. Carbon dioxide released from subduction zones by fluid-mediated reactions. *Nat. Geosci.* 7 (5), 355, doi:[10.1038/ngeo2143](https://doi.org/10.1038/ngeo2143).
- Alt, J., Shanks III, W., 2006. Stable isotope compositions of serpentinite seamounts in the Mariana forearc: serpentinization processes, fluid sources and sulfur metasomatism. *Earth Planet. Sci. Lett.* 242 (3–4), 272–285, doi:[10.1016/j.epsl.2005.11.063](https://doi.org/10.1016/j.epsl.2005.11.063).
- Alt, J. C., Teagle, D. A. H., 1999. The uptake of carbon during alteration of ocean crust. *Geochim. Cosmochim. Acta* 63 (10), 1527–1535, doi:[10.1016/s0016-7037\(99\)00123-4](https://doi.org/10.1016/s0016-7037(99)00123-4).
- Austrheim, H., Prestvik, T., 2008. Rodingitization and hydration of the oceanic lithosphere as developed in the Leka ophiolite, north-central Norway. *Lithos* 104 (1–4), 177–198, doi:[10.1016/j.lithos.2007.12.006](https://doi.org/10.1016/j.lithos.2007.12.006).
- Bach, W., Klein, F., 2009. The petrology of seafloor rodingites: insights from geochemical reaction path modeling. *Lithos* 112 (1–2), 103–117, doi:[10.1016/j.lithos.2008.10.022](https://doi.org/10.1016/j.lithos.2008.10.022).
- Bach, W., Rosner, M., Jöns, N., Rausch, S., Robinson, L. F., Paulick, H., Erzinger, J., 2011. Carbonate veins trace seawater circulation during exhumation and uplift of mantle rock: results from ODP Leg 209. *Earth Planet. Sci. Lett.* 311 (3–4), 242–252, doi:[10.1016/j.epsl.2011.09.021](https://doi.org/10.1016/j.epsl.2011.09.021).
- Ballirano, P., De Vito, C., Ferrini, V., Mignardi, S., 2010. The thermal behaviour and structural stability of nesquehonite, $\text{MgCO}_3 \cdot 3\text{H}_2\text{O}$, evaluated by *in situ* laboratory parallel-beam x-ray powder diffraction: new constraints on CO_2 sequestration within minerals. *J. Hazard. Mater.* 178 (1–3), 522–528, doi:[10.1016/j.jhazmat.2010.01.113](https://doi.org/10.1016/j.jhazmat.2010.01.113).
- Bebout, G. E., Barton, M. D., 1989. Fluid flow and metasomatism in a subduction zone hydrothermal system: Catalina Schist terrane, California. *Geology* 17 (11), 976–980, doi:[10.1130/0091-7613\(1989\)017<0976:ffamia>2.3.co;2](https://doi.org/10.1130/0091-7613(1989)017<0976:ffamia>2.3.co;2).
- Bird, D. K., Spieler, A. R., 2004. Epidote in geothermal systems. *Rev. Mineral. Geochem.* 56 (1), 235–300, doi:[10.2138/gsrmg.56.1.235](https://doi.org/10.2138/gsrmg.56.1.235).
- Black, P. M., 1977. Regional high-pressure metamorphism in New Caledonia: phase equilibria in the Ouégoa District. *Tectonophysics* 43 (1–2), 89–107, doi:[10.1016/0040-1951\(77\)90007-5](https://doi.org/10.1016/0040-1951(77)90007-5).
- Blundy, J., Cashman, K. V., Rust, A., Witham, F., 2010. A case for CO_2 -rich arc magmas. *Earth Planet. Sci. Lett.* 290 (3–4), 289–301, doi:[10.1016/j.epsl.2009.12.013](https://doi.org/10.1016/j.epsl.2009.12.013).
- Caciagli, N. C., Manning, C. R., 2003. The solubility of calcite in water at 6–16 kbar and 500–800 °C. *Contrib. Mineral. Petrol.* 146 (3), 275–285, doi:[10.1007/s00410-003-0501-y](https://doi.org/10.1007/s00410-003-0501-y).

- Cook-Kollars, J., Bebout, G. E., Collins, N. C., Angiboust, S., Agard, P., 2014. Subduction zone metamorphic pathway for deep carbon cycling: I. Evidence from HP/UHP metasedimentary rocks, Italian Alps. *Chem. Geol.* 386, 31–48, doi:[10.1016/j.chemgeo.2014.07.013](https://doi.org/10.1016/j.chemgeo.2014.07.013).
- Craw, D., Landis, C. A., 1980. Authigenic pectolite, stevensite, and pyroaurite in a Quaternary debris flow, Southland, New Zealand. *J. Sediment. Res.* 50 (2), 497–503, doi:[10.1306/212f7a3b-2b24-11d7-8648000102c1865d](https://doi.org/10.1306/212f7a3b-2b24-11d7-8648000102c1865d).
- Dasgupta, R., Hirschmann, M. M., 2010. The deep carbon cycle and melting in Earth's interior. *Earth Planet. Sci. Lett.* 298 (1–2), 1–13, doi:[10.1016/j.epsl.2010.06.039](https://doi.org/10.1016/j.epsl.2010.06.039).
- Dasgupta, R., Hirschmann, M. M., Withers, A. C., 2004. Deep global cycling of carbon constrained by the solidus of anhydrous, carbonated eclogite under upper mantle conditions. *Earth Planet. Sci. Lett.* 227 (1–2), 73–85, doi:[10.1016/j.epsl.2004.08.004](https://doi.org/10.1016/j.epsl.2004.08.004).
- Dasgupta, R., Jackson, M. G., Lee, C.-T. A., 2010. Major element chemistry of ocean island basalts – conditions of mantle melting and heterogeneity of mantle source. *Earth Planet. Sci. Lett.* 289 (3–4), 377–392, doi:[10.1016/j.epsl.2009.11.027](https://doi.org/10.1016/j.epsl.2009.11.027).
- Davies, P. J., Bubela, B., 1973. The transformation of nesquehonite into hydromagnesite. *Chem. Geol.* 12 (4), 289–300, doi:[10.1016/0009-2541\(73\)90006-5](https://doi.org/10.1016/0009-2541(73)90006-5).
- Debret, B., Albers, E., Walter, B., Price, R., Barnes, J. D., Beunon, H., Facq, S., Gillikin, D. P., Mattielli, N., Williams, H., 2019. Shallow forearc mantle dynamics and geochemistry: new insights from IODP Expedition 366. *Lithos* 326–327, 230–245, doi:[10.1016/j.lithos.2018.10.038](https://doi.org/10.1016/j.lithos.2018.10.038).
- Deniel, C., Pin, C., 2001. Single-stage method for the simultaneous isolation of lead and strontium from silicate samples for isotopic measurements. *Anal. Chim. Acta* 426 (1), 95–103, doi:[10.1016/s0003-2670\(00\)01185-5](https://doi.org/10.1016/s0003-2670(00)01185-5).
- D'Hondt, S., Rutherford, S., Spivack, A. J., 2002. Metabolic activity of subsurface life in deep-sea sediments. *Science* 295 (5562), 2067–2070, doi:[10.1126/science.1064878](https://doi.org/10.1126/science.1064878).
- Diessel, C. F. K., Brothers, R. N., Black, P. M., 1978. Coalification and graphitization in high-pressure schists in New Caledonia. *Contrib. Mineral. Petrol.* 68 (1), 63–78, doi:[10.1007/bf00375447](https://doi.org/10.1007/bf00375447).
- Essene, E. J., Fyfe, W. S., Turner, F. J., 1965. Petrogenesis of Franciscan glaucophane schists and associated metamorphic rocks, California. *Beitr. Mineral. Petrol.* 11 (7), 695–704, doi:[10.1007/bf01128709](https://doi.org/10.1007/bf01128709).
- Esteban, J. J., Cuevas, J., Tubía, J. M., Yusta, I., 2003. Xonotlite in rodingite assemblages from the Ronda peridotites, Betic Cordilleras, Southern Spain. *Can. Mineral.* 41 (1), 161–170, doi:[10.2113/gscanmin.41.1.161](https://doi.org/10.2113/gscanmin.41.1.161).
- Falk, E. S., Kelemen, P. B., 2015. Geochemistry and petrology of listvenite in the Samail ophiolite, Sultanate of Oman: complete carbonation of peridotite during ophiolite emplacement. *Geochim. Cosmochim. Acta* 160, 70–90, doi:[10.1016/j.gca.2015.03.014](https://doi.org/10.1016/j.gca.2015.03.014).
- Frezzotti, M. L., Selverstone, J., Sharp, Z. D., Compagnoni, R., 2011. Carbonate dissolution during subduction revealed by diamond-bearing rocks from the Alps. *Nat. Geosci.* 4 (10), 703, doi:[10.1038/ngeo1246](https://doi.org/10.1038/ngeo1246).
- Friedman, I., O'Neil, J. R., 1977. Compilation of stable isotope fractionation factors of geochemical interest. In: Fleischer, M. (Ed.), *Data of geochemistry*, 6th Edition. No. 440 in Geological Survey Professional Paper. Geological Survey.
- Fryer, P., Ambos, E. L., Husson, D. M., 1985. Origin and emplacement of Mariana forearc seamounts. *Geology* 13 (11), 774–777, doi:[10.1130/0091-7613\(1985\)13<774:oaomf>2.0.co;2](https://doi.org/10.1130/0091-7613(1985)13<774:oaomf>2.0.co;2).
- Fryer, P., Fryer, G. J., 1987. Origins of nonvolcanic seamounts in a forearc environment. *Seamounts, Islands, and Atolls* 43, 61–69, doi:[10.1029/gm043p0061](https://doi.org/10.1029/gm043p0061).
- Fryer, P., Mottl, M., Johnson, L., Haggerty, J., Phipps, S., Maekawa, H., 1995. Serpentine bodies in the forearcs of western Pacific convergent margins: origin and associated fluids. *Geoph. Monog. Series* 88, 259–279, doi:[10.1029/gm088p0259](https://doi.org/10.1029/gm088p0259).
- Fryer, P., Pearce, J. A., Stokking, L. B. (Eds.), 1990. Initial Reports. Vol. 125 of Proc. ODP. Ocean Drilling Program, College Station (TX).
- Fryer, P., Wheat, C. G., Williams, T., Albers, E., Bekins, B., Debret, B. P. R., Deng, J., Dong, Y., Eickenbusch, P., Frery, E. A., Ichiyama, Y., Jonson, K., Jonston, R. M., Kevorkian, R. T., Kurz, W.,

- Magalhaes, V., Mantovanelli, S. S., Menapace, W., Menzies, C. D., Michibayashi, K., Moyer, C. L., Mullane, K. K., Park, J.-W., Price, R. E., Ryan, J. G., Shervais, J. W., Sissmann, O. J., Suzuki, S., Takai, K., Walter, B., Zhang, R., 2018a. Expedition 366 summary. Vol. 366 of Proc. IODP. International Ocean Discovery Program, College Station (TX). doi:[10.14379/iodp.proc.366.101.2018](https://doi.org/10.14379/iodp.proc.366.101.2018).
- Fryer, P., Wheat, C. G., Williams, T., Albers, E., Bekins, B., Debret, B. P. R., Deng, J., Dong, Y., Eickenbusch, P., Frery, E. A., Ichiyama, Y., Jonson, K., Jonston, R. M., Kevorkian, R. T., Kurz, W., Magalhaes, V., Mantovanelli, S. S., Menapace, W., Menzies, C. D., Michibayashi, K., Moyer, C. L., Mullane, K. K., Park, J.-W., Price, R. E., Ryan, J. G., Shervais, J. W., Sissmann, O. J., Suzuki, S., Takai, K., Walter, B., Zhang, R., 2018b. Expedition 366 methods. Vol. 366 of Proc. IODP. International Ocean Discovery Program, College Station (TX). doi:[10.14379/iodp.proc.366.102.2018](https://doi.org/10.14379/iodp.proc.366.102.2018).
- Fryer, P., Wheat, C. G., Williams, T., Albers, E., Bekins, B., Debret, B. P. R., Deng, J., Dong, Y., Eickenbusch, P., Frery, E. A., Ichiyama, Y., Jonson, K., Jonston, R. M., Kevorkian, R. T., Kurz, W., Magalhaes, V., Mantovanelli, S. S., Menapace, W., Menzies, C. D., Michibayashi, K., Moyer, C. L., Mullane, K. K., Park, J.-W., Price, R. E., Ryan, J. G., Shervais, J. W., Sissmann, O. J., Suzuki, S., Takai, K., Walter, B., Zhang, R., 2018c. Site U1492. Vol. 366 of Proc. IODP. International Ocean Discovery Program, College Station (TX). doi:[10.14379/iodp.proc.366.105.2018](https://doi.org/10.14379/iodp.proc.366.105.2018).
- Fryer, P., Wheat, C. G., Williams, T., Albers, E., Bekins, B., Debret, B. P. R., Deng, J., Dong, Y., Eickenbusch, P., Frery, E. A., Ichiyama, Y., Jonson, K., Jonston, R. M., Kevorkian, R. T., Kurz, W., Magalhaes, V., Mantovanelli, S. S., Menapace, W., Menzies, C. D., Michibayashi, K., Moyer, C. L., Mullane, K. K., Park, J.-W., Price, R. E., Ryan, J. G., Shervais, J. W., Sissmann, O. J., Suzuki, S., Takai, K., Walter, B., Zhang, R., 2018d. Sites U1493, U1494, and U1495. Vol. 366 of Proc. IODP. International Ocean Discovery Program, College Station (TX). doi:[10.14379/iodp.proc.366.106.2018](https://doi.org/10.14379/iodp.proc.366.106.2018).
- Fryer, P., Wheat, C. G., Williams, T., Albers, E., Bekins, B., Debret, B. P. R., Deng, J., Dong, Y., Eickenbusch, P., Frery, E. A., Ichiyama, Y., Jonson, K., Jonston, R. M., Kevorkian, R. T., Kurz, W., Magalhaes, V., Mantovanelli, S. S., Menapace, W., Menzies, C. D., Michibayashi, K., Moyer, C. L., Mullane, K. K., Park, J.-W., Price, R. E., Ryan, J. G., Shervais, J. W., Sissmann, O. J., Suzuki, S., Takai, K., Walter, B., Zhang, R., 2018e. Site U1496. Vol. 366 of Proc. IODP. International Ocean Discovery Program, College Station (TX). doi:[10.14379/iodp.proc.366.107.2018](https://doi.org/10.14379/iodp.proc.366.107.2018).
- Fryer, P. B., 1992. A synthesis of Leg 125 drilling of serpentinite seamounts on the Mariana and Izu-Bonin forearcs. In: Fryer, P., Pearce, J. A., Stokking, L. B. (Eds.), *Scientific Results*. Vol. 125 of Proc. ODP. Ocean Drilling Program, College Station (TX), pp. 593–614. doi:[10.2973/odp.proc.sr.125.168.1992](https://doi.org/10.2973/odp.proc.sr.125.168.1992).
- Fryer, P. B., 1996. Evolution of the Mariana convergent plate margin system. *Rev. Geophys.* 34 (1), 89–125, doi:[10.1029/95rg03476](https://doi.org/10.1029/95rg03476).
- Fryer, P. B., Gharib, J., Ross, K., Savov, I., Mottl, M. J., 2006. Variability in serpentinite mudflow mechanisms and sources: ODP drilling results on Mariana forearc seamounts. *Geochem. Geophys. Geosyst.* 7 (8), Q08014, doi:[10.1029/2005gc001201](https://doi.org/10.1029/2005gc001201).
- Fryer, P. B., Wheat, C. G., Mottl, M. J., 1999. Mariana blueschist mud volcanism: implications for conditions within the subduction zone. *Geology* 27 (2), 103–106, doi:[10.1130/0091-7613\(1999\)027<0103:mbmvif>2.3.co;2](https://doi.org/10.1130/0091-7613(1999)027<0103:mbmvif>2.3.co;2).
- Füri, E., Hilton, D. R., Tryon, M. D., Brown, K. M., McMurtry, G. M., Brückmann, W., Wheat, C. G., 2010. Carbon release from submarine seeps at the Costa Rica fore arc: implications for the volatile cycle at the Central America convergent margin. *Geochem. Geophys. Geosyst.* 11 (4), Q04S21, doi:[10.1029/2009gc002810](https://doi.org/10.1029/2009gc002810).
- Gharib, J., 2006. *Clastic metabasites and authigenic minerals within serpentinite protrusions from the Mariana forearc: implications for sub-forearc subduction processes*. PhD Thesis, University of Hawai'i, Honolulu, HI.
- Gorman, P. J., Kerrick, D. M., Connolly, J. A. D., 2006. Modeling open system metamorphic decarbonation of subducting slabs. *Geochem. Geophys. Geosyst.* 7 (4), Q04007, doi:[10.1029/2005gc001125](https://doi.org/10.1029/2005gc001125).
- Grossman, E. L., Ku, T.-L., 1986. Oxygen and carbon isotope fractionation in biogenic aragonite: temperature effects. *Chem. Geol.* 59, 59–74, doi:[10.1016/0168-9622\(86\)90057-6](https://doi.org/10.1016/0168-9622(86)90057-6).
- Haggerty, J. A., 1987. Petrology and geochemistry of Neocene sedimentary rocks from Mariana forearc seamounts: implications for emplacement of the seamounts. *Geoph. Monog. Series 4*, 175–185, doi:[10.1029/87MP0001](https://doi.org/10.1029/87MP0001).

- [1029/gm043p0175](#).
- Haggerty, J. A., 1991. Evidence from fluid seeps atop serpentine seamounts in the Mariana forearc: clues for emplacement of the seamounts and their relationship to forearc tectonics. *Mar. Geol.* 102, 293–309, doi:[10.1016/0025-3227\(91\)90013-t](#).
- Harris, M., Coggon, R. M., Smith-Duque, C. E., Cooper, M. J., Milton, J. A., Teagle, D. A. H., 2015. Channelling of hydrothermal fluids during the accretion and evolution of the upper oceanic crust: Sr isotope evidence from ODP Hole 1256D. *Earth Planet. Sci. Lett.* 416, 56–66, doi:[10.1016/j.epsl.2015.01.042](#).
- Helgeson, H. C., Owens, C. E., Knox, A. M., Richard, L., 1998. Calculation of the standard molal thermodynamic properties of crystalline, liquid, and gas organic molecules at high temperatures and pressures. *Geochim. Cosmochim. Acta* 62 (6), 985–1081, doi:[10.1016/s0016-7037\(97\)00219-6](#).
- Hulme, S. M., Wheat, C. G., Fryer, P. B., Mottl, M. J., 2010. Pore water chemistry of the Mariana serpentinite mud volcanoes: a window to the seismogenic zone. *Geochem. Geophys. Geosyst.* 11 (1), Q01X09, doi:[10.1029/2009gc002674](#).
- Jochum, K. P., Weis, U., Stoll, B., Kuzmin, D., Yang, Q., Raczek, I., Jacob, D. E., Stracke, A., Birbaum, K., Frick, D. A., Günther, D., Enzweiler, J., 2011. Determination of reference values for NIST SRM 610–617 glasses following ISO guidelines. *Geostand. Geoanal. Res.* 35 (4), 397–429, doi:[10.1111/j.1751-908x.2011.00120.x](#).
- Johnson, J. W., Oelkers, E. H., Helgeson, H. C., 1992. SUPCRT92: a software package for calculating the standard molal thermodynamic properties of minerals, gases, aqueous species, and reactions from 1 to 5000 bar and 0 to 1000 °C. *Comput. Geosci.* 18 (7), 899–947, doi:[10.1016/0098-3004\(92\)90029-q](#).
- Kahl, W.-A., Jöns, N., Bach, W., Klein, F., Alt, J. C., 2015. Ultramafic clasts from the South Chamorro serpentinite mud volcano reveal a polyphase serpentinization history of the Mariana forearc mantle. *Lithos* 227, 1–20, doi:[10.1016/j.lithos.2015.03.015](#).
- Karpoff, A. M., France-Lanord, C., Lothe, F., Karcher, P., 1992. Miocene tuff from Mariana basin, Leg 129, Site 802: a first deep-sea occurrence of thaumasite. In: Larson, R. L., Lancelot, Y. (Eds.), *Sci. Res. Vol. 129 of Proc. ODP. Ocean Drilling Program, College Station (TX)*, pp. 119–135. doi:[10.2973/odp.proc.sr.129.113.1992](#).
- Kastner, M., 1981. Authigenic silicates in deep-sea sediments: formation and diagenesis. In: Emiliani, C. (Ed.), *The sea, vol. 7: the oceanic lithosphere*. Wiley, London, pp. 515–980.
- Kawagucci, S., Miyazaki, J., Morono, Y., Seewald, J. S., Wheat, C. G., Takai, K., 2018. Cool, alkaline serpentinite formation fluid regime with scarce microbial habitability and possible abiotic synthesis beneath the south chamorro seamount. *Prog. Earth Planet. Sci.* 5, 74, doi:[10.1186/s40645-018-0232-3](#).
- Kelemen, P. B., Manning, C. E., 2015. Reevaluating carbon fluxes in subduction zones, what goes down, mostly comes up. *Proc. Natl. Acad. Sci.* 112 (30), E3997–E4006, doi:[10.1073/pnas.1507889112](#).
- Kerrick, D. M., Connolly, J. A. D., 1998. Subduction of ophicarbonates and recycling of CO₂ and H₂O. *Geology* 26 (4), 375–378, doi:[10.1130/0091-7613\(1998\)026<0375:sooaro>2.3.co;2](#).
- Kerrick, D. M., Connolly, J. A. D., 2001. Metamorphic devolatilization of subducted marine sediments and the transport of volatiles into the Earth's mantle. *Nature* 411 (6835), 293–296, doi:[10.1038/35077056](#).
- Klein, F., Garrido, C. J., 2011. Thermodynamic constraints on mineral carbonation of serpentinized peridotite. *Lithos* 126, 147–160, doi:[10.1016/j.lithos.2011.07.020](#).
- Klein, F., McCollom, T. M., 2013. From serpentinization to carbonation: new insights from a CO₂ injection experiment. *Earth Planet. Sci. Lett.* 379, 137–145, doi:[10.1016/j.epsl.2013.08.017](#).
- Lafuente, B., Downs, R. T., Yang, H., Stone, N., 2016. The power of databases: the RRUFF project. In: *Highlights in mineralogical crystallography*. De Gruyter, pp. 1–29. doi:[10.1515/9783110417104-003](#).
- Leterrier, J., Maury, R. C., Thonon, P., Girard, D., Marchal, M., 1982. Clinopyroxene composition as a method of identification of the magmatic affinities of paleo-volcanic series. *Earth Planet. Sci. Lett.* 59 (1), 139–154, doi:[10.1016/0012-821x\(82\)90122-4](#).
- Maekawa, H., Fryer, P. B., Ozaki, A., 1995. Incipient blueschist-facies metamorphism in the active subduction zone beneath the Mariana forearc. In: Taylor, B., Natland, J. (Eds.), *Active margins and marginal basins of the western Pacific*. Vol. 88. pp. 281–289. doi:[10.1029/gm088p0281](#).
- Maekawa, H., Masaya, S., Ishill, T., Fryer, P., Pearce, J. A., 1993. Blueschist metamorphism in an active

- subduction zone. *Nature* 364, 520–523, doi:[10.1038/364520a0](https://doi.org/10.1038/364520a0).
- McArthur, J. M., Howarth, R. J., Bailey, T. R., 2001. Strontium isotope stratigraphy: LOWESS version 3: best fit to the marine Sr-isotope curve for 0–509 Ma and accompanying look-up table for deriving numerical age. *J. Geol.* 109 (2), 155–170, doi:[10.1086/319243](https://doi.org/10.1086/319243).
- McCollom, T. M., Bach, W., 2009. Thermodynamic constraints on hydrogen generation during serpentinization of ultramafic rocks. *Geochim. Cosmochim. Acta* 73 (3), 856–875, doi:[10.1016/j.gca.2008.10.032](https://doi.org/10.1016/j.gca.2008.10.032).
- McDonough, W. F., Sun, S., 1995. The composition of the Earth. *Chem. Geol.* 120 (3–4), 223–253, doi:[10.1016/0009-2541\(94\)00140-4](https://doi.org/10.1016/0009-2541(94)00140-4).
- Molina, J. F., Poli, S., 2000. Carbonate stability and fluid composition in subducted oceanic crust: an experimental study on H₂O–CO₂-bearing basalts. *Earth Planet. Sci. Lett.* 176 (3), 295–310, doi:[10.1016/s0012-821x\(00\)00021-2](https://doi.org/10.1016/s0012-821x(00)00021-2).
- Mottl, M. J., Komor, S. C., Fryer, P., Moyer, C. L., 2003. Deep-slab fluids fuel extremophilic *Archaea* on a Mariana forearc serpentinite mud volcano: Ocean Drilling Program Leg 195. *Geochem. Geophys. Geosyst.* 4 (11), 9009, doi:[10.1029/2003gc000588](https://doi.org/10.1029/2003gc000588).
- Mottl, M. J., Wheat, C. G., Fryer, P. B., Gharib, J., Martin, J. B., 2004. Chemistry of springs across the Mariana forearc shows progressive devolatilization of the subducting plate. *Geochim. Cosmochim. Acta* 68 (23), 4915–4933, doi:[10.1016/j.gca.2004.05.037](https://doi.org/10.1016/j.gca.2004.05.037).
- Müller, R. D., Sdrolias, M., Gaina, C., Roest, W. R., 2008. Age, spreading rates, and spreading asymmetry of the world's ocean crust. *Geochem. Geophys. Geosyst.* 9 (4), Q04006, doi:[10.1029/2007gc001743](https://doi.org/10.1029/2007gc001743).
- Newton, R. C., Manning, C. E., 2002. Experimental determination of calcite solubility in H₂O–NaCl solutions at deep crust/upper mantle pressures and temperatures: implications for metasomatic processes in shear zones. *Am. Mineral.* 87 (10), 1401–1409, doi:[10.2138/am-2002-1016](https://doi.org/10.2138/am-2002-1016).
- Noack, Y., 1983. Occurrence of thaumasite in a seawater–basalt interaction, Mururoa atoll (French Polynesia, South Pacific). *Mineral. Mag.* 47 (342), 47–50, doi:[10.1180/minmag.1983.047.342.0](https://doi.org/10.1180/minmag.1983.047.342.0).
- Oakley, A. J., Taylor, B., Fryer, P. B., Moore, G. F., Goodliffe, A. M., Morgan, J. K., 2007. Emplacement, growth, and gravitational deformation of serpentinite seamounts on the Mariana forearc. *Geophys. J. Int.* 170 (2), 615–634, doi:[10.1111/j.1365-246x.2007.03451.x](https://doi.org/10.1111/j.1365-246x.2007.03451.x).
- Oakley, A. J., Taylor, B., Moore, G. F., 2008. Pacific plate subduction beneath the central Mariana and Izu-Bonin fore arcs: new insights from an old margin. *Geochem. Geophys. Geosyst.* 9 (6), Q06003, doi:[10.1029/2007gc001820](https://doi.org/10.1029/2007gc001820).
- O'Neil, J. R., Clayton, R. N., Mayeda, T. K., 1969. Oxygen isotope fractionation in divalent metal carbonates. *J. Chem. Phys.* 51 (12), 5547–5558, doi:[10.1063/1.1671982](https://doi.org/10.1063/1.1671982).
- Pälike, H., Lyle, M. W., Nishi, H., Raffi, I., Ridgwell, A., Gamage, K., Klaus, A., Acton, G., Anderson, L., Backman, J., Baldauf, J., Beltran, C., Bohaty, S. M., Bown, P., Busch, W., CHannell, J. E. T., Chun, O. J., Delaney, M., Dewangan, P., Jones, T. D., Edgar, K. M., Evans, H., Fitch, P., Foser, G. L., Gussone, N., Hasegawa, H., Hathorne, E. D., Hayashi, H., Herrle, J. O., Holbourn, A., Hovan, S., Hyeong, K., Iijima, K., Ito, T., Kamikuri, S.-i., Kimoto, K., Kuroda, J., Leon-Rodriguez, L., Malinverno, A., Moore Jr., T. C., Murphy, B. H., Murphy, D. P., Nakamura, H., Ogane, K., Ohneiser, C., Richter, C., Robinson, R., Rohling, E. J., Romero, O., Sawada, K., Scher, H., Schneider, L., Sluijs, A., Takata, H., Tian, J., Tsujimoto, A., Wade, B. S., Westerhold, T., Wilkens, R., Williams, T., Wilson, P. A., Yamamoto, Y., Yamamoto, S., Yamazaki, T., Zeebe, R. E., 2012. A Cenozoic record of the equatorial Pacific carbonate compensation depth. *Nature* 488 (7413), 609–614, doi:[10.1038/nature11360](https://doi.org/10.1038/nature11360).
- Paytan, A., Kastner, M., Campbell, D., Thiemens, M. H., 2004. Seawater sulfur isotope fluctuations in the Cretaceous. *Science* 304 (5677), 1663–1665, doi:[10.1126/science.1095258](https://doi.org/10.1126/science.1095258).
- Piccoli, F., Brovarone, A. V., Beyssac, O., Martinez, I., Ague, J. J., Chaduteau, C., 2016. Carbonation by fluid-rock interactions at high-pressure conditions: implications for carbon cycling in subduction zones. *Earth Planet. Sci. Lett.* 445, 146–159, doi:[10.1016/j.epsl.2016.03.045](https://doi.org/10.1016/j.epsl.2016.03.045).
- Piepgras, D. J., Jacobsen, S. T., 1992. The behavior of rare earth elements in seawater: precise determination of variations in the North Pacific water column. *Geochim. Cosmochim. Acta* 56 (5), 1851–1862, doi:[10.1016/0016-7037\(92\)90315-a](https://doi.org/10.1016/0016-7037(92)90315-a).
- Plank, T., Langmuir, C. H., 1998. The chemical composition of subducting sediment and its consequences for the crust and mantle. *Chem. Geol.* 145 (3), 325–394, doi:[10.1016/s0009-2541\(97\)00150-2](https://doi.org/10.1016/s0009-2541(97)00150-2).

- Pons, M.-L., Quitté, G., Fujii, T., Rosing, M. T., Reynard, B., Moynier, C. D., Albarède, F., 2011. Early Archean serpentine mud volcanoes at Isua, Greenland, as a niche for early life. *Proc. Natl. Acad. Sci.* 108 (43), 17639–17643, doi:[10.1073/pnas.1108061108](https://doi.org/10.1073/pnas.1108061108).
- Rausch, S., 2012. Carbonate veins as recorders of seawater evolution, CO₂ uptake by the ocean crust, and seawater-crust interaction during low-temperature alteration. PhD Thesis, Bremen.
- Robie, R. A., Hemingway, B. S., 1995. Thermodynamic properties of minerals and related substances at 298.15 k and 1 bar (10⁵ pascals) pressure and at higher temperatures. USGS Bulletin 2131, doi:[10.3133/b2131](https://doi.org/10.3133/b2131).
- Robie, R. A., Hemingway, B. S., Fisher, J. R., 1978. Thermodynamic properties of minerals and related substances at 298.15 k and 1 bar (10⁵ pascals) pressure and at higher temperatures. USGS Bulletin 1452, doi:[10.3133/b1452](https://doi.org/10.3133/b1452).
- Schmidt, T., Lothenbach, B., Romer, M., Scrivener, K., Rentsch, D., Figi, R., 2008. A thermodynamic and experimental study of the conditions of thaumasite formation. *Cem. Concr. Res.* 38 (3), 337–349, doi:[10.1016/j.cemconres.2007.11.003](https://doi.org/10.1016/j.cemconres.2007.11.003).
- Schroeder, T., Bach, W., Jöns, N., Jöns, S., Monien, P., Klügel, A., 2015. Fluid circulation and carbonate vein precipitation in the footwall of an oceanic core complex, Ocean Drilling Program Site 1275, Mid-Atlantic Ridge. *Geochem. Geophys. Geosyst.* 16 (10), 3716–3732, doi:[10.1002/2015gc006041](https://doi.org/10.1002/2015gc006041).
- Schwarzenbach, E. M., Caddick, M. J., Petroff, M., Gill, B. C., Cooperdock, E. H. G., Barnes, J. D., 2018. Sulphur and carbon cycling in the subduction zone mélange. *Sci. Rep.* 8 (1), 15517, doi:[10.1038/s41598-018-33610-9](https://doi.org/10.1038/s41598-018-33610-9).
- Shipboard Scientific Party, 1990. Site 780. In: Fryer, P., Pearce, J. A., Stokking, L. B. (Eds.), *Init. Rep. Vol. 125 of Proc. ODP. Ocean Drilling Program, College Station (TX)*, pp. 147–178. doi:[10.2973/odp.proc.ir.125.108.1990](https://doi.org/10.2973/odp.proc.ir.125.108.1990).
- Shipboard Scientific Party, 2000. Leg 185 summary: inputs to the Izu-Mariana subduction system. In: Plank, T., Ludden, J. N., Escutia, C. (Eds.), *Init. Rep. Vol. 185 of Proc. ODP. Ocean Drilling Program, College Station (TX)*, pp. 1–63. doi:[10.2973/odp.proc.ir.185.101.2000](https://doi.org/10.2973/odp.proc.ir.185.101.2000).
- Shock, E. L., Helgeson, H. C., 1988. Calculation of the thermodynamic and transport properties of aqueous species at high pressures and temperatures: correlation algorithms for ionic species and equation of state predictions to 5 kb and 1000 °C. *Geochim. Cosmochim. Acta* 52 (8), 2009–2036, doi:[10.1016/0016-7037\(88\)90181-0](https://doi.org/10.1016/0016-7037(88)90181-0).
- Shock, E. L., Sassani, D. C., Willis, M., Sverjensky, D. A., 1997. Inorganic species in geologic fluids: correlations among standard molal thermodynamic properties of aqueous ions and hydroxide complexes. *Geochim. Cosmochim. Acta* 61 (5), 907–950, doi:[10.1016/s0016-7037\(96\)00339-0](https://doi.org/10.1016/s0016-7037(96)00339-0).
- Sieber, M. J., Hermann, J., Yaxley, G. M., 2018. An experimental investigation of C–O–H fluid-driven carbonation of serpentinites under forearc conditions. *Earth Planet. Sci. Lett.* 496, 178–188, doi:[10.1016/j.epsl.2018.05.027](https://doi.org/10.1016/j.epsl.2018.05.027).
- Sleep, N. H., Zahnle, K., 2001. Carbon dioxide cycling and implications for climate on ancient Earth. *J. Geophys. Res.* 106 (E1), 1373–1399, doi:[10.1029/2000je001247](https://doi.org/10.1029/2000je001247).
- Stipp, M., Kunze, K., 2008. Dynamic recrystallization near the brittle-plastic transition in naturally and experimentally deformed quartz aggregates. *Tectonophysics* 448 (1–4), 77–97, doi:[10.1016/j.tecto.2007.11.041](https://doi.org/10.1016/j.tecto.2007.11.041).
- Sverjensky, D. A., 1984. Europium redox equilibria in aqueous solution. *Earth Planet. Sci. Lett.* 67 (1), 70–78, doi:[10.1016/0012-821x\(84\)90039-6](https://doi.org/10.1016/0012-821x(84)90039-6).
- Sverjensky, D. A., Stagno, V., Huang, F., 2014. Important role for organic carbon in subduction-zone fluids in the deep carbon cycle. *Nat. Geosci.* 7 (12), 909–913, doi:[10.1038/ngeo2291](https://doi.org/10.1038/ngeo2291).
- Tran, T. H., Kato, K., Wada, H., Fujioka, K., Matsuzaki, H., 2014. Processes involved in calcite and aragonite precipitation during carbonate chimney formation on Conical Seamount, Mariana Forearc: evidence from geochemistry and carbon, oxygen and strontium isotopes. *J. Geochem. Explor.* 137, 55–64, doi:[10.1016/j.gexplo.2013.11.013](https://doi.org/10.1016/j.gexplo.2013.11.013).
- Uyeda, S., Kanamori, H., 1979. Back-arc opening and the mode of subduction. *J. Geophys. Res.* 84 (B3), 1049, doi:[10.1029/jb084ib03p01049](https://doi.org/10.1029/jb084ib03p01049).
- Wheat, C. G., Fournier, T., Paul, C., Menzies, C. D., Price, R. E., Ryan, J. G., Sissman, O. J., 2018. Data

-
- report: IODP Expedition 366 pore water trace element (V, Mo, Rb, Cs, U, Ba, and Li) compositions. Vol. 366 of Proc. IODP. International Ocean Discovery Program, College Station (TX), pp. 1–8. doi:[10.14379/iodp.proc.366.201.2018](https://doi.org/10.14379/iodp.proc.366.201.2018).
- Wilson, S. A., Dipple, G. M., Power, I. M., Thom, J. M., Anderson, R. G., Raudsepp, M., Gabites, J. E., Southam, G., 2009. Carbon dioxide fixation within mine waters of ultramafic-hosted ore deposits: examples from the Clinton Creek and Cassiar Chrysotile deposits, Canada. *Econ. Geol.* 104 (1), 95–112, doi:[10.2113/gsecongeo.104.1.95](https://doi.org/10.2113/gsecongeo.104.1.95).
- Zheng, Y.-F., 1993a. Calculation of oxygen isotope fractionation in anhydrous silicate minerals. *Geochim. Cosmochim. Acta* 57 (5), 1079–1091, doi:[10.1016/0016-7037\(93\)90042-u](https://doi.org/10.1016/0016-7037(93)90042-u).
- Zheng, Y.-F., 1993b. Calculation of oxygen isotope fractionation in hydroxyl-bearing silicates. *Earth Planet. Sci. Lett.* 120 (3–4), 247–263, doi:[10.1016/0012-821x\(93\)90243-3](https://doi.org/10.1016/0012-821x(93)90243-3).
- Zheng, Y.-F., 1999. Oxygen isotope fractionation in carbonate and sulfate minerals. *Geochem. J.* 33 (2), 109–126, doi:[10.2343/geochemj.33.109](https://doi.org/10.2343/geochemj.33.109).

4 Shallow subduction zone serpentinization

<i>Full title</i>	Shallow subduction zone serpentinization traps fluid-mobile elements: implications for element mobilization from serpentinite mud volcanism (Mariana forearc)
<i>Authors</i>	Elmar Albers, ^{*†} Wolf-Achim Kahl, [*] Lena Beyer, ^{*‡} Wolfgang Bach ^{*†}
<i>Affiliations</i>	[*] Department of Geosciences, University of Bremen, Germany; [†] MARUM – Center for Marine Environmental Sciences, Bremen, Germany; [‡] now at Institute for Spatial Analysis and Planning in Areas of Intensive Agriculture, University of Vechta, Germany
<i>Publication status</i>	In preparation for submission to <i>Lithos</i>

Abstract

Serpentinite mud volcanism at the forearc of the Mariana subduction zone provide a window into an active subduction system. Trace elemental inventories of upwelling slab-derived fluids and serpentinized mantle wedge materials reflect processes significant for the understanding of fluid–rock interactions and related mass transfers in subduction zones. To elucidate the mobilization of fluid-mobile elements (FMEs) at forearc depths, we investigated variably serpentinized ultramafic clasts from Yinazao, Fantangisña, and Asùt Tesoru serpentinite mud volcanoes recovered on International Ocean Discovery Program Expedition 366. These mud volcanoes sample the slab–wedge interface at depths of ~13 to 18 km and temperatures of ~80 to 250 °C. The samples originate from the basal plane of the mantle wedge and exhibit a multi-phase serpentinization history, as apparent from microfabrics, mineralogy, and *in situ* major and trace elemental analyses in distinct generations of serpentine. Initial hydration occurred under reducing conditions by Si-rich fluids. Serpentine is characterized by generally high concentrations of Li, B, Sr, Rb, Cs, and Ba. Subsequent interactions with Si- and FME-poor fluids occurred in the serpentinite mud volcano conduits and resulted in the abundant presence of Fe-rich brucite. Oxidic conditions prevailed during alteration of the clasts at the seafloor. Variations of FMEs in serpentine, being a function of slab depth, allowed us to reconstruct FME and fluid sources. Serpentine from the shallow-sourced Yinazao exhibits high Rb/Cs ratios of ≤ 37 , highest concentrations of Li and B, but lowest Rb, Sr, Ba, and Cs contents. Serpentinization fluids were influenced by pore waters and the breakdown of opal in the subducted sediments. Serpentine at intermediate-sourced Fantangisña has Rb/Cs ratios of < 10 , and lower B and higher Rb and Cs contents as Yinazao. These represent the

H₂O- and FME-release from clays in the subducting sediments. Fluids at deep-sourced Asùt Tesoru as well originate from clay breakdown but highest concentrations of Rb, Sr, Cs, and Ba are further indicative of beginning dehydration of altered oceanic crust. Including data from South Chamorro serpentinite mud volcano (18 km slab depth; Kahl et al., 2015, doi:[10.1016/j.lithos.2015.03.015](https://doi.org/10.1016/j.lithos.2015.03.015)), we provide a continuous record of slab dehydration reactions at forearc depths and the related mobilization of FMEs as well as their transport into the mantle wedge. Some of the FMEs contained in serpentinite are transported back to the seafloor in the Mariana subduction zone, they will remain at depth in most other active continental margins.

4.1 Introduction

Fluids and fluid–rock interactions in subduction zones mediate mass transfers, global element cycling, and arc volcanism. A continuum of diagenetic and metamorphic dehydration and devolatilization reactions takes place in the downgoing slab during the progressive burial of H₂O-rich sediments and hydrated lithosphere (e. g., Kastner et al., 1991; Peacock, 1996; Kerrick and Connolly, 2001; Scambelluri et al., 1995; Poli and Schmidt, 1995; Schmidt and Poli, 1998). These reactions implicate the release of fluids and chemical components from the downgoing plate, making them particularly significant for chemical cycling (e. g., Bebout, 1995; Elliott et al., 1997; Manning, 2004; Moriguti and Nakamura, 1998; Pabst et al., 2012; Peacock, 1990; Marschall and Schumacher, 2012). Identifying and comprehending fluid-related processes in convergent margins is hence crucial for the understanding of petrological and geochemical changes and their consequences in the subducting slab as well as in the overriding plate.

Common approaches to study subduction zone processes include the sampling of the downgoing plate to compile a geochemical reference for what is being subducted and, to budget what is being released, the investigation of eruptives at volcanic arcs (e. g., Defant and Drummond, 1990; Hawkesworth et al., 1993; Plank and Langmuir, 1998; Codillo et al., 2018). Whereas studying the subducting lithosphere provides a good overview on subduction zone inputs, studying arc outputs merely reflects processes that take place deep within the subduction zone. Processes affecting the subducting plate as well as the overriding plate at shallower stages are, if at all, not well represented by this approach; they yet seem to be of major importance for the transfer of mass.

Shallow fluid fluxes and the hydration of the suprasubduction zone mantle wedge have consequently been in the focus of recent investigations (e. g., Hyndman and Peacock, 2003; Scambelluri et al., 2004; D’Antonio and Kristensen, 2004; Tibi et al., 2008; Alt and Shanks III, 2006; Xia et al., 2008; DeShon and Schwartz, 2004; Bostock et al., 2002). These and other studies generally agree that fluids released from the incoming slab at shallow depths serpentinize the upper plate’s mantle. With the fluids, chemical components are transferred into the mantle wedge and incorporated in the serpentinite (e. g., Pagé and Hattori, 2017; Bebout, 1995; Hattori and Guillot, 2003; Hattori and Guillot, 2007). Mantle wedge serpentinites consequently exhibit high concentrations of fluid-mobile elements (FMEs; e. g., Deschamps et al., 2010; Deschamps et al., 2011; Peters

et al., 2017). Some of these FME-rich serpentinites mechanically mix with the downgoing plate within the subduction channel and are dragged downward with it (e.g., Tatsumi, 1989; Stern, 2011; Straub and Layne, 2003). At subarc depths, the breakdown of the high-pressure serpentine variety antigorite causes the liberation of fluids and FMEs (e.g., Ulmer and Trommsdorff, 1995; Schmidt and Poli, 1998). They migrate into the upper mantle where they contribute to hydrous mantle melting and arc magma compositions, respectively (e.g., Tenthorey and Hermann, 2004; Deschamps et al., 2013; John et al., 2011).

No coherent picture of the processes that lead to the initial FME-enrichments of mantle wedge serpentinites has yet been established. For instance, Sadofsky and Bebout (2003) showed evidence that no substantial loss of FMEs from the subducting sediments occurred at conditions of up to 1 GPa and 300 °C. These authors investigated metasediments from a paleo-subduction zone that are now obducted in the Franciscan Complex, California, and the Western Baja Terrane, Baja California, Mexico; their data show that FMEs such as B, As, Rb, Sb, and Cs are present at concentrations indistinguishable from their likely seafloor protoliths. Sadofsky and Bebout hence suggested that most FMEs are not mobilized but rather retained to depths of up to 40 km in relatively cool subduction zones. But high trace elemental concentrations of fluids released at depths of <30 km in the Mariana forearc stand in contrast with these findings (e.g., Mottl and Alt, 1992; Mottl et al., 2004; Hulme et al., 2010; Wheat et al., 2018). These fluids actively upwell from the slab–mantle interface through the deeply faulted forearc and vent at the seafloor (Fryer et al., 1985; Haggerty, 1991; Fryer et al., 1999). Their elemental compositions mirror dehydration reactions taking place in the subducting lithosphere: the compositions vary across the forearc but are generally characterized by high contents of fluid-mobile elements, suggesting that mobilization of these in fact does occur at shallow subduction levels (Mottl et al., 2004; Hulme et al., 2010; Wheat et al., 2018).

Together with the fluids, serpentinite mud and rock clasts buoyantly rise to the forearc seafloor, where they erupt as mudflows that pile up to vast serpentinite mud volcanoes (Fryer et al., 1985; Haggerty, 1991). The serpentinite clasts represent forearc mantle materials that were hydrated by slab-derived fluids (e.g., Fryer et al., 1995; Kahl et al., 2015). The investigation of the clasts hence allows insight into the nature of the fluids at a more pristine stage, potentially before they were strongly altered by fluid–rock interactions within the subduction channel or mantle wedge. Indeed, similar to the upwelling fluids, serpentinite clasts from the serpentinite mud volcanoes as well exhibit high contents of fluid-mobile elements, illustrating that these elements are transported from the subducting lithosphere into the mantle wedge at subduction depths as low as ~13 km (e.g., Benton et al., 2001; Savov et al., 2005, 2007; Pabst et al., 2012; ?). Kahl et al. (2015) showed that it is possible to track distinct episodes of fluid fluxing by examining microfabrics and *in situ* mineral analyses in serpentine veins within the clasts. Variations in fluid-mobile element contents revealed that the clasts experienced multi-stage serpentinitization histories. The fluid-mobile element inventories, in particular B, Rb, Sr, Cs, and Ba, thereby recorded the interaction with chemically distinct fluids; these are thought to have changed as a function of metamorphic processes in the downgoing slab

and by fluid–rock interactions within the subduction channel and the mud volcanoes' conduits. With this study, Kahl et al. compiled a dataset reflecting processes occurring below one of the deeper-sourced serpentinite mud volcanoes, namely South Chamorro, which has a depth to the subducting slab of ~18 km (Hulme et al., 2010).

Within this study we take advantage of IODP (International Ocean Discovery Program) Expedition 366 to the Mariana forearc, during which three shallower-sourced serpentinite mud volcanoes were drilled. We investigated serpentinite clasts recovered Yinazao, Fantangisña, and Asùt Tesoru serpentinite mud volcanoes, which are situated 13 to 18 km above the downgoing slab. We present microtextural observations coupled with *in situ* major and trace element data, on the basis of which we reconstruct the serpentinization conditions and fluids. Across-arc changes in fluid-mobile element contents in distinct generations of serpentine veins indicate varying trace elemental compositions of the serpentinizing fluids. These are a function of fluid sources and metamorphic conditions within the subducting plate—we are able to trace an evolution from the release of pore waters at shallow depths over the dominant dehydration of sedimentary opal and clays towards an increasing influence of fluids released from the altered oceanic crust at the deep-sourced mud volcanoes.

Study area Deep-rooted, pervasive faults in the outer forearc of the non-accretionary Mariana subduction system act as permeable pathways for fluids released from the subducting Pacific plate (Fig. 4.1; e. g., Uyeda and Kanamori, 1979; Fryer, 1992, 1996; Fryer et al., 1990). Together with mobilized fault gouge these fluids rise through the Philippine Sea plate to the seafloor, where they form active serpentinite mud volcanoes tens of km in diameter and up to 2.5 km high (Fryer and Fryer, 1987; Fryer, 1992). They are composed principally of unconsolidated flows of serpentinite muds, containing clasts of serpentinized forearc mantle peridotite and rare other lithologies including materials derived from the subducted Pacific plate (e. g., Maekawa et al., 1995; Fryer, 2012; Pabst et al., 2011). The mud volcanoes exist at varying distances to the trench, i. e., the depth to the subducting slab varies and so do the pressure and temperature conditions at the location of fluid release (Oakley et al., 2007; Hulme et al., 2010). The mud volcanoes in the Mariana forearc hence provide direct access to deep-sourced fluids and materials from the subduction channel and suprasubduction zone. They are of primary scientific interest as they provide unique insight into shallow subduction zone processes. Serpentinite mud volcanism is proposed to have occurred worldwide since the Archean and maybe longer (e. g., Pons et al., 2011; Lockwood, 1972).

The chemical compositions of the deep-sources pore waters that upwell at the mud volcanoes systematically change across the forearc, reflecting metamorphic conditions within the subducting slab (e. g., Mottl et al., 2004; Hulme et al., 2010; Wheat et al., 2018). Increases in pressure and temperature lead to sediment compaction, opal dehydration, clay diagenesis and desorbed water release, decarbonation, and clay decomposition take place within the subducted sediments and crust (see also Fryer et al., 2018).

Five seamounts have been in the past been targeted by ocean drilling campaigns: IODP Expedition 366 drilled the slopes and summits of Yinazao (55 km distance to the Mariana

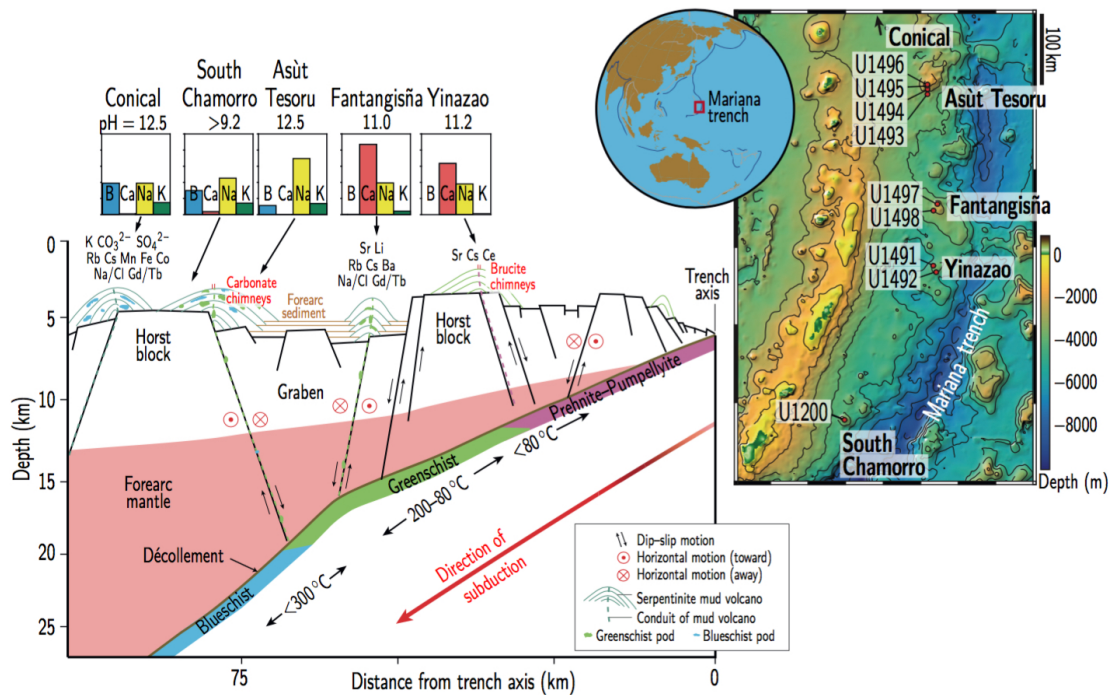


Figure 4.1 Study area in the Mariana forearc with the locations of the serpentinite mud volcanoes and of sites drilled during IODP Expedition 366 and ODP Leg 195 (**right**). Idealized cross-section through the forearc with changes in chemistry of upwelling fluids and interpreted devolatilization reactions at the slab interface (**left**). All elemental concentrations in mM, but B was multiplied by 10 and Na was divided by 10. Figures modified from Fryer et al. (2018), including data from Hulme et al. (2010).

trench; ~13 km depth to slab; ~80 °C at the slab–mantle wedge interface), Fantangisña (62 km to trench; ~14 km to slab; ~150 °C), and Asút Tesoru (72 km to trench; ~18 km to slab; ~250 °C), South Chamorro was cored during ODP Leg 195 (78 km to trench; ~18 km to slab; ~250–350 °C), and Conical (86 km to trench; ~19 km to slab; ~250–350 °C) during ODP Leg 125 (distances to trench and slab temperatures after Hulme et al., 2010, depths to slab after Oakley et al., 2007, 2008; Maekawa et al., 1993; Fryer et al., 2006).

4.2 Methodology

Thin sections of representative samples of the main alteration types were examined with a standard petrographic microscope in transmitted and reflected light. Primary and secondary fabrics and mineral phase assemblages were further evaluated on the basis of backscattered electron imaging (SEM) and energy-dispersive X-ray spectroscopy (EDX). Alteration stages, in particular of distinct vein generations present in the samples, were distinguished on the basis of crosscutting relations.

4.2.1 Electron microprobe analyses

Elemental compositions of minerals were obtained with a CAMECA SX100 EPMA at the University of Bremen. The device is equipped with four wavelength dispersive spectrometers. Analytical conditions included accelerating voltages of 15 kV and beam currents of 10 to 15 nA. Peak counting times varied between 20 to 40 s per element and analyses were carried out with a focused beam. The built-in PAP correction was applied for data reduction and correction. Repeated analyses of natural silicate and carbonate standards guaranteed data quality. Averaged precision is better than 3.5% for elements with concentrations >1 wt.%, except for TiO₂ (14.6%) and averaged accuracy is better than 2.5% except for Na₂O (6.2%).

4.2.2 Laser ablation ICP-MS analyses

Analyses of trace elements (Li, B, V, Rb, Sr, Cs, and Ba) were carried out using a Thermo Finnigan Element2 ICP-MS coupled to a New Wave UP193 solid-state laser ablation system at the University of Bremen. Analytical conditions included an irradiance of ~1 GW cm⁻² for ablation, spot sizes of 25 to 100 μm and a laser pulse rate of 5 Hz. Helium (0.7 L min⁻¹) and Ar (0.9 L min⁻¹) were used as sample and make-up gases, respectively. All isotopes were analyzed at low resolution with five samples in a 20% mass window and a total dwell time of 25 ms per isotope. The glass standard NIST 610 was measured after every 4 to 8 samples for external calibration using the values from Jochum et al. (2011). The ²⁵Mg isotope was used as internal standard and concentrations were calculated with the Cetac GeoPro™ software. Analytical quality was controlled by repeated analyses of USGS reference materials NIST610, BCR-2G, and BHVO-2G and comparison of our data with the GeoReM database (as of September 2018). For most elements, averaged precision is better than 5% and averaged accuracy is better than 9% (Supplementary Information Tab. A.3.1).

4.3 Petrography

We studied 14 ultramafic rock clasts from flank and summit sites of Yinazao, Fantangisña, and Asùt Tesoru (Fig. 4.1, Tab. 4.1), recovered during IODP Expedition 366. The clasts were enclosed in the serpentinite mud matrix and were mostly few cm in size except for two that represent rims and inner parts of rock clasts up to three dm in size.

Four samples are of dunitic composition, nine are harzburgites, and one is a lherzolite. They are from ~15 to 100% serpentinized; the degree of serpentinization often varies on a cm-scale and seems independent of lithology or recovery site.

4.3.1 Primary lithologies

Primary ultramafic lithologies are preserved in few of the investigated clasts (Tab. 4.1). Unserpentinized parts of the peridotites show a variety of microfabrics, which reveal information on the protolith textures. The microstructures can exhibit coarse (e. g., sample

Table 4.1 List of investigated samples.

Mud volcano	Sample	Depth (m b. s. f.)	Lithology	Alteration (%)
Yinazao	U1491B-5H-CC, 0–3 cm	19.30	Du	~60
Yinazao	U1492A-1H-3, 115–135 cm, A	5.32	Hz	100
Yinazao	U1492A-1H-3, 115–135 cm, B	5.32	Hz	100
Yinazao	U1492C-1H-2, 18–20 cm	1.68	Hz	100
Fantangisña	U1498A-3R-2, 27–29 cm ^a	16.39	Hz	~75
Fantangisña	U1498B-2R-1, 6–8 cm	9.56	Lz	~95
Fantangisña	U1498B-4R-1, 94–97 cm	29.84	Du	~99
Fantangisña	U1498B-13R-3, 49–51 cm ^b	114.12	Hz	~70
Fantangisña	U1498B-23R-3, 19–23 cm	202.79	Hz	~95
Asùt Tesoru	U1493B-9X-1, 59–62 cm	30.19	Du	~15
Asùt Tesoru	U1493B-9X-CC, 14–16 cm	30.67	Hz	100
Asùt Tesoru	U1494A-1F-3, 60–62 cm	2.21	Du	100
Asùt Tesoru	U1496C-5R-1, 17–19 cm	36.77	Hz	100
Asùt Tesoru	U1496C-11R-1, 28–30 cm	94.18	Hz	~80

Degree of alteration estimated by point counting.

^a Outer part of a dm-sized clast.

^b Inner part of a dm-sized clast.

Abbreviations: Du, dunite; Hz, harzburgite; Lz, lherzolite; b. s. f., below seafloor.

U1498B-23R-3, 19–23 cm, with common grain sizes of ~2.5–3.5 mm) or microgranular olivine (e. g., sample U1491B-5H-CC, 0–3 cm, with olivine grains ~0.15–0.35 mm in size). Deformation of olivine is indicated by the common occurrence of kink bands. One sample exhibits a strong alignment of olivine crystals that are up to 2.5 to 3 mm long and ~0.5 mm wide. Orthopyroxene is commonly up to ~3.5 mm in size. Clinopyroxene is much less frequent than orthopyroxene and is usually less than 0.5 mm in diameter (e. g., sample U1496C-11R-1, 28–30 cm) but grains may be up to ~6 mm large (sample U1498B-2R-1, 6–8 cm). It often, but not exclusively, occurs close to orthopyroxene or in the cores of orthopyroxene crystals (e. g., sample U1493B-9X-1, 59–62 cm), within exsolution lamellae of orthopyroxene (sample U1496C-5R-1, 17–19 cm), or intergrown with spinel (sample U1498B-23R-3, 19–23 cm). Ortho- and clinopyroxene frequently show undulatory extinction and cleavage planes. Spinel is present in all samples and can exhibit euhedral (e. g., sample U1494A-1F-3, 60–62 cm) to sub- or anhedral (e. g., sample U1498B-4R-1, 94–97 cm) or vermicular (e. g., sample U1498A-3R-2, 27–29 cm) faces. It can be up to ~0.6 mm in size (e. g., samples U1493B-9X-CC, 14–16 cm, or U1496C-11R-1, 28–30 cm) and often shows embayments indicative of resorption (e. g., sample U1496C-11R-1, 28–30 cm).

4.3.2 Serpentinization

Prolonged water–rock interaction caused extensive serpentinization of the samples, several stages of which are distinguishable from microfabrics and textural relationships. Serpentinization led to pseudomorphic mesh and hourglass textures after olivine and to bastite after ortho- and, less frequent, after clinopyroxene. Serpentinization products

are further present in veins of several generations. Alongside serpentine, these products include abundant brucite and minor amounts of magnetite and Fe-alloys. During early serpentinization stages, brucite is developed in the centers of an early network of narrow veinlets, whereas serpentine occurs towards the host olivine. Brucite is further present in intimate intergrowth with serpentine in later veins and in few cases as solitary crystals in the centers of recrystallized mesh textures or in veins. Minor magnetite occurs together with serpentine and brucite in early veins and in mesh vein networks. It is usually fine grained but alignment of crystals may appear as long bands. Iowaite is present in areas affected by alteration, locally together with hematite. Four samples contain hydroandradite that is developed as euhedral crystals up to 50 μm in diameter or as dissolution–precipitation product with anhedral crystal shapes. Iowaite is present in four samples; its existence is linked to late-stage alteration of the clasts. Iowaite co-occurs with calcium carbonates in two clasts from Yinazao.

Early veins and pervasive serpentinization Early phases of (pervasive) serpentinization are preserved in the not fully serpentinized samples (Tab. 4.1). In these clasts, first serpentinization stages of the pristine ultramafic rock are exhibited as transgranular veins of serpentine, brucite, and minor magnetite (Fig. 4.2a,b,c). The veins are up to 0.5 mm wide. Serpentine replaces olivine, brucite occurs mainly in the vein centers, sometimes together with bands or aggregates of magnetite (Fig. 4.2c). Millimeter- to cm-wide halos are locally developed. Incipient pervasive serpentinization took place along networks of narrow veins that emanated from the first veins into the peridotites and along olivine grain boundaries, leading to intergranular serpentine textures (Fig. 4.2b,c,d). The veinlets, usually <25 μm in width, consist of serpentine and minor magnetite and awaruite (Ni_3Fe) or of serpentine, brucite, and minor magnetite and awaruite. Serpentine is developed in the outer veins in contact to olivine; disseminated crystals of magnetite and Fe-alloys are present in vein centers or in contact to olivine. If present, brucite occurs exclusively in vein centers. When intersecting pyroxene, veinlets exclusively contain serpentine and minor magnetite. In fully altered samples, pervasive serpentinization of olivine led to the formation of hourglass textures. Mesh centers usually consist of serpentine only (Fig. 4.2e) but in few samples of serpentine and magnetite and sulfides. Pyroxene is altered to serpentine in bastite textures. Depending on the degree of alteration, orthopyroxene may be preserved in exsolution lamellae. Bastite after orthopyroxene locally has a strong green color.

Veins postdating early serpentinization Late veins typically consisting of pure serpentine are present in most samples and crosscut pervasively serpentinized areas as well as earlier vein generations (Fig. 4.3a). Some of these veins are straight to curvilinear and do not necessarily follow earlier deformation directions whereas others are developed along the centers of earlier veins, apparently reactivating these fluid pathways. Serpentine veins crosscutting bastite textures often exhibit a greenish color; halos of greenish serpentine and secondary clinopyroxene in bastite after orthopyroxene are locally developed.

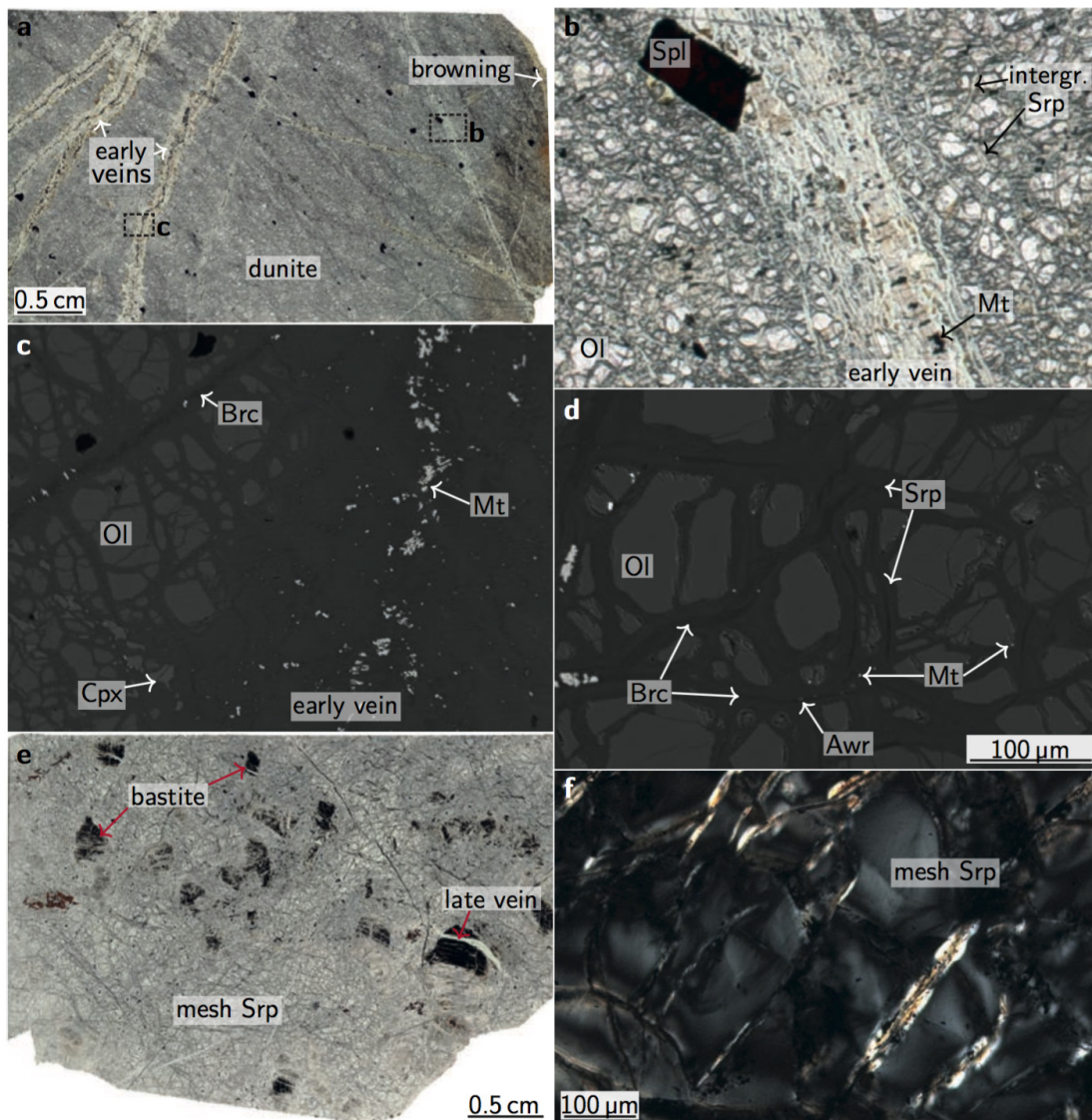


Figure 4.2 Representative photomicrographs and SEM images of ultramafic clasts and microfabrics. (a) Dunite clast exhibiting incipient serpentinization along early veins (sample U1493B-9X-1, 59–62 cm, PPL). Inward-migrating late alteration overprints previous textures. Close-ups depict (b) an early vein consisting of Srp–Mt that cuts through fresh olivine (PPL) and (c) an wide early vein with Mg-rich brucite and anhedral magnetite in its center. Also note the intergranular serpentinization along minute fractures and olivine grain boundaries. (d) Intergranular serpentine with Mg-rich brucite, magnetite, and Fe-alloys in the vein centers (sample U1496C-5R-1, 17–19 cm). (e) Completely serpentinized harzburgite with mesh serpentine and late veins of pure serpentine (sample U1492A-1H-3, 115–135 cm, B). Bastite serpentine is blackened (see also Supplementary Information Fig. A.3.1). (f) Serpentine mesh textures (sample 92A-1H-3, U1492A-1H-3, 115–135 cm, A, XPL). Abbreviations: Awr, awaruite; Brc, brucite; Cpx, clinopyroxene; Intergr., intergranular; Mt, magnetite; Ol, olivine; PPL, plane polarized light; Spl, spinel; XPL, crossed polarized light.

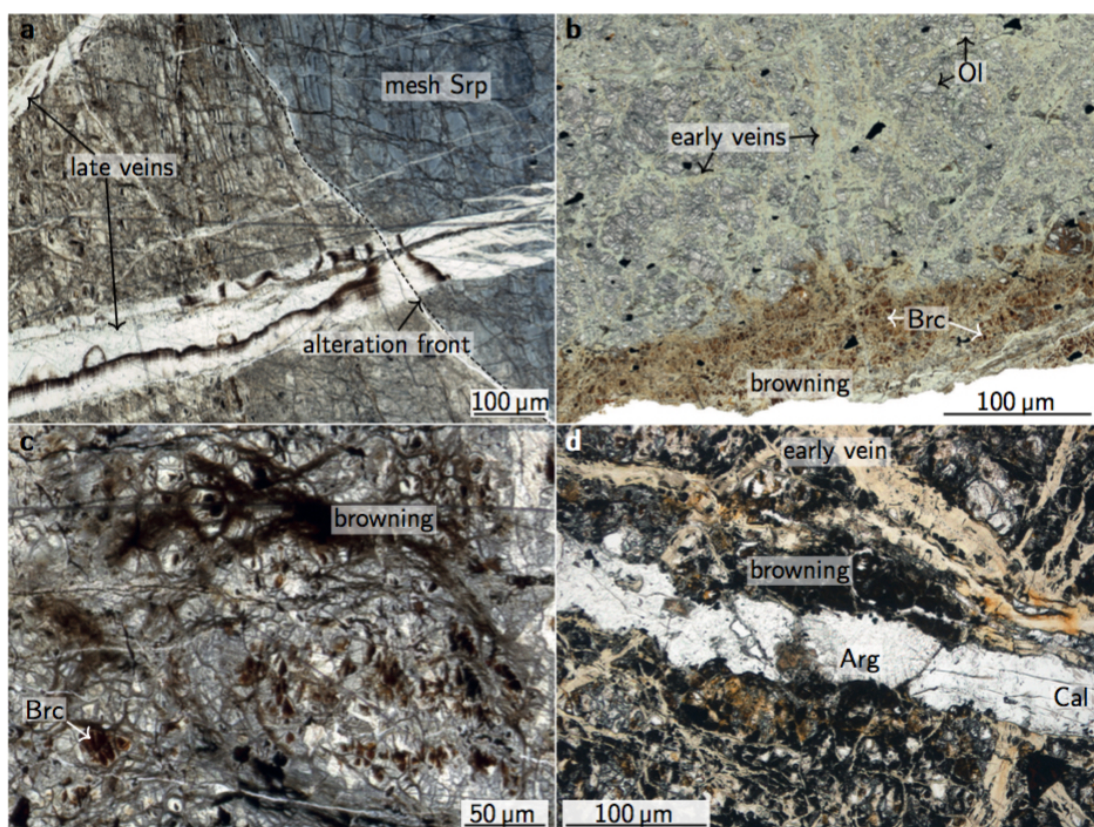


Figure 4.3 Representative photomicrographs of ultramafic clasts and microfabrics. (a) Late veins of pure serpentine crosscutting mesh serpentine (sample U1498B-4R-1, 94–97 cm, PPL). Late alteration overprints all previous fabrics, including the late vein. (b) Partially serpentinized clasts overprinted by inward-migrating late browning (sample U1496C-11R-1, 28–30 cm, PPL). Olivine is replaced by brown brucite. (c) Browning is as well present within some clasts, in this case overprinting mesh serpentine and earlier narrow veins (U1498A-3R-2, 27–29 cm, PPL). (d) Vein containing aragonite and calcite crosscutting a partially serpentinized clast (sample U1491B-5H-CC, 0–3 cm, PPL). Large parts of the clast have been affected by browning. Abbreviations: Arg, aragonite; Brc, brucite; Cal, calcite; Ol, olivine; PPL, plane polarized light.

Alteration and late fluid–rock interactions Most samples show late-stage alteration that led to a ‘browning’ the clasts. The browning pervasively migrates inward either from the clasts’ margins or from earlier veins. It is not related to the clasts’ internal fabrics but instead overprints all previous textures (Figs. 4.2a, 4.3b,c,d; cf. Kahl et al., 2015). High proportions of brown-colored brucite formed during this alteration stage: it replaces serpentine in mesh centers after olivine and frequently occurs in veins, either intergrown with serpentine and/or other phases, or filling voids. In four clasts, former serpentine mesh centers or of bastite textures in four clasts are ‘blackened’ (Fig. 4.2e, Supplementary Information Fig. A.3.1b,c); these areas contain brucite and abundant sulfide mineralizations. In the serpentinized lherzolite, abundant sulfides occur as <10 μm-large crystals

disseminated in the narrow vein network surrounding mesh serpentine (Supplementary Information Fig. A.3.1a,b). Several samples exhibit intimate intergrowth of brucite and iowaite, either in veins or within the clasts' browned outer rims (Supplementary Information Fig. A.3.1e,f). Serpentine has developed in voids close to the browned margin of one clast. Two samples from Yinazao and one from Asùt Tesoru are crosscut by veins that overprint all previous textures and contain aragonite and calcite (Fig. 4.3d) and, at Yinazao, also iowaite and hematite. The calcium carbonates show well-developed crystal faces, typically 0.3 to 0.6 mm in size; some crystals have radial growth structures. Iowaite in these veins may be developed with acicular textures. Growth structures of both carbonate and iowaite suggest precipitation in void space in equilibrium with a fluid. Hematite co-occurs with iowaite in one sample.

4.4 Mineral chemistry

4.4.1 Major element mineral chemistry

Primary minerals

Olivine is Mg-rich throughout the samples, with $X_{\text{Mg}} = \text{Mg}/(\text{Mg} + \text{Fe}^{2+})$ of 0.91 to 0.93 (Fig. 4.4). X_{Mg} ratios of orthopyroxene are 0.91 to 0.92, Al_2O_3 contents of 1.39 to 3.11 wt.%, and Cr_2O_3 of 0.46 to 0.86 wt.% (Figs. 4.4 and 4.5). Clinopyroxene has X_{Mg} of 0.94 to 0.96, Al_2O_3 of <0.01 to 0.2 wt.%, and Cr_2O_3 of 0.01 to 0.99 wt.% (Figs. 4.4 and 4.5). Spinel is Cr-rich with $X_{\text{Cr}} = \text{Cr}/(\text{Cr} + \text{Al})$ of 0.40 to 0.63 and X_{Mg} of 0.45 to 0.62; overgrowth in strongly serpentinized areas approaches ferritchromite composition with X_{Cr} of 0.84 to 0.90 and X_{Mg} of 0.36 to 0.43. Exemplary compositions of primary phases are given in Table 4.2.

Secondary minerals

Early veins and pervasive serpentinization Serpentine and brucite occurring in veins and narrow vein networks preceding the pervasive serpentinization are Mg-rich, with X_{Mg} typically in the range of 0.90 to 0.96 for serpentine and of 0.89 to 0.92 for brucite (Fig. 4.3, Tab. 4.3). Pseudomorphic serpentine in mesh and hourglass textures after olivine has X_{Mg} of 0.90 to 0.95 and show slightly elevated contents of Al_2O_3 and CaO with respect to olivine (Fig. 4.5, Tab. 4.3). Serpentine in bastite textures has X_{Mg} of 0.90 to 0.94 and high contents of Al_2O_3 (>0.8 wt.%), Cr_2O_3 (0.2–1.4 wt.%), and CaO (>0.1 wt.%) indicative of its pyroxene precursor (Fig. 4.5, Tab. 4.3).

Late serpentine veins Serpentine in late veins usually has X_{Mg} of 0.92 to 0.96 and low Al_2O_3 (<0.25 wt.%), Cr_2O_3 (<0.15 wt.%), and CaO (<0.1 wt.%), except when the veins crosscut bastite textures (comparable X_{Mg} , $\text{Al}_2\text{O}_3 \leq 2.2$ wt.%, $\text{Cr}_2\text{O}_3 \leq 0.8$ wt.%, $\text{CaO} \leq 0.4$ wt.%; Figs. 4.4 and 4.5, Tab. 4.3). Halos developed around Srp-only veins in few cases; they are somewhat less magnesian ($X_{\text{Mg}} \approx 0.87$). SiO_2 contents of serpentine in early veins match those expected for pure serpentine, confirming the absence of brucite in this alteration stage.

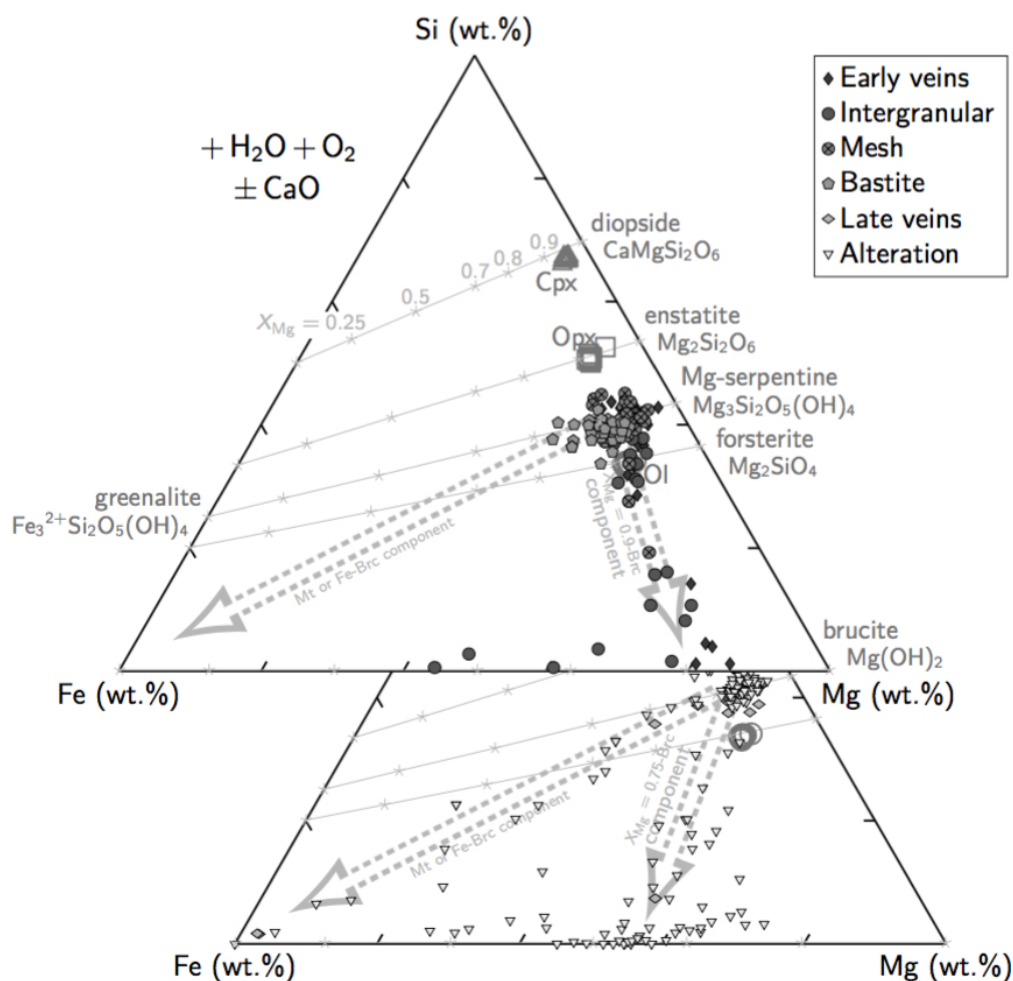


Figure 4.4 Si–Mg–Fe compositional variability of primary and secondary minerals. (**Top**) Alteration phases occurring in early veins and intergranular are serpentine \pm Mg-rich brucite. Mesh and bastite serpentine are usually pure serpentine; apparent lower- X_{Mg} analyses represent brucite with finely intergrown magnetite. (**Bottom**) Late veins are pure, Mg-rich serpentine, whereas alteration-affected clasts are commonly exhibit brucite with X_{Mg} of 0.5 to 0.6. Primary minerals are shown for comparison; they have X_{Mg} of >0.90 .

Alteration and late fluid–rock interactions Late brucite precipitates are considerably richer in Fe as compared to brucite formed during early serpentinization stages; X_{Mg} is mostly in the range of 0.73 to 0.87, but may be as low as 0.52 (Fig. 4.4, Tab. 4.3). Serpentine that has grown in voids is as well Fe-rich ($X_{Mg} \approx 0.72$). The presence of S-bearing phases in several browned mesh centers is confirmed by EDX.

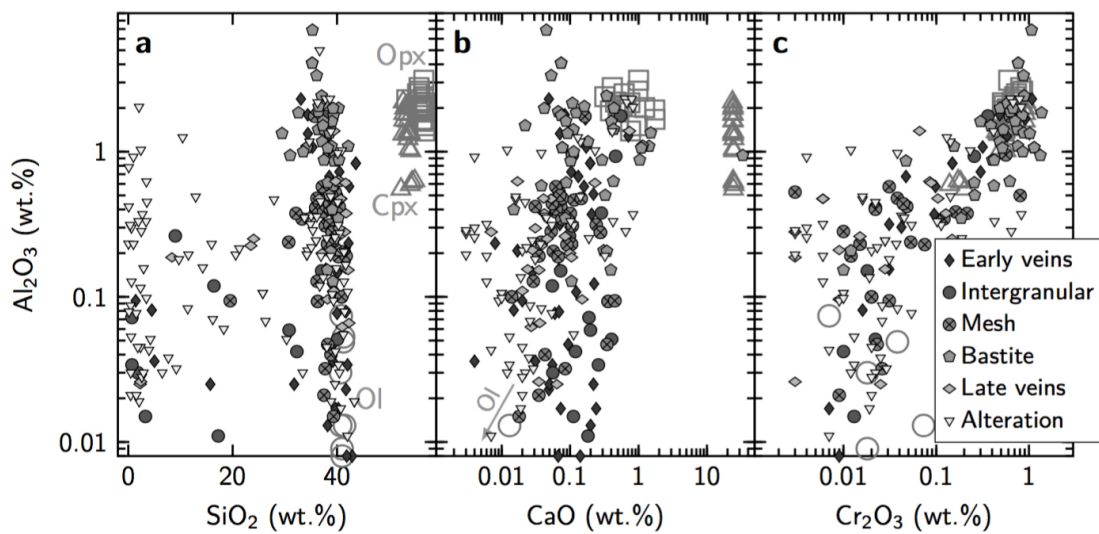


Figure 4.5 Variations of SiO_2 , CaO , and Cr_2O_3 vs. Al_2O_3 in primary and secondary minerals. Serpentine grown after olivine or in late serpentinization phases exhibit low to intermediate Al_2O_3 contents, whereas serpentine after pyroxene contains Al_2O_3 similarly high as primary pyroxene. Bastite serpentine as well reflects higher CaO contents relative to serpentine formed from olivine or during later events. Yet, all serpentine generations are enriched in CaO in comparison to primary olivine. Bastites also contain highest Cr_2O_3 , again ranging up to levels of their pyroxene precursors. By comparison, Cr_2O_3 in other serpentinization products is usually lower.

4.4.2 Trace element mineral chemistry

Nickel and V concentrations of early-generation serpentine and/or brucite reflect the concentrations of their precursors. Serpentine and regions of serpentine–brucite intergrowth formed after olivine commonly have up to $4000 \mu\text{g g}^{-1}$ Ni and $<25 \mu\text{g g}^{-1}$ V, corresponding to the high Ni and low V concentrations of unaltered olivine (usually in the range of ~ 2500 – $4000 \mu\text{g g}^{-1}$ Ni and $<10 \mu\text{g g}^{-1}$ V; Supplementary Information Fig. A.3.2). Nickel contents in bastite serpentine are usually below $1200 \mu\text{g g}^{-1}$ but it contains up to $\sim 110 \mu\text{g g}^{-1}$ V; primary ortho- and clinopyroxene have $<1200 \mu\text{g g}^{-1}$ and $<800 \mu\text{g g}^{-1}$ Ni but up to $\sim 110 \mu\text{g g}^{-1}$ and $150 \mu\text{g g}^{-1}$ V, respectively (Supplementary Information Fig. A.3.2). These results mirror observations by Kahl et al. (2015). Contents of FMEs in primary phases are low and often close to or below the detection limit (Fig. 4.6), as expected for materials from the highly depleted mantle (e. g., Salters and Stracke, 2004).

Concentrations of fluid-mobile Li, B, Rb, Sr, Cs, and Ba strongly vary within secondary phases but are generally enriched with respect to primary olivine and pyroxene (Fig. 4.6, Tab. 4.3). Most elevated contents are observed within pure serpentine or where the serpentine component dominates sub-microscopic intergrowth of serpentine and brucite; analyses of pure brucite usually exhibit low FME concentrations. Noteworthy are B concentrations, which show strong enrichments in all serpentinization products regardless of precursor phase and formation stage (Fig. 4.6b). In contrast, contents of Li, Rb, Sr, Cs, and Ba are linked to the distinct stages of alteration: except for few cases, serpentine

developed during early phases of fluid–rock interactions yields higher concentrations than serpentine and/or brucite in later veins or in browned areas (Fig. 4.6).

In greater detail, early veins at Yinazao exhibit Li up to $20 \mu\text{g g}^{-1}$ whereas those at Fantangisña and Asùt Tesoru contain $<10 \mu\text{g g}^{-1}$ (Fig. 4.6a). Similar low concentrations are observed in intergranular and mesh serpentine at Fantangisña and Asùt Tesoru, and in late veins at all sites. Lithium concentrations in bastite are strongly enriched, with up to $\sim 70 \mu\text{g g}^{-1}$ at Yinazao. Considerably enriched (typically up to $\sim 30 \mu\text{g g}^{-1}$ Li) are also browned areas at Asùt Tesoru; two data points at Yinazao as well indicate high concentrations, but all other are $<15 \mu\text{g g}^{-1}$ and hence within the range of early veins.

Early veins reveal a decrease of B contents with increasing slab-depth, with up to $\sim 450 \mu\text{g g}^{-1}$ at Yinazao, typically $<150 \mu\text{g g}^{-1}$ at Fantangisña, and $<80 \mu\text{g g}^{-1}$ at Asùt Tesoru (Fig. 4.6b). Mesh serpentine contains considerably more B than intergranular serpentine (up to $350 \mu\text{g g}^{-1}$ *vs.* $<50 \mu\text{g g}^{-1}$ at Fantangisña, up to $400 \mu\text{g g}^{-1}$ *vs.* $<90 \mu\text{g g}^{-1}$ at Asùt Tesoru). Boron concentrations in bastite are within the ranges of mesh serpentine. Similar to the trend in early veins, late veins illustrate substantially higher contents at Yinazao as compared to the deeper-sourced mud volcanoes. Browned areas have concentrations within the range of early vein, mesh, or bastite serpentine; brucite in altered areas contains up to $120 \mu\text{g g}^{-1}$ B at Yinazao but very low contents at Fantangisña and Asùt Tesoru.

Concentrations of Rb are generally $<1 \mu\text{g g}^{-1}$ at Yinazao and Fantangisña, except for bastite serpentine, which commonly contains up to $4 \mu\text{g g}^{-1}$ (Fig. 4.6c). At Asùt Tesoru, up to $\sim 3 \mu\text{g g}^{-1}$ Rb are detected in early veins and intergranular serpentine, and up to $9 \mu\text{g g}^{-1}$ in serpentine after pyroxene. Late veins contain $\ll 1 \mu\text{g g}^{-1}$ Rb, but alteration-affected areas typically have up to $5 \mu\text{g g}^{-1}$.

Strontium contents in early veins are commonly up to $10 \mu\text{g g}^{-1}$ throughout at all samples (Fig. 4.6d). At Yinazao, later-formed serpentine has similar low concentrations; however, serpentine in browned areas exhibits up to $\sim 25 \mu\text{g g}^{-1}$ and brucite up to $8 \mu\text{g g}^{-1}$ Sr. At Fantangisña and Asùt Tesoru, intergranular, mesh, and bastite serpentine frequently exhibit Sr contents of up to $20 \mu\text{g g}^{-1}$. Concentrations in late veins at these deeper-sourced mud volcanoes are $<10 \mu\text{g g}^{-1}$, similar to Yinazao. Browned areas contain low ($<10 \mu\text{g g}^{-1}$) to particularly high (up to $\sim 65 \mu\text{g g}^{-1}$) Sr at Fantangisña and Asùt Tesoru, respectively.

Cesium contents are generally below $0.5 \mu\text{g g}^{-1}$ in serpentine of all generations at Yinazao and Fantangisña, except for bastite at Fantangisña, which can contain up to $\sim 4 \mu\text{g g}^{-1}$ Cs (Fig. 4.6e). Serpentine occurring in early veins and intergranular at Asùt Tesoru exhibit Cs concentrations up to $1 \mu\text{g g}^{-1}$; bastite serpentine can contain up to $\sim 4 \mu\text{g g}^{-1}$ Cs, similar to bastite at Fantangisña. Late veins do not contain considerable Cs ($\ll 0.5 \mu\text{g g}^{-1}$), whereas contents in serpentine affected by browning may be as high as $2 \mu\text{g g}^{-1}$.

Table 4.2 Representative geochemistry of primary phases.

Sample	U1493B- 9X-1, 59–62 cm	U1496C- 11R-1, 28–30 cm	U1498B- 13R-3, 49–51 cm	U1493B- 9X-1, 59–62 cm	U1496C- 11R-1, 28–30 cm	U1498B- 13R-3, 49–51 cm	U1493B- 9X-1, 59–62 cm	U1496C- 11R-1, 28–30 cm	U1498B- 23R-3, 19–23 cm	U1491B- 5H-CC, 0–3 cm	U1498B- 4R-1, 94–97 cm
Phase	Ol	Ol	Ol	Opx	Opx	Opx	Cpx	Cpx	Cpx	Spl	Spl
wt. %											
SiO ₂	40.6	41.0	41.0	56.1	56.5	56.7	53.6	54.4	54.2	0.1	b. d. l.
TiO ₂	0.01	0.02	b. d. l.	0.01	0.01	0.01	0.02	0.01	0.02	0.04	0.04
Al ₂ O ₃	b. d. l.	0.01	b. d. l.	2.09	2.39	1.77	1.23	0.62	1.02	25.16	5.03
Cr ₂ O ₃	0.03	0.02	b. d. l.	0.72	0.70	0.78	0.55	0.18	0.57	43.43	64.52
FeO	8.62	8.90	8.85	5.77	5.84	5.47	1.49	1.81	1.58	17.23	23.07
MgO	51.0	51.2	51.6	35.3	35.6	35.0	18.2	18.6	18.4	12.7	7.4
MnO	0.15	0.12	0.21	0.17	0.19	0.13	0.10	0.13	0.11	0.21	0.41
NiO	0.39	0.36	0.42	0.09	0.15	0.07	0.04	0.06	0.03	0.07	0.02
CaO	b. d. l.	b. d. l.	0.01	0.51	0.32	1.50	24.82	24.43	24.62	b. d. l.	b. d. l.
Na ₂ O	b. d. l.	b. d. l.	b. d. l.	0.01	b. d. l.	b. d. l.	0.08	0.05	0.07	0.05	0.02
K ₂ O	b. d. l.	b. d. l.	b. d. l.	b. d. l.	b. d. l.	b. d. l.	b. d. l.	b. d. l.	b. d. l.	b. d. l.	b. d. l.
Total	100.8	101.6	102.1	100.8	101.7	101.4	100.1	100.3	100.6	99.0	100.5
Cations p. f. u.											
Si	0.99	0.99	0.99	1.93	1.92	1.93	1.95	1.97	1.96	0.00	0.00
Ti	0.00	0.00	0.00	0.00	0.00	0.00	0.00	0.00	0.00	0.00	0.00
Al	0.00	0.00	0.00	0.08	0.10	0.07	0.05	0.03	0.04	0.91	0.20
Cr	0.00	0.00	0.00	0.02	0.02	0.02	0.02	0.01	0.02	1.06	1.76
Fe	0.18	0.18	0.18	0.17	0.17	0.16	0.05	0.05	0.05	0.44	0.66
Mg	1.85	1.84	1.85	1.80	1.80	1.78	0.99	1.01	0.99	0.59	0.38
Mn	0.00	0.00	0.00	0.00	0.01	0.00	0.00	0.00	0.00	0.01	0.01
Ni	0.01	0.01	0.01	0.00	0.00	0.00	0.00	0.00	0.00	0.00	0.00
Ca	0.00	0.00	0.00	0.02	0.01	0.05	0.97	0.95	0.95	0.00	0.00
Na	0.00	0.00	0.00	0.00	0.00	0.00	0.01	0.00	0.01	0.00	0.00
K	0.00	0.00	0.00	0.00	0.00	0.00	0.00	0.00	0.00	0.00	0.00
Sum	3.02	3.02	3.02	4.03	4.02	4.02	4.02	4.02	4.02	3.01	3.02
X _{Mg}	0.91	0.91	0.91	0.92	0.92	0.92	0.96	0.95	0.95	0.57	0.36

Stoichiometries recalculated on the basis of 4 O (olivines and spinels) and 6 O (pyroxenes).

Abbreviations: b. d. l., below detection limit; Cpx, clinopyroxene; n. c., not calculated; Ol, olivine; Opx, orthopyroxene; p. f. u., per formula unit.

Table 4.3 Representative geochemistry of serpentine and brucite and mixtures thereof.

Sample	U1493- 9X-1, 59- 62 cm	U1498A- 3R-2, 28- 29 cm	U1493- 9X-1, 59- 62 cm	U1496C- 11R-1, 28- 30 cm	U1498B- 13R-3, 49- 51 cm	U1496C- 5R-1, 17- 19 cm	U1494A- 1F-3, 60- 62 cm	U1498B- 2R-1, 6-8 cm	U1493B- 9X-CC, 14- 16 cm	U1498B- 13R-3, 49- 51 cm	U1492A- 1H-3, 115- 135 cm, A	U1493B- 9X-CC, 14- 16 cm	U1491B- 5H-CC, 0-3 cm	U1498B- 2R-1, 6-8 cm	U1498B- 23R-3, 19- 23 cm	U1496C- 11R-1, 28- 30 cm	U1496C- 5R-1, 17- 19 cm
Phase Alteration stage	Srp early vein	Srp early vein	Brc early vein	Srp intergr.	Srp intergr.	Brc-Srp intergr.	Srp mesh	Srp mesh	Srp bastite	Srp bastite	Srp late vein	Srp late vein	Srp alter- ation	Srp alter- ation	Brc-Srp alter- ation	Brc alter- ation	Brc alter- ation
wt. %																	
SiO ₂	39.2	39.4	4.5	31.8	40.1	9	38.5	39.2	37.2	40.5	40.7	42.2	40.5	34.4	7.4	0.4	1.8
Al ₂ O ₃	0.04	0.37	0.08	0	0.05	0.26	0	0.23	1.17	0.21	0.47	0.01	0.03	0.21	0	0.31	0.05
FeO	5.1	5.3	9.9	9.1	7.9	10.8	4.1	5.2	5.4	7.4	4	4.6	4.7	4.8	26.8	34.2	32.6
MgO	38.4	38.2	71.5	44.1	36	64.2	34.4	37.5	38.7	37.1	34.6	40.7	39.6	32.1	43.6	40.2	45.4
MnO	0.07	0.05	0.28	0.14	0.1	0.12	0.04	0.11	0.12	0.2	0.03	0.07	0.09	0.01	0.54	1.99	1.24
CaO	0.03	0.21	0.02	0.16	0.4	0.1	0.06	0.09	0.18	0.31	0.05	0.02	0.05	0.08	0.26	0.22	0.11
Si/(Mg+Fe)	0.68	0.68	0.04	0.44	0.67	0.09	0.75	0.69	0.63	0.67	0.79	0.7	0.69	0.7	0.07	0	0.02
X _{Mg}	0.93	0.93	0.93	0.90	0.89	0.91	0.94	0.93	0.93	0.9	0.94	0.94	0.94	0.92	0.74	0.68	0.71
µg g⁻¹																	
V	0.2	5.1	b. d. l.	0.5	5.1	b. d. l.	22.2	3.3	55.9	11.6	16.2	3.5	12.3	10.8	b. d. l.	b. d. l.	b. d. l.
Ni	2609	416	432	2522	770	416	990	2758	919	809	951	b. d. l.	1721	3096	251	118	b. d. l.
Li	7.6	2.0	b. d. l.	2.4	6.1	b. d. l.	1.8	2.0	10.0	25.6	0.1	0.7	7.2	1.2	b. d. l.	b. d. l.	b. d. l.
B	56	80	b. d. l.	76	23	b. d. l.	351	318	64	22	68	15	304	111	b. d. l.	b. d. l.	b. d. l.
Rb	0.951	0.196	b. d. l.	0.156	1.836	b. d. l.	0.154	0.066	0.306	8.737	0.174	b. d. l.	0.211	b. d. l.	b. d. l.	b. d. l.	b. d. l.
Sr	4.22	1.22	b. d. l.	5.93	17.18	b. d. l.	2.94	5.05	13.15	7.93	1.98	1.17	5.91	2.90	b. d. l.	b. d. l.	b. d. l.
Cs	0.596	0.058	b. d. l.	0.091	1.217	b. d. l.	0.050	0.084	b. d. l.	4.125	0.014	0.064	0.021	0.002	b. d. l.	b. d. l.	b. d. l.
Ba	1.49	0.97	b. d. l.	3.51	2.30	b. d. l.	0.46	0.26	2.49	2.55	0.94	0.95	0.61	1.16	b. d. l.	b. d. l.	b. d. l.
Rb/Cs	1.60	3.38	n/a	1.71	1.51	n/a	3.08	0.79	n/a	2.12	12.43	n/a	10.05	n/a	n/a	n/a	n/a

Si/(Mg+Fe) is in wt.%, X_{Mg} is on a molar basis.

Abbreviations: Brc, brucite; intergr., intergranular; n/a, not available; Srp, serpentine.

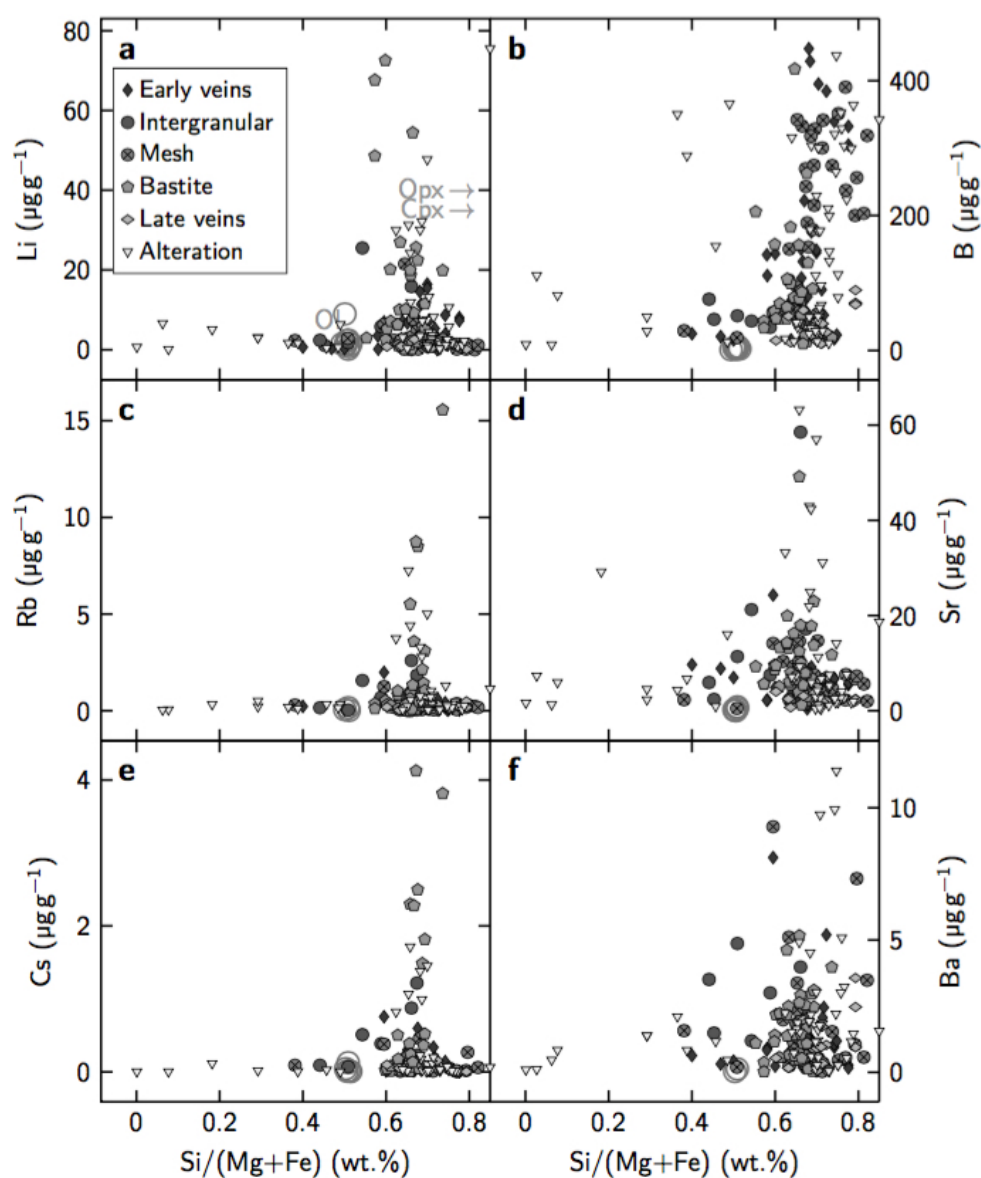


Figure 4.6 Variations of Li, B, Rb, Sr, Cs, and Ba in serpentine and serpentine–brucite mix analyses. Concentrations are usually highest in analyses of pure serpentine, whereas analyses in which brucite predominates exhibit considerably lower contents of the respective species. Furthermore, FME contents are generally enriched in early products of fluid–rock interaction relative to later products. Concentrations in primary minerals are indicated for comparison. Abbreviations: Cpx, clinopyroxene; Ol, olivine; Opx, orthopyroxene.

Whereas Ba contents in early veins are low ($<2 \mu\text{g g}^{-1}$) at Yinazao and Fantangisña, intergranular and mesh serpentine at Fantangisña and Asùt Tesoru contain up to $5 \mu\text{g g}^{-1}$ or more Ba (Fig. 4.6f). Concentrations in bastite at Fantangisña and Asùt Tesoru are enriched with respect to primary pyroxene, with up to $4 \mu\text{g g}^{-1}$ and $5 \mu\text{g g}^{-1}$, respectively;

$<2 \mu\text{g g}^{-1}$ Ba are contained in bastite from Yinazao. In contrast, late serpentine veins exhibit highest Ba at Yinazao (up to $4 \mu\text{g g}^{-1}$ vs. $<2 \mu\text{g g}^{-1}$ at Fantangisña and Asùt Tesoru). Areas affected by late alteration have contents as high as $\sim 6 \mu\text{g g}^{-1}$, $2 \mu\text{g g}^{-1}$, and $\sim 12 \mu\text{g g}^{-1}$ at Yinazao, Fantangisña, and Asùt Tesoru.

Systematic variations in FME concentrations could not be observed between serpentinization products of the different lithologies, i. e., between dunites, harzburgites, and the lherzolite.

Detailed analyses of clasts with inward-migrating alteration show that late fluid–rock interactions did not lead to further enrichments in FMEs in the browned areas. For instance, comparing FME contents in unserpentinized peridotite or in serpentine to those in areas affected by browning shows comparable or lower concentrations in samples from Fantangisña and Asùt Tesoru (Supplementary Information Figs. A.3.3 and A.3.4).

4.5 Discussion

4.5.1 Polyphase serpentinization at the basal plane of the mantle wedge

Source region of the ultramafic clasts Microfabrics and *in situ* mineral analyses of the ultramafic clasts reveal a multi-phase serpentinization history with distinct episodes of fluid–interaction. In order to reconstruct the conditions under which the metamorphism occurred, we firstly deduce the origin of the clasts. We thereby follow Kahl et al. (2015), who investigated FME inventories of serpentinized ultramafic clasts from the South Chamorro serpentinite mud volcano (78 km distance to the trench, 18 km depth to the subducting slab). Kahl et al. (2015) state that the most likely source region of the clasts is the basal plane of the suprasubduction mantle wedge. These authors argue that the systematically differing enrichments in FMEs in their samples as compared to serpentinite mud from South Chamorro provide strong evidence for this theory, since no such enrichments related to subsequent vein generations would exist if the materials came from the second potential source regions: the mud volcanoes' conduits. The fluids serpentinizing clasts (to be mobilized) from the conduit wall rocks would derive from the rising mud, which would hence have to carry the FMEs and would likely show similar enrichments. We hence agree with the interpretation by Kahl et al. (2015) of the basal mantle wedge as the source region for the samples investigated here. Serpentinite muds at Yinazao, Fantangisña, and Asùt Tesoru generally exhibit lower concentrations of Li, B, Rb, Sr, Cs, and Ba (J. Ryan, unpubl. data), despite systematic changes that are related to increasing slab depths (e. g., Fryer et al., 2018; Wheat et al., 2018).

We further agree with the conclusion by Kahl et al. (2015) that, after erosion, it is likely that the clasts were dragged down from shallower depth in the subduction channel. This is evident from variations in FME contents with respect to the different alteration stages within individual clasts. These variations were induced by changes in the geochemistries of the serpentinizing fluids; however, if the fluid (and element) supply from the subducting lithosphere is considered constant, it can be assumed that the serpentinizing fluid chemistry at a particular slab depth does not change over time.

In contrast, changes in fluid chemistry occur with progressive subduction as a function of prograde metamorphism at depth (e. g., Mottl et al., 2004; Fryer et al., 2018). Clasts travelling from shallower to deeper depth in the décollement should hence interact with chemically variable fluids. The here studied samples are considered to have recorded these variations, analogous to the samples studied by Kahl et al. (2015).

Conditions during successive serpentinization events Microfabrics of the ultramafic clasts prove of multiple phases of serpentinization and fluid–rock interactions under changing conditions. Early veins consisting of serpentine ± Mg-rich brucite ± iron alloys and/or magnetite reflect the first reactions with infiltrating Si-rich fluids into the mantle wedge. Along these fluid pathways, the first hydration of the ultramafic rock led to the formation of serpentine, likely via the reaction $3 \text{Mg}_2\text{SiO}_4 + 4 \text{H}_2\text{O} + 2 \text{SiO}_2 \longrightarrow \text{Mg}_3\text{Si}_2\text{O}_5(\text{OH})_4$ (e. g., Frost and Beard, 2007). SiO_2 is continuously being consumed in this reaction, leading to the progressively depletion in Si within the fluid. Accompanied with this, the effective portions of rock participating in the reaction would be rather small during channelized fluid flow along these early veins, resulting in high water/rock ratios. Within the vein centers, these water/rock ratios led the formation of high- X_{Mg} brucite and minor magnetite in the vein centers. These results are in consistence with results from thermodynamic computations (e. g., Klein et al., 2009; McCollom and Bach, 2009).

Emanating from these early veins, fluids penetrated the ultramafic rock along narrower veinlets or along grain boundaries. Hydration continued under conditions of high a_{SiO_2} , as indicated by the decreased presence of brucite, iron alloys, and/or magnetite in intergranular and mesh textures; one would expect brucite to form if a_{SiO_2} was low (*cf.* Bach et al., 2004).

Similarly to the pervasive hydration, serpentine in late veins formed from Si-rich fluids. In contrast to earlier alteration stages, however, the serpentine did not grow by dissolution–precipitation of olivine and/or bastite but by precipitation from a Mg–Si-rich fluid in void space. Late veins do hence not contain brucite and/or iron alloys or magnetite.

Fe-rich brucite developed during late-stage alteration (browning) of the clasts was previously described by Kahl et al. (2015). According to these authors, the browning corresponds to the re-equilibration of the clasts with fluids that lack buffering by quartz-rich lithologies of the descending slab. Kahl et al. (2015) assign this process to potentially occur in the mud volcano conduits, where the slab-derived fluids are most evolved and presumably lost the bulk of their initially high amounts of Si. Blackening, which led to the formation of abundant sulfides, likely took place under the same conditions since it commonly occurs in conjunction with browned areas.

The precipitation of Ca carbonates has previously been assigned to fluid–rock reactions within the serpentinite mud volcano, where slab-derived fluids mix with seawater (Albers et al., in preparation; see Chapter 3). Iowaite that co-occurs with carbonates in veins further suggests that this alteration of the clasts occurred under oxidative, Cl-rich

conditions (e. g., Heling and Schwarz, 1992; Nielsen et al., 2015), likely in contact with seawater.

We hence observe an overall shift in alteration conditions from a reducing environment with high $a\text{SiO}_2$ during early serpentinization to low $a\text{SiO}_2$ and, ultimately, oxidizing conditions during late fluid–rock interactions. Early Si-rich fluids were thereby likely induced by the dehydration of opal-CT and diagenesis and decomposition of clays in the downgoing slab (Mottl et al., 2004; Hulme et al., 2010; Fryer et al., 2018). We ascribe serpentine formation of the following distinct alteration stages to be induced by Si-rich fluids: serpentine in early veins (see discussion above); pervasive serpentinization including intergranular, mesh, and bastite serpentine; late veins. The cavities or cracks in which late vein-serpentine is observed are thought to have developed while the respective lithologies were still attached to the mantle wedge and sufficient strain could build up. Serpentine in these late veins may have formed before or after the detachment from the wall rock.

The drop in $a\text{SiO}_2$ during continuing serpentinization can generally be ascribed to the process of serpentine formation, following the reaction $3\text{Mg}_2\text{SiO}_4 + \text{SiO}_2(\text{aq}) + 4\text{H}_2\text{O} \longrightarrow 2\text{Mg}_3\text{Si}_2\text{O}_5(\text{OH})_4$, that induces Si-incorporation from the fluid in the ultramafic lithology (e. g., Frost and Beard, 2007; Klein et al., 2009). Whereas Si may steadily be supplied by metamorphic breakdown reactions in the subduction channel, the above stated reaction presumably causes a drop in Si-saturation in the serpentinizing fluids within the mud volcano conduits. This process likely accounts for the late browning, i. e., the brucite-dominated alteration, of the clasts. The formation of Fe-rich brucite in serpentinites from mid-ocean ridges is assigned to the reaction $2\text{Mg}_{1.8}\text{Fe}_{0.2}\text{SiO}_4 + 3\text{H}_2\text{O} \longrightarrow \text{Mg}_{2.85}\text{Fe}_{0.15}\text{Si}_2\text{O}_5(\text{OH})_4 + \text{Mg}_{0.75}\text{Fe}_{0.25}(\text{OH})_2$ (e. g., Bach et al., 2006).

The generally low contents of magnetite in most of the samples are suggestive of serpentinization temperatures $<300^\circ\text{C}$ (Klein et al., 2014; also see discussion by Kahl et al., 2015). This is also in line with Debret et al. (2019), who interpreted magnetite-poor chrysotile- and lizardite-rich serpentinites recovered during IODP Expedition 366 to have formed below 240°C . We hence presume that the bulk of the fluid–rock interactions of the here investigated clasts occurred below this temperature. Debret et al., however, also reported on antigorite-bearing assemblages that are characterized by significantly higher contents of magnetite as compared to the chrysotile- and lizardite-bearing clasts; these authors suggest that the antigorite formed at up to $\sim 400^\circ\text{C}$. We found magnetite-rich vein in three clasts from the deeper-sourced Fantangisña and Asùt Tesoru; these may have formed at temperatures above the estimate of 240°C (see above).

4.5.2 Evolution of serpentinizing fluids and FME sources

Fluid evolution within individual mud volcano root zones The relative chronology of the microfabric evolution yields information on changing geochemical environments in which the respective samples underwent alteration. Independent of the samples origin, i. e., shallower- or deeper-sourced mud volcano, we are able to reconstruct general changes in the character of the interacting fluids.

For all clasts, initial interaction of the ultramafic lithologies with SiO₂- and FME-rich fluids led to the formation of serpentine with generally high levels of Li, B, Rb, Sr, Cs, and Ba. Yet, domains with increased fractions of Mg-rich brucite show lower FME concentrations relative to areas consisting of pure serpentine (Fig. 4.6). Above, we ascribed the occurrence of brucite to prolonged fluid flow within early veins or intergranular textures. The ongoing fluid flow (and peridotite reaction) likely also led to the observed decrease in the fluids' FME contents. The ongoing flow causes the progressive loss of Si from the fluid, leading to the formation of brucite—our data indicate that FMEs are lost from the fluid via the same process. The brucite-bearing early serpentinization stages hence illustrate a (local) early alteration of the fluid. FME contents in mesh and bastite textures are similarly or stronger enriched with respect to serpentine from earlier fluid–rock interactions. Serpentinizing fluid during this pervasive stage carried high amounts of FMEs, implying a relatively unaltered fluid. The absence of brucite implies a sufficiently high *a*SiO₂, strengthening this conclusion. Late veins record a shift towards the interaction with fluids that exhibit decreased contents of FMEs. This results in serpentine with overall lower concentrations of all species. The compositions of these veins depict the advancing influence of fluids that may originate from a different source; however, the fluids remain Si-rich at this stage. Ultimately, alteration of the clasts that we ascribe to have taken place within the in the feeding conduits and/or after eruption of mud matrix and clasts at the seafloor (see Section ‘**Conditions during successive serpentinization events**’) was induced by the interaction with low-*a*SiO₂, low-FME fluids. Serpentine and Fe-brucite formed during this stage lack significant amounts of the here-considered elements. This loss of Si and FMEs from the fluids is attributed to earlier phases of fluid–rock interaction. After the mudflow eruption at the seafloor, venting fluids mixed with seawater and the alteration environment changed to more oxic conditions, leading to the formation of iowaite and Ca carbonates (Albers et al., in preparation; see Chapter 3). FME contents of these latest alteration products are among the lowest in the studied samples. Serpentine affected by these late alteration phases however exhibits concentrations similar to the early and pervasive stages of fluid–rock interaction, implying that FME contents are not being reset once incorporated (see Section 4.4.2).

These conclusions are generally very consistent with proposed fluid–rock interactions affecting ultramafic clasts at South Chamorro (Kahl et al., 2015). These authors attribute the lack of high FME contents of fluids from which late veins form to the complete resetting of these by serpentinization and continued diagenetic and metamorphic processes within the subduction channel (see also, e. g., Moore and Saffer, 2001; Kastner et al., 2014).

Despite this overall consensus between the samples from the different mud volcanoes, we determined systematic variations in FME contents of the different alteration phases that occur as a function of slab depth: normalized for subducted bulk sediment from ODP Sites 800 and 801 located east of the Mariana trench (Plank and Langmuir, 1998), serpentine FME contents are shown in Figure 4.7 as a function of alteration stage and mud volcano. We therefore recalculated the element concentrations of LA-ICP-MS analyses

of mixed serpentine–brucite analyses to the element concentrations of the serpentine proportion of the intergrown phase (on the basis of the Si/(Mg + Fe) ratios of the respective analyses). Including with data from Kahl et al. (2015), we provide a dataset giving insight into the mobilization FMEs at subduction depth of 13 to 18 km. Boron contents are generally highest at Yinazao and strongly drop towards Fantangisña and Asùt Tesoru; towards South Chamorro, concentrations increase slightly. Mesh B concentrations are, however, highest at Fantangisña. Similarly, Li contents are highest in early veins at Yinazao, whereas mesh and bastite exhibit enrichments similar to Asùt Tesoru. Lithium concentrations are particularly low in early veins at Fantangisña. Rubidium, Sr, Cs, and Ba contents in serpentine generally increase across the forearc. Concentrations of Rb and Cs are particularly low throughout all alteration phases at Yinazao; Rb concentrations in mesh and late veins remain at low levels towards South Chamorro. Strontium exhibits high contents in all serpentine generations, except for late veins, at Asùt Tesoru and South Chamorro. Likewise, Ba concentrations display a strong increase with increasing slab depth, but contents in late veins decrease. We interpret these changes as to result from changing sources that contribute to the serpentinizing fluid (see below).

FME sources as a function of slab depth In accordance with the generally highly refractory composition of forearc mantle material (e. g., Salters and Stracke, 2004), FME contents in the here studied primary minerals are very low. The forearc mantle can consequently be excluded as a source for the here-studied FMEs. Instead, potential FME sources are subducted sediments and subducted (altered) oceanic crust. Subducting sediments and basement are considerable reservoirs for these species as, e. g., inferred from drilling constraints east of the Mariana trench. Bulk sediment comprises $\sim 19 \mu\text{g g}^{-1}$ Li, $>30 \mu\text{g g}^{-1}$ B and Rb, $\gg 150 \mu\text{g g}^{-1}$ Sr and Ba, and $\sim 1.3 \mu\text{g g}^{-1}$ Cs (e. g., Plank and Langmuir, 1998; Plank, 2014); concentrations in the crust are a function of the degree of alteration and vary strongly with up to $>30 \mu\text{g g}^{-1}$ Li, $>100 \mu\text{g g}^{-1}$ Rb, Sr, and Ba, and $>1 \mu\text{g g}^{-1}$ Cs (Alt et al., 1992; Kelley et al., 2003).

The *in situ* FME inventories in serpentine allow the reconstruction of potential sources for these (*cf.* Kahl et al., 2015). These authors recognize subducting sediments to be the major FME source at the 18 km-deep-sourced South Chamorro. They base this interpretation on fairly uniform Rb/Cs ratios between 1 and 10 that well overlap with hydrothermal fluid compositions derived from experiments by You et al. (1996; Fig. 4.8a). You et al. investigated reactions between sediments and a synthetic NaCl–CaCl₂ solution in order to simulate geochemical processes during sediment subduction. Fluid Rb/Cs ratios evolve from ~ 3 to 11 during the temperature increase from 25 to 350 °C at 80 MPa in these experiments. By comparison, variably altered oceanic crust east of the Mariana trench usually exhibits Rb/Cs ratios in the order of >10 to 100 (Kelley et al., 2003; see also discussion and Fig. 8 in Kahl et al., 2015).

Rb/Cs ratios at Yinazao strongly differ from the data presented by Kahl et al. (2015). Considerably higher median Rb/Cs ratios of ~ 10 to 37 indicate the interaction with a different fluid at this shallow-sourced mud volcano (Fig. 4.8b), i. e., to reflect the influence of (a) high-Rb/Cs fluid source(s). We propose that early serpentinizing fluids

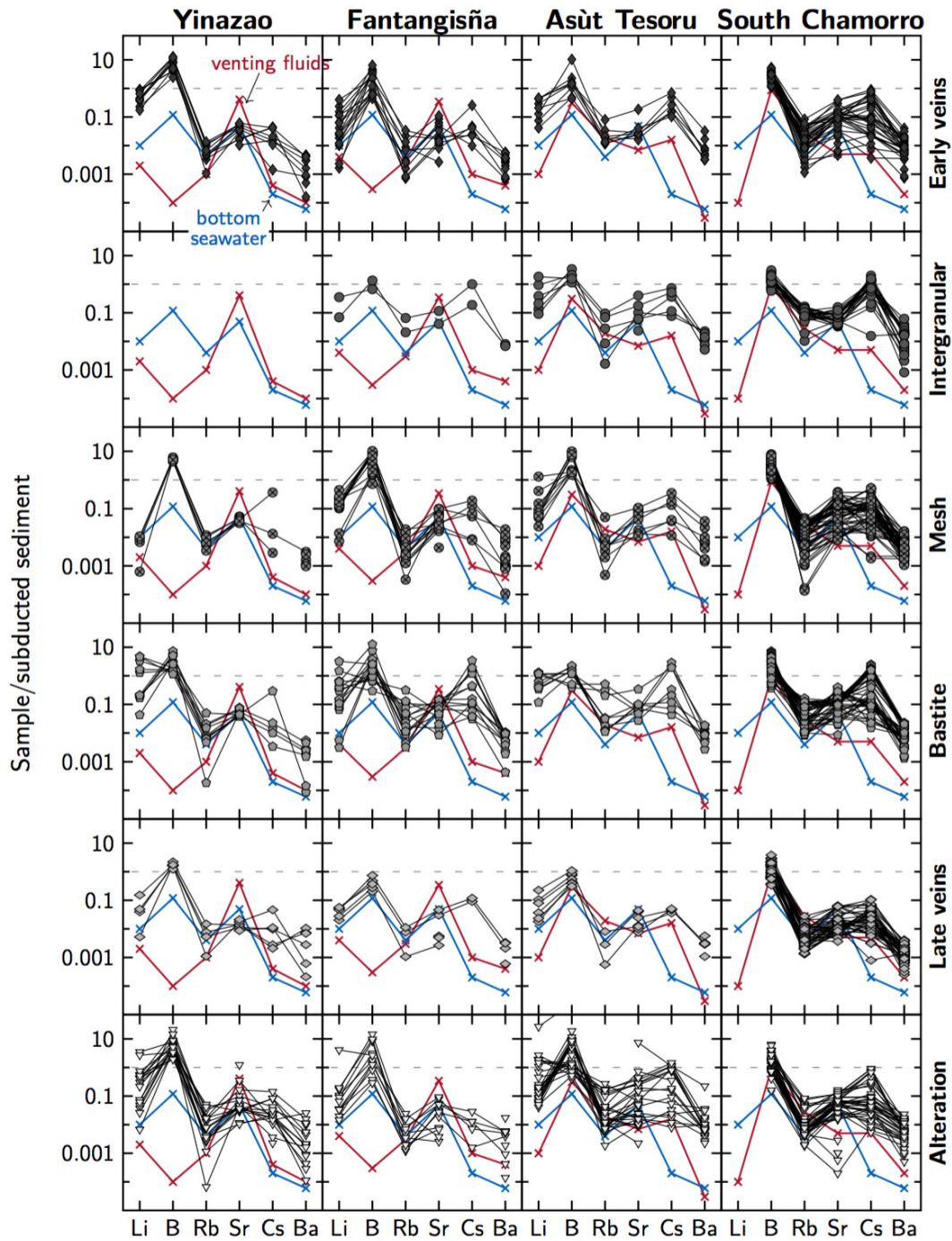


Figure 4.7 Changes in serpentine FME contents of the individual mud volcanoes as a function of increasing slab-depth (from Yinazao to South Chamorro), normalized for subducting sediment (Plank and Langmuir, 1998). Systematic changes reflect progressive metamorphic conditions in the subduction channel. At the same time, evolution of serpentinizing fluids over time at the individual mud volcanoes can be tracked, i. e., the general loss of FMEs during early alteration stages. See text for further discussion. Compositions of venting fluids and bottom seawater (Mottl et al., 2004; Wheat et al., 2018) are shown for comparison.

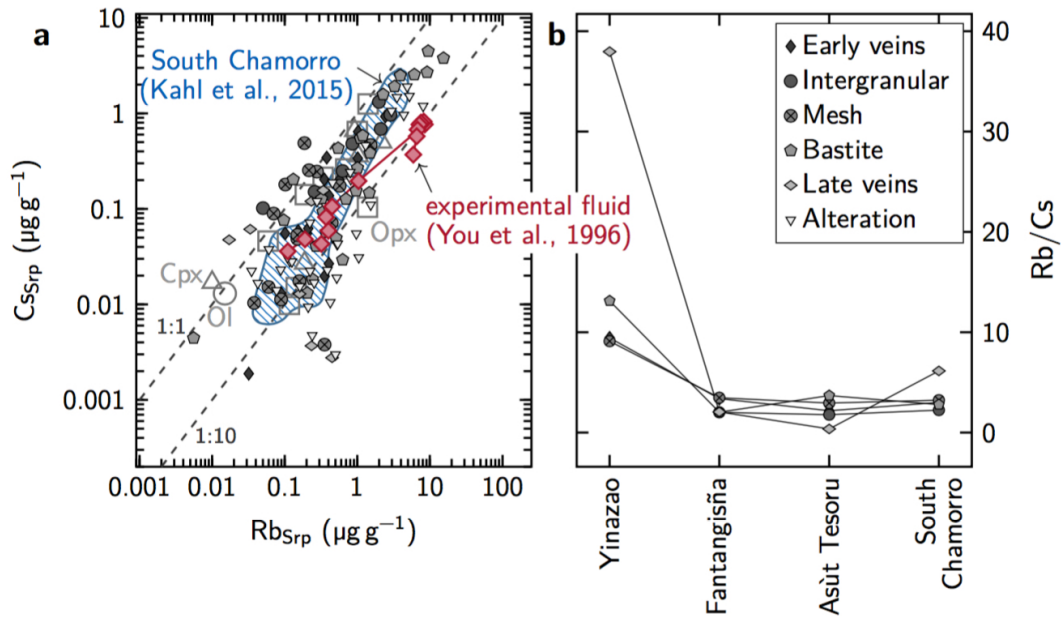


Figure 4.8 Variations in Rb *vs.* Cs contents and Rb/Cs ratios in serpentine. (a) Concentrations of Rb and Cs vary strongly within serpentine of the different alteration stages and from the different seamounts. They, however, generally plot within a ratio of 1 : 1 to 1 : 10. Data overlap with those of serpentine from clasts from the deeper-sourced South Chamorro (Kahl et al., 2015) and with experimental fluids of You et al. (1996). Concentrations in primary phases are shown for comparison. (b) Evolution of serpentine Rb/Cs ratios with increasing slab depth. Ratios are highest at shallow-sourced Yinazao, where pore waters from the downgoing sediments and dehydration of sedimentary opal are thought to primarily contribute to the serpentinizing fluid. By contrast, lower Rb/Cs at deeper-sourced Fantangisña, Asùt Tesoru, and South Chamorro indicate the serpentinizing fluids to have been significantly influenced by the decomposition of clays and altered oceanic crust.

in the shallow portions of the subduction zone were dominated by the interplay of pore waters and fluids derived from opal dehydration. Large volumes of pore water are released during the compaction of subducting sediments. Assuming that the chemistry of sediment pore water approximately resembles that of seawater, its Rb/Cs ratios should be ~ 400 (e.g., Mottl et al., 2004). Further, shallow subduction processes include the dehydration of opal-A and opal-CT, most importantly the transformation of opal in diatom- and radiolarian-rich sediments to quartz (Kastner et al., 2014, and references therein). Subducting chert and radiolarite at the Mariana trench contain up to $\sim 34 \mu\text{g g}^{-1}$ Rb and $\sim 2 \mu\text{g g}^{-1}$ Cs, resulting in Rb/Cs ratios of ~ 17 to 26 (Plank and Langmuir, 1998). Mixing of these two sources likely lead to high Rb/Cs ratios in serpentine recovered from Yinazao. The very high Rb/Cs ratios of pore waters are thereby buffered by lower Rb/Cs of opal breakdown. Opal decomposition on the other hand contributed Rb and Cs to the serpentinizing fluid.

In serpentine from the intermediate- to deep-sourced Fantangisña and Asùt Tesoru, Rb/Cs ratios generally plot within the range of 1 to 8, hence overlapping with data from

South Chamorro (Fig. 4.8b). Compliant with Kahl et al. (2015), we presume that the major fluid and FME sources in the intermediate portions of the subduction zone is related to the decomposition of clay-rich sediment. This is further in accordance with earlier investigations suggesting that sediment metamorphic processes primarily mediate fluid chemistries in these portions of the Mariana subduction zone (e. g., Mottl et al., 2004; Hulme et al., 2010; Fryer et al., 2018). However, increases in absolute concentrations of several FMEs imply that dehydration of oceanic crust progressively contributes to the fluid at greater depth. Hulme et al. (2010) argue that, for instance, the increase in Rb in venting fluids signifies this transition. These authors highlighted a rise in Rb/K ratios that occurs concomitant with the higher Rb concentrations; this is interpreted to reflect a shift from dehydrating sediments with low Rb/K ratios at shallow and intermediate slab depth to the dehydration of higher Rb/K ratio basaltic crust at greater depth. Similarly, increases in Cs and Ba concentrations of upwelling fluids with greater slab depths are suggested to be evoked by the growing influence of oceanic crust dehydration (Mottl et al., 2004; Hulme et al., 2010). Contents of Cs and Ba in here studied serpentine show a similar rise with increasing slab depth (Fig. 4.7) so that we follow the interpretation by Mottl et al. (2004) and Hulme et al. (2010) that the dehydration of sediment is likely accompanied by decomposition of oceanic basement below Asùt Tesoru.

We conclude that the serpentinized mantle wedge records changing metamorphic conditions at the slab–mantle interface across the outer Mariana forearc (Fig. 4.9). FME contents in serpentine reflect the varying conditions expected to contribute to the dehydration of the subducting slab, namely pore water release and opal dehydration at shallow depth, followed by clay diagenesis at intermediate depth, and dehydration of the oceanic crust at the deepest levels (e. g., Moore and Saffer, 2001; Hyndman and Peacock, 2003; Jarrard, 2003; Fryer and Salisbury, 2006; Kastner et al., 2014).

As shown above, similarly conclusions were drawn from trends in the geochemistry of fluids upwelling in the mud volcanoes (e. g., Mottl et al., 2004; Hulme et al., 2010; Wheat et al., 2018). Yet, here observed data of B and Sr stand in contrast with reported upwelling fluid chemistry—boron concentrations increase in venting fluids across the forearc but decrease in serpentine, and Sr contents decrease in venting fluids across the forearc but are higher in deep-sourced relative to shallow-sourced serpentine.

Mottl et al. (2004) explain the increasing B contents by its increased mobilization as the temperature in the slab rises. Mottl et al. refer to experiments in which B was taken up by sediment at $\sim 50^\circ\text{C}$ and leached from sediment only at temperatures above $\sim 100^\circ\text{C}$ (James et al., 2003). In contrast to this hypothesis, we recorded highest B concentrations in serpentine at Yinazao for which slab temperatures of $\sim 80^\circ\text{C}$ were proposed (Hulme et al., 2010). We hence presume that leaching of B from sediments occurs under substantially lower temperature (and pressure) conditions as proposed by Mottl et al. (2004). Our data are corroborated by experiments by You et al. (1996), which showed that B gets enriched in fluids reacting with sediment at temperatures $\geq 25^\circ\text{C}$ on. However, B contents in venting fluids of only $0.2\ \mu\text{M}$ (Wheat et al., 2018) strongly imply that most of the B is consumed during fluid–rock interactions at depth (or during the rise of the fluids towards the seafloor). The slight rise of B concentrations in serpentine from

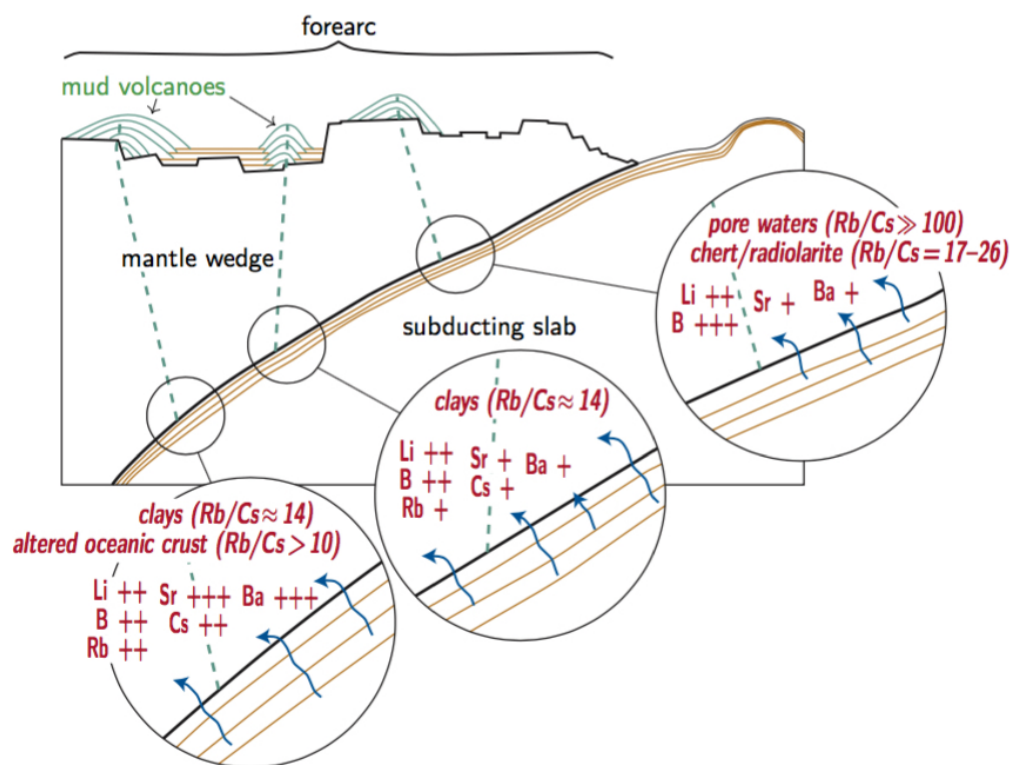


Figure 4.9 Evolution of serpentinizing fluids with progressive subduction. Fluids originate from the compaction of sediments (pore waters) and the breakdown of opal (chert/radiolarite-rich sediment) at shallowest subduction levels. These fluids are enriched in Li and B, but also carry minor Sr and Ba. At greater depth, fluids have their origin in the breakdown of clays. Boron contents decrease with increasing slab depth, whereas Sr and Ba become progressively more enriched. Rubidium and Cs are as well leached from sediments at intermediate and even more from altered oceanic crust at greater depth. See text for further discussion. Figure in parts modified after Fryer et al. (2018).

Asùt Tesoru towards South Chamorro may indicate the higher-temperature leaching of B from basalt as suggested by Mottl et al. (Mottl et al.; see also Mottl and Holland 1978).

High Sr concentrations are proposed to result from a pore water source associated with the collapse of smectite at Yinazao and from decarbonation at greater depth (Hulme et al., 2010). At the deep-sourced mud volcanoes, Sr contents in upwelling fluids are thought to be buffered, together with Ca, to low concentrations by the formation of Ca carbonates at depth (e.g., Mottl et al., 2004). Higher Sr contents in serpentine at deep- relative to shallow-sourced mud volcanoes presented here and by Kahl et al. (2015) indicate that Sr (and likely also Ca) was indeed efficiently mobilized at depth but must again have been incorporated at depth, resulting in low concentrations in rising fluids. The recovery of Ca carbonates and Ca- and Sr-bearing silicates from Fantangisña and Asùt Tesoru, which are proposed to have formed within the subduction channel, imply that these species are incorporated at depth (Albers et al., in preparation; see Chapter 3).

The general depletion of most elements relative to bulk sediment (Fig. 4.7) implies

that either only a fraction of the sediment releases its FME inventories at these shallow to intermediate subduction depths, or that there is an upper limit of how much of the respective species can be incorporated into serpentine. The fact that concentrations of particular elements (e. g., Sr at Yinazao) are high in serpentine as well as in fluids upwelling at the mud volcanoes could lend credit to this conclusion. But even higher concentrations of Sr in serpentine at Asùt Tesoru or South Chamorro contradict this idea. These contents are concomitant with very low Sr contents in upwelling fluids, strongly arguing for (an) additional parameter(s) that control the fate of FMEs after mobilization from the subducting slab. Furthermore, the example of Sr, but also those of B or other species illustrated above, emphasize that sampling of the upwelling fluids provide incomplete and in some cases distorted insight into the processes at depth.

4.6 Summary and conclusions

The investigated samples were affected by multiple serpentinization phases as evidenced by their microfabrics and major and trace element chemistry. Based on FME contents we were able to show that the clasts originate from the basal plane of the mantle wedge. Initial serpentinization by slab-derived fluids occurred before the samples got detached from the wedge. Fluid interactions proceeded within the subduction channel and the mud volcano conduits as well as after the clasts' eruption in the mud volcanoes. FMEs mobilized during prograde metamorphic processes in the downgoing slab were incorporated into serpentine during these interactions. *In situ* analyses of the serpentine allowed us to track the evolution of serpentinizing fluids within the subduction channel and the mobility of FMEs within the downgoing plate.

Serpentine, Mg-rich brucite, and minor magnetite as well as generally high FME concentrations in serpentine characterize the early serpentinization stages throughout the investigated samples. This implies serpentinization by unaltered slab-derived fluids laden with FMEs and a high a_{SiO_2} . Later serpentinization stages, by contrast, exhibit serpentine, Fe-rich brucite, and low FME contents. Silica activities were lower and the previously FME-laden fluids are interpreted to have lost most of their FMEs during earlier interaction with rock or sediments in the subduction channel.

Fluids that led to the serpentinization of the forearc mantle are released from the subducting slab. Based on our data, we recognize a general change in fluid and FME sources as a function of slab depth. Serpentine in clasts from the shallow-sourced mud volcano Yinazao reveal higher Rb/Cs ratios (up to ~37), higher contents of Li and B, and lower contents of Sr, Ba, and Cs relative to samples from the deeper-sourced mud volcanoes. We interpret these as influence of predominantly sediment pore waters and of opal breakdown in chert- and radiolarite-rich sediments on the fluids that hydrate the mantle wedge. With increasing depth-to-slab, Rb/Cs ratios decrease to <10, as expected for the dehydration of clay-rich sediments. Serpentine recovered at Fantangisña is constituted of higher Rb, Cs, and Ba concentrations whereas Li, B, and Sr concentrations are decreased in comparison to Yinazao. Towards Asùt Tesoru and South Chamorro, the deepest-sourced mud volcanoes, Rb/Cs ratios remain low. Contents of Rb, Sr,

Cs, and Ba are most elevated, suggesting that the dehydration of the altered oceanic crust progressively constitutes to the serpentinizing fluids at depth. Lithium and B concentrations are lower as compared to the shallower-sourced mud volcanoes.

Our data show that FMEs are effectively mobilized even at shallow portions of the Mariana subduction zone. The chemistries of fluids that upwell at the mud volcanoes do not necessarily mirror the elements that are mobilized at depth. For instance, B concentrations in upwelling fluids increase from Yinazao to South Chamorro but decrease in serpentine. Vice versa, Sr contents in upwelling fluids are particularly low at mud volcanoes far away from the trench but highest in serpentine in the very same mud volcanoes. We hence conclude that fluids are massively altered during their rise to the seafloor.

A portion of the serpentinized material is returned to the ocean floor at the Mariana subduction system, whereas hydrated forearc lithologies will get buried to greater depth at most other convergent margins. At those, fluids and FMEs stored in the hydrated ultramafic rocks will be released during the eventual dehydration of serpentine, where they likely contribute to the formation and composition of arc magmas (e. g., Deschamps et al., 2011; Evans et al., 2013).

Acknowledgements

We are grateful to the captain and crew of the *JOIDES Resolution*, to the co-chief scientists P. Fryer and G. Wheat and the members of the Science Party. Patrick Monien is thanked for help with LA-ICP-MS analyses. This research used samples and data provided by IODP. Funding was provided by the Deutsche Forschungsgemeinschaft (German Research Foundation), grant no. BA 1605/18-1.

References

- Alt, J., Shanks III, W., 2006. Stable isotope compositions of serpentinite seamounts in the Mariana forearc: serpentinization processes, fluid sources and sulfur metasomatism. *Earth Planet. Sci. Lett.* 242 (3–4), 272–285, doi:[10.1016/j.epsl.2005.11.063](https://doi.org/10.1016/j.epsl.2005.11.063).
- Alt, J. C., France-Lanord, C., Floyd, P. A., Castillo, P., Galy, A., 1992. Low-temperature hydrothermal alteration of Jurassic ocean crust, Site 801. In: Larson, R. L., Lancelot, Y., Leg 129 Shipboard Scientists (Eds.), *Sci. Res. Vol. 129 of Proc. ODP. Ocean Drilling Program, College Station (TX)*, pp. 415–427. doi:[10.2973/odp.proc.sr.129.132.1992](https://doi.org/10.2973/odp.proc.sr.129.132.1992).
- Bach, W., Garrido, C. J., Paulick, H., Harvey, J., Rosner, M., 2004. Seawater–peridotite interactions: first insights from ODP Leg 209, MAR 15° N. *Geochem. Geophys. Geosyst.* 5 (9), Q09F26, doi:[10.1029/2004gc000744](https://doi.org/10.1029/2004gc000744).
- Bach, W., Paulick, H., Garrido, C. J., Ildefonse, B., Meurer, W. P., Humphris, S. E., 2006. Unraveling the sequence of serpentinization reactions: petrography, mineral chemistry, and petrophysics of serpentinites from MAR 15° N (ODP Leg 209, Site 1274). *Geophys. Res. Lett.* 33 (13), L13306, doi:[10.1029/2006gl025681](https://doi.org/10.1029/2006gl025681).
- Bebout, G. E., 1995. The impact of subduction-zone metamorphism on mantle-ocean chemical cycling. *Chem. Geol.* 126 (2), 191–218, doi:[10.1016/0009-2541\(95\)00118-5](https://doi.org/10.1016/0009-2541(95)00118-5).

- Benton, L. D., Ryan, J. G., Tera, F., 2001. Boron isotope systematics of slab fluids as inferred from a serpentine seamount, Mariana forearc. *Earth Planet. Sci. Lett.* 187 (3–4), 273–282, doi:[10.1016/S0012-821X\(01\)00286-2](https://doi.org/10.1016/S0012-821X(01)00286-2).
- Bostock, M. G., Hyndman, R. D., Rondenay, S., Peacock, S. M., 2002. An inverted continental Moho and serpentinization of the forearc mantle. *Nature* 417 (6888), 536–538, doi:[10.1038/417536a](https://doi.org/10.1038/417536a).
- Codillo, E. A., Le Roux, V., Marschall, H. R., 2018. Arc-like magmas generated by mélange-peridotite interaction in the mantle wedge. *Nat. Commun.* 9 (1), doi:[10.1038/s41467-018-05313-2](https://doi.org/10.1038/s41467-018-05313-2).
- D'Antonio, M., Kristensen, M. B., 2004. Serpentine and brucite of ultramafic clasts from the South Chamorro seamount (Ocean Drilling Program Leg 195, Site 1200): inferences for the serpentinization of the Mariana forearc mantle. *Mineralog. Mag.* 68 (6), 887–904, doi:[10.1180/0026461046860229](https://doi.org/10.1180/0026461046860229).
- Debret, B., Albers, E., Walter, B., Price, R., Barnes, J. D., Beunon, H., Facq, S., Gillikin, D. P., Mattielli, N., Williams, H., 2019. Shallow forearc mantle dynamics and geochemistry: new insights from IODP Expedition 366. *Lithos* 326–327, 230–245, doi:[10.1016/j.lithos.2018.10.038](https://doi.org/10.1016/j.lithos.2018.10.038).
- Defant, M. J., Drummond, M. S., 1990. Derivation of some modern arc magmas by melting of young subducted lithosphere. *Nature* 347 (6294), 662–665, doi:[10.1038/347662a0](https://doi.org/10.1038/347662a0).
- Deschamps, F., Godard, M., Guillot, S., Hattori, K., 2013. Geochemistry of subduction zone serpentinites: a review. *Lithos* 178, 96–127, doi:[10.1016/j.lithos.2013.05.019](https://doi.org/10.1016/j.lithos.2013.05.019).
- Deschamps, F., Guillot, S., Godard, M., Andreani, M., Hattori, K., 2011. Serpentinites act as sponges for fluid-mobile elements in abyssal and subduction zone environments. *Terra Nova* 23 (3), 171–178, doi:[10.1111/j.1365-3121.2011.00995.x](https://doi.org/10.1111/j.1365-3121.2011.00995.x).
- Deschamps, F., Guillot, S., Godard, M., Hattori, K., 2010. In situ characterization of serpentinites from forearc mantle wedges: timing of serpentinization and behavior of fluid-mobile elements in subduction zones. *Chem. Geol.* 269 (3–4), 262–277, doi:[10.1016/j.chemgeo.2009.10.002](https://doi.org/10.1016/j.chemgeo.2009.10.002).
- DeShon, H. R., Schwartz, S. Y., 2004. Evidence for serpentinization of the forearc mantle wedge along the Nicoya Peninsula, Costa Rica. *Geophys. Res. Lett.* 31 (21), L21611, doi:[10.1029/2004gl021179](https://doi.org/10.1029/2004gl021179).
- Elliott, T., Plank, T., Zindler, A., White, W., Bourdon, B., 1997. Element transport from slab to volcanic front at the Mariana arc. *J. Geophys. Res. Solid Earth* 102 (B7), 14991–15019, doi:[10.1029/97jb00788](https://doi.org/10.1029/97jb00788).
- Evans, B. W., Hattori, K., Baronnet, A., 2013. Serpentinite: what, why, where? *Elements* 9 (2), 99–106, doi:[10.2113/gselements.9.2.99](https://doi.org/10.2113/gselements.9.2.99).
- Frost, B. R., Beard, J. S., 2007. On silica activity and serpentinization. *J. Petrol.* 48 (7), 1351–1368, doi:[10.1093/petrology/egm021](https://doi.org/10.1093/petrology/egm021).
- Fryer, P., Ambos, E. L., Hussong, D. M., 1985. Origin and emplacement of Mariana forearc seamounts. *Geology* 13 (11), 774–777, doi:[10.1130/0091-7613\(1985\)13<774:oaomf>2.0.co;2](https://doi.org/10.1130/0091-7613(1985)13<774:oaomf>2.0.co;2).
- Fryer, P., Fryer, G. J., 1987. Origins of nonvolcanic seamounts in a forearc environment. *Seamounts, Islands, and Atolls* 43, 61–69, doi:[10.1029/gm043p0061](https://doi.org/10.1029/gm043p0061).
- Fryer, P., Mottl, M., Johnson, L., Haggerty, J., Phipps, S., Maekawa, H., 1995. Serpentine bodies in the forearcs of western Pacific convergent margins: origin and associated fluids. *Geoph. Monog. Series* 88, 259–279, doi:[10.1029/gm088p0259](https://doi.org/10.1029/gm088p0259).
- Fryer, P., Pearce, J. A., Stokking, L. B. (Eds.), 1990. Initial Reports. Vol. 125 of Proc. ODP. Ocean Drilling Program, College Station (TX).
- Fryer, P., Wheat, C. G., Williams, T., Albers, E., Bekins, B., Debret, B. P. R., Deng, J., Dong, Y., Eickenbusch, P., Frery, E. A., Ichiyama, Y., Jonson, K., Jonston, R. M., Kevorkian, R. T., Kurz, W., Magalhaes, V., Mantovanelli, S. S., Menapace, W., Menzies, C. D., Michibayashi, K., Moyer, C. L., Mullane, K. K., Park, J.-W., Price, R. E., Ryan, J. G., Shervais, J. W., Sissmann, O. J., Suzuki, S., Takai, K., Walter, B., Zhang, R., 2018. Expedition 366 summary. Vol. 366 of Proc. IODP. International Ocean Discovery Program, College Station (TX). doi:[10.14379/iodp.proc.366.101.2018](https://doi.org/10.14379/iodp.proc.366.101.2018).
- Fryer, P. B., 1992. A synthesis of Leg 125 drilling of serpentinite seamounts on the Mariana and Izu-Bonin forearcs. In: Fryer, P., Pearce, J. A., Stokking, L. B. (Eds.), *Scientific Results*. Vol. 125 of Proc. ODP. Ocean Drilling Program, College Station (TX), pp. 593–614. doi:[10.2973/odp.proc.sr.125.168.1992](https://doi.org/10.2973/odp.proc.sr.125.168.1992).
- Fryer, P. B., 1996. Evolution of the Mariana convergent plate margin system. *Rev. Geophys.* 34 (1), 89–125, doi:[10.1029/95rg03476](https://doi.org/10.1029/95rg03476).
- Fryer, P. B., 2012. Serpentinite mud volcanism: observations, processes, and implications. *Ann. Rev.*

- Mar. Sci. 4 (1), 345–373, doi:[10.1146/annurev-marine-120710-100922](https://doi.org/10.1146/annurev-marine-120710-100922).
- Fryer, P. B., Gharib, J., Ross, K., Savov, I., Mottl, M. J., 2006. Variability in serpentinite mudflow mechanisms and sources: ODP drilling results on Mariana forearc seamounts. *Geochem. Geophys. Geosyst.* 7 (8), Q08014, doi:[10.1029/2005gc001201](https://doi.org/10.1029/2005gc001201).
- Fryer, P. B., Salisbury, M. H., 2006. Leg 195 synthesis: Site 1200—serpentinite seamounts of the Izu-Bonin/Mariana convergent plate margin (ODP Leg 125 and 195 drilling results). In: Shinohara, M., Salisbury, M. H., Richter, C. (Eds.), *Sci. Res. Vol. 195 of Proc. ODP. Integrated Ocean Drilling Program, College Station (TX)*. doi:[10.2973/odp.proc.sr.195.112.2006](https://doi.org/10.2973/odp.proc.sr.195.112.2006).
- Fryer, P. B., Wheat, C. G., Mottl, M. J., 1999. Mariana blueschist mud volcanism: implications for conditions within the subduction zone. *Geology* 27 (2), 103–106, doi:[10.1130/0091-7613\(1999\)027<0103:mbmvif>2.3.co;2](https://doi.org/10.1130/0091-7613(1999)027<0103:mbmvif>2.3.co;2).
- Haggerty, J. A., 1991. Evidence from fluid seeps atop serpentine seamounts in the Mariana forearc: clues for emplacement of the seamounts and their relationship to forearc tectonics. *Mar. Geol.* 102, 293–309, doi:[10.1016/0025-3227\(91\)90013-t](https://doi.org/10.1016/0025-3227(91)90013-t).
- Hattori, K. H., Guillot, S., 2003. Volcanic fronts form as a consequence of serpentinite dehydration in the forearc mantle wedge. *Geology* 31 (6), 525–528, doi:[10.1130/0091-7613\(2003\)031<0525:vffaac>2.0.co;2](https://doi.org/10.1130/0091-7613(2003)031<0525:vffaac>2.0.co;2).
- Hattori, K. H., Guillot, S., 2007. Geochemical character of serpentinites associated with high- to ultrahigh-pressure metamorphic rocks in the Alps, Cuba, and the Himalayas: recycling of elements in subduction zones. *Geochem. Geophys. Geosyst.* 8 (9), Q09010, doi:[10.1029/2007gc001594](https://doi.org/10.1029/2007gc001594).
- Hawkesworth, C. J., Gallagher, K., Hergt, J. M., McDermott, F., 1993. Mantle and slab contributions in arc magmas. *Annu. Rev. Earth Planet. Sci.* 21, 175–204, doi:[10.1146/annurev.ea.21.050193.001135](https://doi.org/10.1146/annurev.ea.21.050193.001135).
- Helwig, D., Schwarz, A., 1992. Iowaite in serpentinite muds at Sites 778, 779, 780, and 784: a possible cause for the low chlorinity of pore waters. In: Fryer, P. B., Pearce, J. A., Stokking, L. B. (Eds.), *Sci. Res. Vol. 125 of Proc. ODP. Ocean Drilling Program, College Station (TX)*, pp. 313–323. doi:[10.2973/odp.proc.sr.125.176.1992](https://doi.org/10.2973/odp.proc.sr.125.176.1992).
- Hulme, S. M., Wheat, C. G., Fryer, P. B., Mottl, M. J., 2010. Pore water chemistry of the Mariana serpentinite mud volcanoes: a window to the seismogenic zone. *Geochem. Geophys. Geosyst.* 11 (1), Q01X09, doi:[10.1029/2009gc002674](https://doi.org/10.1029/2009gc002674).
- Hyndman, R. D., Peacock, S. M., 2003. Serpentinization of the forearc mantle. *Earth Planet. Sci. Lett.* 212 (3–4), 417–432, doi:[10.1016/s0012-821x\(03\)00263-2](https://doi.org/10.1016/s0012-821x(03)00263-2).
- James, R. H., Allen, D. E., Seyfried, W. E., 2003. An experimental study of alteration of oceanic crust and terrigenous sediments at moderate temperatures (51 to 350 °C): insights as to chemical processes in near-shore ridge-flank hydrothermal systems. *Geochim. Cosmochim. Acta* 67 (4), 681–691, doi:[10.1016/s0016-7037\(02\)01113-4](https://doi.org/10.1016/s0016-7037(02)01113-4).
- Jarrard, R. D., 2003. Subduction fluxes of water, carbon dioxide, chlorine, and potassium. *Geochem. Geophys. Geosyst.* 4 (5), 8905, doi:[10.1029/2002gc000392](https://doi.org/10.1029/2002gc000392).
- Jochum, K. P., Weis, U., Stoll, B., Kuzmin, D., Yang, Q., Raczek, I., Jacob, D. E., Stracke, A., Birbaum, K., Frick, D. A., Günther, D.,ENZWEILER, J., 2011. Determination of reference values for NIST SRM 610–617 glasses following ISO guidelines. *Geostand. Geoanal. Res.* 35 (4), 397–429, doi:[10.1111/j.1751-908x.2011.00120.x](https://doi.org/10.1111/j.1751-908x.2011.00120.x).
- John, T., Scambelluri, M., Frische, M., Barnes, J. D., Bach, W., 2011. Dehydration of subducting serpentinite: implications for halogen mobility in subduction zones and the deep halogen cycle. *Earth Planet. Sci. Lett.* 308 (1–2), 65–76, doi:[10.1016/j.epsl.2011.05.038](https://doi.org/10.1016/j.epsl.2011.05.038).
- Kahl, W.-A., Jöns, N., Bach, W., Klein, F., Alt, J. C., 2015. Ultramafic clasts from the South Chamorro serpentinite mud volcano reveal a polyphase serpentinization history of the Mariana forearc mantle. *Lithos* 227, 1–20, doi:[10.1016/j.lithos.2015.03.015](https://doi.org/10.1016/j.lithos.2015.03.015).
- Kastner, M., Elderfield, H., Martin, J. B., 1991. Fluids in convergent margins: what do we know about their composition, origin, role in diagenesis and importance for oceanic chemical fluxes? *Phil. Trans. R. Soc. A* 335 (1638), 243–259.
- Kastner, M., Solomon, E. A., Harris, R. N., Torres, M. E., 2014. Fluid origins, thermal regimes, and fluid and solute fluxes in the forearc of subduction zones. In: Stein, R., Blackman, D. K., Inagaki, F.,

- Larsen, H.-C. (Eds.), Earth and life processes discovered from seafloor environments: a decade of science achieved by the Integrated Ocean Drilling Program (IODP). Vol. 7 of Developments in marine geology. Elsevier, pp. 671–733. doi:[10.1016/b978-0-444-62617-2.00022-0](https://doi.org/10.1016/b978-0-444-62617-2.00022-0).
- Kelley, K. A., Plank, T., Ludden, J., Staudigel, H., 2003. Composition of altered oceanic crust at ODP Sites 801 and 1149. *Geochim. Geophys. Geosyst.* 4 (6), 8910, doi:[10.1029/2002gc000435](https://doi.org/10.1029/2002gc000435).
- Kerrick, D. M., Connolly, J. A. D., 2001. Metamorphic devolatilization of subducted marine sediments and the transport of volatiles into the Earth's mantle. *Nature* 411 (6835), 293–296, doi:[10.1038/35077056](https://doi.org/10.1038/35077056).
- Klein, F., Bach, W., Humphris, S. E., Kahl, W.-A., Jöns, N., Moskowitz, B., Berquó, T. S., 2014. Magnetite in seafloor serpentinite—some like it hot. *Geology* 42 (2), 135–138, doi:[10.1130/g35068.1](https://doi.org/10.1130/g35068.1).
- Klein, F., Bach, W., Jöns, N., McCollom, T., Moskowitz, B., Berquó, T. S., 2009. Iron partitioning and hydrogen generation during serpentinization of abyssal peridotites from 15°N on the Mid-Atlantic Ridge. *Geochim. Cosmochim. Acta* 73 (22), 6868–6893, doi:[10.1016/j.gca.2009.08.021](https://doi.org/10.1016/j.gca.2009.08.021).
- Lockwood, J. P., 1972. Possible mechanisms for the emplacement of alpine-type serpentinite. *Geol. Soc. Am. Mem.* 132, 273–288, doi:[10.1130/mem132-p273](https://doi.org/10.1130/mem132-p273).
- Maekawa, H., Fryer, P. B., Ozaki, A., 1995. Incipient blueschist-facies metamorphism in the active subduction zone beneath the Mariana forearc. In: Taylor, B., Natland, J. (Eds.), *Active margins and marginal basins of the western Pacific*. Vol. 88. pp. 281–289. doi:[10.1029/gm088p0281](https://doi.org/10.1029/gm088p0281).
- Maekawa, H., Masaya, S., Ishill, T., Fryer, P., Pearce, J. A., 1993. Blueschist metamorphism in an active subduction zone. *Nature* 364, 520–523, doi:[10.1038/364520a0](https://doi.org/10.1038/364520a0).
- Manning, C. E., 2004. The chemistry of subduction-zone fluids. *Earth Planet. Sci. Lett.* 223 (1–2), 1–16, doi:[10.1016/j.epsl.2004.04.030](https://doi.org/10.1016/j.epsl.2004.04.030).
- Marschall, H. R., Schumacher, J. C., 2012. Arc magmas sourced from mélange diapirs in subduction zones. *Nature Geoscience* 5 (12), 862–867, doi:[10.1038/ngeo1634](https://doi.org/10.1038/ngeo1634).
- McCollom, T. M., Bach, W., 2009. Thermodynamic constraints on hydrogen generation during serpentinization of ultramafic rocks. *Geochim. Cosmochim. Acta* 73 (3), 856–875, doi:[10.1016/j.gca.2008.10.032](https://doi.org/10.1016/j.gca.2008.10.032).
- Moore, J. C., Saffer, D., 2001. Updip limit of the seismogenic zone beneath the accretionary prism of southwest Japan: an effect of diagenetic to low-grade metamorphic processes and increasing effective stress. *Geology* 29 (2), 183–186, doi:[10.1130/0091-7613\(2001\)029<0183:ulotsz>2.0.co;2](https://doi.org/10.1130/0091-7613(2001)029<0183:ulotsz>2.0.co;2).
- Moriguti, T., Nakamura, E., 1998. Across-arc variation of Li isotopes in lavas and implications for crust/mantle recycling at subduction zones. *Earth Planet. Sci. Lett.* 163 (1–4), 167–174, doi:[10.1016/s0012-821x\(98\)00184-8](https://doi.org/10.1016/s0012-821x(98)00184-8).
- Mottl, M. J., Alt, J. C., 1992. Data report: minor and trace element and sulfur isotopic composition of pore waters from sites 778 through 786. In: Fryer, P. B., Pearce, J. A., Stokking, L. B. (Eds.), *Sci. Res. Vol. 125 of Proc. ODP. Ocean Drilling Program, College Station (TX)*, pp. 683–688. doi:[10.2973/odp.proc.sr.125.184.1992](https://doi.org/10.2973/odp.proc.sr.125.184.1992).
- Mottl, M. J., Holland, H. D., 1978. Chemical exchange during hydrothermal alteration of basalt by seawater—I. Experimental results for major and minor components of seawater. *Geochim. Cosmochim. Acta* 42 (8), 1103–1115, doi:[10.1016/0016-7037\(78\)90107-2](https://doi.org/10.1016/0016-7037(78)90107-2).
- Mottl, M. J., Wheat, C. G., Fryer, P. B., Gharib, J., Martin, J. B., 2004. Chemistry of springs across the Mariana forearc shows progressive devolatilization of the subducting plate. *Geochim. Cosmochim. Acta* 68 (23), 4915–4933, doi:[10.1016/j.gca.2004.05.037](https://doi.org/10.1016/j.gca.2004.05.037).
- Nielsen, S. G., Klein, F., Kading, T., Blusztajn, J., Wickham, K., 2015. Thallium as a tracer of fluid–rock interaction in the shallow Mariana forearc. *Earth Planet. Sci. Lett.* 430, 416–426, doi:[10.1016/j.epsl.2015.09.001](https://doi.org/10.1016/j.epsl.2015.09.001).
- Oakley, A. J., Taylor, B., Fryer, P. B., Moore, G. F., Goodliffe, A. M., Morgan, J. K., 2007. Emplacement, growth, and gravitational deformation of serpentinite seamounts on the Mariana forearc. *Geophys. J. Int.* 170 (2), 615–634, doi:[10.1111/j.1365-246x.2007.03451.x](https://doi.org/10.1111/j.1365-246x.2007.03451.x).
- Oakley, A. J., Taylor, B., Moore, G. F., 2008. Pacific plate subduction beneath the central Mariana and Izu-Bonin fore arcs: new insights from an old margin. *Geochim. Geophys. Geosyst.* 9 (6), Q06003, doi:[10.1029/2007gc001820](https://doi.org/10.1029/2007gc001820).
- Pabst, S., Zack, T., Savov, I. P., Ludwig, T., Rost, D., Tonarini, S., Vicenzi, E. P., 2012. The fate of subducted oceanic slabs in the shallow mantle: insights from boron isotopes and light element

- composition of metasomatized blueschists from the Mariana forearc. *Lithos* 132–133, 162–179, doi:[10.1016/j.lithos.2011.11.010](https://doi.org/10.1016/j.lithos.2011.11.010).
- Pabst, S., Zack, T., Savov, I. P., Ludwig, T., Rost, D., Vicenzi, E. P., 2011. Evidence for boron incorporation into the serpentine crystal structure. *Am. Mineral.* 96 (7), 1112–1119, doi:[10.2138/am.2011.3709](https://doi.org/10.2138/am.2011.3709).
- Pagé, L., Hattori, K., 2017. Tracing halogen and B cycling in subduction zones based on obducted, subducted and forearc serpentinites of the Dominican Republic. *Sci. Rep.* 7 (1), 17776, doi:[10.1038/s41598-017-18139-7](https://doi.org/10.1038/s41598-017-18139-7).
- Peacock, S. A., 1990. Fluid processes in subduction zones. *Science* 248 (4953), 329–337, doi:[10.1126/science.248.4953.329](https://doi.org/10.1126/science.248.4953.329).
- Peacock, S. M., 1996. Thermal and petrologic structure of subduction zones. *Geoph. Monog. Series* 96, 119–133, doi:[10.1029/gm096p0119](https://doi.org/10.1029/gm096p0119).
- Peters, D., Bretscher, A., John, T., Scambelluri, M., Pettke, T., 2017. Fluid-mobile elements in serpentinites: constraints on serpentinisation environments and element cycling in subduction zones. *Chem. Geol.* 466, 654–666, doi:[10.1016/j.chemgeo.2017.07.017](https://doi.org/10.1016/j.chemgeo.2017.07.017).
- Plank, T., 2014. The chemical composition of subducting sediments. In: *Treatise on geochemistry*. Elsevier, pp. 607–629. doi:[10.1016/b978-0-08-095975-7.00319-3](https://doi.org/10.1016/b978-0-08-095975-7.00319-3).
- Plank, T., Langmuir, C. H., 1998. The chemical composition of subducting sediment and its consequences for the crust and mantle. *Chem. Geol.* 145 (3), 325–394, doi:[10.1016/s0009-2541\(97\)00150-2](https://doi.org/10.1016/s0009-2541(97)00150-2).
- Poli, S., Schmidt, M. W., 1995. H₂O transport and release in subduction zones: experimental constraints on basaltic and andesitic systems. *J. Geophys. Res. Solid Earth* 100 (B11), 22299–22314, doi:[10.1029/95jb01570](https://doi.org/10.1029/95jb01570).
- Pons, M.-L., Quitté, G., Fujii, T., Rosing, M. T., Reynard, B., Moynier, C. D., Albarède, F., 2011. Early Archean serpentine mud volcanoes at Isua, Greenland, as a niche for early life. *Proc. Natl. Acad. Sci.* 108 (43), 17639–17643, doi:[10.1073/pnas.1108061108](https://doi.org/10.1073/pnas.1108061108).
- Sadofsky, S. J., Bebout, G. E., 2003. Record of forearc devolatilization in low-T, high-P/T metasedimentary suites: significance for models of convergent margin chemical cycling. *Geochem. Geophys. Geosyst.* 4 (4), 9003, doi:[10.1029/2002gc000412](https://doi.org/10.1029/2002gc000412).
- Salters, V. J. M., Stracke, A., 2004. Composition of the depleted mantle. *Geochem. Geophys. Geosyst.* 5 (5), Q05004, doi:[10.1029/2003gc000597](https://doi.org/10.1029/2003gc000597).
- Savov, I. P., Ryan, J. G., Antonio, M. D., Fryer, P., 2007. Shallow slab fluid release across and along the Mariana arc-basin system: insights from geochemistry of serpentinized peridotites from the Mariana fore arc. *J. Geophys. Res.* 112 (B9), B09205, doi:[10.1029/2006jb004749](https://doi.org/10.1029/2006jb004749).
- Savov, I. P., Ryan, J. G., Antonio, M. D., Kelley, K., Mattie, P., 2005. Geochemistry of serpentinized peridotites from the Mariana forearc conical seamount, odp leg 125: implications for the elemental recycling at subduction zones. *Geochem. Geophys. Geosyst.* 6 (4), Q04J15, doi:[10.1029/2004gc000777](https://doi.org/10.1029/2004gc000777).
- Scambelluri, M., Fiebig, J., Malaspina, N., Müntener, O., Pettke, T., 2004. Serpentinite subduction: implications for fluid processes and trace-element recycling. *Int. Geol. Rev.* 46 (7), 595–613, doi:[10.2747/0020-6814.46.7.595](https://doi.org/10.2747/0020-6814.46.7.595).
- Scambelluri, M., Müntener, O., Hermann, J., Piccardo, G. B., Trommsdorff, V., 1995. Subduction of water into the mantle: history of an Alpine peridotite. *Geology* 23 (5), 459–462, doi:[10.1130/0091-7613\(1995\)023<0459:sowitm>2.3.co;2](https://doi.org/10.1130/0091-7613(1995)023<0459:sowitm>2.3.co;2).
- Schmidt, M. W., Poli, S., 1998. Experimentally based water budgets for dehydrating slabs and consequences for arc magma generation. *Earth Planet. Sci. Lett.* 163 (1–4), 361–379, doi:[10.1016/s0012-821x\(98\)00142-3](https://doi.org/10.1016/s0012-821x(98)00142-3).
- Stern, C. R., 2011. Subduction erosion: rates, mechanisms, and its role in arc magmatism and the evolution of the continental crust and mantle. *Gondwana Res.* 20 (2–3), 284–308, doi:[10.1016/j.gr.2011.03.006](https://doi.org/10.1016/j.gr.2011.03.006).
- Straub, S. M., Layne, G. D., 2003. Decoupling of fluids and fluid-mobile elements during shallow subduction: evidence from halogen-rich andesite melt inclusions from the Izu arc volcanic front. *Geochem. Geophys. Geosyst.* 4 (7), 9003, doi:[10.1029/2002gc000349](https://doi.org/10.1029/2002gc000349).
- Tatsumi, Y., 1989. Migration of fluid phases and genesis of basalt magmas in subduction zones. *J. Geophys. Res. Solid Earth* 94 (B4), 4697–4707, doi:[10.1029/jb094ib04p04697](https://doi.org/10.1029/jb094ib04p04697).

- Tenthorey, E., Hermann, J., 2004. Composition of fluids during serpentinite breakdown in subduction zones: evidence for limited boron mobility. *Geology* 32 (10), 865–868, doi:[10.1130/g20610.1](https://doi.org/10.1130/g20610.1).
- Tibi, R., Wiens, D. A., Yuan, X., 2008. Seismic evidence for widespread serpentinitized forearc mantle along the Mariana convergence margin. *Geophys. Res. Lett.* 35 (13), L13303, doi:[10.1029/2008g1034163](https://doi.org/10.1029/2008g1034163).
- Ulmer, P., Trommsdorff, V., 1995. Serpentine stability to mantle depths and subduction-related magmatism. *Science* 268 (5212), 858–861, doi:[10.1126/science.268.5212.858](https://doi.org/10.1126/science.268.5212.858).
- Uyeda, S., Kanamori, H., 1979. Back-arc opening and the mode of subduction. *J. Geophys. Res.* 84 (B3), 1049, doi:[10.1029/jb084ib03p01049](https://doi.org/10.1029/jb084ib03p01049).
- Wheat, C. G., Fournier, T., Paul, C., Menzies, C. D., Price, R. E., Ryan, J. G., Sissman, O. J., 2018. Data report: IODP Expedition 366 pore water trace element (V, Mo, Rb, Cs, U, Ba, and Li) compositions. Vol. 366 of *Proc. IODP. International Ocean Discovery Program, College Station (TX)*, pp. 1–8. doi:[10.14379/iodp.proc.366.201.2018](https://doi.org/10.14379/iodp.proc.366.201.2018).
- Xia, S., Zhao, D., Qiu, X., 2008. Tomographic evidence for the subducting oceanic crust and forearc mantle serpentinitization under Kyushu, Japan. *Tectonophysics* 449 (1–4), 85–96, doi:[10.1016/j.tecto.2007.12.007](https://doi.org/10.1016/j.tecto.2007.12.007).
- You, C. F., Castillo, P. R., Gieskes, J. M., Chan, L. H., Spivack, A. J., 1996. Trace element behavior in hydrothermal experiments: implications for fluid processes at shallow depths in subduction zones. *Earth Planet. Sci. Lett.* 140 (1–4), 41–52, doi:[10.1016/0012-821x\(96\)00049-0](https://doi.org/10.1016/0012-821x(96)00049-0).

5 Conclusions and outlook

Within this thesis, my co-authors and I investigated mass transfers induced by interactions between fluid and rock at divergent and convergent plate boundary settings. The main aims were to examine (i) the association of hydrothermal alteration of hybrid ultramafic–mafic lithologies with detachment faulting, (ii) the formation of carbonate-rich veins in metavolcanic clasts from the forearc of an active subduction zone, and (iii) the mobilization of fluid-mobile elements at shallow subduction levels and their incorporation into forearc serpentinites. The data obtained within this thesis bring hitherto novel insights into fluid–rock interactions that affect the oceanic lithosphere during its life cycle. The main findings are presented in three standalone manuscripts. A summary of the findings is given below—together with new questions and aspects that arose in the course of this project. These can provide a basis for future research.

The first manuscript addressed the abundance of mechanically weak minerals in shear zone rocks of oceanic detachment faults and their potential importance for tectonic seafloor spreading. Based on reaction path modeling, we were able to show that assemblages rich in chlorite and amphibole form where hybrid ultramafic–mafic lithologies are altered by seawater at temperatures of 500 to 600 °C. Such hybrid lithologies are frequent at detachment faults worldwide, often formed during the impregnation of ultramafic complexes with basaltic melts. By contrast, purely peridotitic or gabbroic rocks do not substantially weaken within this temperature window. The investigation of fault rock samples from the 15°20' N Fracture Zone area, Mid-Atlantic Ridge, lend credit to our modeling approach. Microtextural observations revealed that strain primarily localizes in the hydrothermally altered hybrid areas, leading to their deformation. Based on these results we proposed a positive feedback loop between melt impregnation of ultramafic bodies, their weakening during hydration, strain localization, and faulting—the latter of which in turn leads to further hydration and weakening of the rock. This process of metamorphic weakening of hybrid lithologies may play a key role in the evolution of detachment faults at slow-spreading ridges worldwide.

The proposed feedback well accounts for the evolution and longevity of detachment faults within an intermediate temperature window, i. e., below magmatic temperatures but above temperatures where serpentinization occurs. The lower-temperature evolution of detachment faults may be explained by substantial weakening of ultramafic lithologies during serpentinization; this likely lubricates fault planes and promotes slip even in low-angle faults. However, it is not yet clear how detachment faults initiate at magmatic temperatures. Is there a relation to the melt impregnation? Could, for instance, the presence of melts provoke initial strain localization? Such initial localization of strain could lead to deformation and faulting at high temperatures that enables fluid flow and causes an incipient hydration of the hybrid lithologies. Such hydration is required for our suggested feedback to kick in.

Our study highlights the presence of variably evolved melts present as impregnations within ultramafic host rocks at detachment faults worldwide. It is not yet clear if and how the nature of the melt impregnations affects the strength of the lithologies. For instance, how much Si does the melt need to contain so that weak chlorite and amphibole form? Under which circumstances does talc, which is particularly prone to deformation, form and what are the consequences for the detachment? Could metasomatism by Si-rich melts lead to talc formation or, more generally, could fluid-induced metasomatism induce similar weakening effects as the presence of melt impregnations?

Rock samples from many detachment faults already exist to tackle these questions. In particular, the well-studied Atlantis Massif, located at the inside corner of the intersection of the Atlantis Fracture Zone and the Mid-Atlantic Ridge, may be a promising study site: profiles have been drilled across the oceanic core complex during the recent IODP Expedition 357, which provide three-dimensional insight into detachment faulting processes that led to the formation of the core complex.

The fate of subducted carbon in the shallow portions of a subduction zone was examined in the second manuscript. Based on petrographic and geochemical data, we showed evidence for the presence of carbonic fluids within the subduction channel at depths <20 km. These fluids were released during dehydration reactions affecting sediments and crust of the subducting slab. Precipitation of carbonates occurred in veins of metavolcanic and metasedimentary clasts under oxidizing conditions in the subduction channel; the clasts were subsequently erupted at the seafloor via serpentinite mud volcanism. Our results imply that the decarbonation of the incoming plate starts at shallow depth in the Mariana subduction system. A portion of this carbon is stored as carbonate precipitates at depth, suggesting that the forearcs of subduction zones worldwide may potentially act as a sink for carbon. However, some of the carbon is directly transported back into the short-term carbon cycle via upwelling fluids.

Our data demonstrate that considering deep portions of subduction zones only depicts a fraction of processes that affect the deep carbon cycle at convergent margins. This reflects recent studies attempting to budget fluxes of carbon in subduction zones: its mobilization at shallow depth is in many cases neglected or provided with large uncertainties. This is not least because modeling approaches predicted minor decarbonation at forearc depth.

To further improve the understanding of the long-term carbon cycle at forearc depth, I plan to conduct geochemical reaction path modeling in the near future. This approach will include the equilibration of materials of the incoming slab with a hypothetical subduction channel fluid, and the subsequent reaction of the resultant fluid with the forearc mantle wedge and subducted oceanic basement. Breaking down the materials of the incoming slab into chert- and carbonate-rich sediment and altered oceanic crust will allow to determine how much the individual lithologies contribute to the overall decarbonation. These models will be compiled for the Mariana forearc region; however, further computations, for instance for a ‘hot’ subduction zone, could extend our comprehension of decarbonation at shallow depth to a global level.

Furthermore, metamorphic mineral assemblages within the metavolcanic clasts hosting the carbonate veins bear the potential to better constrain the pressure and temperature

conditions within the subduction channel of the Mariana subduction zone. I am currently working on the computation of pseudo-sections for the metavolcanic clasts, which will be included into a petrographic and mineral chemical study by Yuji Ichiyama, a Japanese participant of IODP Expedition 366.

Within the third manuscript, my co-authors and I investigated the mobilization of fluid-mobile elements at shallow subduction levels. We showed evidence that dehydration reactions within the downgoing sediments and crust liberate Li, B, Rb, Sr, Cs, and Ba, and that these are incorporated into mantle wedge serpentinites. The abundances of these elements vary relative to each other with increasing slab depth. Our data highlight that the serpentinization fluids evolved from shallow to greater depth, from having been sourced by sediment pore waters and the dehydration of opal-rich sediments over primarily originating from the dehydration of clays towards an increasing contribution of fluids released from altered oceanic crust. Further, across-forearc fluid-mobile element trends can considerably deviate from those in fluids that upwell in the serpentinite mud volcanoes. Within this manuscript we provided a first continuous dataset that gives insight into the cycling of fluid-mobile elements at subduction depths of ~13 to 18 km; in contrast to similar studies that were carried out on obducted forearc materials, our samples have not been altered by obduction-related or on-land processes.

The breakdown of forearc serpentinites at subarc depths is proposed to contribute to a large degree to the fluid release that eventually causes hydrous mantle melting; elements released within the same process migrate into the mantle wedge with the fluids. This mass transfers likely cause the long-term sequestration of fluid-mobile elements far from the exosphere. It is, however, not yet clear to which extent fluid-mobile elements subsequently contribute to the 'slab signature' of arc magmas, i. e., what portion of the elements may be erupted during arc volcanism. Detailed investigation of fluid-mobile elements in arc eruptives, in particular by considering isotopic fractionation processes, may provide clues on this deep element cycling.

Additional insights into forearc processes at the Mariana subduction zone will come from observatories that will be deployed in cased boreholes within the serpentinite mud volcanoes in the near future. Geoffrey Wheat, co-chief of IODP Expedition 366, is currently preparing a proposal to raise funds for 'CORK-Lite' instrumentations, which will enable downhole monitoring, experimental capabilities, and a collection of slab-derived fluids. Scientists from the University of Bremen, including Achim Kopf and Wolfgang Bach, will participate in this project.

To further examine the role of serpentinite mud volcanism in the geologic past, Wolfgang Bach and I have submitted a research proposal, which is currently being reviewed. We plan to study on-land deposits of 'sedimentary serpentinite' that have previously been suggested to represent ancient, now obducted serpentinite mud volcanoes. Their investigation will give insight into processes in paleo-subduction zones and may or may not lend credit to the proposed origin of life on Earth within serpentinite mud volcanism.

Acknowledgements

I would first of all like to express my gratitude to Wolfgang Bach for the opportunity to work in the exciting field of fluid–rock interactions and for providing a great deal of help and support over the last years. Besides giving me the freedom to pursue my own ideas, Wolfgang offered a variety of opportunities that helped to push forward my research (even though in return I had to throw quite a number of discs).

I am very thankful to Timm John for agreeing to review this dissertation.

Further thanks go to my collaborators, namely Timothy Schroeder, Frieder Klein, Catriona D. Menzies, Friedrich Lucassen, Wolf-Achim Kahl, and Lena Beyer, for their scientific expertise as well as for stimulating discussions and constructive feedback. A special thank you also goes to the Scientific Party of IODP Expedition 366, in particular to the co-chiefs Patricia Fryer and C. Geoffrey Wheat.

Stefan Sopke, Andreas Klügel, and especially Patrick Monien are thanked for technical assistance. I would also like to acknowledge support by Walter Hale, Bastian Bieseler, Bernhard Schnetger, and Harald Strauß for help during sampling, preparation of samples, and analyses. Frank Lisker and Wolf-Achim Kahl are thanked for being part of my Thesis Committee.

This research was funded by the Deutsche Forschungsgemeinschaft and financially supported by GLOMAR, Bremen International Graduate School for Marine Sciences, and BremenIDEA out, a combined program from the University of Bremen and the DAAD (German Academic Exchange Service).

Special thanks go to my colleagues from the working group ‘Petrology of the Ocean Crust,’ namely Alex, Andreas K., Andreas T., Christian, Flo, Janis, Frau Ait-Majdari, Karin, Leslie, Lucy, Nikki, Patrick, Petra, Tony, Stefan, and Wolfgang, for enjoyable three years both within and outside the department.

Finally, I would especially like to thank my friends, my mom, dad, and sisters, and Sofie. I could always rely on your support and encouragement!

Appendix

A.1 Supplementary Information to Chapter 2, 'High-temperature hybrid rock hydration'

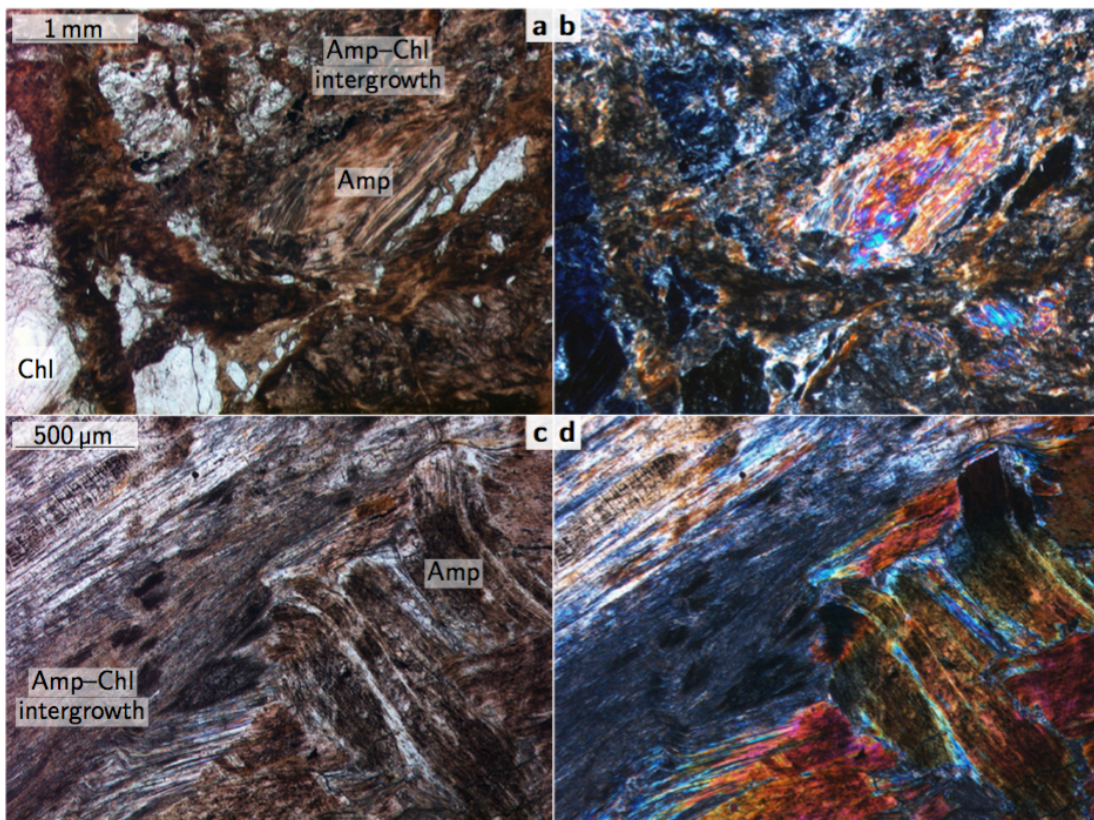


Figure A.1.1 Photomicrographs depicting amphibole deformation. (a, b) Phacoidal amphibole in a groundmass of amphibole-chlorite intergrowth. Sample 1271B-10R-1, 59–65 cm, PPL and XPL, respectively. (c, d) Lath-shaped amphibole, deformed towards a shear zone with finely intergrown amphibole and chlorite. Sample 1271B-17R-1, 17–19 cm, PPL and XPL, respectively. Abbreviations: Amp, amphibole; Chl, chlorite; PPL, plane polarized light; XPL, crossed polarized light.

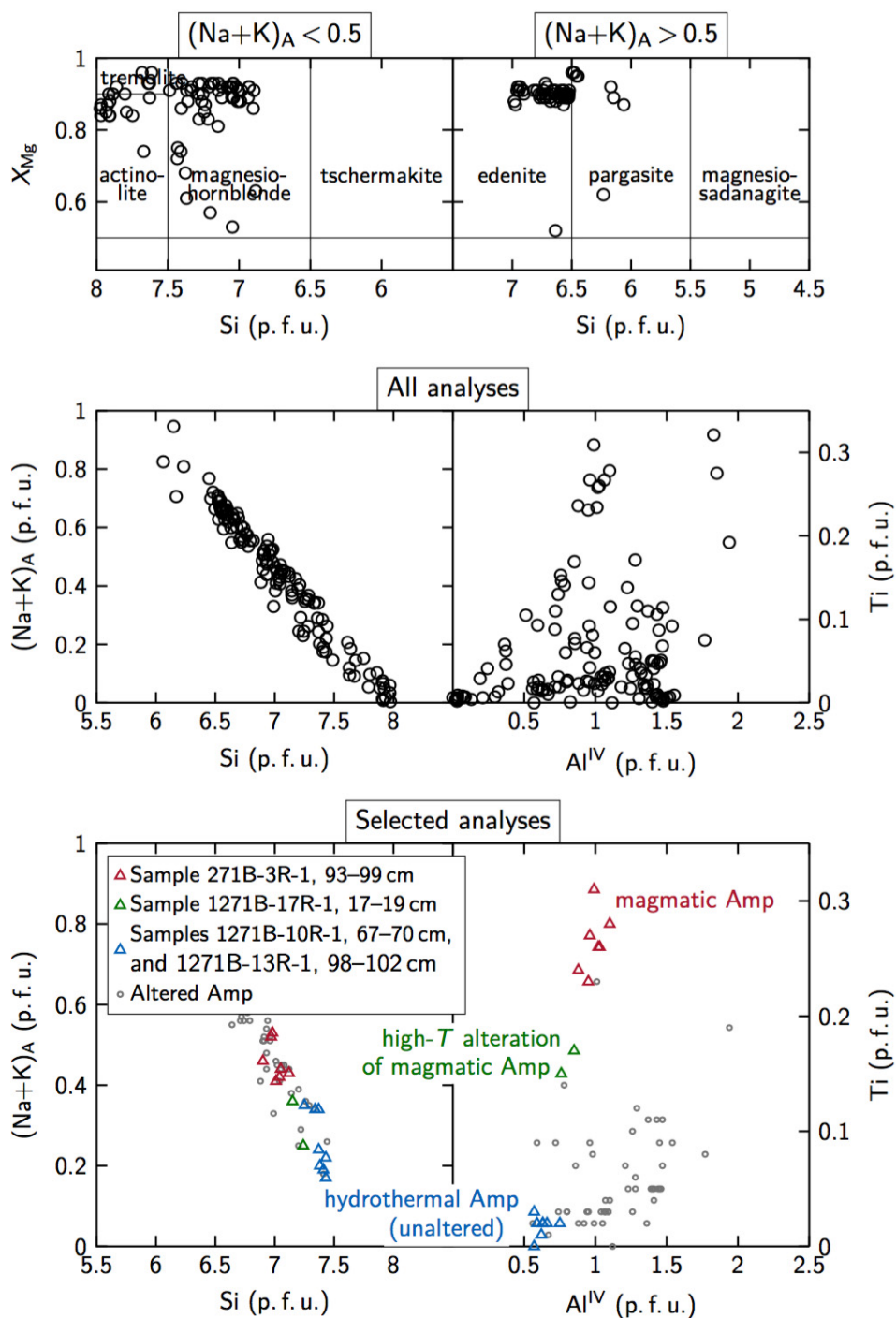


Figure A.1.2 Amphibole classification diagrams and chemical compositions. Representative analyses depict (i) low Si but high Ti, Al^{IV} , and alkalis of magmatic amphibole, (ii) hydrothermal amphibole with high Si and low Ti, Al^{IV} , and alkalis, and (iii) secondary amphibole after magmatic amphibole with intermediate compositions. Other analyses of secondary amphibole after one of the amphibole types or after pyroxene are variable in composition. Diagrams and stoichiometric recalculations after Leake et al. (1997). Abbreviations: Amp, amphibole.

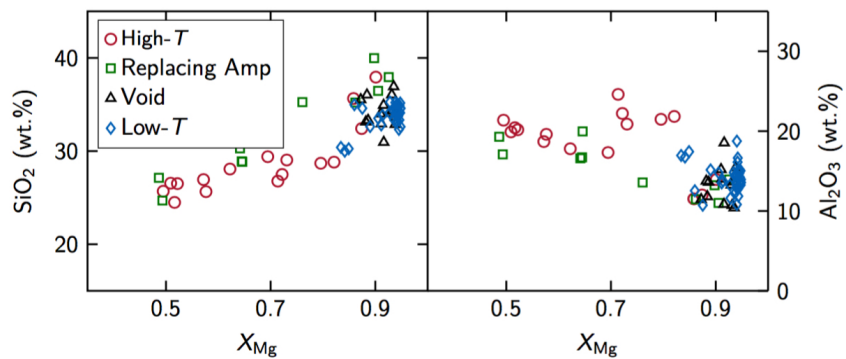


Figure A.1.3 Chlorite compositions. Stoichiometries recalculated on the basis of 14 O. Abbreviations: Amp, amphibole.

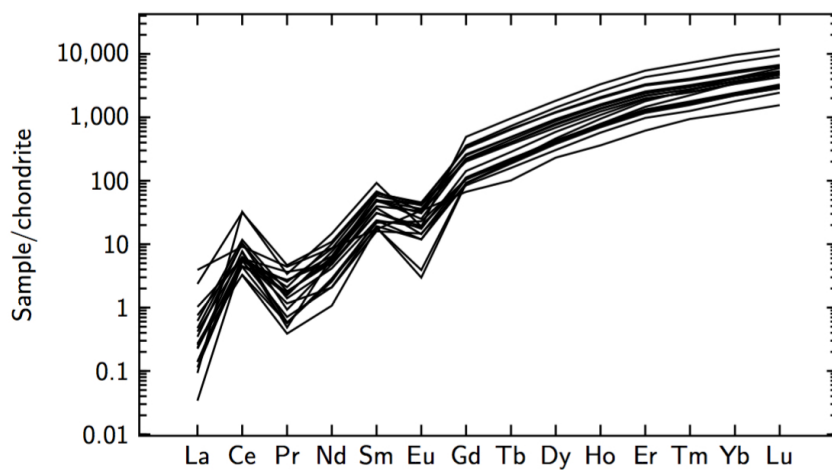


Figure A.1.4 Chondrite-normalized rare earth element concentrations of zircon. Chondrite composition after McDonough and Sun (1995).

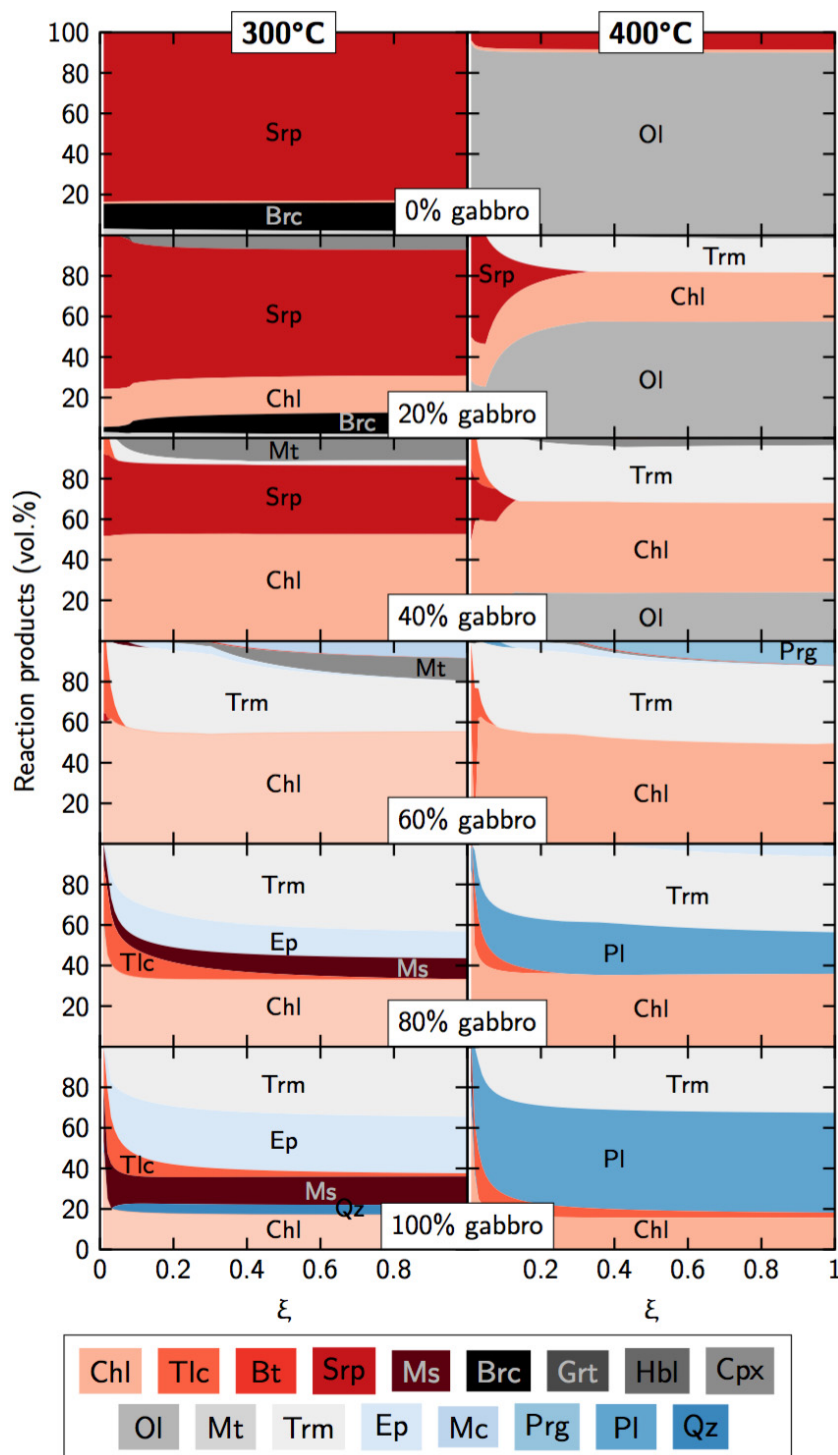


Figure A.1.5 EQ3/6 modeling results for 300°C and 400°C, respectively, for different peridotite–gabbro mixing ratios. The x-axis depicts water/rock ratios, changing from fluid-dominated (towards left) to rock-dominated (towards right). All olivine from peridotite-dominated protoliths reacts to serpentine at 300°C whereas large amounts are stable at 400°C. Chlorite and chlorite–amphibole assemblages dominate hybrid precursor rocks at both temperatures. Alteration assemblages of gabbro-dominated rocks further include epidote, talc, muscovite, and quartz (300°C) and talc and plagioclase (400°C). Abbreviations: Brc, brucite; Bt, biotite; Chl, chlorite; Cpx, clinopyroxene; Ep, epidote; Grt, garnet; Hbl, hornblende; Mc, microcline; Ms, muscovite; Mt, magnetite; Ol, olivine; Pl, plagioclase; Prg, pargasite; Qz, quartz; Srp, serpentine; Tlc, talc; Trm, tremolite.

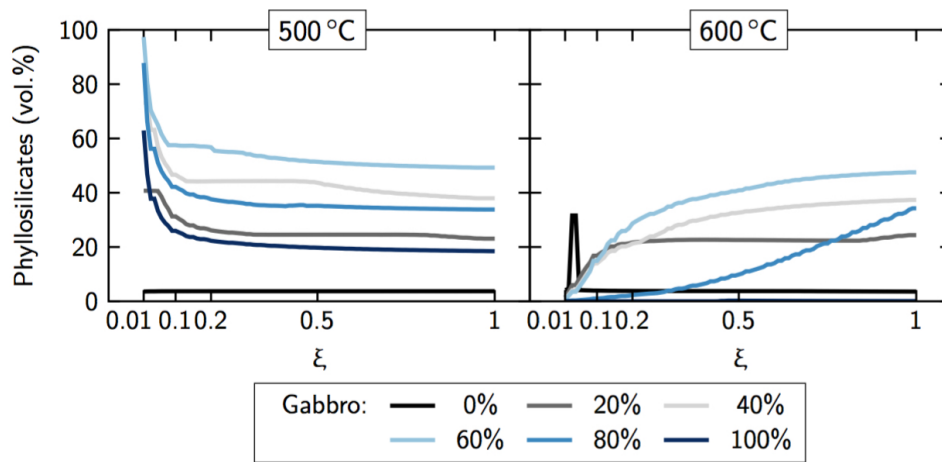


Figure A.1.6 EQ3/6 modeling results depicting relative amounts of phyllosilicates predicted to form at different water/rock ratios as a function of temperature and protolith composition.

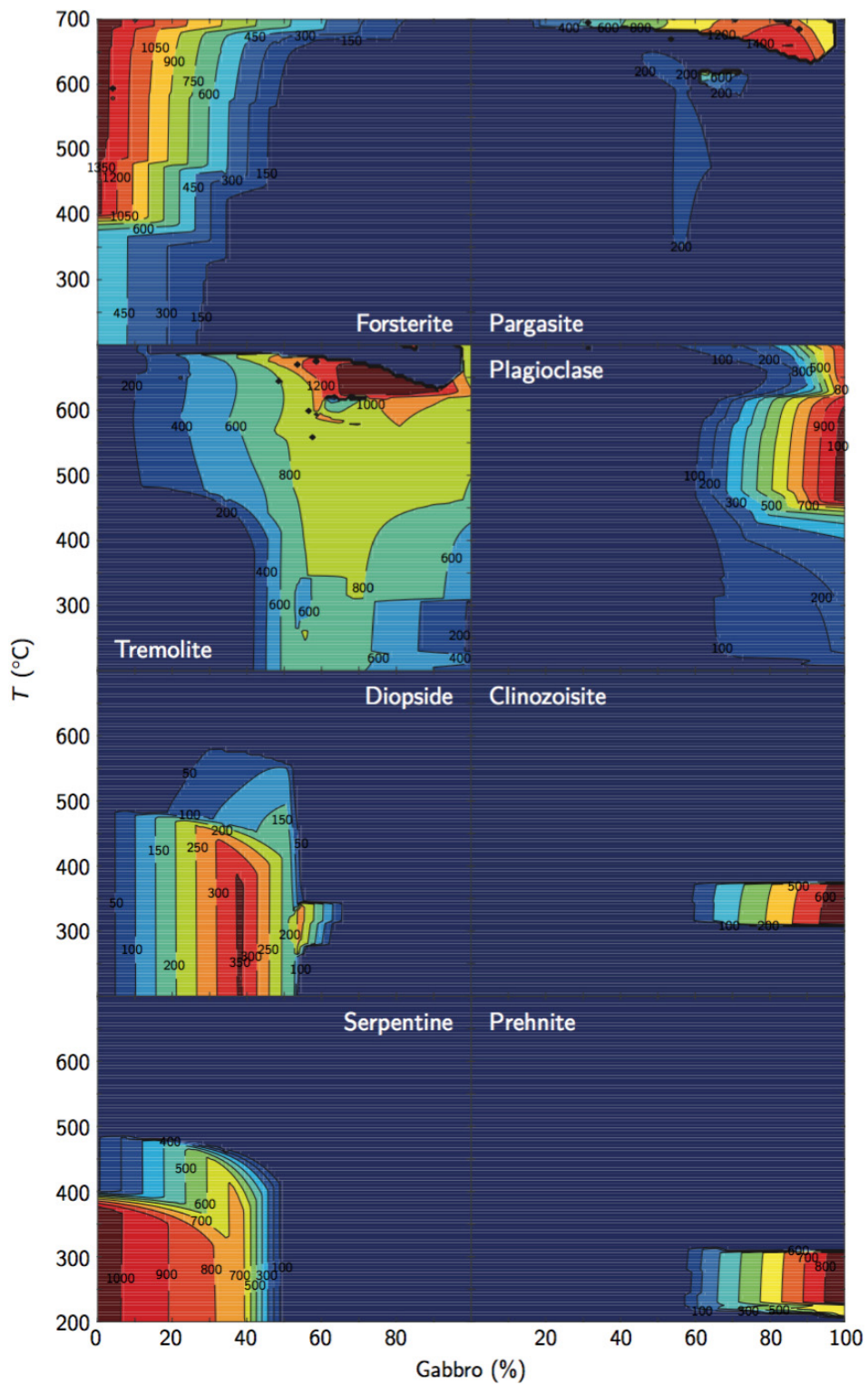


Figure A.1.7 Theriak/Domino modeling results depicting olivine- and serpentine-rich and plagioclase-, epidote-, and prehnite-rich secondary assemblages for peridotitic and gabbroic precursor lithologies, respectively. All values in cm^3 .

Table A.1.1 Estimated degrees of melt impregnation (X_{Gabbro}) for the individual samples. Also given are the squared residuals (r_i^2) between actual whole-rock compositions and the estimated compositions as based on X_{Gabbro} and the compositions from Paulick et al. (2006).

Sample	1271B-1R- 1, 8–13 cm	1271B-3R- 1, 17–20 cm	1271B- 13R-1, 27–31 cm	1271B- 13R-1, 52–59 cm	1271B- 14R-1, 45–48 cm	1271B- 18R-1, 81–84 cm	1271B- 18R-1, 93–96 cm	1271B- 20R-1, 0–2 cm
Estimated degrees of impregnation, normalized								
X_{Gabbro}	52.2	46.5	27.0	28.4	58.9	26.9	33.2	56.4
σ	6.8	7.1	3.1	5.7	4.7	3.4	0.7	8.1
Squared residuals (r_i^2) between actual and predicted values								
SiO ₂	13.3	26.2	4.4	11.4	3.1	4.1	0.9	20.5
TiO ₂	0.0	0.0	0.0	0.0	1.0	0.0	0.1	0.0
Al ₂ O ₃	23.9	26.0	3.8	9.8	13.2	7.0	0.0	41.6
Fe ₂ O ₃	5.8	9.2	4.2	3.4	0.6	0.1	0.0	0.9
MnO	0.0	0.0	0.0	0.0	0.0	0.0	0.0	0.0
MgO	0.0	0.5	0.0	3.7	0.6	0.5	0.7	0.2
CaO	10.1	6.4	0.0	10.6	3.7	0.3	0.2	13.4
Na ₂ O	0.2	0.2	0.0	0.0	0.1	0.1	0.1	0.0
K ₂ O	0.0	0.0	0.0	0.0	0.0	0.0	0.0	0.0
Sum r_i^2	53.3	68.5	12.5	39.0	22.3	12.0	2.1	76.6

A.2 Supplementary Information to Chapter 3, ‘Clues on carbon cycling’

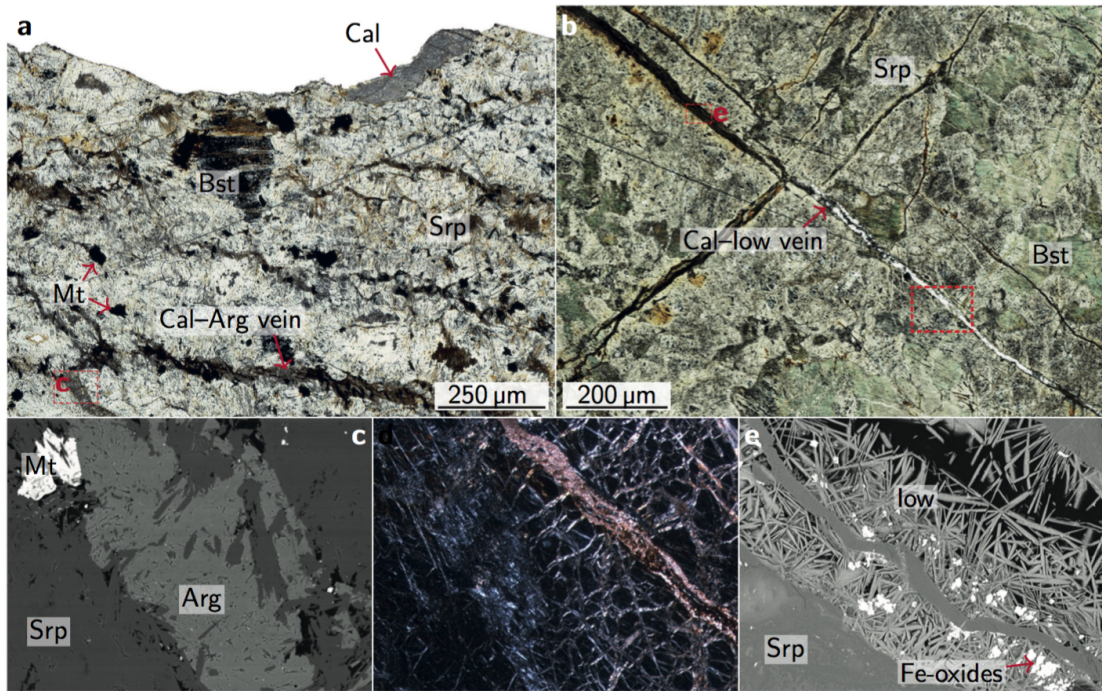


Figure A.2.1 Carbonate phases in serpentinite clasts. Thin section scans of (a) a serpentinitized dunite from Asùt Tesoru with calcite and aragonite veins (sample U1495B-5G-CC, 1–3 cm) and (b) a serpentinitized harzburgite from Yinazao crosscut by a narrow calcite–iowaite vein (sample U1492C-1H-2, 18–20 cm). Red rectangles mark positions of close-ups shown in lower panels. (c) SEM image of blocky aragonite. (d, e) Photomicrograph of calcite and SEM image of acicular iowaite occurring within the same vein. Abbreviations: Arg, aragonite; Bst, bastite; Cal, calcite; low, iowaite; Mt, magnetite.

Table A.2.1 Representative geochemistry of metamorphic phases.

Sample	U1498B- 8R-1, 32- 34 cm	U1495B- 5G-CC, 1-3 cm	U1497A- 12F-1, 93- 95 cm	U1498B- 8R-1, 32- 34 cm	U1496B- 8X-CC, 33- 41 cm	U1496B- 10F-2, 10- 12 cm	U1496B- 8X-CC, 33- 41 cm	U1496B- 8X-CC, 33- 41 cm	U1498B- 8R-1, 32- 34 cm	U1496A- 10G- CC, 23- 26 cm	U1497A- 12F-1, 93- 95 cm	U1496B- 8X-CC, 33- 41 cm	U1498B- 8R-1, 10- 15 cm	U1496A- 10G- CC, 23- 26 cm	U1498B- 8R-1, 0-4 cm	U1498B- 8R-1, 32- 34 cm
Phase	Chl	Chl	Cpx	Cpx	Gln	Gln	Lws	Lws	Pct	Pct	Ph	Ph	Pmp	Pmp	Prh	Prh
wt. %																
SiO ₂	30.7	32.9	46.5	45.8	53.3	52.5	38.1	38.3	53.1	53.4	52.3	54.4	34.1	35.9	42.3	42.6
TiO ₂	0.01	0.04	2.66	1.98	0.08	0.43	0.14	0.20	0.05	b. d. l.	0.53	0.06	0.44	0.15	0.01	0.21
Al ₂ O ₃	14.9	15.1	6.73	4.91	4.86	4.89	32.1	32.0	b. d. l.	0.06	17.0	20.6	21.5	22.5	24.4	24.5
Cr ₂ O ₃	0.25	0.62	0.05	0.10	0.02	0.01	0.03	0.03	b. d. l.	0.02	b. d. l.	0.01	0.08	0.05	0.02	0.03
MgO	19.8	34.2	13.3	9.8	1.41	2.9	0.02	0.03	0.02	0.01	6.25	5.14	2.63	7.49	b. d. l.	0.10
FeO	19.8	3.62	8.22	16.0	22.6	18.0	1.11	1.54	0.33	0.07	10.07	3.87	6.39	6.30	0.08	0.38
MnO	0.17	b. d. l.	0.11	0.25	0.15	1.35	0.04	0.01	1.10	0.08	0.11	0.07	0.10	0.03	b. d. l.	0.03
CaO	0.92	0.06	22.1	19.2	2.91	5.07	16.5	16.6	32.4	33.4	0.69	0.12	20.8	17.4	25.4	26.5
Na ₂ O	0.19	0.11	0.50	0.51	10.7	9.53	0.02	b. d. l.	8.23	8.14	0.52	0.19	0.28	0.54	0.08	0.08
K ₂ O	0.02	0.02	0.01	0.01	0.06	0.34	0.09	0.14	b. d. l.	0.00	7.54	10.5	0.01	0.10	b. d. l.	0.00
Total	86.7	86.7	100.2	98.6	96.1	95.1	88.2	88.8	95.1	95.2	95.0	95.0	86.3	90.4	92.2	94.4
Cations p. f. u.^a																
Si	3.172	3.123	1.744	1.800	8.173	8.065	2.005	2.006	3.006	3.010	3.609	3.665	2.947	2.920	3.002	2.970
Ti	0.001	0.003	0.075	0.059	0.009	0.049	0.005	0.008	0.002	0.000	0.028	0.003	0.029	0.009	0.001	0.011
Al	1.813	1.685	0.298	0.227	0.878	0.885	1.993	1.975	0.000	0.004	1.385	1.636	2.191	2.156	2.036	2.012
Cr	0.021	0.047	0.001	0.003	0.002	0.001	0.001	0.001	0.000	0.001	0.000	0.001	0.005	0.003	0.001	0.002
Mg	3.055	4.846	0.745	0.576	0.321	0.672	0.001	0.002	0.001	0.001	0.643	0.516	0.339	0.908	0.000	0.010
Fe	1.712	0.287	0.258	0.526	2.895	2.308	0.049	0.068	0.015	0.003	0.582	0.218	0.462	0.428	0.004	0.022
Mn	0.015	0.000	0.003	0.008	0.019	0.176	0.002	0.000	0.053	0.004	0.006	0.004	0.007	0.002	0.000	0.002
Ni	0.000	0.000	0.000	0.000	0.005	0.000	0.000	0.000	0.000	0.000	0.000	0.000	0.000	0.001	0.000	0.000
Ca	0.102	0.006	0.889	0.807	0.479	0.834	0.932	0.933	1.964	2.019	0.051	0.009	1.922	1.515	1.928	1.976
Na	0.038	0.020	0.036	0.039	3.184	2.836	0.002	0.000	0.904	0.890	0.069	0.025	0.047	0.085	0.011	0.010
K	0.003	0.002	0.000	0.001	0.011	0.067	0.006	0.009	0.000	0.000	0.664	0.900	0.001	0.010	0.000	0.000
Sum	9.931	10.019	4.050	4.046	15.976	15.894	4.997	5.002	5.944	5.933	7.037	6.976	7.950	8.039	6.984	7.017

^a Cations p. f. u. calculated on the basis of 14 O for Chl, 6 O for Cpx, 23 O for Gln, 8 O for Lws, 8.5 O for Pct, 11 O for Ph, 12 O for Pmp, 11 O for Prh. Abbreviations: Chl, chlorite; Cpx, clinopyroxene; Gln, glaucophane; Lws, lawsonite; Pct, pectolite; pfu, per formula unit; Ph, phengite; Pmp, pumpellyite; Prh, prehnite.

Table A.2.2 Pore water Sr concentrations and isotopic compositions.

Sample	Seamount	Depth (m b. s. f) ^a	Sr (μM)	$^{87}\text{Sr}/^{86}\text{Sr}$
U1492C-1H-2	Yinazao	0.0	536	0.705 98
U1492C-1H-4	Yinazao	0.0	660	0.705 84
U1492C-3F-1	Yinazao	7.0	688	0.705 66
U1492C-3F-2	Yinazao	7.0	687	0.705 66
U1492C-5F-2	Yinazao	14.2	667	0.705 68
U1492C-8F-2	Yinazao	28.2	679	0.705 66
U1492C-11F-2	Yinazao	37.6	681	0.705 67
U1492C-12F-1	Yinazao	42.3	688	0.705 69
U1492C-13F-1	Yinazao	47.0	687	0.705 67
U1492C-16F-1	Yinazao	61.1	503	0.705 94
U1492C-19F-2	Yinazao	75.2	613	0.705 69
U1492C-22F-1	Yinazao	89.3	741	0.705 67
U1492C-24F-2	Yinazao	98.7	738	0.705 67
U1492C-26F-1	Yinazao	108.1	729	0.705 66
U1492C-27F-1	Yinazao	112.8	746	0.705 67
U1497A-2F-2	Fantangisña	0.9	265	0.705 85
U1497A-6F-1	Fantangisña	16.7	629	0.704 95
U1497B-3F-2	Fantangisña	8.4	336	0.705 73
U1497B-6F-1	Fantangisña	17.8	584	0.705 07
U1496A-2F-1	Asùt Tesoru	3.2	15	0.705 14
U1496A-3F-4	Asùt Tesoru	7.9	20	0.705 15
U1496A-6F-3	Asùt Tesoru	22.0	17	0.705 16
U1496A-9F-1	Asùt Tesoru	36.1	20	0.705 27
U1496B-2F-1	Asùt Tesoru	1.9	9	0.705 88
U1496B-3F-2	Asùt Tesoru	6.6	11	0.705 26
U1496B-3F-5	Asùt Tesoru	6.6	12	0.705 17
U1496B-5F-2	Asùt Tesoru	16.0	10	0.705 10
U1496C-12G-3	Asùt Tesoru	98.8	21	0.705 76
U1496C-13G-3	Asùt Tesoru	102.5	22	0.705 49
U1496C-WSTP ^b	Asùt Tesoru	42.0	87	0.706 75

^a Given depths are tops of individual cores.

^b WSTP is water-sampling temperature probe; the sample was collected 9.5 days after circulation of drilling fluids had ceased in the bore hole; see Fryer et al. (2018e) for details.

A.3 Supplementary Information to Chapter 4, 'Shallow subduction zone serpentinization'

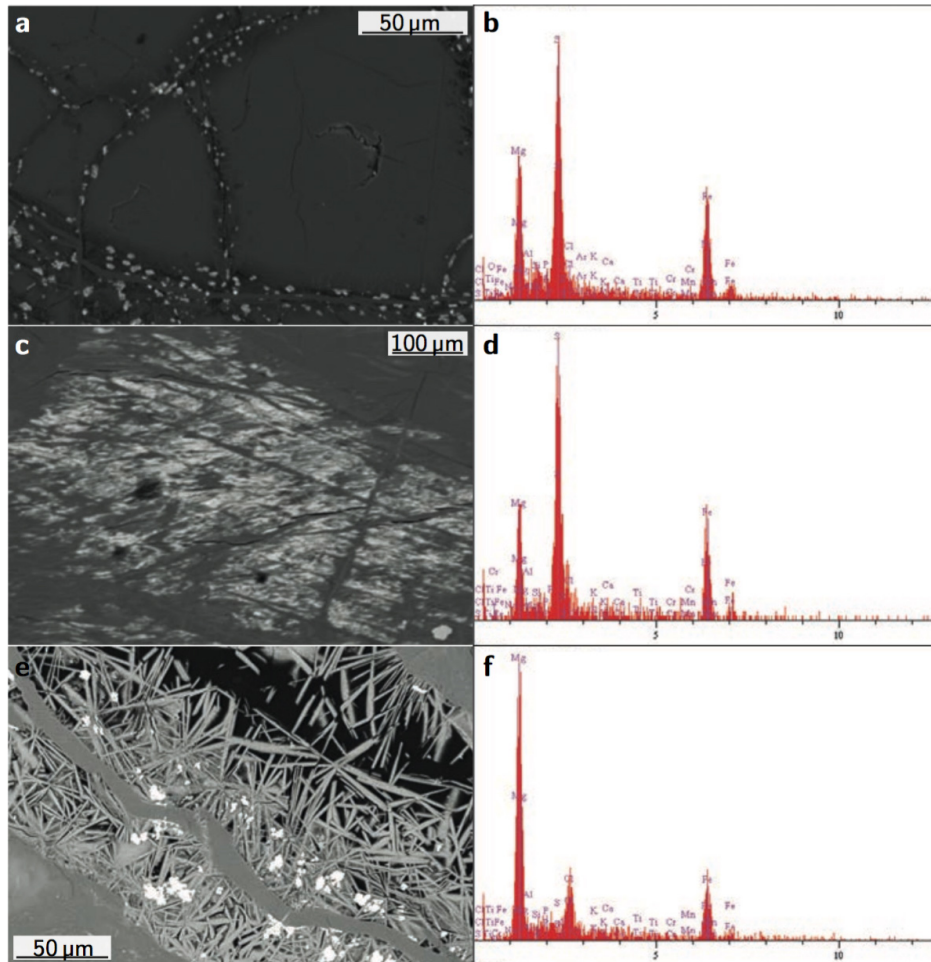


Figure A.3.1 SEM images and EDX spectra of alteration assemblages. (a, b) Minute S-rich phases, presumably awaruite, surrounding an olivine grain (sample U1498B-2R-1, 6–8 cm). (c, d) Blackened bastite serpentine that is rich in S-rich phases, presumably sulfides (sample U1492A-1H-3, 115–135 cm B). Also note the hydroandradite grain at the lower right (light gray). (e, f) Late acicular iowaite that grew in void space (sample U1492C-1H-2, 18–20 cm). The bright phases are Fe-oxides, presumably hematite.

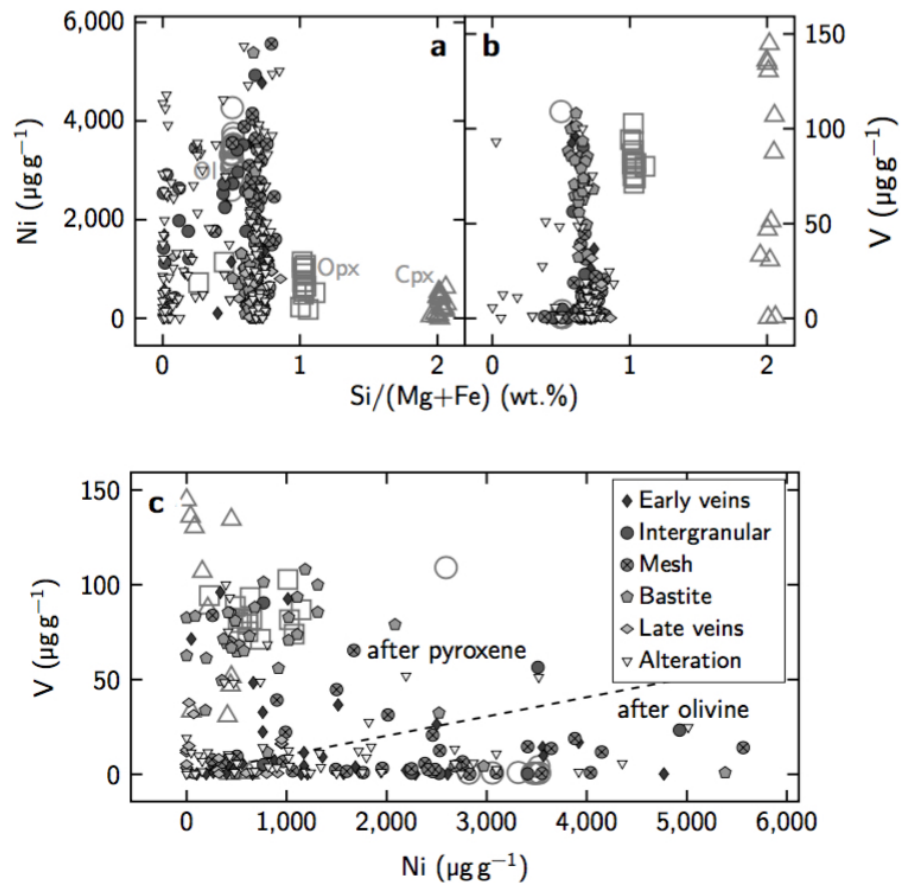


Figure A.3.2 Variations of Ni and V *vs.* Si/(Mg+Fe) in primary and secondary minerals. **(a)** Elevated Ni contents in serpentine after olivine reflect high concentrations in their precursors. Concentrations are considerably lower in areas with serpentine–brucite intergrowth, i. e., with lower Si/(Mg+Fe), in bastites, and in later-stage serpentine. **(b)** Conversely, V is elevated mainly in bastites, whereas serpentine after olivine and in later veins have low V contents. **(c)** Serpentine precursor minerals can be identified by their Ni *vs.* V characteristics.

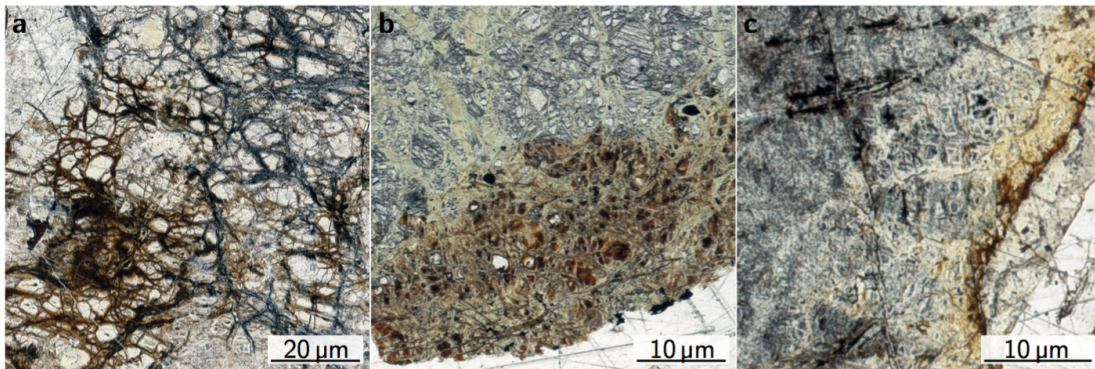


Figure A.3.3 Alteration-affected samples. (a) Browning along veins (sample U1498B-2R-1, 6–8 cm, PPL). (b, c) Inward-migrating browning (samples U1496C-11R-1, 28–30 cm, and U1494A-1F-3, 60–62 cm). All panels in plane polarized light.

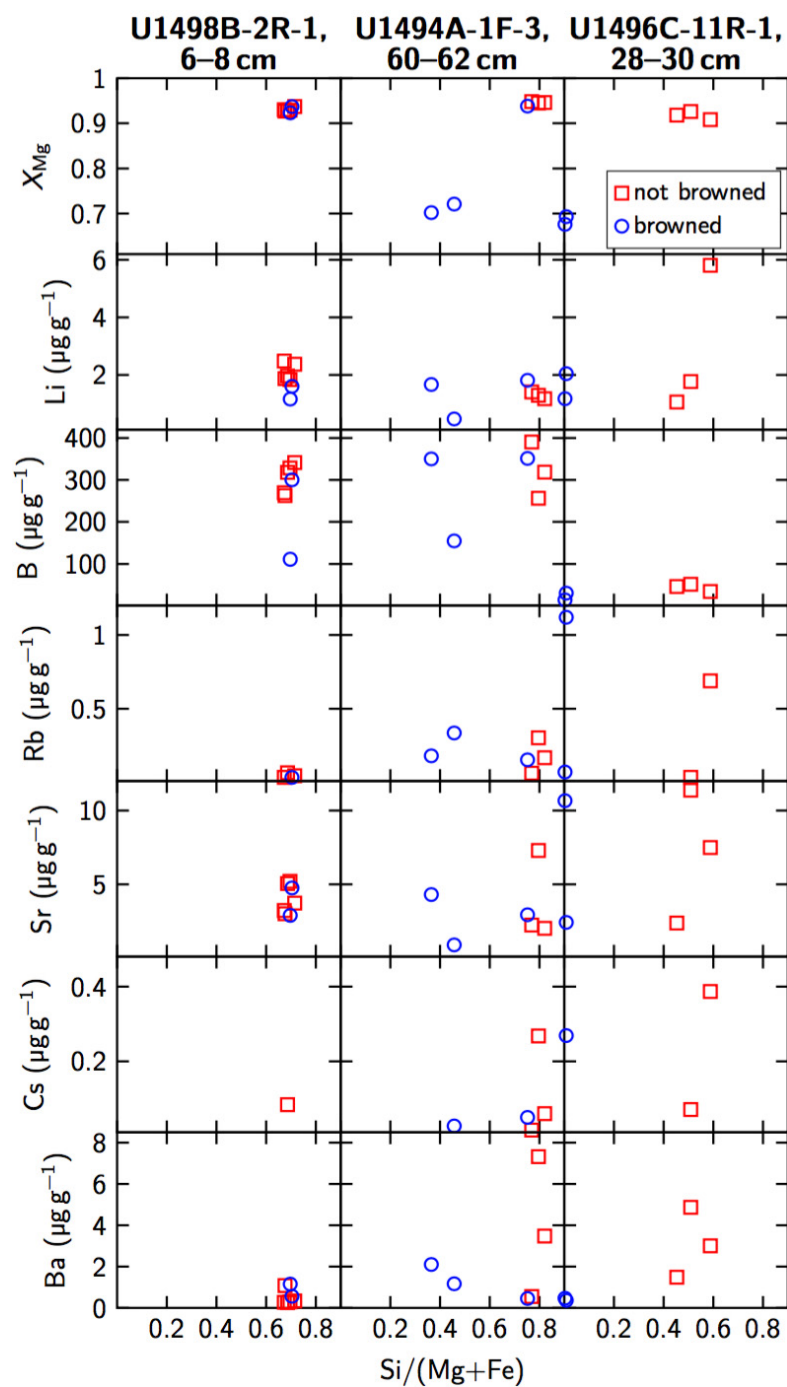


Figure A.3.4 Comparison of FME contents in areas affected by brownning *vs.* areas unaffected by brownning. Browned areas generally exhibit similar or lower FME concentrations, implying that no further enrichment took place during this alteration stage.

Table A.3.1 Analytical quality of laser ablation ICP-MS analyses.

	Li	B	V	Rb	Sr	Cs	Ba
Calibration std.	BHVO-2G	NIST 610	BHVO-2G	BHVO-2G	BHVO-2G	NIST 610	BHVO-2G
NIST 610							
Mean	432	–	392	413	484	–	416
Std. dev.	18	–	12	15	11	–	8
Reference value	471	–	449	419	504	–	431
BHVO-2G							
Mean	–	5.46	–	–	–	0.091	–
Std. dev.	–	1.89	–	–	–	0.053	–
Reference value	–	n/a	–	–	–	0.100	–
BCR-2G							
Mean	9.22	7.77	412	48.5	347	1.24	698
Std. dev.	0.47	1.79	17	2.3	9	0.06	16
Reference value	9.00	6.00	425	47.0	342	1.16	683

All values in $\mu\text{g g}^{-1}$.

Abbreviations: dev., deviation; n/a, not available; std., standard.

B Additional publications related to this PhD project

Peer-reviewed articles

Shallow forearc mantle dynamics and geochemistry: New insights from the IODP Expedition 366

Authors Baptiste Debret, **Elmar Albers**, Bastien Walter, Roy Price, Jaime D. Barnes, Hugues Beunon, Sebastien Facq, David P. Gillikin, Nadine Mattielli, Helen Williams

Publication status Debret, B., Albers, E., Walter, B., Price, R., Barnes, J.D., Beunon, H., Facq, S., Gilliken, D.P., Mattielli, N., Williams, H. (2019) *Shallow forearc mantle dynamics and geochemistry: New insights from IODP Expedition 366*, *Lithos* 326–327, 230–245. doi:[10.1016/j.lithos.2018.10.038](https://doi.org/10.1016/j.lithos.2018.10.038)

Abstract The Mariana forearc is a unique setting on Earth where serpentinite mud volcanoes exhume clasts originating from depths of 15 km and more from the forearc mantle. These peridotite clasts are variably serpentinized by interaction with slab derived fluid, and provide a record of forearc mantle dynamics and changes in geochemistry with depth. During International Oceanic Discovery Program (IODP) Expedition 366, we recovered serpentinized ultramafic clasts contained within serpentinite muds of three different mud volcanoes located at increasing distance from the Mariana trench and at increasing depth to the slab/mantle interface: Yinazao (distance to the trench: 55 km / depth to the slab/mantle interface: 13 km), Fantangisña (62 km / 14 km) and Asùt Tesoru (72 km / 18 km). Four different types of ultramafic clasts were recovered: blue serpentinites, lizardite-serpentinites, antigorite/lizardite- and antigorite-serpentinites. Lizardite-serpentinites are primarily composed of orange serpentine, forming mesh and bastite textures. Raman and microprobe analyses revealed that these textures contain a mixture of Fe-rich brucite ($X_{Mg} \sim 0.84$) and lizardite/chrysotile. Antigorite/lizardite- and antigorite-serpentinites record the progressive recrystallization of mesh and bastite textures to antigorite, magnetite and pure Fe-poor brucite ($X_{Mg} \sim 0.92$). Oxygen isotope compositions of clasts and pore fluids showed that the transition from lizardite to antigorite is due to the increase in temperature from 200 °C to about 400 °C within the forearc area above the slab/mantle interface. Lizardite-, antigorite/lizardite- and antigorite-serpentinites displayed U-shaped chondrite normalized Rare Earth Element (REE) patterns and are characterized by high fluid mobile element concentrations (Cs, Li, Sr, As, Sb, B, Li) relative to abyssal

peridotites and/or primitive mantle. The recrystallization of lizardite to antigorite is accompanied by a decrease in Cs, Li and Sr, and an increase in As and Sb concentrations in the bulk clasts, whereas B concentrations are relatively constant. Some clasts are overprinted by blue serpentine, often in association with sulfides. Most of these blue serpentinites were recovered at Yinazao and the uppermost units of Fantangisña and Asùt Tesoru suggesting alteration in the shallower portions of the forearc, possibly during exhumation of the clasts. This episode of alteration resulted in a flattening of REE spectra and an increase of Zn concentrations in serpentinites. Otherwise, no systematic changes of ultramafic clasts chemistry or mineralogy were observed with increasing depth to the slab. The samples document previously undescribed prograde metamorphic events in the shallow portions of the Mariana subduction zone, consistent with a continuous burial of the serpentinitized forearc mantle during subduction. Similar processes, induced by the interaction with fluids released from the downgoing slab, likely occur in subduction zones worldwide. At greater depth, breakdown of brucite and antigorite will result in the massive transfer of fluids and fluid mobile elements, such as As, Sb and B, to the source of arc magmas.

Cruise reports

Proceedings of the International Ocean Discovery Program, Volume 366

Authors Patricia Fryer, C. Goeffrey Wheat, Trevor Williams, **Elmar Albers**, Barbara Bekins, Baptiste P. R. Debret, Jianghong Deng, Yanhui Dong, Philip Eickenbusch, Emanuelle A. Frery, Yuji Ichiyama, Kevin Johnson, Raymond M. Jonston, Richard T. Kevorkian, Walter Kurz, Vitor Magalhaes, Simone S. Mantovanelli, Walter Menapace, Catriona D. Menzies, Katsuyoshi Michibayashi, Craig L. Moyer, Kelli K. Mullane, Jung-Woo Park, Roy E. Price, Jeffrey G. Ryan, John W. Shervais, Shino Suzuki, Olivier, J. Sissmann, Ken Takai, Bastien Walter, Rui Zhang

Published as Fryer, P., Wheat, C.G., Williams, T., the Expedition 366 Scientists (2018) *Mariana Convergent Margin and South Chamorro seamount*, Proceedings of the International Ocean Discovery Program 366, College Station (TX), doi:[10.14379/iodp.proc.366.101.2018](https://doi.org/10.14379/iodp.proc.366.101.2018).

Expedition 366 Preliminary Report: Mariana convergent margin and South Chamorro seamount

- Authors* Patricia Fryer, C. Goeffrey Wheat, Trevor Williams, **Elmar Albers**, Barbara Bekins, Baptiste P. R. Debret, Jianghong Deng, Yanhui Dong, Philip Eickenbusch, Emanuelle A. Frery, Yuji Ichiyama, Kevin Johnson, Raymond M. Jonston, Richard T. Kevorkian, Walter Kurz, Vitor Magalhaes, Simone S. Mantovanelli, Walter Menapace, Catriona D. Menzies, Katsuyoshi Michibayashi, Craig L. Moyer, Kelli K. Mullane, Jung-Woo Park, Roy E. Price, Jeffrey G. Ryan, John W. Shervais, Shino Suzuki, Olivier, J. Sissmann, Ken Takai, Bastien Walter, Rui Zhang
- Published as* Fryer, P., Wheat, C.G., Williams, T., the Expedition 366 Scientists (2017) *Expedition 366 Preliminary Report: Mariana convergent margin and South Chamorro seamount*, International Ocean Discovery Program, doi:[10.14379/iodp.pr.366.2017](https://doi.org/10.14379/iodp.pr.366.2017).

Geology and hard rock petrology

- Authors* Alexander Diehl, **Elmar Albers**, Christopher R. German, Kevin P. Hand, Wolfgang Bach
- Published as* Diehl, A., Albers, E., German, C.R., Hand, K.P., Bach, W., *Geology and hard rock petrology*, in: Boetius A, Purser A (eds.) *The expedition PS101 of the Research Vessel POLARSTERN to the Arctic Ocean in 2016*, Reports on Polar and Marine Research 706, 41–50, doi:[10.2312/BzPM_0706_2017](https://doi.org/10.2312/BzPM_0706_2017).

Physical oceanography and biogeochemistry of hydrothermal plumes

- Authors* Maren Walter, **Elmar Albers**, Jana Bäger, Alexander Diehl, Chris German, Kevin P. Hand, Myriel Horn, Janna Köhler, Jill McDermott, Massimiliano Molari, Bermann Steimacher, Gunter Wegener, Laura Wischnewski, Christian Mertens, Jürgen Sültenfuß, Mario Hoppmann, Ellen Damm, Wolfgang Bach, Jeff Seewald
- Published as* Walter, M., Albers, E., Bäger, J., Diehl, A., German, C., Hand, K.P., Horn, M., Köhler, J., McDermott, J., Molari, M., Steimacher, B., Wegener, G., Wischnewski, L., Mertens, C., Sültenfuß, J., Hoppmann, M., Damm, E., Bach, W., Seewald, J. (2017) *Physical oceanography and biogeochemistry of hydrothermal plumes*, in: Boetius A, Purser A (eds.) *The expedition PS101 of the Research Vessel POLARSTERN to the Arctic Ocean in 2016*, Reports on Polar and Marine Research 706, 63–80, doi:[10.2312/BzPM_0706_2017](https://doi.org/10.2312/BzPM_0706_2017).

Conference contributions

Carbon cycling in the shallow Mariana forearc

Authors **Elmar Albers**, Frieder Klein, Wolfgang Bach
Presented as Conference talk at the IODP Exp. 366 post-cruise meeting, 09/2018, Honolulu (HI), USA

Role of the forearc in the geochemistry of subduction zones: new insights from the IODP Expedition 366

Authors Baptiste Debret, Nadine Mattielli, **Elmar Albers**, Bastien Walter, Roy Price, Jaime D. Barnes, Hugues Beunon, Helen Williams
Presented as Conference talk at the Goldschmidt Conference, 08/2018, Boston (MA), USA

Carbon mobilisation in the shallow Mariana subduction zone: insights from IODP Exp. 366

Authors **Elmar Albers**, Frieder Klein, Wolfgang Bach, the Expedition 366 Scientists
Presented as Conference talk at the EGU Galileo Conference, 06/2018, Leibnitz, Austria*

Carbonate–silicate–sulfate veins in metavolcanic clasts recovered from serpentinite mud volcanoes in the Mariana forearc (IODP Exp. 366)

Authors **Elmar Albers**, Frieder Klein, Wolfgang Bach, the Expedition 366 Scientists
Presented as Conference poster at the EGU General Assembly, 04/2018, Vienna, Austria

IODP Expedition 366: Mariana convergent margin & South Chamorro seamount

Authors **Elmar Albers**, Walter Menapace, the Expedition 366 Scientists
Presented as Cruise report at the IODP/ICDP Kolloquium, 03/2018, Bochum, Germany

IODP Exp. 366 to the Mariana forearc: blue mud from serpentinite mud volcanoes

Authors **Elmar Albers**, the Expedition 366 Scientists
Presented as Conference talk at the GeoBremen, 09/2017, Bremen, Germany

Polyphase alteration of ultramafic clasts from a serpentinite mud volcano (Mariana forearc) unveils shallow subduction zone processes

Authors Lena Beyer, **Elmar Albers**, Wolf-Achim Kahl, Wolfgang Bach, the Expedition 366 Scientists

Presented as Conference poster at the GeoBremen, 09/2017, Bremen, Germany

High-temperature hydration of melt impregnated lithospheric mantle in the 15°20' N F. Z. area, MAR

Authors **Elmar Albers**, Tim Schroeder, Wolfgang Bach

Presented as Conference poster at the Goldschmidt Conference, 08/2017, Paris, France, abstract no. 45*

Geochemistry, physics, and dispersion of a Gakkel Ridge hydrothermal plume, 87° N, 56° E

Authors Jill McDermott, **Elmar Albers**, Wolfgang Bach, Alexander Diehl, Christopher German, Kevin Hand, Janna Koehler, Jeffrey Seewald, Maren Walter, Gunter Wegener, Laura Wischnewski

Presented as Conference talk at the Goldschmidt Conference, 08/2017, Paris, France, abstract no. 2654

Geological settings of hydrothermal vents at 6°15' W and 55°30' E on the Gakkel Ridge, Arctic Ocean

Authors Yann Marcon, Autun Purser, Alexander Diehl, **Elmar Albers**, Andreas Türke, Jill McDermott, Christopher German, Kevin Hand, Vera Schlindwein, Boris Dorschel, Gunter Wegener, Antje Boetius, Wolfgang Bach

Presented as Conference poster at the Goldschmidt Conference, 08/2017, Paris, France, abstract no. 2566

Ultramafic clasts from serpentine mud volcanoes (Mariana forearc)

Authors **Elmar Albers**, Wolfgang Bach, Wolf-Achim Kahl

Presented as Conference poster at the DMG Sektionstreffen Petrologie/Petrophysik & Geochemie, 06/2016, Bremen, Germany

* The Bremen International Graduate School for Marine Sciences (GLOMAR) is thanked for financial support to attend these conferences.